

A STUDY OF MICROWAVE INDUCED PLASMAS.

P.E.BURKE

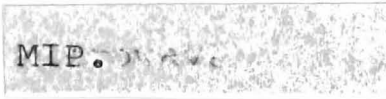
A THESIS SUBMITTED TO THE COUNCIL  
FOR NATIONAL ACADEMIC AWARDS AS  
PARTIAL FULFILMENT FOR THE DEGREE OF  
DOCTOR OF PHILOSOPHY.

SCHOOL OF APPLIED PHYSICS,  
POLYTECHNIC OF NORTH LONDON.  
AND  
PYE UNICAM LTD., CAMBRIDGE.

MARCH 1987.

## Contents

Title Page.	
Contents List.	1
Acknowledgements.	5
List of Figures.	6
List of Tables.	9
Abstract.	11
Chapter 1	The MIP used for Spectrochemical Analysis. 12
1.1	Introduction. 12
1.2	Sample Introduction Techniques. 17
1.2.1	Pneumatic Nebulizers. 18
i)	Crossflow Nebulizer.
ii)	Concentric Nebulizer.
iii)	Babington Nebulizer.
1.2.2	Ultrasonic Nebulizers. 21
1.2.3	Spray Chambers 23
1.2.4	Aerosol Desolvation and Dry Sample Introduction Techniques. 26
1.2.5	Discharge Tubes and Plasma Stability. 28
1.3	Introduction to Plasma Diagnostics and Plasma Models. 30
1.3.1	Plasma Diagnostics 31
1.3.2	Plasma Models 32
i)	The Thermal Equilibrium Model.
ii)	The Local Thermal Equilibrium Model.
iii)	The Partial Local Thermal Equilibrium Model.
iv)	The Radiative Ionisation Recombination Model.
v)	The Saturation Phase Model.
Chapter 2	Introduction to the Microwave Aspects of the MIP. 37
2.1	Microwave Cavity Review. 37
2.2	Transmission Line Theory Applied to the design of a Microwave Cavity. 45
2.3	The Scattering Parameter Representation of the Slab-line Cavity. 47

Chapter 3	Spectroscopic Instrumentation.	53
3.1	Configurations of MIP Investigated.	53
3.2	The Entrance Optical System and Calibration Lamp.	61
3.3	The Monochromator and it's Operation.	65
3.4	The Photomultiplier Tube.	68
3.5	The DC Amplifier.	70
3.6	Data Recording Devices.	74
3.6.1	Pen Chart Recorder	74
3.6.1	Data Logger	77
3.7	Calibration of the Optical System.	79
3.8	Determination of Spectral Line Intensity.	84
3.8.1	Determination of Line Area by Simpson's Method.	86
3.8.2	Determination of Line Area by Data Logger.	88
Chapter 4	Impedance Measurements on the MIP. 	89
4.1	Tuning of the Unloaded Slab-line Cavity.	89
4.2	Microwave Plasma Excitation and Measurement System.	94
4.3	Microwave Measurements Method.	97
4.4	Relationship Between Load Impedance and Electron Density.	100
4.5	Microwave Impedance of the Dry Argon MIP.	103
4.5.1	Dependence of Impedance on Argon Flowrate and Input Power.	103
4.5.2	Dependence of Impedance on Dimensions of Discharge Tube.	108
4.5.3	Dependence of Impedance on Water Vapour Content of Argon Plasma Gas.	109
4.6	Preliminary Discussion of Impedance Results.	110

Chapter 5	Spectroscopic Measurements on the MIP.	111
5.1	Argon Excitation Temperature.	113
5.1.1	Argon Excitation Temperature of the Dry Argon MIP.	117
5.1.2	Argon Excitation Temperature of the Analytical MIP.	121
5.2	Iron Excitation Temperature.	131
5.3	OH Rotational Temperature.	136
5.3.1	Rotational Temperature of the Dry Argon MIP.	139
5.3.2	Rotational Temperature of the Analytical MIP.	141
5.4	Electron Density Measurements.	144
5.4.1	Practical Electron Density Measurements in the MIP.	147
5.4.2	Electron Density in the Dry Argon MIP.	154
5.4.3	Electron Density in the Analytical MIP.	161
Chapter 6	The Spectrochemical Investigation of the MIP.	166
6.1	Introduction.	166
6.2	Modifications to the Detection System.	168
6.2.1	The Brookdeal Amplifier.	169
6.2.2	The Signal Integrator.	170
6.2.3	The Light Path Chopper.	171
6.3	Sample Introduction Systems.	172
6.3.1	The Nebulizer.	172
	A) The Crossflow Nebulizer.	
	B) The Babington Nebulizer.	
6.3.2	The Spray Chamber, Discharge Tube and Drain.	175
6.3.3	Sample Solution Preparation and Delivery.	181
6.4	Definition of Spectrochemical Parameters.	183



6.5	Optimization of the Plasma Operation Parameters.	186
6.5.1	Optimization of the Viewing Position.	186
6.5.2	Optimization of the Sample Uptake Rate.	189
6.6	Results for the MIP Generated in the Slab-line Cavity.	191
6.6.1	Detection Limits.	191
6.6.2	Matrix Factors.	195
6.7	Results for the MIP Generated in the $TM_{010}$ Cavity.	197
6.7.1	Detection Limits.	197
6.7.2	Matrix Factors.	199
6.8	Discussions on Spectrochemical Performance.	200
6.8.1	Performance of MIP's Investigated.	200
6.8.2	Comparison of Spectrochemical Results with Published Values for the MIP.	202
6.8.3	Comparison of Spectrochemical Results with Published Values for Competing Analytical Plasma Systems.	207
Chapter 7	Conclusions.	216
7.1	Plasma Models Applicable to the MIP.	216
7.2	Conclusions on Simultaneous Electron Density and Plasma Load Impedance Measurements.	221
7.3	Correlation Between Electron Density and Matrix Factors in the Analytical MIP Generated in the Slab-line Cavity.	222
	List of References.	224
Appendix A1	Scattering Parameter Representation of a General Two Port Network.	a1
A2	Engineering Drawings of the $TM_{010}$ Cavity and Input Coupling.	a5
A3	Microwave Impedance Computer Program.	a8
A4	Spectral Line Intensity Computer Program.	a19
A5	Electron Density, Spectral Line Profile Convolution Computer Program.	a26

### Acknowledgements.

I would like to thank the many people who have assisted in this work, too many to mention by name but in particular my supervisors, Dr M Outred and Mr L R Morris. I am grateful to the Science and Engineering Research Council and Pye-Unicam (Cambridge) for their financial assistance. Special thanks to my typist, Mrs E Kilbey and also to Sally for her patience.

### Statement of Advanced Studies Undertaken in Connection with the Programme of Research.

The list of lecture, short course and conferences attended may be found in the pocket at the back of the thesis. Attendance on these courses was intended to provide the necessary knowledge as required by CNAA regulations 3.8 - 3.10.

### Material Previously Published.

A summary of the research work dealing with the atmospheric pressure argon MIP incorporating sample aerosol introduction was presented in the form of a poster at the 23rd Colloquium Spectroscopicum Internationale (CSI) in Amsterdam, 1983. The abstract of this work, published in Spectrochim Acta 38B, Supplement (1983) is located in the back pocket of the thesis.

## List of Figures.

Figure 1.1	Typical MIP System for the Spectrochemical Analysis of Solutions.	16
Figure 1.2	The Crossflow, Concentric and Babington Nebulizers.	19
Figure 1.3	The Ultrasonic Nebulizer.	22
Figure 1.4	The Scott and ICP Type Spray Chamber.	24
Figure 1.5	Novel Discharge Tube for use with MIP.	29
Figure 2.1	The $3\lambda/4$ Broida Cavity, $\lambda/4$ Evenson Cavity and the $TM_{013}$ Cavity.	38
Figure 2.2	The $TM_{010}$ Cavity and the Slab-line Cavity.	40
Figure 2.3	The Capacitively Coupled Microwave Plasma and the Surfatron.	43
Figure 2.4	The $\lambda/2$ Slab-line Cavity.	47
Figure 2.5	Schematic of $\lambda/4$ Slab-line Cavity.	51
Figure 3.1	Gas Supply Apparatus for the Dry Argon MIP.	54
Figure 3.2	Configurations of MIP Generated in the Slab-line Cavity.	55
Figure 3.3.	Plate of Analytical MIP Generated in the Slab-line Cavity.	57
Figure 3.4	MIP Generated in the $TM_{010}$ Cavity.	59
Figure 3.5	Optical Measurement System and Associated Equipment.	62
Figure 3.6	Entrance Optics Arrangement for the $TM_{010}$ Cavity.	64
Figure 3.7	PMT Dynode Biasing Circuit.	69
Figure 3.8	Schematic of DC Amplifier.	71
Figure 3.9	Equipment to Check Dynamic Range of DC Amplifier.	73
Figure 3.10	DC Amplifier Calibration Curve.	73
Figure 3.11	Interconnection Schematic for Data Recording Devices.	75
Figure 3.12	Optical System Calibration Curve.	80
Figure 3.13	Observed Spectral Line and Output Profile.	83
Figure 3.14	Observed Spectral Lines and Output Profiles.	85
Figure 3.15	Line Area Determined Using Simpson's Method.	87
Figure 3.16	Automatic Determination of Line Area.	87

Figure 4.1	Microwave System for Measuring Phase of Cavity Input Reflection Coefficient.	90
Figure 4.2	Slab-line Cavity Inner Conductors.	92
Figure 4.3	Phase of Cavity Input Reflection Coefficient versus Frequency.	93
Figure 4.4	System for Excitation of MIP and Measurement of Plasma Impedance.	95
Figure 4.5	Measurement Sequence for Method of Bracketing.	97
Figure 4.6	Real and Imaginary Parts of Complex Load Impedance as a Function of Microwave Input Power.	104
Figure 4.7	Real and Imaginary Parts of Complex Load Impedance as a Function of Flowrate.	106
Figure 4.8	Real Part of Complex Load Impedance as a Function of Gas Flowrate. <del>Impedance as a Function of Flowrate</del> Transposition of Data in Figure 4.7.	106
Figure 5.1	Viewing Zone in the Dry Argon MIP Generated in the Slab-line Cavity.	116
Figure 5.2	Graph of $\ln(I \lambda / gA)$ vs E for Ar I.	118
Figure 5.3	Viewing Zones Used by the Optical Measurement System for Analytical MIP Generated in Slab-line Cavity.	120
Figure 5.4	Graph of $\ln(I \lambda / gA)$ vs E for Ar I.	122
Figure 5.5	Graph of $\ln(I \lambda / gA)$ vs E for Ar I.	125
Figure 5.6	Graph of $\ln(I \lambda / gA)$ vs E for Ar I.	126
Figure 5.7	Graph of $\ln(I \lambda / gA)$ vs E for Ar I.	129
Figure 5.8	Graph of $\ln(I \lambda^3 / g_1 f)$ vs E for Fe I.	134
Figure 5.9	Graph of $\log I_K - \log A_K$ vs E for OH.	140
Figure 5.10	Graph of $\log I_K - \log A_K$ vs E for OH.	142
Figure 5.11 a)	Experimental and Theoretical $H_\beta$ Profiles.	150
Figure 5.11 b)	Experimental and Theoretical $H_\beta$ Profiles	151
Figure 5.12	Dependence of Electron Density on Position in Dry Argon MIP Generated in Slab-line Cavity.	153
Figure 5.13	Electron Density and $H_\beta$ Intensity as a Function of Flowrate in the Dry Argon MIP Generated in the Slab-line Cavity.	155
Figure 5.14	Electron Density as a Function of Microwave Input Power in Dry Argon MIP.	157

Figure 5.15	Enlarged View of Slab-line Cavity Inner Conductor and Discharge Tubes.	160
Figure 6.1	The Crossflow Nebulizer.	173
Figure 6.2	The Babington Nebulizer.	173
Figure 6.3	Baffled Spray Chamber.	176
Figure 6.4	ICP Type Spray Chamber.	178
Figure 6.5	The Pulse Damper.	182
Figure 6.6	Analyte, Background and Net Line Signals.	183
Figure 6.7	Plate of Analytical MIP Generated in Slab-line Cavity.	185
Figure 6.8	Graph of $\sigma_B$ , SBR and $C_L$ as a Function of Position in Analytical MIP Generated in Slab-line Cavity.	187
Figure 6.9	Graph of $\sigma_B$ , SBR and $C_L$ as a Function of Sample Uptake Rate in Analytical MIP Generated in Slab-line Cavity.	190

## List of Tables.

Table 3.1	Equipment Used in the Optical System.	63
Table 3.2	Data Recording Devices Equipment.	76
Table 3.3	The Reference Wavelengths.	81
Table 4.1	Equipment Used to Tune the Unloaded Slab-line Cavity.	90
Table 4.2	Slab-line Cavity Parameters.	92
Table 4.3	Equipment to Produce MIP in Slab-line Cavity.	95
Table 4.4	Variation of Load Impedance as a Function of Discharge Tube Dimensions.	108
Table 4.5	Dependence of Impedance and Electron Density on Water Vapour Content of Argon Plasma Gas.	109
Table 5.1	MIP Spectral Features Observed.	111
Table 5.2	Spectral Line Data for Argon I.	114
Table 5.3	Argon Excitation Temperature as a Function of Flowrate in the Dry Argon MIP.	119
Table 5.4	Argon Excitation Temperature - Dependence on Position in Analytical MIP and Sample Uptake Rate.	123
Table 5.5	Argon Excitation Temperature in the Analytical MIP Generated in Slab-line Cavity - Dependence on Sample.	127
Table 5.6	Argon Excitation Temperature in the Analytical MIP Generated in $TM_{010}$ Cavity - Dependence on Sample.	130
Table 5.7	Spectral Line Data for Iron I.	132
Table 5.8	Iron Excitation Temperature in the Analytical MIP's Generated in the Slab- line and $TM_{010}$ Cavity.	135
Table 5.9	Spectral Line Data for OH.	137
Table 5.10	OH Rotational Temperature in the Analytical MIP's Generated in the Slab- line and $TM_{010}$ Cavity.	143
Table 5.11	Dependence of Electron Density on Flowrate in the Dry Argon MIP.	156
Table 5.12	Discharge Tube Sizes Used and Measured Electron Density.	159

Table 5.13	Dependence of Electron Density in the Analytical MIP on Viewing Zone and Sample Uptake Rate.	162
Table 5.14	Dependence of Electron Density on Sample Constituents in Analytical MIP Generated in Slab-line Cavity.	163
Table 5.15	Dependence of Electron Density on Sample Constituents in the Analytical MIP Generated in $TM_{010}$ Cavity.	165
Table 6.1	Table of Elements Investigated in MIP.	167
Table 6.2	Equipment Added to the Monochromator Detection System.	168
Table 6.3	Spectrochemical Results for the $0.1 \text{ l min}^{-1}$ MIP Generated in Slab-line Cavity.	192
Table 6.4	Spectrochemical Results for the $1.0 \text{ l min}^{-1}$ MIP Generated in Slab-line Cavity.	193
Table 6.5	Spectrochemical Results for the $1.0 \text{ l min}^{-1}$ MIP Generated in the $TM_{010}$ Cavity.	198
Table 6.6	Comparison of Detection Limits for Various MIP's.	203
Table 6.7	Comparison of Spectrochemical Results for MIP Generated in Slab-line Cavity with Competing Spectroscopic Analytical Systems.	208
Table 6.8	Matrix Factors for the Conventional ICP and MIP Generated in the Slab-line Cavity.	213
Table 6.9	Matrix Factors for the Low Flowrate ICP and MIP Generated in the Slab-line Cavity.	215
Table 7.1	Summary of Excitation and Electron Temperatures and Electron Densities in the MIP.	218

## ABSTRACT

### Microwave Induced Plasmas.

P.E.Burke.

In a microwave induced plasma (MIP) generated in argon under atmospheric pressure using slab-line and  $TM_{010}$  cavities, the electron density ( $N_e$ ), excitation and rotational temperatures, detection limit and matrix factor for nine elements and microwave impedance have been determined for a range of operation conditions.

Simultaneous measurement of  $N_e$  and microwave impedance in a dry argon MIP provide little evidence of a link between these two parameters in the slab-line cavity.

Two 'analytical' MIP's incorporating sample aerosol introduction have been used with the slab-line cavity. One being supported on an argon flowrate of  $0.1 \text{ l min}^{-1}$  using a Babington nebulizer, the other on a flowrate of  $1.0 \text{ l min}^{-1}$  using a crossflow nebulizer. The crossflow nebulizer was also used for an analytical MIP generated in a  $TM_{010}$  cavity.

Detection limits obtained for both analytical MIP's in the slab-line cavity were similar for the analytes used. In general, with  $1 \text{ mg ml}^{-1}$  K added, it has been noted that analyte signal was suppressed in the  $1.0 \text{ l min}^{-1}$  MIP, whereas enhancement occurred in the  $0.1 \text{ l min}^{-1}$  MIP. This was found to correlate with an increase and reduction respectively in  $N_e$ , the effect being attributed to slight positional changes of MIP.

Detection limits in the analytical MIP generated in the  $TM_{010}$  cavity were poorer than those found for the slab-line cavity, due mainly to lower signal to background ratios.

Spectroscopic measurement of  $N_e$ , excitation and rotational temperatures demonstrates a lack of LTE in any of the MIP's investigated. However pLTE may exist in certain parts of the analytical MIP generated in the slab-line cavity. In the dry argon MIP and at the optimum viewing zone used for spectrochemical analysis in all analytical MIP's, pLTE is unlikely and a collisional-radiative model may be more appropriate.



## Chapter 1. The MIP Used For Spectrochemical Analysis.

### 1.1 Introduction.

In recent years there has been a considerable amount of interest shown by analytical chemists in various types of gaseous plasmas as atomic excitation sources for use in spectrochemical analysis. This interest has undoubtedly been spurred by the growing demand there has been for accurate, sensitive and practical methods of analysing the constituents of a range of sample materials from industry, medicine and the natural environment. This demand has meant that plasma excitation sources have rapidly progressed from the experimental equipment of the physics laboratory to the commercial equipment found in analytical laboratories all over the world. A good example of this rapid progress is the inductively coupled plasma (ICP) which, from the early experiments of Greenfield et al, 1964 (1) when it's potential was first realised, has evolved into an extremely sensitive analytical tool capable of detection of most of the elements in the periodic table at low concentrations and in a variety of difficult chemical matrices. The conventional ICP is now regarded by many as the standard atomic emission source used in the spectrochemical analysis of solutions. This is probably due to the continued efforts of two research groups, that led by V.A.Fassel of the Ames Laboratory, Iowa, USA and the other by P.W.J.M. Boumans of the Philips Research Laboratory, Eindhoven, Netherlands.

The microwave induced plasma (MIP) has not developed at the same pace as the ICP but does offer distinct advantages in certain areas. The MIP may be operated at much lower gas flowrates and input powers than the ICP. Conventional ICP's typically operate at gas flowrates up to  $20 \text{ l min}^{-1}$  and RF input powers up to 2 kW whereas the MIP may be operated at a gas flowrate of as little as  $0.1 \text{ l min}^{-1}$  and 100 W of input power.

Like the ICP, argon has been the most popular choice of plasma gas for the MIP but other gases have been used, partly to identify plasma which provide more efficient excitation of analyte spectra and partly to reduce running costs. Beenakker, 1976 (2) suggested that an atmospheric pressure MIP operated in helium gave significantly better detection limits for certain elements compared to the argon MIP described by Dagnall et al, 1972 (3). A reduction in operating costs has been proposed by Deutsch and Hieftje, 1984 (4) for an MIP operated in nitrogen compared to an argon MIP although any savings would presumably be minimal considering the typically low gas consumption requirements of the MIP. Also, the intense molecular spectra emitted by such an MIP precludes the use of certain parts of the spectrum to avoid interference with analyte spectral lines. More significant reductions in operating costs might be expected from the nitrogen ICP described by Barnes et al, 1984 (5) compared to a conventional argon ICP.

The importance of these unfavourable comparisons between the ICP and the MIP cannot be over-emphasized in light of the recent development of the low flowrate ICP, which is a direct consequence of the high gas and power consumption requirements of the conventional ICP. Initial experiments using a normal size ICP torch, Allemand and Barnes, 1977 (6) succeeded in reducing gas consumption by a half. Greater reductions in gas flow and input power have been achieved by the minaturization of the ICP torch and modifications to the RF induction coil and power supply. Kornblum et al, 1979 (7) operated an ICP on a total argon flowrate of  $2 \text{ l min}^{-1}$  although rather poor detection limits were reported. The high gas consumption of the conventional ICP is primarily due to the cooling function of the outer gas flow, which if reduced without some other

provision for cooling being made, results in melting of the torch. Further developments of the low flow ICP have therefore concentrated on alternative means of cooling the torch. Kawaguchi et al, 1980 (8) have used a water cooled torch to operate an argon ICP at a total flowrate of  $5 \text{ l min}^{-1}$  whereas Ripson et al, 1982 (9) have operated an argon ICP at  $0.85 \text{ l min}^{-1}$  using a torch cooled by forced air.

There would always appear to have been a strong desire to view the MIP as a "miniature ICP" and in attempting to fulfill this desire we probably find the main reason why development of the MIP has lagged behind the ICP, namely the problems encountered when using direct sample aerosol introduction. The MIP is not particularly tolerant to large amounts of introduced water vapour and in many instances where the MIP has been used for the analysis of sample materials, these problems have been avoided by using a dry sample introduction technique. Beenakker et al, 1980 (10) used an electro-thermal atomizer (ETA) to introduce sample into a helium MIP and found this particularly successful in the determination of halogen compounds. Where an ICP type nebulizer has been used many experimenters, eg. Fallgatter et al, 1971 (11) have been forced to use some kind of aerosol desolvation apparatus to remove the majority of the water vapour prior to entering the plasma. However there are drawbacks involved with using desolvation apparatus, e.g. the memory effect, described by Boumans and de Boer, 1972 (12) which do not make this an attractive proposition for routine laboratory sample analysis.

An alternative to the MIP and ICP which will be considered in this thesis is the capacitively-coupled microwave plasma (CMP). The CMP described by Feuerbacher, 1981 (13) shares many common features with the MIP but instead of being confined within a discharge tube the plasma is formed in free air. The relative merits of this alternative spectroscopic source will be discussed in chapter 6.

The aim of the research reported in this thesis was to undertake a study of the fundamental physical properties of the atmospheric pressure argon MIP and to investigate their dependence on operating parameters, e.g. gas flow-rate, microwave input power and plasma constituents.

Relative spectral line intensity measurements have been made to determine argon and iron excitation temperatures,  $T_{\text{EXC}}$  and an OH molecular rotational temperature,  $T_{\text{ROT}}$ . The Stark broadened  $H\beta$  spectral line has been measured to determine the electron density,  $N_e$  (chapter 5).

For the dry argon MIP, the plasma impedance,  $Z_L$  has been determined from measurements on the standing wave set up on the transmission line connecting the microwave cavity to the generator (chapter 4).

Initial studies were made on an MIP produced using dry argon from an industrial cylinder but a further requirement was the development of a sample introduction system using a pneumatic nebulizer for the introduction of sample solutions into the plasma. This sample introduction system (chapter 6) was to function at the low plasma gas flowrates, less than  $1 \text{ l min}^{-1}$ , at which the MIP is capable of being sustained.

Further to this development, the spectrochemical performance of this 'Analytical' MIP with sample introduction system was to be assessed, related to the plasma's fundamental physical properties and compared to the analytical performance of the competing techniques of ICP and CMP.

Recent reviews of the MIP published in the literature e.g. Zander and Hieftje, 1981 (14) and Carnahan, 1983 (15) describe the current status of the MIP as an analytical tool. Also the thesis by Lichter, 1973 (16) includes an account of the history of the development of the MIP as an excitation source for use in spectrochemical analysis. The review presented here will therefore concentrate only on the most recent developments of the MIP, especially on those which have been found to be important in this work.

A review of the microwave cavities commonly used to generate both atmospheric and reduced pressure MIP's is deferred until chapter 2.

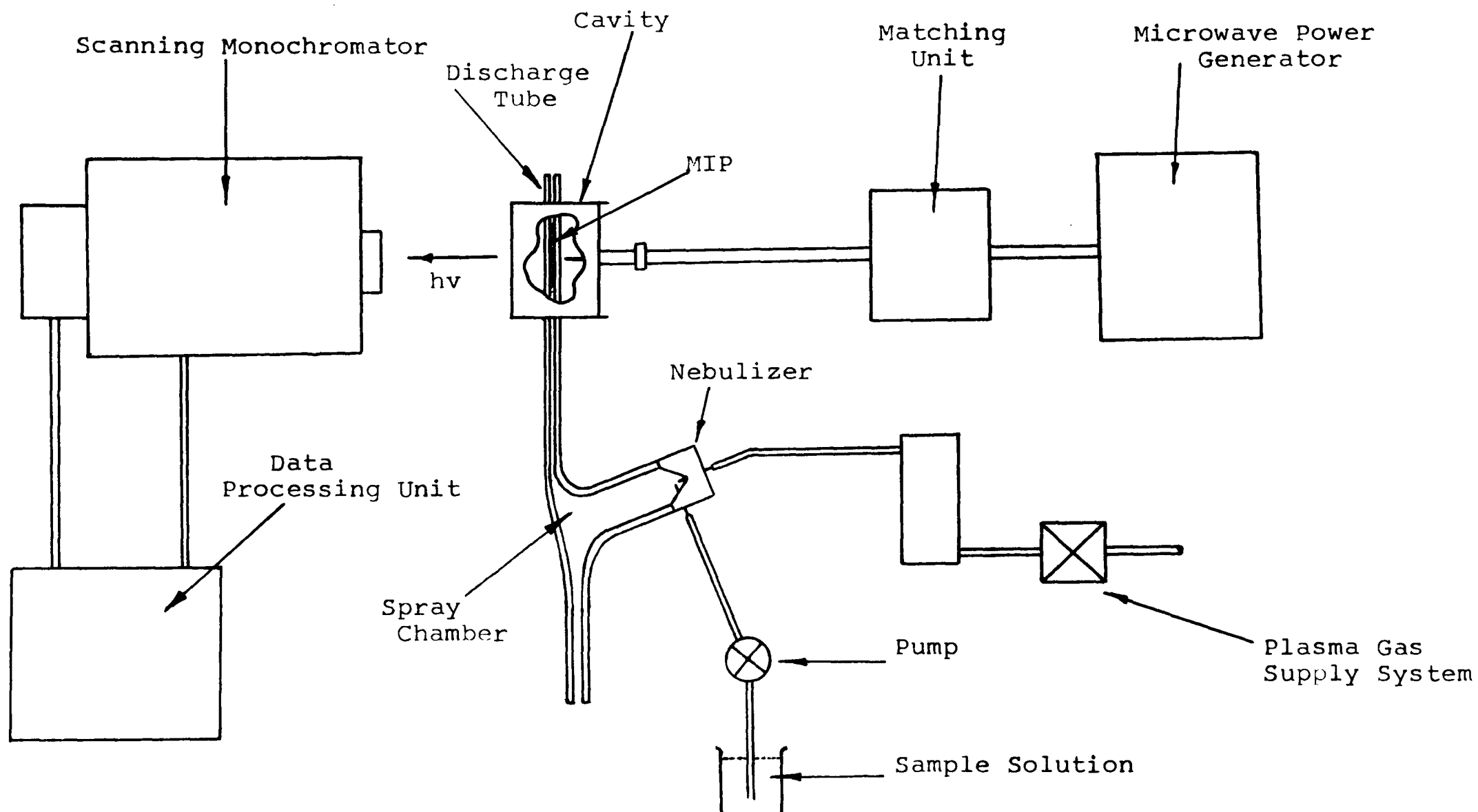


Figure 1.1    Typical MIP System for the Spectrochemical Analysis of Solutions

## 1.2 Sample Introduction Techniques.

There are a great variety of sample introduction techniques which have been used with the MIP, the most widespread of which has probably been the gas chromatograph, see e.g. Beenakker, 1977 (17). Apart from gas chromatography a popular method of sample introduction into the MIP has been to use a nebulizer, coupled to a spray chamber and feeding into the plasma often via some type of desolvation apparatus (figure 1.1 ). The following section will concentrate on this and associated techniques since a nebulizer has been used in this work.

The use of a nebulizer, especially a pneumatic type coupled to a spray chamber is undoubtedly the most popular method of sample introduction used with the ICP. Therefore much of the development of this method was originally done on the ICP and with the arrival of commercially available ICP equipment, much of the hardware used for the MIP has been copied or borrowed. This is not unreasonable since the two plasma systems are fundamentally similar although the operational differences between them often require modifications to the individual parts of the sample introduction system.

### 1.2.1 Pneumatic Nebulizers.

The three types of pneumatic nebulizer normally used are.

#### i) Crossflow Nebulizer.

The crossflow nebulizer was first described in its modern form by Valente and Schrenk, 1970 (18) for introducing samples into a DC plasma used for solution analysis. Kniseley et al, 1974 (19) improved on this design by using stainless steel capillary tubes to resist attack from the chemicals used in spectrochemistry. The crossflow nebulizer (figure 1.2a), operated at a gas flowrate of  $1 \text{ l min}^{-1}$  is used in the commercial Philips PV 8490 ICP plasma source unit and has also been used in a number of MIP sample introduction systems, Beenakker et al, 1978 (20).

#### ii) Concentric Nebulizer

The concentric nebulizer, described by Veillon and Margoshes, 1968 (21) is similar to the type widely used in modern atomic absorption (AA) spectrometers. However such AA nebulizers typically operate at gas flowrates of  $5 \text{ l min}^{-1}$  which is unnecessarily high for most MIP's. A commercial ICP concentric nebulizer (figure 1.2b) as described by Meinhard, 1978 (22) and operating at a gas flowrate of  $1 \text{ l min}^{-1}$  has however, been used for sample aerosol introduction into the toroidal MIP described by Kollotzek et al, 1984 (23).

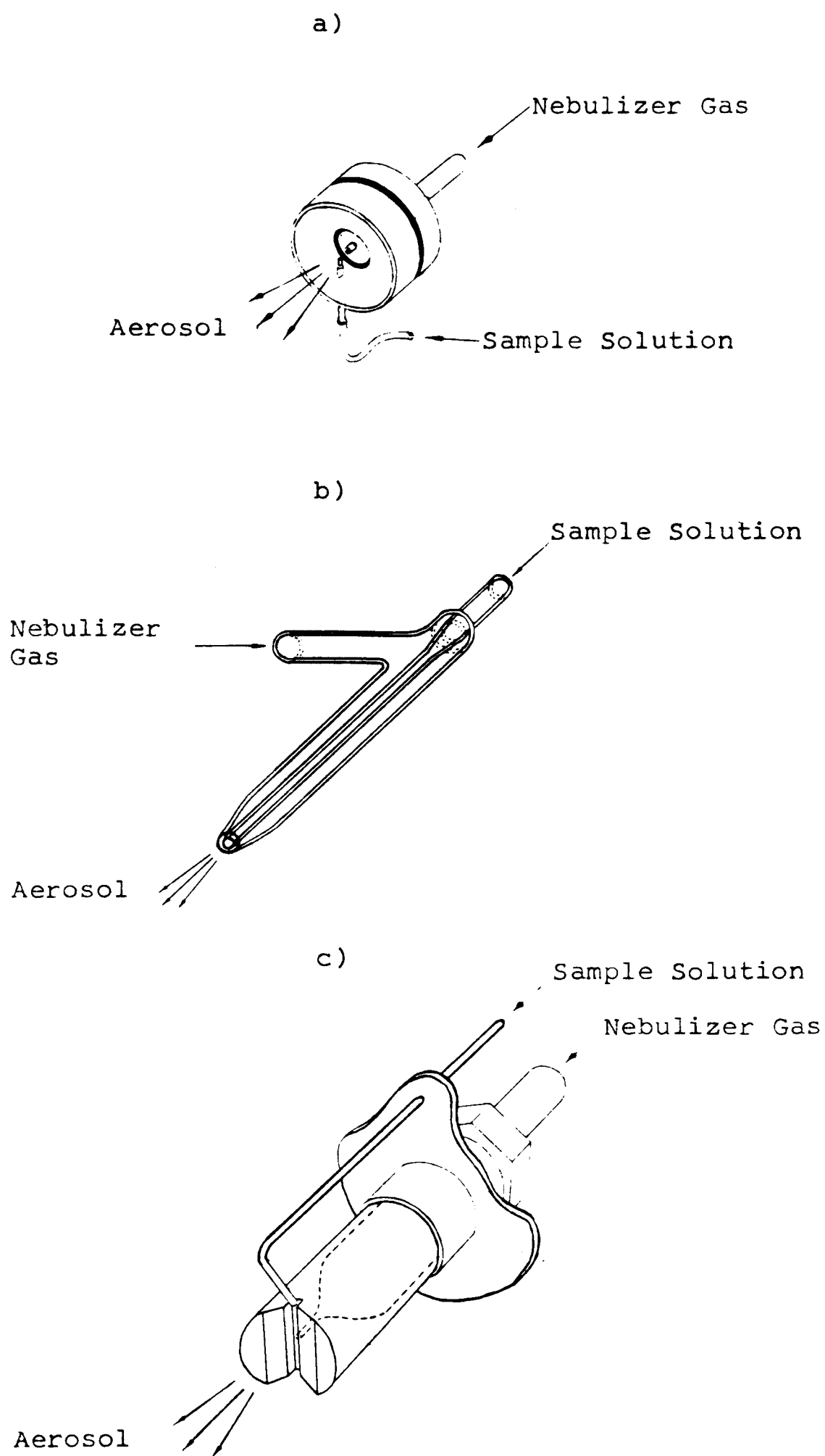


Figure 1.2 a) The Crossflow Nebulizer,  
 b) The Concentric Nebulizer and  
 c) The Babington Nebulizer.



### iii) Babington Nebulizer.

The principle of the Babington nebulizer was first described for the application of paint spraying by Babington, 1973 (24). This type of nebulizer does not require that the sample solutions pass through any capillary tube. Many applications have therefore been found for this type of nebulizer in atomic spectroscopy, a) for the aspiration of high solids samples into an AA flame spectrometer as described by Fry and Denton, 1979 (25), b) for the aspiration of high salt content samples into an ICP as described by Wolcott and Butler-Sobel, 1978 (26) and c) for slurry atomization in a DC plasma as described by Mohammed et al, 1981 (27).

In their investigations of an ICP operated at reduced gas flows Ripson and de Galan, 1981 (28) and Ripson et al, 1982 (9) described a nebulizer based on the Babington principle which operated at an argon flowrate of just  $0.1 \text{ l min}^{-1}$ . Such a nebulizer (figure 1.2c) has been used in this work to produce an argon MIP operating at a flowrate of  $0.1 \text{ l min}^{-1}$  (chapter 6).

### 1.2.2 Ultrasonic Nebulizers.

The ultrasonic transducer nebulizer, operated at frequencies from 50 to 1000 MHz has been suggested as an alternative to the pneumatic nebulizer because of its greater efficiency, up to 30% compared to the 3% for the typical pneumatic device.

Boumans and de Boer, 1975 (29) conducted a number of investigations into the ICP using an ultrasonic nebulizer (figure 1.3) for sample introduction and report detection limits for certain elements of 1 to 2 orders of magnitude better than similar ICP systems utilising commercially available pneumatic nebulizers, eg Winge et al, 1979 (30). Olson et al, 1977 (31) compared the nebulization efficiency of an improved ultrasonic nebulizer to that of a conventional pneumatic device coupled to an ICP used for the determination of multi-element detection limits.

Kawaguchi et al, 1972 (32) used an ultrasonic nebulizer as a means of sample introduction in their studies of an argon MIP but relatively poor detection limits were reported (section 6.8). Since then few attempts have been made to use an ultrasonic nebulizer, probably due to the MIP's poor tolerance to the large amounts of water vapour that can be introduced. Thus in the case of the MIP, the superior efficiency of the ultrasonic nebulizer may well be more of a hindrance to the improvement of operational stability with no benefit with regard to improved detection limits.

Problems with the long term stability and general reliability of ultrasonic nebulizers have also been reported by Boumans and de Boer, 1976 (33) which have prevented their widespread adoption with ICP's. Considering the inherent difficulties of operating an MIP with sample aerosol introduction anyway, additional problems with ultrasonic nebulizers are better avoided and by comparison, a pneumatic nebulizer coupled to a suitable spray chamber is a simple and reliable device.

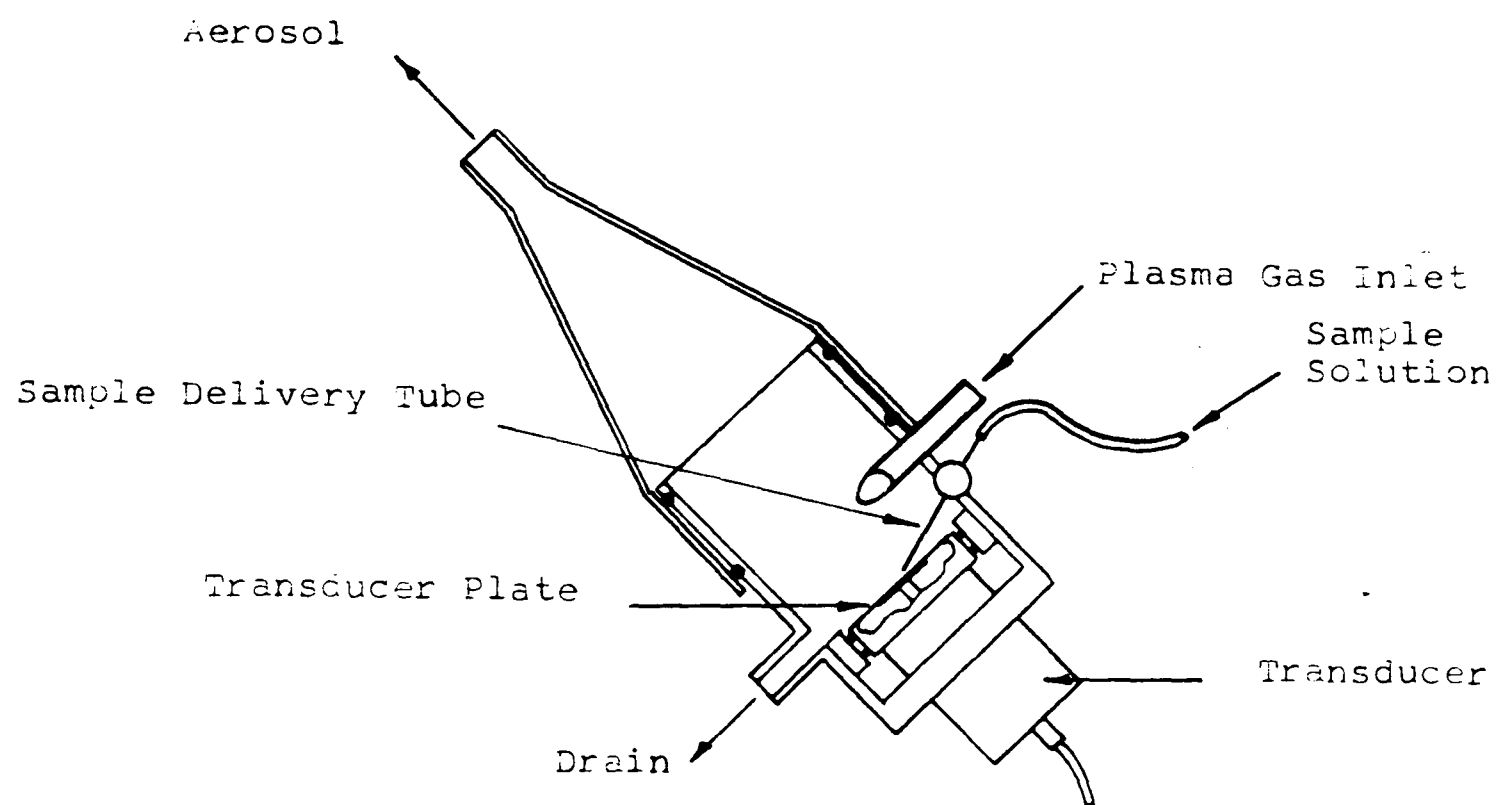
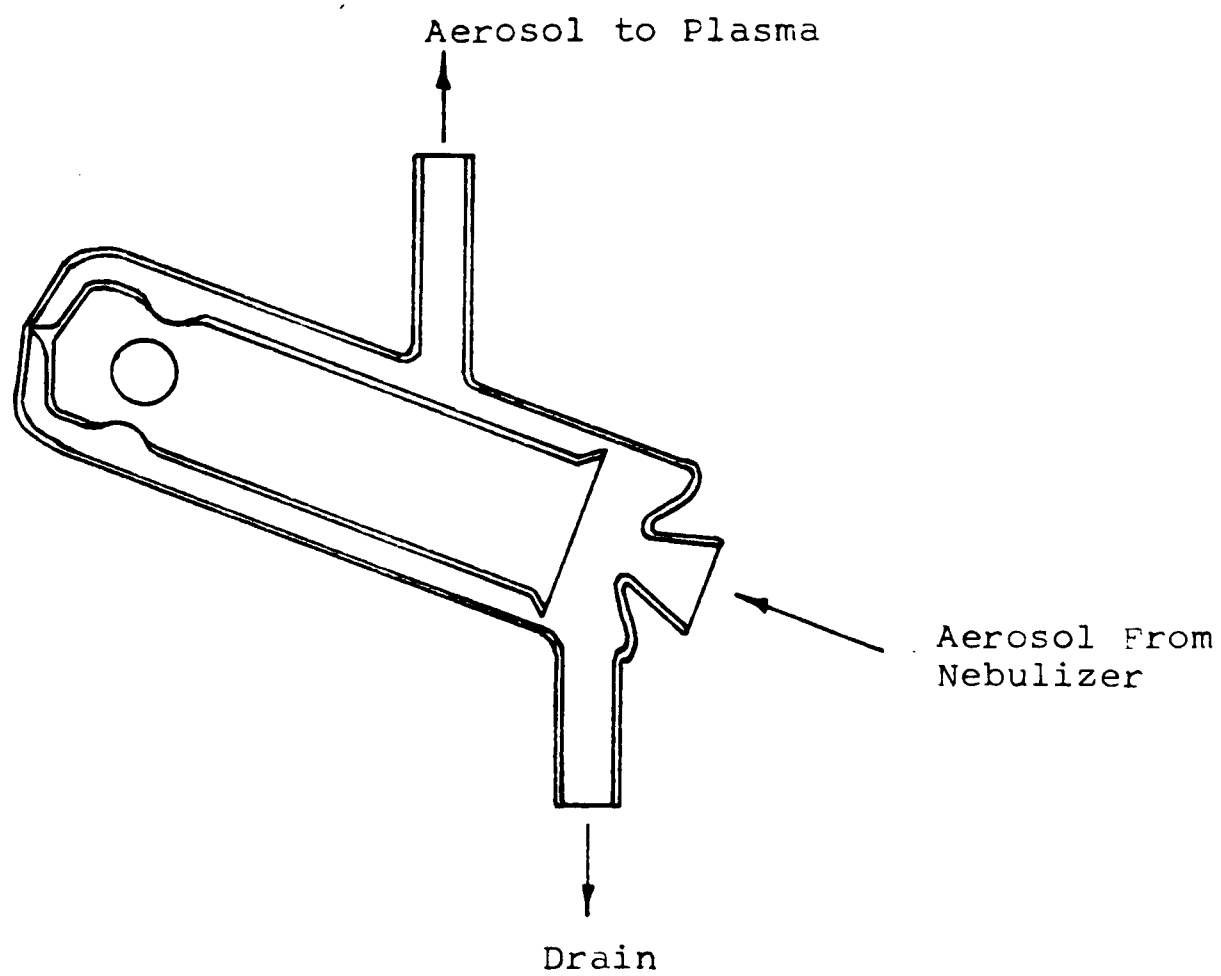


Figure 1.3     The Ultrasonic Nebulizer

### 1.2.3. Spray Chambers

The design of spray chamber with which the nebulizer is coupled is critical to the operation of any excitation source used for the spectrochemical analysis of solutions. Most pneumatic nebulizers produce large amounts of water droplets of diameter greater than 10  $\mu\text{m}$ . These are not atomized in the plasma and it is the function of the spray chamber to remove such droplets from the aerosol stream. In recent studies of pneumatic nebulizer performance, Browner and Boorn, 1984 (34), it has been deduced that the optimum diameter of water droplet, for introduction into an ICP, is 5  $\mu\text{m}$  and that the presence of larger droplets causes significant analyte signal fluctuations and hence poor analytical precision. In an MIP they also produce gross positional instability frequently leading to the extinguishing of the plasma.

In the majority of recently reported studies of MIP's with sample aerosol introduction, the spray chambers used have their origins in the double concentric tubular design (figure 1.4a) described by Scott et al, 1974 (35). Beenakker et al, 1978 (20) used a modified form of this spray chamber in their studies of an MIP generated in the  $\text{TM}_{010}$  cavity and used for solution analysis. Dahmen, 1981 (36) also used this type of spray chamber but with two aerosol outlets in his investigation of the CMP. The large internal surface area of the 'Scott' spray chamber makes it efficient at condensing the larger water droplets from the aerosol. However, persistence of a previous analyte signal in the plasma can be a problem due to water droplets being knocked from the chamber walls by the action of the aerosol. Removal of the inner tube has therefore been attempted by many experimenters, e.g. Ripson and de Galan, 1981 (28) when used with their low flowrate ICP.



b)

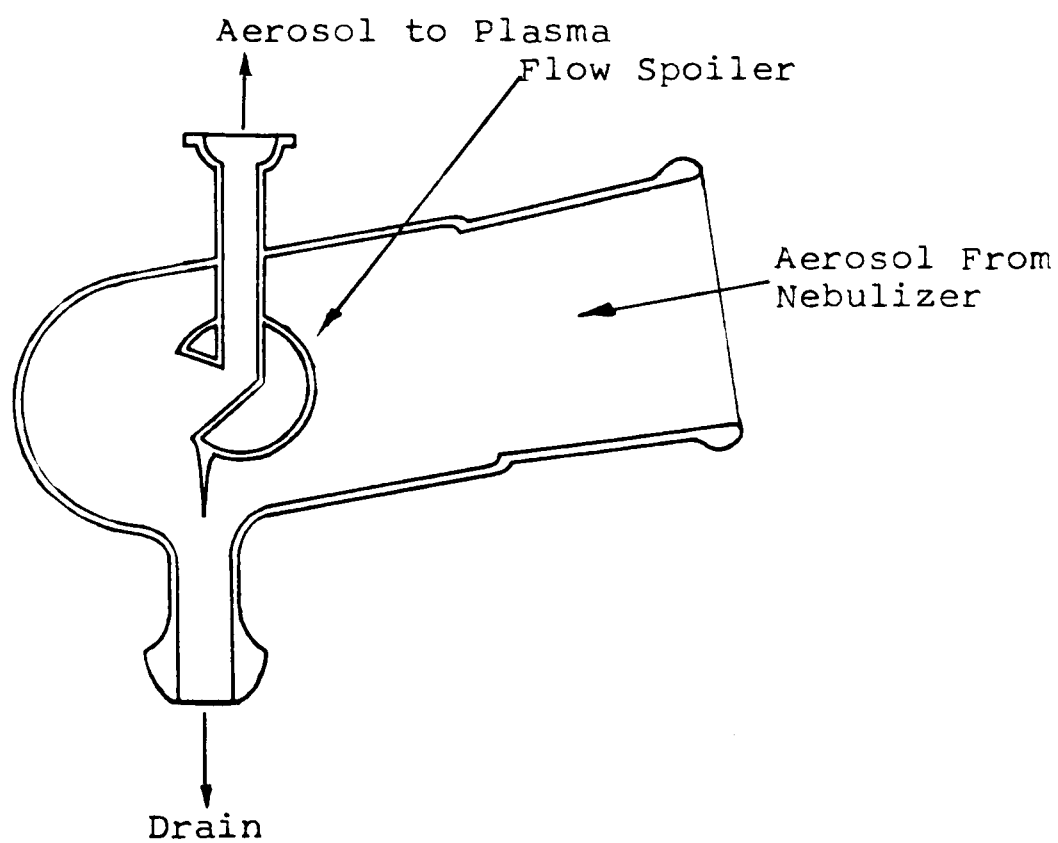


Figure 1.4 a) The 'Scott' Spray Chamber and  
b) The ICP Type Spray Chamber with 'Flow Spoiler'.

A different type of spray chamber (figure 1.4b) has been described by Boumans and Lux-Steiner, 1982 (37) which has a spherical 'flow spoiler' onto which the aerosol impinges. The flow spoiler further breaks down the larger water droplets and also creates a calm area behind it from which the fine aerosol droplets are lead to the plasma.

This spray chamber has now been employed in a commercial ICP system. Variations on this theme in designs of spray chambers have been used by a) Kollotzek et al, 1982 (38) in their investigations into multiple filament MIP's, b) by Feuerbacher, 1981 (13) in his initial studies of the CMP and c) in the investigation of an MIP generated in a slab-line cavity and used for solution analysis (chapter 6).

#### 1.2.4 Aerosol Desolvation and Dry Sample Introduction Techniques.

As has been mentioned previously, the MIP operated at atmospheric pressure in either argon or helium gas is not particularly tolerant to large amounts of introduced water vapour. However, the presence of large quantities of water vapour in the MIP are unavoidable if direct sample aerosol introduction is required, unless the aerosol is dried prior to entering the plasma. This 'desolvation' of the aerosol, which significantly reduces the water vapour loading of the plasma, was found to be necessary by Fallgatter et al, 1971 (11) and Lichte and Skogerboe, 1973 (39). Skogerboe and Coleman, 1976 (40) reported an order of magnitude improvement in the detection limits of certain elements in a MIP with desolvation compared to one without, but the apparatus did introduce chemical interference effects, observed when large concentrations of sodium or potassium were added to the samples.

In their series of investigations of an ICP used for the simultaneous multi-element analysis of solutions Boumans and de Boer, 1975 (29) also reported 'desolvation interferences'. In an earlier paper, Boumans and de Boer, 1972 (12) reported 'memory' effects caused by the persistence of the analyte atoms within the desolvation apparatus, it taking up to 2 minutes to completely flush through the desolvator before the analyte signal is no longer detected in the plasma. This memory effect would be expected to be worse at the much lower flowrates at which the MIP is capable of operating.

Some experimenters have avoided these desolvation problems by using an inherently dry sample introduction method. Beenakker et al, 1980 (10) and Matousek et al, 1984 (41) both used types of electro-thermal atomizer (ETA) device for sample introduction into helium and argon MIP's respectively. Recently Deutsch and Hieftje, 1984 (4) have described a high voltage 'micro-arc' atomizer for sample introduction into a nitrogen MIP operated at atmospheric pressure.

Other experimenters have used a vapour phase sample introduction method. Lichte and Skogerboe, 1972 (42) placed an arsine generator in the gas supply line to an argon MIP generated in a quarter wave Evenson cavity (Fehsenfeld et al, 1964 (43)). Using a similar cavity system Watling, 1975 (44) determined mercury at the pico-gram level from quartz amalgamation tubes placed in the gas supply line to the plasma.



#### 1.2.5. Discharge Tubes and Plasma Stability.

The type of plasma containment vessel used has typically been a plain cylindrical capillary tube fabricated in either quartz or alumina. The quartz discharge tube allows the plasma to be viewed radially but does suffer from corrosion when water vapour is introduced into the plasma. This occurs primarily where the plasma attaches itself to the inside wall of the tube as reported in this work (chapter 6). When Beenakker et al, 1978 (20) encountered this problem they change to using alumina discharges tubes. The opaqueness of alumina tubes was not a problem as the plasma generated in the  $TM_{010}$  cavity was viewed axially by the optical measuring system.

The MIP generated using the  $TM_{010}$  cavity in this work was found to wander around the inside wall of the plain quartz capillary discharge tube used (section 6.7) and this type of behaviour has been reported by Kollotzek et al, 1984 (23) who discussed the problem in their studies of single and multiple filament MIP's generated in the  $TM_{010}$  cavity. Their solution was to use a precision mechanism for aligning the plain quartz discharge tube to the cavity central axis.

Bollo-Kamara and Coddling, 1981 (45) have described an MIP generated in the  $TM_{010}$  cavity which used a novel quartz discharge tube arrangement (figure 1.5). This consisted of two concentric tubes, similar to an ICP torch with a threaded insert to create a tangential, helical flow of the outer plasma support gas. They report efficient mixing of the sample aerosol introduced via the centre tube with a 'suspended' filamentary MIP, possessing good positional stability and since no part of the discharge actually touches the tube walls, corrosion is eliminated.

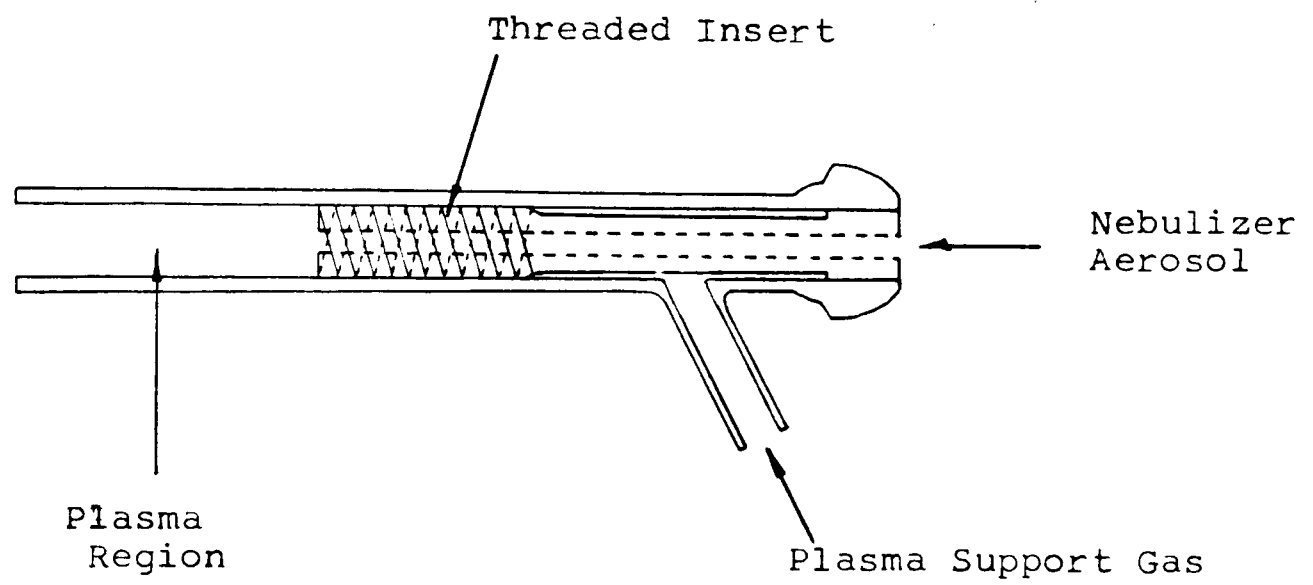


Figure 1.5    Novel Discharge Tube for use with MIP  
Bollo-Kamara and Coddling, 1981 (45).

### 1.3 Introduction to Plasma Diagnostics and Plasma Models.

A plasma can be defined as a partly ionized gas consisting of atoms, ions and free electrons. In studies of various plasmas, including the argon and helium MIP, a number of plasma models have been proposed or used to describe the excitation conditions prevalent between the plasma species. The model considered appropriate depends on the operating pressure regime (or more precisely the concentration of electrons per unit volume) of the plasma.

For an argon MIP operated at atmospheric pressure most investigations reported in the literature have proposed explanations of the internal excitation processes in terms of a 'local thermal equilibrium' (LTE) model (Tanabe et al, 1983 (46) and Abdullah and Mermet, 1982 (47)).

A review of plasma models applicable to a range of high frequency analytical plasmas by van Montford and Agterdenbos, 1981 (48) does not mention the 'saturation phase' model first postulated by Fujimoto et al, 1972 (49). Further work on saturation phase models of various types of plasmas by van der Mullen et al, 1980 (50) and Raaijmakers et al, 1983 (51) have confirmed their importance especially for atmospheric pressure plasmas.

Prior to a more specific introduction to plasma models, a brief introduction to the spectroscopic plasma diagnostic techniques typically used will be given. These techniques are discussed further in chapter 5.

### 1.3.1      Plasma Diagnostics.

Formulation of a plasma model to describe the excitation conditions within an MIP or ICP requires some measure of the fundamental plasma parameters. The parameters most often measured are the density of free electrons,  $N_e$  within the plasma and one or more plasma temperatures.

Plasma temperatures may conveniently be determined from the relative intensity of spectral lines emitted by the atomic, ionic and molecular species comprising the plasma gas. The scope of applicability of the temperature determined is, to a great extent dependant on the state of the plasma and the type of spectra used.

If the relative intensities of a number of argon spectral lines are measured and a Boltzmann distribution assumed for the population of excited states in the atom, then an argon excitation temperature may be determined.

If the plasma is known to be in a state of thermal equilibrium then this temperature is unique to the entire plasma system. However, if a state of thermal equilibrium does not exist then the temperature parameter determined is applicable only to argon. Thus if iron (Fe) was introduced into the plasma and it's spectra used to measure a similar excitation temperature, a different result would be obtained. Measurement of temperatures from different plasma species is therefore a monitor on the extent of thermal equilibrium as noted by Kornblum and de Galan, 1974 (52) in their studies of the spatial characteristics of an ICP.

Alder et al, 1980 (53) report for an argon ICP, where an excitation temperature was determined from the relative intensity of 20 Fe spectral lines that 'no unique excitation temperature for Fe was found'. However, Uchida et al, 1981 (54), in their study of the spatial distribution of plasma parameters in an ICP, measured an argon excitation temperature using only the spectral lines arising from electronic transitions between the 5p and 4s excited levels. A similar method was adopted by Tanabe et al, 1983 (46) in a study of an atmospheric pressure MIP.

Given the lack of evidence for a state of LTE existing in such plasmas it is doubtful whether these temperatures are unique to the systems studied.

A popular method of measuring  $N_e$  has been to use the Stark broadening of spectral lines emitted by the atoms and ions of the plasma gas. The technique requires that the electron density is large enough so that Stark line broadening is observable over and above the Doppler broadening of the spectral lines caused by the random thermal motion of the gas particles and any instrumental effects.

Allemand and Barnes, 1978 (55) have measured the electrical impedance of an argon ICP by substitution with a dummy load and suggest the probability of a link with electron density. This method was used to produce an electrical model of the ICP for use in the design of an efficient matching network. The geometry of most microwave cavity designs prevents the direct measurement of the impedance of the MIP. However, Hammond, 1978 (56) has measured the microwave impedance of a reduced pressure MIP generated in the slab-line cavity.

### 1.3.2 Plasma Models.

#### i) The Thermal Equilibrium Model.

When a plasma is in thermal equilibrium every energy exchange process is exactly balanced by the reverse process and no energy enters or leaves the plasma region. Therefore for every absorption of a photon (energy =  $h\nu$ ) per unit time by the plasma atoms, causing an electronic energy level transition from say, level 1 to 2 there is a corresponding emission of a similar photon due to an electronic energy level transition from level 2 to 1. Similarly for non-radiative collisional energy exchanges, every excitational transition from level 1 to 2 is exactly balanced by the corresponding de-excitational transition from level 2 to 1.

Collisional energy exchange is said to occur between dissimilar and similar plasma particles and over a time scale such that a large number of collisions take place. Under these conditions the population of excited states in the plasma is described by the Maxwell-Boltzmann formula.

$$n_E = (n \cdot g_E \exp(-E/kT)) / Z(T)$$

where  $n_E$  = number of particles with state of energy E  
 $g_E$  = degeneracy of this state  
 $n$  = total number of particles  
 $Z(T)$  = partition function, calculated such that

$$\sum_{E=0}^{\infty} n_E = n$$

$T$  = temperature parameter for the plasma.

When a plasma is in thermal equilibrium the temperature parameter,  $T$  is unique to the entire system, ie. it describes the temperature of the plasma gas atoms,  $T_{GAS}$ , the electron temperature,  $T_e$ , and the distribution of energy in the excited states of the gas atoms, expressed as the excitation temperature,  $T_{EXC}$ .

## ii) The Local Thermal Equilibrium Model

Perfect thermal equilibrium seldom exists anywhere other than in stellar atmospheres. To achieve such a state the plasma must be optically 'thick' at all wavelengths, ie. all emitted radiation must be re-absorbed before it can leave the region. Laboratory plasmas, because of their finite (and usually small) size never fulfil this requirement, a large part of the emitted radiation leaves the region unabsorbed. Most laboratory plasmas do not exhibit a uniform temperature over their entire extent, therefore at best it would be possible to regard the plasma as consisting of a number of volume elements, each characterized by it's own temperature. However, if the processes of energy loss, eg. by radiation and energy gain by the action of an external field on the plasma particles is small compared to the total energy of

the system then a state of 'local thermal equilibrium' (LTE) is said to exist (Montford and Agterdenbos 1981 (48)) in the separate volume elements of the plasma. For LTE to exist the collisional energy exchange processes between the particles (but not between the particles and the walls of the containing vessel) must dominate the plasma and therefore a sufficiently high particle density needs to be maintained (Griem, 1964 (57) ). In such a plasma there is an ionization-recombination equilibrium between the ground state of the ion and the excited and ground states of the neutral atom. This is often referred to as "Saha equilibrium".

iii) The Partial Local Thermal Equilibrium Model.

In some plasma, the radiative de-excitation of certain energy levels may so dominate their collisional de-excitation due to a reduced impact cross-section for collisions with the plasmas free electrons, that not even a state of LTE exists (van der Mullen et al, 1980 (50) ). This situation normally occurs for energy levels with large radiative transition probabilities near the ground state of the atom and they are said to be below the 'thermal limit'. However, for energy levels above this limit the distribution of energy may still be described by "Saha equilibrium" and Maxwell-Boltzmann statistics still apply. A plasma in such a state is said to be in partial LTE (pLTE) (Raaijmakers et al, 1983 (51) ).

With a plasma in pLTE it is then only possible to consider thermal equilibrium for groups of plasma particles or systems and there is no longer one unique temperature parameter. Plasma temperatures determined will therefore depend not only on the plasma species used for the measurement but also on the precise energy levels used.

iv) The Radiative Ionization Recombination Model.

The radiative ionization recombination (RIR) model was originally proposed by Schluter, 1963 (58) and Drawin, 1966 (59) to explain the excitation conditions in a low pressure, high frequency plasma. Compared to an atmospheric pressure MIP, the electron density in such a plasma is greatly reduced and the radiative de-excitation of the excited atomic states dominates over the collisional de-excitation process, i.e. the converse of LTE type plasmas.

In such a model, there are postulated to be two groups of electrons both possessing Maxwellian velocity distributions but characterized by different temperatures. The ionization process is attributed to a high energy, low density group of electrons and the radiative recombination process to a low energy, high density group of electrons. The plasma is sustained by this ionization/recombination equilibrium.

Investigation of the fundamental properties of a reduced pressure, 1 to 34 mbar argon MIP reported by Busch and Vickers, 1973 (60) were based on the assumption of a RIR model of the plasma. The RIR model has also been compared to an LTE model with regard to explaining the excitation conditions in a low pressure, 0.1 to 0.7 mbar mixed gas MIP reported by Brassem et al, 1976 (61) and 1978 (62).

v) The Saturation Phase Model.

The existence of 'saturation phases' has been postulated in a positive column hydrogen discharge by Fujimoto et al, 1972 (49) and in a positive column argon discharge by Tachibana and Fukuda, 1973 (63) and a 'collisional-radiative' (CR) model has been used to explain the excitation processes in such plasmas. The CR model involves a general formula which includes 'rate coefficients' to describe the relative importance of the collisional and radiative parts of the excitation process.



In the transition from radiation to collision dominated plasmas (as the electron density increases), the population of the higher excited states in the atom become collision dominated well before the establishment of the Saha equilibrium characteristic of LTE type plasmas (van der Mullen et al, 1980 (50) ). In the case where the lower excited atomic states are still radiation dominated, a 'quasi-saturation phase' is said to exist, but as all the excited levels become saturated a 'complete saturation phase' is reached (Raaijmakers et al, 1983 (51) ).

In the complete saturation phase the plasma is entirely collision dominated, but instead of the ionization-recombination equilibrium found in LTE type plasmas, the dominant excitation mechanism in the complete saturation phase postulated by Raaijmakers et al, 1983 (51) is a 'ladder like' excitation and de-excitation to and from adjacent excited levels.

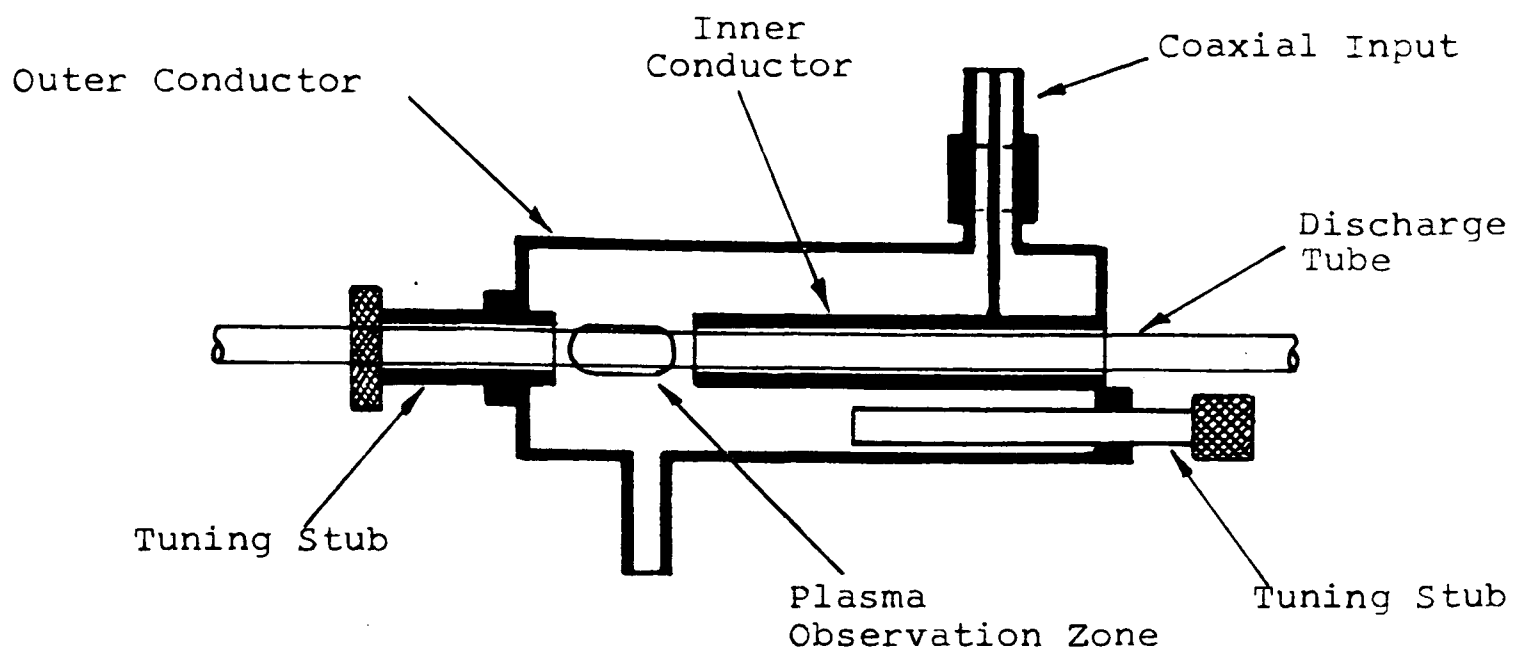
## Chapter 2. Introduction to the Microwave Aspects of the MIP.

### 2.1 Microwave Cavity Review.

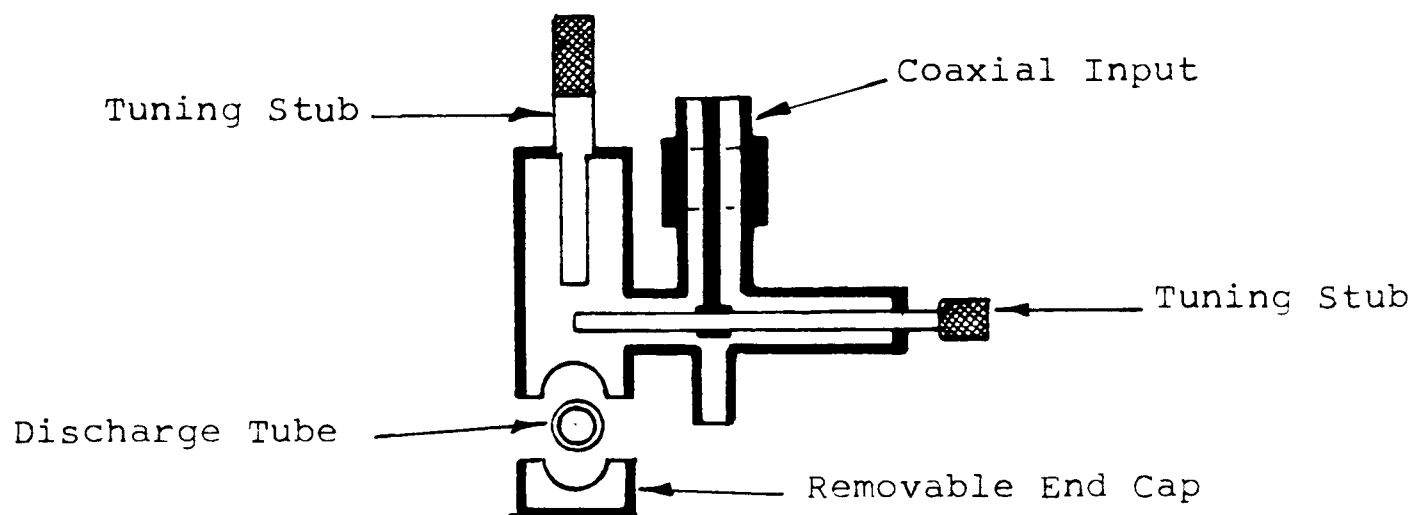
Prior to 1976 most reported studies of MIP's were undertaken using one of the cavity types described by Fehsenfield et al, 1964 (43) who compared the performance of most of the cavity designs then available. Of these, the three cavity designs which subsequently became most widely used are illustrated in figure 2.1. All microwave cavities described here have been designed to operate at 2.45 GHz.

In the  $3\lambda/4$  Broida coaxial cavity (figure 2.1a), the inner conductor is 'foreshortened' to provide a capacitive load for the cavity. The plasma is contained in a discharge tube positioned along the axis of the inner conductor and is created in the gap between the end of the inner conductor and the end wall of the cavity. The far end of this coaxial resonant cavity is terminated in a short circuit and microwave energy is coupled into it at a point  $\lambda/4$  away. The usual coaxial transverse electro-magnetic (TEM) mode of excitation is dominant. Tuning is accomplished by varying the length of the gap using the threaded tuning stub. Since usually the plasma would be confined within the cavity it is necessary to cut an aperture in the outer conductor to permit radial viewing of light emitted from the plasma. This aperture behaves as a waveguide below cut-off so that no radiation is lost from the cavity.

The  $3\lambda/4$  Broida cavity is supplied commercially by Electro-Medical Supplies (EMS) as the type '210L'. A modified version of this cavity, with reduced dimensions to accommodate smaller diameter discharge tubes and with water cooling jackets provided on the outer conductor is also supplied by EMS as the type '215L'.



b)



c)

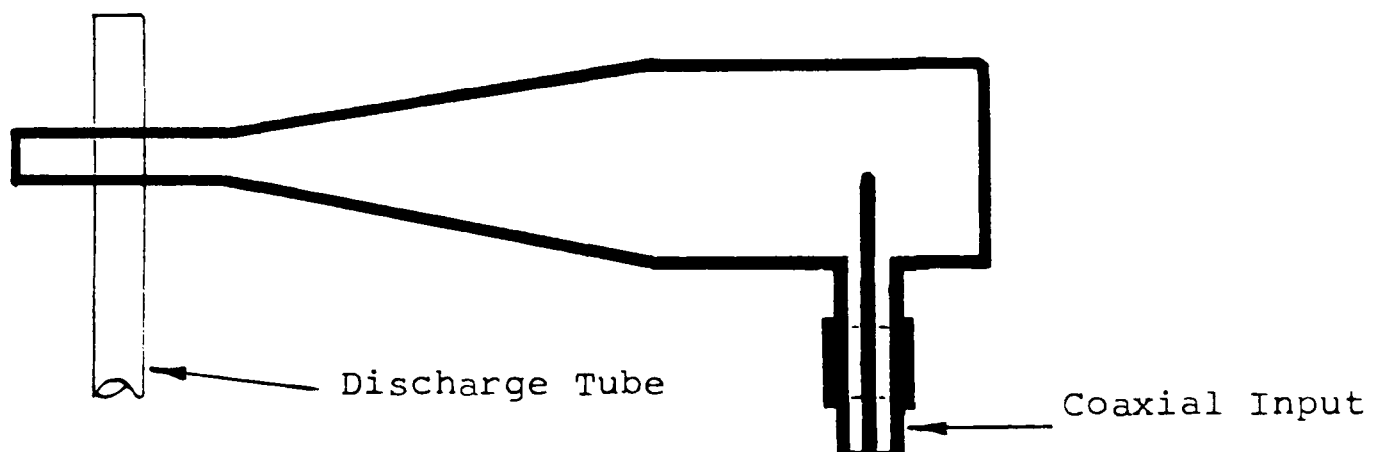


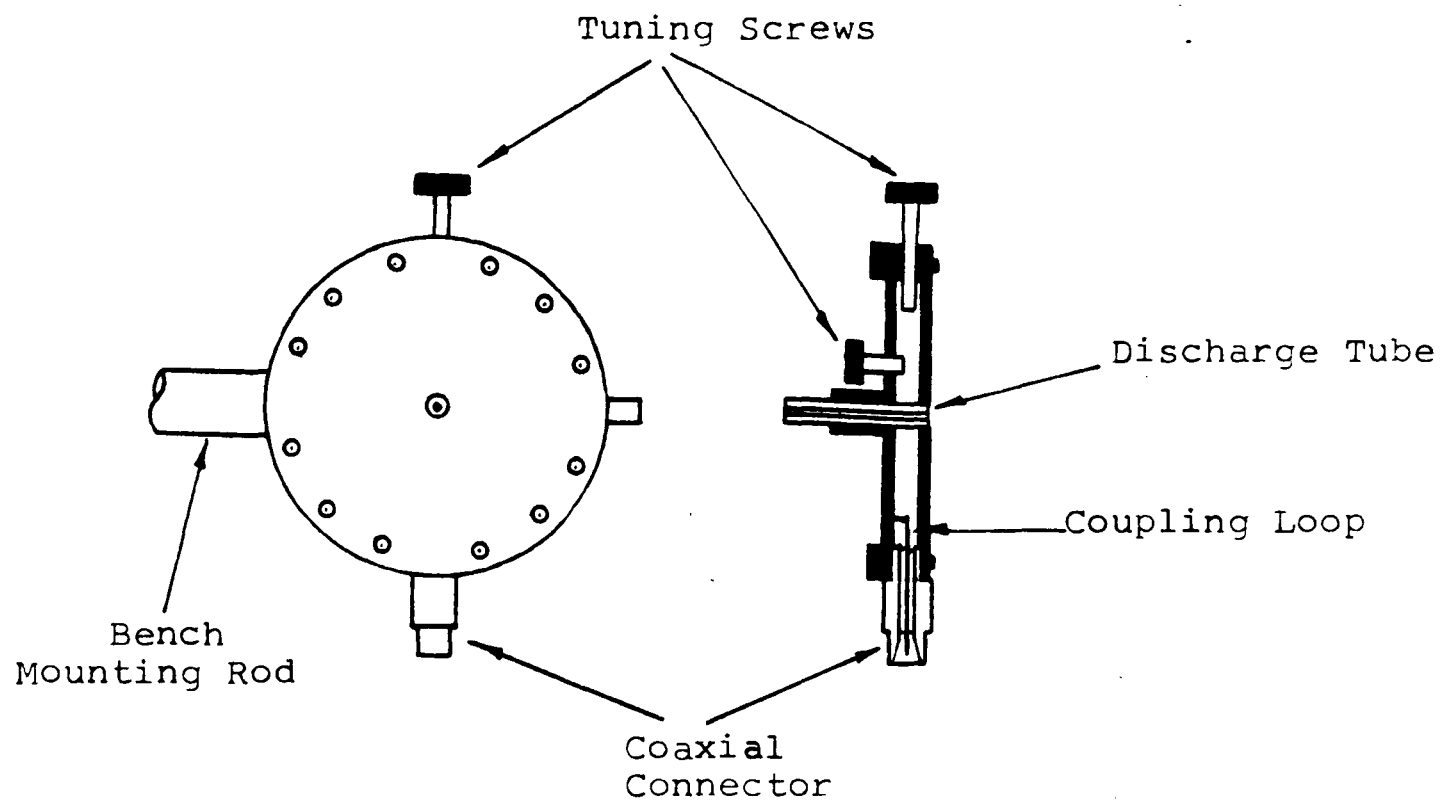
Figure 2.1 a) The  $3 \lambda / 4$  Broda Cavity  
 b) The  $\lambda / 4$  Evenson Cavity and  
 c) The  $TM_{013}$  Waveguide Cavity

The  $\lambda/4$  Evenson cavity (figure 2.1b) is another coaxial resonant cavity where the TEM mode of excitation is the dominant mode. The discharge tube is positioned transversely to the inner conductor and unlike the  $3\lambda/4$  Broida cavity, the gap in the inner conductor is of fixed length. The open structure of the  $\lambda/4$  cavity permits greater flexibility in viewing light emitted by the plasma but the penalty for this would appear to be a high level of stray microwave radiation as intimated by Haarsma et al, 1974 (64). Hammond, 1978 (56) suggested that the supposedly efficient energy coupling into this cavity reported by Fehsenfeld et al, 1964 (43) may in fact be due to the energy being radiated away from the cavity and not actually coupled into the plasma.

The  $\lambda/4$  cavity has nevertheless been successfully employed for the excitation of MIP's at reduced pressure by Brassem and Maessen, 1974 (65) and Avni and Winefordner, 1975 (66). With some minor modifications Lichte and Skogerboe, 1973 (39) used it to produce an atmospheric pressure MIP with direct sample aerosol introduction. The  $\lambda/4$  Evenson cavity is also supplied commercially by EMS as the type '214L'.

Figure 2.1c illustrates one of the early cavity resonators used for the excitation of MIP's. The tapered rectangular cavity operates in the  $TM_{013}$  waveguide mode of excitation. Despite its large size it can be conveniently aligned to a discharge tube without, for example disturbing any vacuum system which might be connected. Although not necessarily recommended by Fehsenfeld et al, 1964 (43) for use at high pressures, this cavity has been used to generate an atmospheric pressure argon MIP with sample aerosol introduction by Kawaguchi et al, 1972 (32). Falgatter et al, 1971 (11) generated a similar MIP using a commercial tapered rectangular cavity supplied by Raytheon.

In 1976, Beenakker (2) described a cavity, operated in the  $TM_{010}$  waveguide mode of excitation, which could be used to support both argon and helium MIP's at atmospheric pressure. This cylindrical cavity (figure 2.2a) is



b)

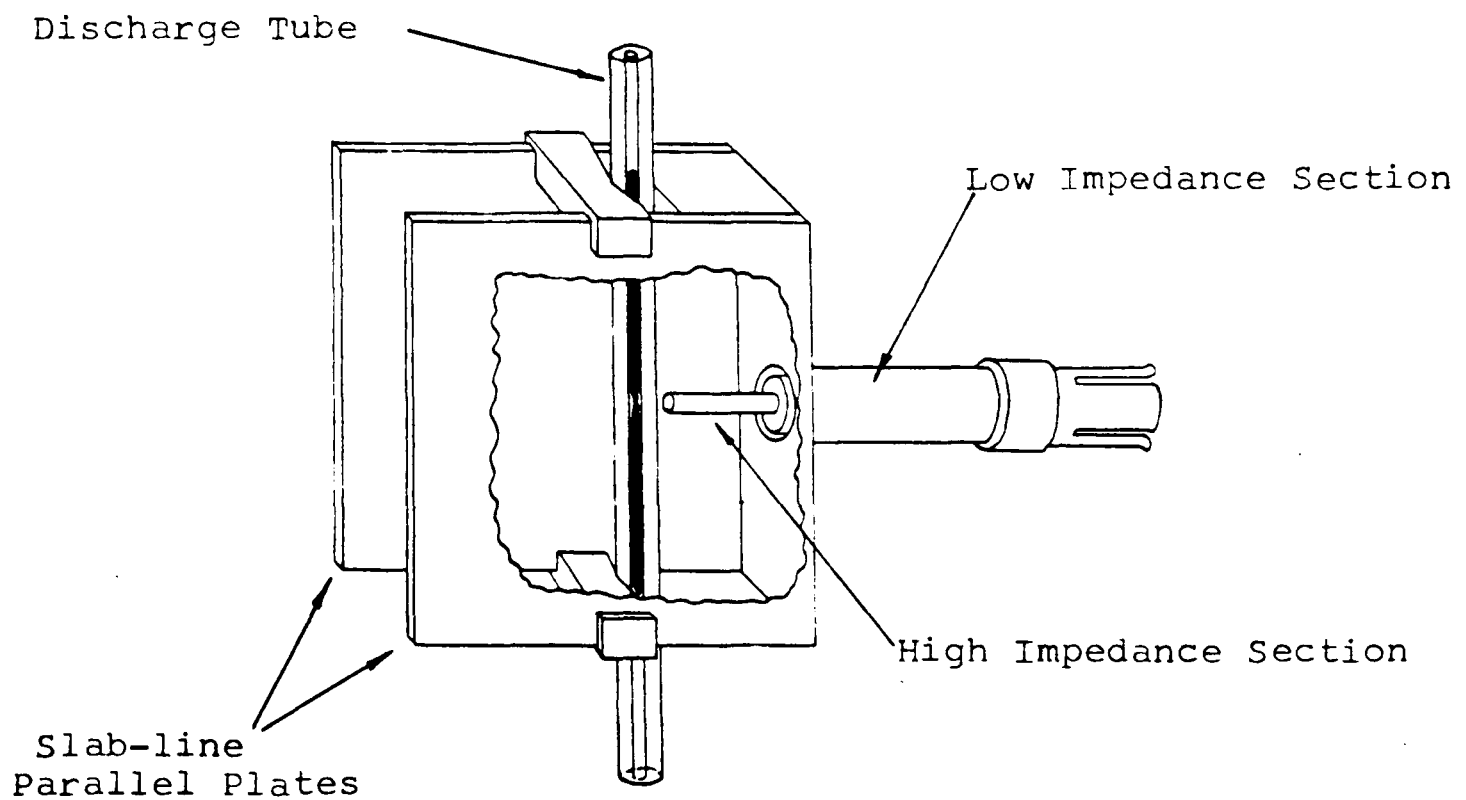


Figure 2.2. a) The  $TM_{010}$  Beenakker Cavity and  
b) The Slab-line Cavity.

similar to the foreshortened  $\lambda/4$  radial cavity described by Fehsenfeld, 1964 (43). The plasma containment tube is placed in the centre of the cavity in the position of maximum electric field strength.

Beenakker, 1977 (17) showed the  $TM_{010}$  cavity to be capable of supporting atmospheric pressure helium MIP's for use as element sensitive detectors in gas chromatography and argon MIP's used for spectrochemical analysis of solutions, Beenakker et al, 1978 (20).

Fairly extensive modifications to the  $TM_{010}$  cavity were suggested by van Dalen et al, 1978 (67) whereby the inductive coupling loop input is replaced by a capacitive antenna fabricated from part of a  $\lambda/4$  Evenson cavity and the brass tuning screws are replaced by dielectric rods within the cavity. This is said to give better energy coupling into the cavity and improved tuning performance.

The  $TM_{010}$  cavity has become widely adopted for studies of reduced pressure MIP's (Goode et al, 1985 (68)) atmospheric pressure MIP's (Tanabe et al, 1983 (46)) and as an element selective detector in gas chromatography (Carnahan et al, 1981 (69)). Bollo-Kamara and Coddington, 1981 (45) used a  $TM_{010}$  cavity to support an atmospheric pressure MIP contained in a dual gas flow discharge tube. Köllotzek et al, 1984 (23) used a modified  $TM_{010}$  cavity in their studies of atmospheric pressure filamentary argon MIP's for use in the spectrochemical analysis of solutions.

Hammond and Outred, 1976 (70) developed a slab-line cavity (figure 2.2.b) which was designed for excitation of the 1st ionised spectra of inert gases in reduced pressure electrode-less discharge tubes (EDT). The slab-line cavity was comprised of a low impedance co-axial transmission line section feeding directly into a high impedance cavity section. The cavity section used two parallel plates as the outer conductor and had a cylindrical inner conductor. The very open structure of the slab-line cavity permitted radial viewing through the side wall of the EDT with little danger from stray microwave radiation.

In 1981, Feuerbacher (13) and Dahmen (36) described a capacitively-coupled microwave plasma (CMP) operating in nitrogen or nitrogen/argon mixture at atmospheric pressure and used for the analysis of solutions by optical emission spectroscopy (OES). The CMP (figure 2.3a) is similar to the MIP generated in the  $3 \lambda / 4$  Broda cavity described by Fehsenfeld et al, 1964, (43) but instead of being contained in a glass capillary tube the plasma is formed in free air at the tip of a gold electrode and is stabilized via an annular flow of nitrogen gas. The CMP is thus operated in a similar way to the ICP and therefore avoids the problems of discharge tube corrosion which traditionally cause difficulties when viewing the MIP through the wall of the containment vessel.

A very different type of plasma generator, which is not necessarily a resonant cavity has been described by Hubert et al, 1979(71) and Darrah, 1979 (72). This is a surface wave device known as a 'surfatron' (figure 2.3b) but has only found limited use in plasma spectroscopy.

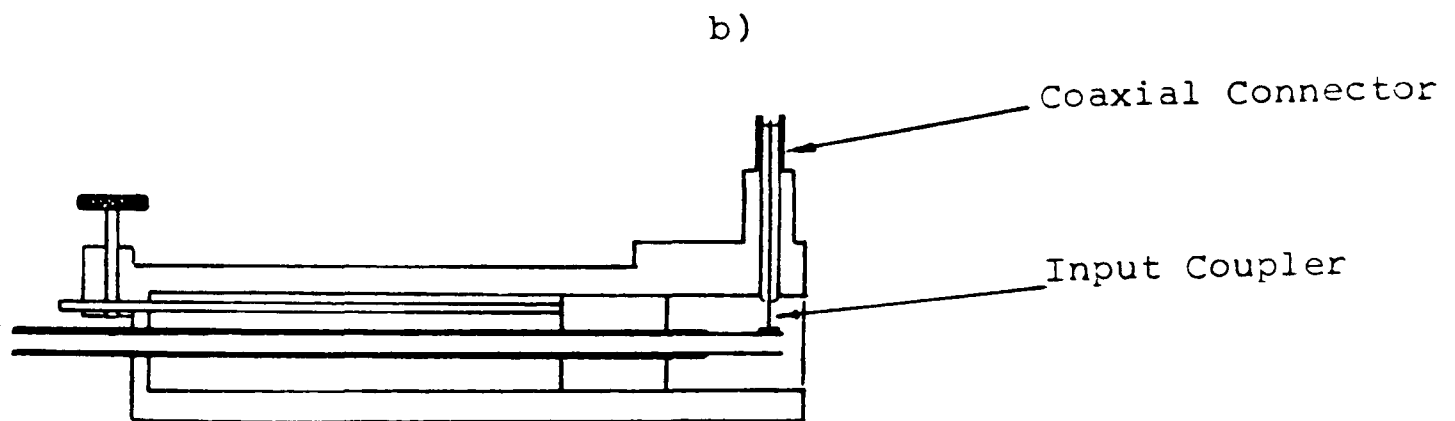
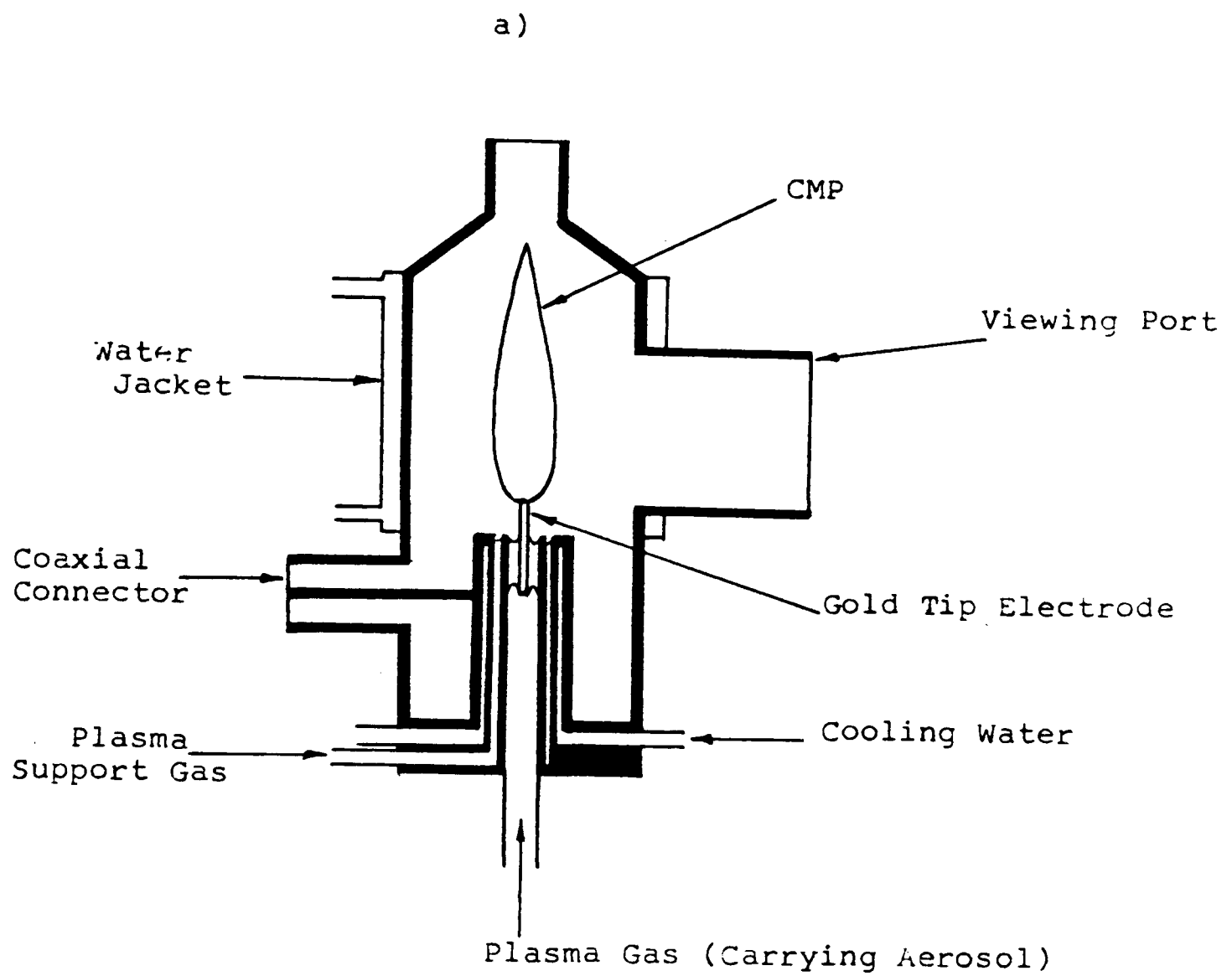


Figure 2.3 a) The Capacitively Coupled Microwave Plasma.  
 b) The Surfatron



Currently there is a great deal of concern about the levels of stray radiation to which the operators of microwave equipment are exposed. Considering the thermal effect of microwave radiation alone, the USA and UK recommend  $10 \text{ mW cm}^{-2}$  as a safety limit. However the USSR set a safety limit 1000 times more stringent at  $0.01 \text{ mW cm}^{-2}$  following studies on the biological effect of microwave radiation.

There are many situations in the use of MIP's where stray radiation may occur. It has already been suggested that the  $\lambda/4$  Evenson cavity has a significant stray radiation problem due to its very open structure. Outred and Howard, 1978 (73) report for the  $3 \lambda/4$  Broida cavity that provided the plasma does not extend outside the confines of the cavity, nor completely fill the entire length of the discharge tube, stray radiation is minimal.

As already mentioned the slab-line cavity, despite its very open structure produces very little stray radiation. With a dry argon plasma load the slab-line cavity was found to emit no measurable stray radiation. However, when loaded with an MIP saturated with water vapour, introduced via the nebulizer, the slab-line cavity was found to emit significant and very directional levels of stray radiation. At most angular positions in front of the open end of the slab-line cavity this stray radiation was at a level of  $2 \text{ mW cm}^{-2}$  or less, measured at a distance of 5 cm from the cavity. However a strong 'lobe' at a level of  $40 \text{ mW cm}^{-2}$  was measured along a path parallel to the axis of cavity inner conductor.

In this work, orientation of the experimental apparatus prevented the stray radiation becoming a health hazard but screening of the optical system electronics was required to prevent interference. The level of stray radiation emitted was also found to be directly dependent on the amount of water vapour introduced into the MIP.

## 2.2 Transmission Line Theory Applied to the Design of a Microwave Cavity.

A full description of a microwave cavity, of the type used to generate an atmospheric pressure MIP involves the geometrical shape of the cavity, wall losses and the method of coupling energy into it. Consideration of these three factors simultaneously presents the cavity designer with a formidable problem to solve. The problem may be simplified by applying the exact mathematical treatment to a lossless cavity, the electric and magnetic field patterns within this cavity determined and then the wall losses and the input coupling method used can be introduced as causing perturbations of the original field patterns. Such an approach to cavity design was described in general terms, by Slater, 1952 (74). Even with such an approach, however, the mathematical treatment of the cavity is still complex and it is not always easy to identify the parameters required to optimize the design.

An alternative, and very much simpler approach is to describe the cavity in terms of an equivalent tuned circuit comprising discrete inductances, capacitances and resistances. Unfortunately this equivalent circuit is often so far removed from the physical reality that the cavity is seldom adequately represented.

Hammond, 1978 (56) adopted an approach, described briefly by Ramo et al, 1965 (75) which is mid-way in complexity between the detailed mathematical treatment and the oversimplified equivalent circuit analogy of the cavity. In this the cavity is treated as a section of transmission line,  $\lambda/2$  long and terminated at each end by a short circuit. The transmission line carries two waves, propagating in opposite directions along the cavity axis which, with multiple reflections from the short circuited ends of the cavity produce a standing wave with an electric field maxima at the cavity centre. For cavity structures of this type, where the cross section normal to the axis is constant, longitudinal symmetry is said to exist.

The coupling of energy into the cavity is accomplished by assuming that one of the short circuits is partly transparent. At the frequency of 2.45 G Hz at which the cavity is operated, this partly transparent boundary was conveniently represented by a set of scattering (S) parameters. The use of S parameters to describe the reflection and transmission of energy at the boundaries of a general two port network are described in appendix A1. Wall losses within the cavity are accounted for by extending the analysis to include not only the S parameters of the boundary(s) but also the transmission (T) parameters for the lengths of cavity sections which are dependent on the finite conductivity of the (brass) material used in the cavity construction. For cavity structures of this type possessing longitudinal symmetry, the electric and magnetic components of the travelling waves within the cavity may be conveniently expressed in terms of equivalent voltage and current waves. This allows use of the well known transmission line equations to be used in the analysis of the cavity.

### 2.3 The Scattering Parameter Representation of the Slab-line Cavity.

A full discussion of Hammond's design procedure for the slab-line cavity is given in his thesis (Hammond, 1978 (56)) but since the microwave impedance of the atmospheric pressure MIP is to be determined it is necessary to outline the general approach and explain how the S parameters are used to evaluate the plasma impedance.

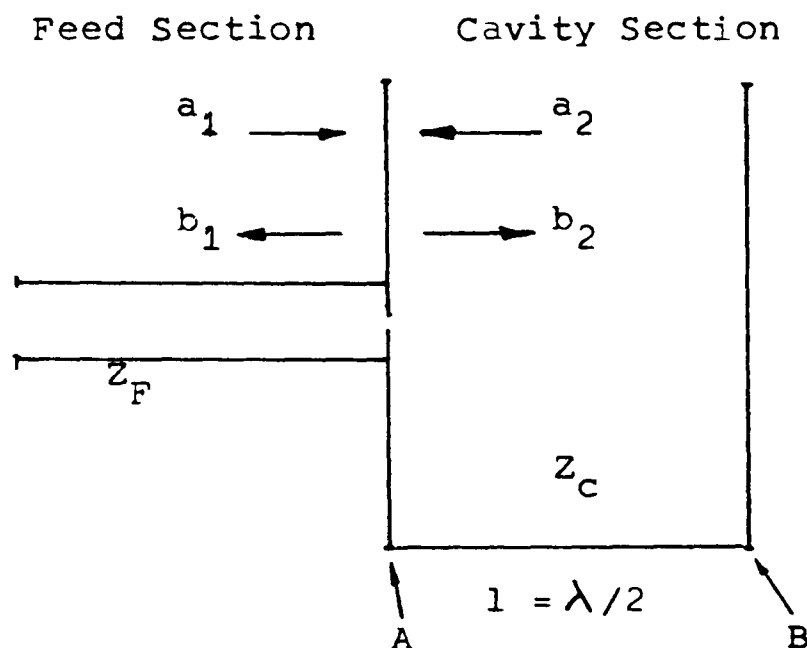


Figure 2.4 The  $\lambda/2$  Slab-line Cavity.

In the basic configuration of slab-line cavity shown in figure 2.4 the short circuits A & B terminating each end of the cavity section are  $\lambda/2$  apart where  $\lambda$  is the wavelength of the excitation energy. The inner conductors have been omitted from figure 2.4 for the sake of clarity. On either side of the partially transparent boundary A, where energy is coupled into the cavity there exists the normalized incident and reflected voltage like waves  $a_1$  and  $b_1$  (in the feed section) and  $a_2$  and  $b_2$  (in the cavity section). As for the general two-port

network (see Appendix A1), a set of S parameters may be defined for this boundary by

$$b_1 = S_{11}a_1 + S_{12}a_2$$

$$b_2 = S_{21}a_1 + S_{22}a_2$$

The wave  $a_2$ , incident on the partially transparent boundary A is produced by reflection of wave  $b_2$  from boundary B. The relationship between  $a_2$  and  $b_2$  may thus be established if the behaviour of travelling waves inside the cavity is considered. On any transmission line the change incurred in a wave,  $\phi$  travelling through a distance  $l$  is expressed in terms of a propagation coefficient,  $\gamma$  ie.

$$\phi(y) = \phi(x) e^{-\gamma l}$$

where  $\gamma$ , a complex quantity is given by

$$\gamma = \alpha + j\beta$$

where  $\alpha$  is the attenuation coefficient and  $\beta$  the phase coefficient for travelling waves on the line. The value of  $\beta$  is given by

$$\beta = 2\pi/\lambda$$

If it is assumed that boundary B of the slab-line cavity is lossless, ie reflection coefficient = -1 then the relationship between  $a_2$  and  $b_2$  may be established namely,

$$a_2 = -b_2 e^{-2(\alpha + j\beta)l}$$

For the cavity considered  $l = \lambda/2$  therefore the second term in the exponent vanishes since  $e^{-2j\beta l}$  becomes  $e^{-2j\pi}$  which equals unity. The expression then simplifies to

$$a_2 = -b_2 e^{-2\alpha l}$$

An input reflection coefficient  $\rho_{IN}$  as seen at the boundary A was defined by

$$\rho_{IN} = \frac{b_1}{a_1} = \frac{s_{11} - \frac{s_{12}s_{21} e^{-2\alpha l}}{1 + s_{22} e^{-2\alpha l}}}{1}$$

Furthermore, these equations also give an expression for the voltage at the centre of cavity,  $V_c$  by

$$V_c = ja_2 e^{\alpha l/2} - jb_2 e^{-\alpha l/2}$$

which, when expressed in terms of the incident voltage is defined by Hammond 1978 (56) as the unloaded resonant cavity gain,  $G_{OR}$  given by the equation

$$G_{OR} = \left| \frac{\text{Voltage at Cavity Centre}}{\text{Incident Voltage}} \right|$$

The value of  $G_{OR}$  may then be calculated from the S parameters by

$$G_{OR} = \left| \frac{-js_{21} e^{-\alpha l/2} (1 + e^{-\alpha l})}{1 + s_{22} e^{-2\alpha l}} \right|$$

The unloaded gain of the slab-line cavity is determined taking full account of the energy coupling considerations via the S parameters and energy losses in the cavity through  $\alpha$ .

The effect of cavity tuning, where the length is not equal to  $\lambda/2$  may be illustrated by recalculating the above equation using the full relationship between  $a_2$  and  $b_2$ , ie.

$$a_2 = -b_2 e^{-2(\alpha + j\beta)l}$$

The expression for  $G_{OR}$  then becomes

$$G_{OR} = \left| \frac{s_{21} e^{-(\alpha + j\beta)l/2} (1 - e^{-(\alpha + j\beta)l})}{1 + s_{22} e^{-2(\alpha + j\beta)l}} \right|$$

Cavity tuning may therefore be affected either by variation of  $l$  or  $\lambda$ . The slab-line cavity is tuned, and hence the value of  $G_{OR}$  maximised when  $l = \lambda/2$ . The voltage subsequently developed across a load placed at the cavity centre is thus considerably greater than the voltage incident upon the cavity.

A slab-line cavity comprising two short circuits separated by a distance of  $\lambda/2$  is not, however the final configuration adopted by Hammond. He notes that the cavity tuning conditions are also met if boundary B is an open circuit placed at a distance  $\lambda/4$  away from boundary A. Essentially similar expressions for  $P_{IN}$  and  $G_{OR}$  may be then calculated as previously described. Although design of the open circuit boundary must be carefully considered to prevent leakage of radiation and spurious modes of excitation being set up with the cavity the benefits are considerable. The shorter length means that there are less electrical losses in the cavity structure. The unavoidable 'fringing' electric fields at the open circuit boundary do however necessitate the fine tuning of the cavity (section 4.1), but since the electric field maxima occurs at this position it is an ideal place to position the quartz discharge tube containing an argon MIP. Light emitted from the plasma may then be viewed from a number of different angles by some optical measurement system, including radially through the wall of the quartz tube, since the cavity is completely open. Figure 2.5 illustrates a possible arrangement of the  $\lambda/4$  slab-line cavity used with an MIP.

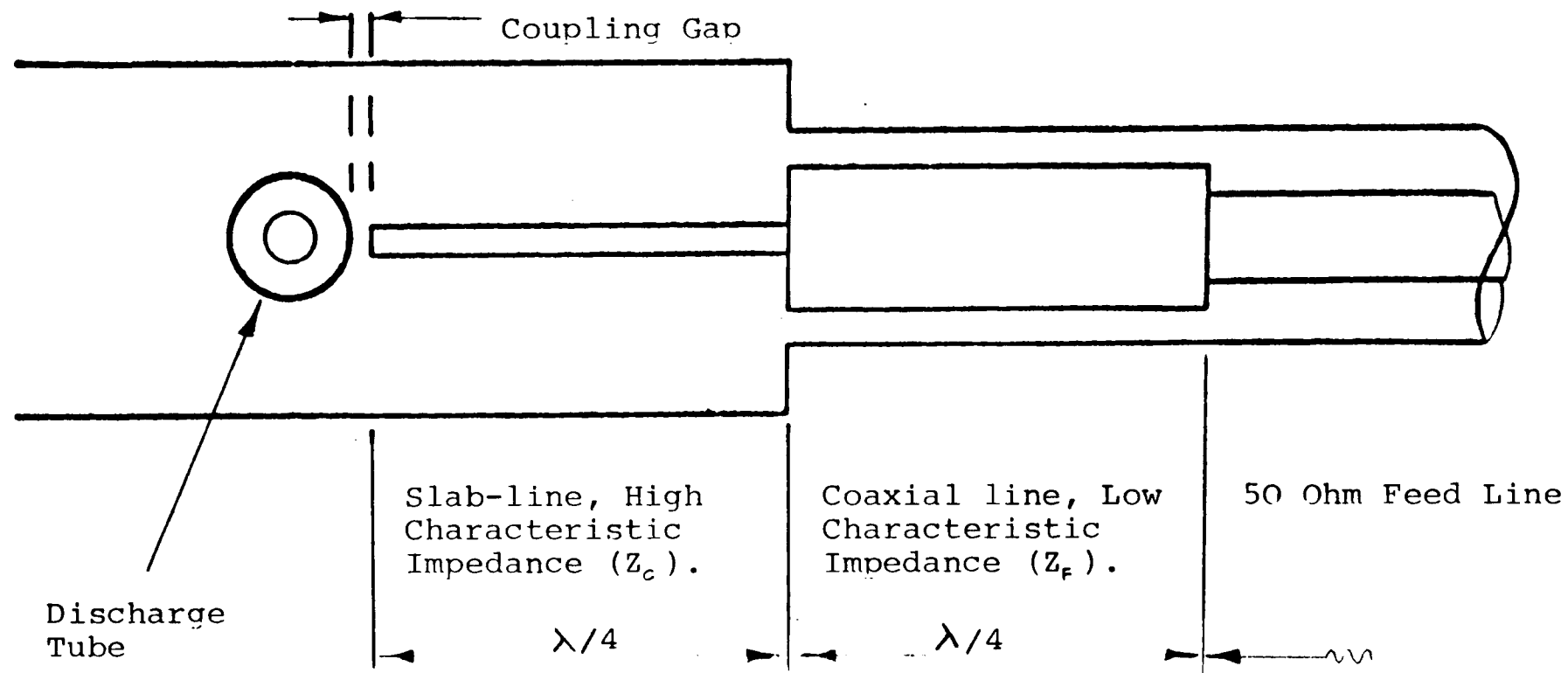


Figure 2.5    Schematic Representation of the  $\lambda/4$  Slab-line Cavity.



Expressions for loaded cavity gain and input reflection coefficient may be calculated as previously done for the unloaded cavity. In the case of the input reflection coefficient it is a simple matter to extend the previously used expression to include the effect of the load reflection coefficient,  $\rho_L$  ie

$$\rho_{IN} = \frac{s_{11} - s_{12}s_{21}\rho_L e^{-2\alpha l}}{1 + s_{22}\rho_L e^{-2\alpha l}}$$

Measurement of the modulus,  $|\rho_{IN}|$  and argument  $\phi_{IN}$  of the cavity input reflection coefficient therefore enable the value of the plasma load impedance to be determined (section 4.3). Knowledge of the S parameters is, naturally also required and these are determined by the physical structure of the slab-line cavity. In the simplest analysis of the  $\lambda/4$  slab-line cavity, assuming it to be a reciprocal and lossless network (Appendix A1), the number of independent parameters is reduced and the normalized scattering matrix can be shown to be

$$\begin{bmatrix} S^N \end{bmatrix} = \begin{bmatrix} s_{11} & s_{12} \\ s_{21} & s_{22} \end{bmatrix} = \begin{bmatrix} \frac{Z_f^2 - Z_c Z_o}{Z_f^2 + Z_c Z_o} & \frac{-j2Z_f \sqrt{Z_c Z_o}}{Z_f^2 + Z_c Z_o} \\ \frac{-j2Z_f \sqrt{Z_c Z_o}}{Z_f^2 + Z_c Z_o} & \frac{Z_f^2 - Z_c Z_o}{Z_f^2 + Z_c Z_o} \end{bmatrix}$$

where the impedances  $Z_c$  and  $Z_f$  are those previously defined for the cavity and feed sections of the slab-line cavity and  $Z_o$  is the impedance of the transmission line carrying microwave power from the generator to the cavity.

### Chapter 3. Spectroscopic Instrumentation.

The following sections describe the construction and use of the optical system for making spectroscopic measurements on the MIP.

#### 3.1 Configurations of MIP Investigated.

Two types of atmospheric pressure MIP have been investigated using the slab-line cavity described by Hammond and Outred, 1976 (70), the dry argon MIP and the argon MIP incorporating sample aerosol introduction. The  $TM_{010}$  cavity described by Beenakker, 1976 (2) was also used to generate an argon MIP with sample aerosol introduction.

Both types of MIP were operated on industrial grade argon from a normal British Oxygen Company cylinder. Figure 3.1 illustrates the gas supply apparatus used to support the dry argon MIP. A pressure of 1.5 to 2.0 bar was set on the cylinder regulator, the large pressure differential across the needle valve ensuring that the MIP was operated at atmospheric pressure. The flow-meters were calibrated accordingly.

The cold trap was used to remove the majority of the impurity water vapour present in the argon and so to determine any effect on the plasma excitation conditions as reported in chapter 5. The cold trap was fabricated from a length of coiled copper tube which, when required, was immersed in a dewar flask containing a solid  $CO_2$ /acetone mixture at a temperature of  $-80^{\circ}C$ . Measurement of the intensity of OH molecular and atomic hydrogen spectra indicated that the cold trap removed 80% of the water vapour from the argon.

The additional items of equipment used to affect direct sample aerosol introduction into the MIP are described in section 6.3.

When the MIP was generated in the slab-line cavity the quartz discharge tube was placed at a position of maximum electric field strength in one of the configurations shown in figure 3.2.

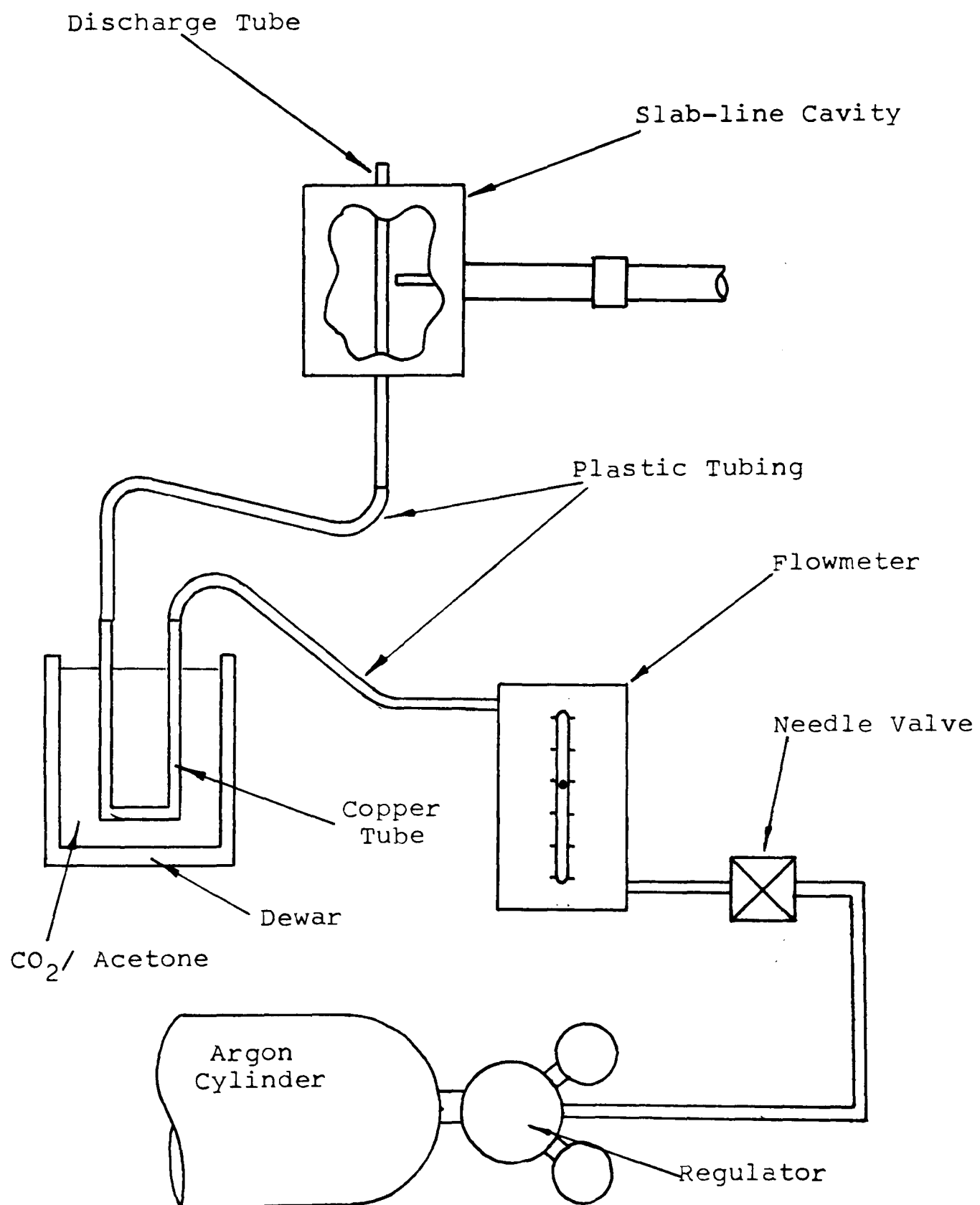
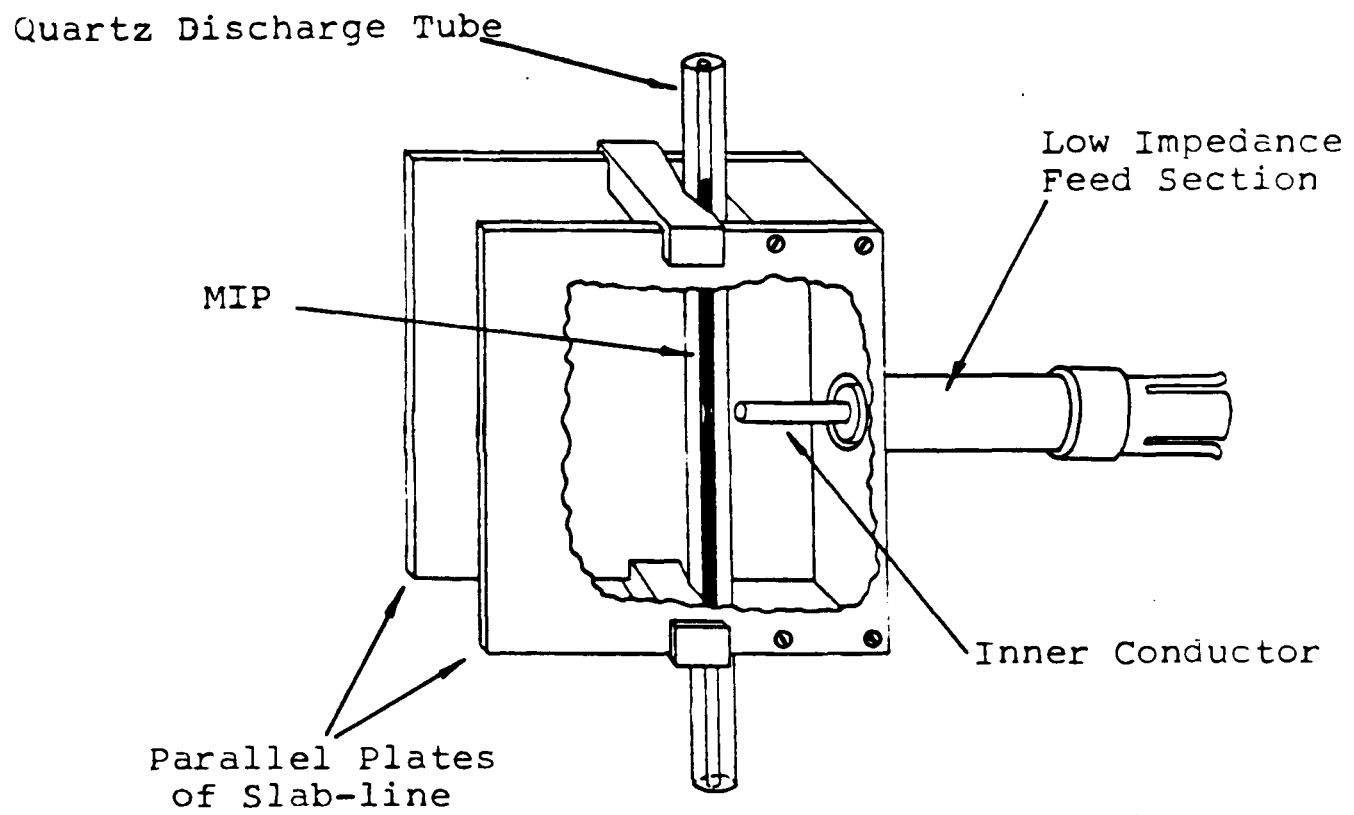


Figure 3.1. Gas Supply Apparatus for the Dry Argon MIP.

### Configuration A



### Configuration B

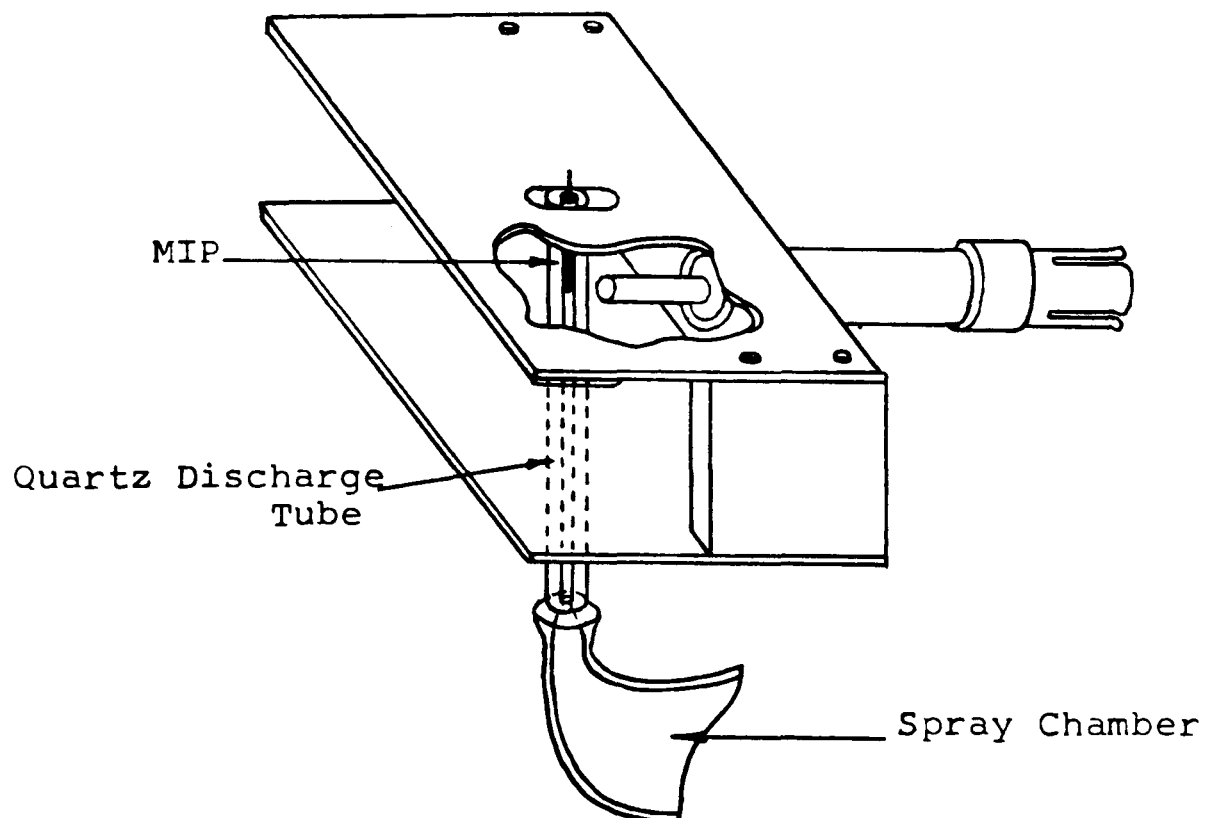


Figure 3.2      Configurations of the MIP Generated in the  
Slab-line Cavity.

The dry argon MIP formed when configuration B was used typically comprised a number of plasma filaments positioned around the inside wall of the quartz tube. These filaments were prone to positional instabilities, which made spectroscopic measurements somewhat difficult.

It was found to be preferable to use configuration A, when a stable dry argon MIP was formed which filled almost the entire cross-section of the discharge tube and to a varying length depending on the net microwave input power used.

When the sample aerosols were introduced into the MIP it proved to be impossible to reliably sustain a plasma using configuration A. This is probably due to the large amounts of water vapour in the gas absorbing energy from the microwave field within the cavity and detuning it to a point where the energy density was insufficient to maintain the MIP. However, the filamentary plasma formed when configuration B was used became a single stable filament within the discharge tube. Optimum microwave input power conditions were found, using the double stub tuner (section 4.2) with the MIP either occupying the entire length of the discharge tube or the top half only, between the end of the inner conductor and the top cavity plate (figure 3.3). In the latter mode of operation it was found that the MIP could be reliably maintained, for periods up to 10 hours using argon flowrates of 0.1 and 1.0 l min<sup>-1</sup> and sample uptake rates between 0.5 and 1.5 ml min<sup>-1</sup>. Tolerance to introduced sample aerosol was improved by the use of a 2 mm internal diameter discharge tube.

Except for some initial investigations, light from the MIP generated in the slab-line cavity was always viewed radially through the wall of the quartz discharge tube. With the discharge tube vertical, this was found to be more convenient to image a given length of plasma onto the vertical entrance slit of the monochromator (section 3.3) than the spot image formed when the light was viewed axially. In addition, radial viewing provided the opportunity to investigate spatial variations of the plasma parameters and to locate the optimum viewing zone for spectrochemical performance (section 6.5.1).

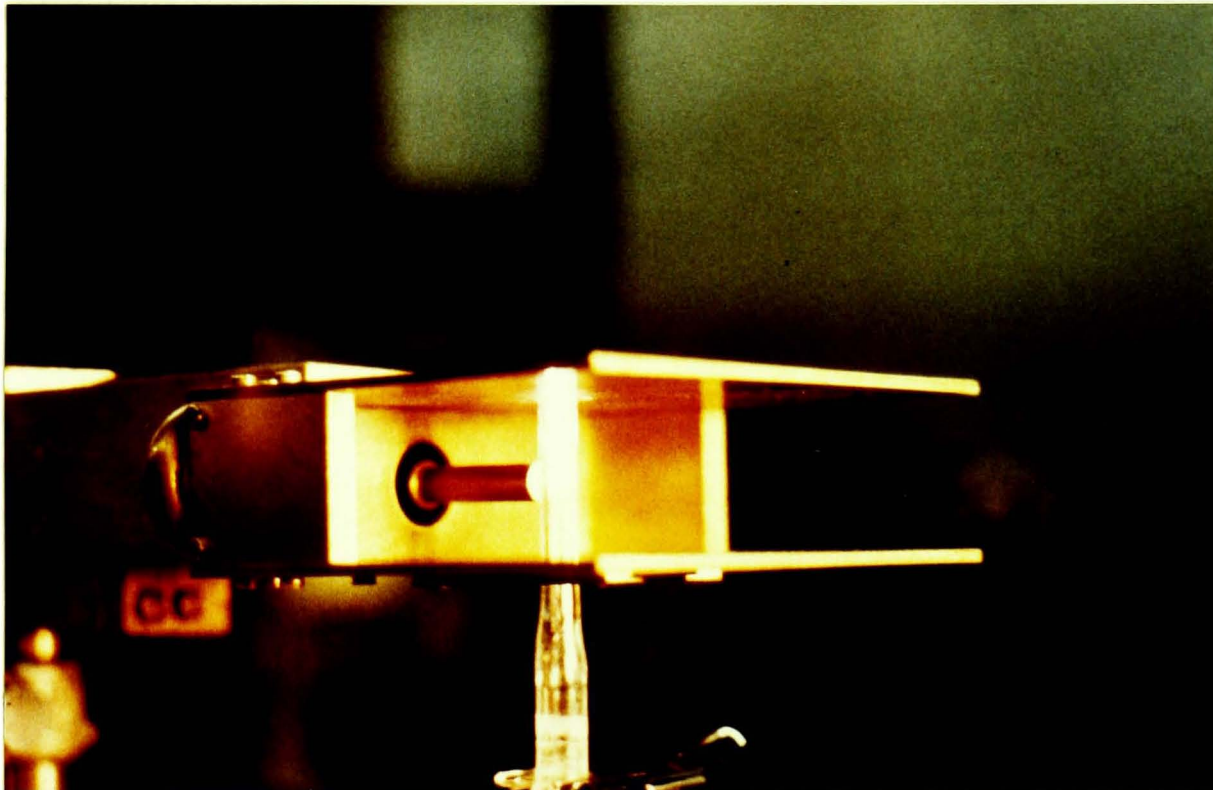


Figure 3.3      Plate of Analytical Argon MIP Generated  
in the Slab-Line Cavity.

The  $TM_{010}$  cavity used to support an argon MIP with sample aerosol introduction was constructed in the development model-shop of Pye-Unicam Ltd., to an engineering drawing (appendix A2). The cavity depth could be set to either 6 or 10 mm depending on which side plates were bolted to the main structure.

The discharge tube was positioned in the centre of the cavity (figure 3.4) with its end flush with the side plate as recommended by Beenakker et al, 1978 (20). The plasma formed attached itself to one part of the tube's inner wall and typically extended the full depth of the cavity but not beyond it.

Microwave power was coupled into the cavity using a modified UHF connector terminated with an inductive coupling loop (appendix A2). The connector was clamped into the cavity such that the plane of the coupling loop was perpendicular to the lines of magnetic flux circulating around the cavity, thus maximizing energy transfer. Special care was taken to ensure a constant  $50\ \Omega$  impedance throughout the length of the UHF connector to avoid the overheating problems reported by Van Dalen et al, 1978 (65) and to maximize energy transfer into the cavity.

It proved to be difficult to reliably maintain the MIP in the 10 mm deep  $TM_{010}$  cavity for even short periods with the  $0.5\text{ cm}^2$  coupling loop initially used. However, increasing the loop area to  $1.5\text{ cm}^2$  mostly cured this problem. Maintenance of the MIP in the 6 mm deep  $TM_{010}$  cavity was even more unreliable and with limited space available, only modest increases in the coupling loop area were possible without it extending well into the centre of the cavity and causing spurious modes of excitation. In practice it proved to be impossible to achieve the reliability obtained with the 10 mm deep cavity, with which, therefore all subsequent spectroscopic measurements for the  $TM_{010}$  cavity MIP were made.

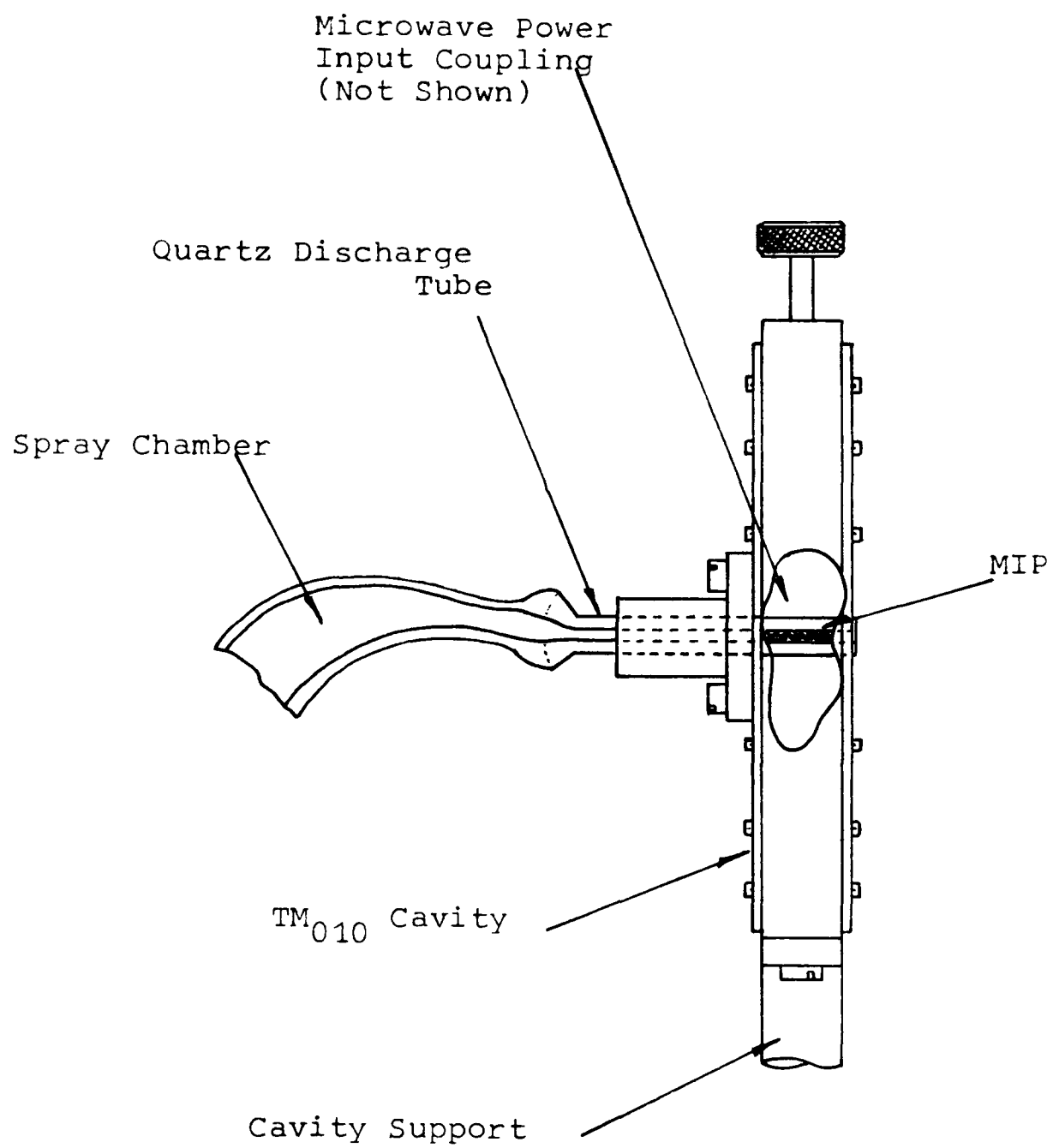


Figure 3.4      MIP Generated in the  $TM_{010}$  Cavity.



It was observed that over a period of 2 to 3 hours the plasma would wander about the inner wall of the discharge tube. This tendency could be minimized by carefully positioning the discharge tube 'off cavity axis', exploiting the clearance in the cavity side plate holes. Thus one part of the discharge tube inner wall was then nearest to the position of maximum electric field in the cavity, where the plasma presumably preferentially attached itself.

The closed structure of the  $TM_{010}$  cavity meant that light from the MIP could only successfully be viewed axially down the length of the discharge tube.

### 3.2 Description of Entrance Optics and Calibration Lamp.

The schematic diagram of the optical system used for making spectroscopic measurements on the MIP generated in the slab-line cavity is shown in figure 3.5. Table 3.1 lists the equipment employed with the exception of the data recording devices (section 3.6).

Light from the MIP was imaged onto the entrance slit of the monochromator by the simple 10 cm focal length quartz lens, Li via the front silvered mirror, Mi. Object and image distances were chosen to give an enlarged image of the MIP on the entrance slit with a magnification of 1.5. With this arrangement the internal optics of the monochromator itself were optimally filled when an entrance slit length of 1.2 cm was used.

In order that relative spectral line intensity measurements could be made over the wavelength range 300 to 800 nm, the instrument response function, denoted  $H(\lambda)$  (section 3.7) was determined using the tungsten ribbon filament lamp. Light from the filament lamp was imaged onto the entrance slit of the monochromator when mirror Mi was rotated through  $90^\circ$ .  $H(\lambda)$  was therefore determined using identical entrance optics to those employed for measurements on the MIP itself.

After a correction for the surface emissivity of tungsten, the filament lamp is essentially a black body radiator with a spectral output described by the Planck radiation formula. Filament temperature, calculated from the DC filament current using data supplied with the lamp, therefore uniquely defined the actual spectral output of the lamp, enabling  $H(\lambda)$  to be determined. Relative spectral intensity measurements were unaffected by the transmission coefficient of the quartz window since this is constant over the wavelength range considered.

When 1st order spectral lines with wavelengths greater than 500 nm were scanned, an OY4 filter (Chance Pilkington) was placed between Li and the entrance slit to eliminate 2nd order spectra from the monochromator grating.  $H(\lambda)$  was directly compensated for the 10% attenuation of this OY4 in its pass band by using the filter also during calibration of the optical system.

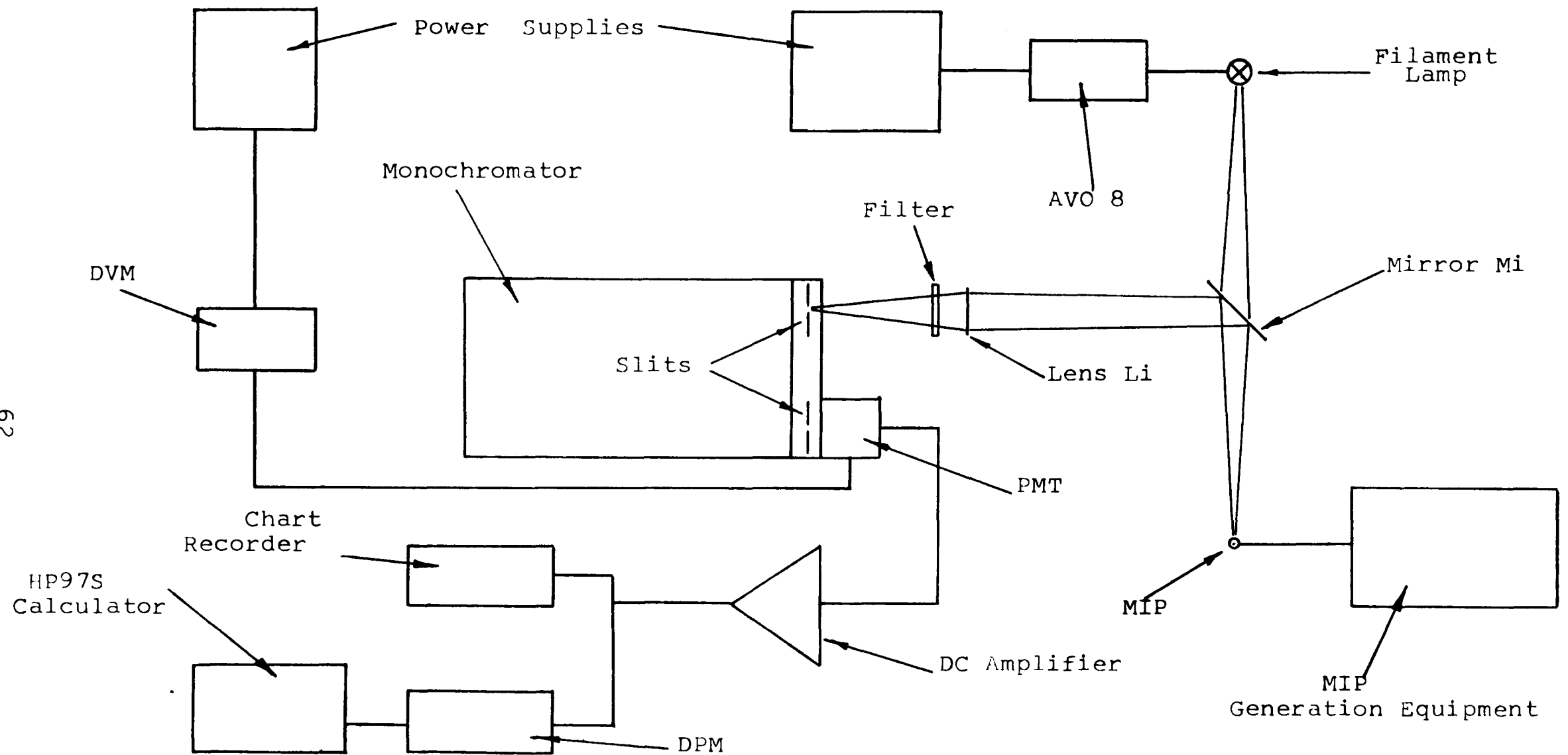


Figure 3.5. Optical Measurement System and Associated Equipment.

Similar entrance optics were used when the MIP was generated in the  $TM_{010}$  cavity except that mirror  $M_1$  was omitted, and the cavity placed on the axis of the optical system as shown in figure 3.6. Since light from the MIP is viewed axially down the length of the discharge tube the image formed on the monochromator entrance slit is a spot of approximately 1 to 2 mm diameter. The slit length was therefore reduced to a value just greater than the extent of the MIP image to reduce the effect of stray light.

In order to ensure that the same entrance optics were used when taking either spectral line scans of the MIP or a system calibration it was necessary to remove the  $TM_{010}$  cavity and replace it with the filament lamp.

---

Scanning Monochromator	Ebert Mounting 0.8 metre focal length 200-880 nm Reciprocal Linear Dispersion = $1.1 \text{ nm.mm}^{-1}$	Philips Scientific & Industrial Inst.Ltd.
Grating	1200 Rule Grooves $\text{mm}^{-1}$ Active Area $8 \times 7 \text{ cm}^2$	
PMT	Type 9558 B: 11 Dynodes: 52 mm Diameter Cathode with S20 response	Thorn EMI Electron Tubes Division.
PMT Power Supply	Type 532A: 0 - 2 kV	Isotype Developments Ltd.
D.V.M.	Type 169	Keithly Electronics Ltd.
Filament Lamp Power Supply	DC: 8V: 6A: Stabilized	Farnell Inst. Ltd.,
Tungsten Ribbon Filament Lamp	W2KG v11 Filament dimensions = $1 \times 10 \text{ mm}$ Quartz Window = 93% transmission between 300 and 800 nm Time for stable filament temperature = 20 mins.	Philips Electrical Ltd.
Optical Bench		Precision Instruments Ltd.

---

Table 3.1     Equipment used in the Optical System.

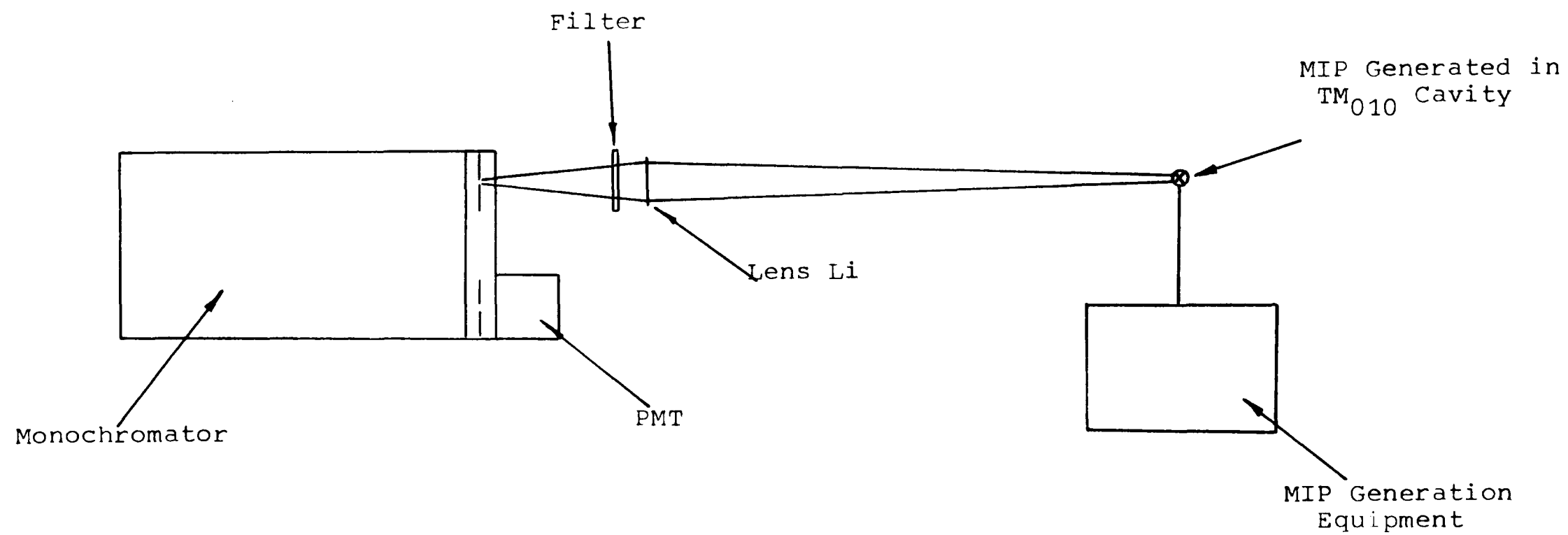


Figure 3.6      Entrance Optics Arrangement for the  $TM_{010}$  Cavity

### 3.3. The Monochromator and it's Operation.

The optical system was mounted on a dexion metal framework, one half of which carried the optical bench and the entrance optics components. The other half, bolted to a laboratory bench for additional support carried the Ebert scanning monochromator, loaned by Pye-Unicam for the duration of this work. The specifications of the monochromator may be found in table 3.1.

The monochromator's illuminated wavelength scale, reading from 170 to 880 nm, was accurate to within 0.5 nm of the true air wavelength over the entire range but for greater accuracy the scale was calibrated using the spectrum emitted by the argon MIP.

All spectral line scans were started at a sufficient distance from the line centre so that the mechanical backlash in the drive gears was always taken up and the spectral background intensity was adequately recorded. Where possible, reversal of the scan direction was avoided so that additional backlash was not introduced.

The coupled entrance and exit slits were simultaneously adjusted via one micrometer drive. In this work, equal entrance and exit slit widths of 0.012 and 0.026 mm were used.

For first order spectra from the grating, assuming normal incidence, the reciprocal linear dispersion of the monochromator is approximately  $1.1 \text{ nm mm}^{-1}$ . For an entrance slit width of 0.026 mm this equates to an instrument bandpass (section 3.8) of 0.029 nm. Measured values of bandpass were somewhat larger than this, 0.032 nm from a scan of the 632.0 nm line emitted by a 400 mW He-Ne laser and 0.035 nm from a scan of the 415.89 nm Ar I line, emitted by the MIP. Both these lines were assumed to be significantly narrower than the instrument bandpass itself. The values of instrument bandpass measured using the He-Ne laser were felt to be more reliable than the theoretical values and consequently were used in calculations of electron density from the Stark broadened  $H\beta$  spectral line (section 5.4.1).

The process of measuring  $H(\lambda)$  requires that with no light entering the entrance slit of the monochromator, there is zero electrical output registered on the digital voltmeter. To satisfy this zero light requirement certain modifications were necessary to reduce the sensitivity of the monochromator to 'stray light' which enters the entrance slit off axis and the monochromator and PMT enclosures directly through small gaps. The monochromator enclosure itself was found to be reasonably light tight but it was necessary to renew the sponge sealing tape between the two parts of the PMT enclosure, sealing all entrance holes with suitable grommets and tape.

A severe problem was encountered whereby light entering the slit enclosure from the source used was reflected directly across to the aperture which passed light from the exit slit to the PMT enclosure, ie. completely bypassing the monochromator itself.

This 'crosstalk' between the slits produced a larger electrical output signal than that obtained from the UV emissions of the tungsten filament lamp itself, so corrupting  $H(\lambda)$ . An inspection of the internals of the slit mechanism revealed little attempt on the part of the manufacturers to control this crosstalk which was subsequently and dramatically reduced by the construction of a blocking wall, made of high density sponge tape between the slits. Further reductions in crosstalk were made by spraying polished internal components with matt black paint. To block any other stray light entering, all apertures in the slit housing were taped over when not in use.

The resultant sensitivity of the spectrometer to stray light was then checked to ensure that the zero light condition could be achieved. A 6 W tungsten filament lamp was focussed onto the entrance slit of the monochromator. For a DC amplifier gain of 5, PMT supply voltage of 790 V, slit width of 0.026 mm and length of 1.2 cm, a total stray light output signal of 1.0 mV was measured at a monochromator wavelength setting of 350 nm when an OY1 filter was placed in the filter holder to

eliminate wavelengths less than 500 nm. When the exit slit was blanked off from inside the monochromator the output signal fell to 0.0 mV confirming that all stray light was passing through the monochromator itself. When a 240 V, 60 w inspection lamp was critically aimed at close range on the entrance slit to maximise any remaining crosstalk between the slits the output signal rose to 0.2 mV.

Secondly, with the OY1 filter and internal exit slit blank removed, a black suede screen was placed directly in front of the grating inside the monochromator. For the same instrument parameters as in the first check, a total stray light output signal of 1.0 mV was again observed and this remained constant to within  $\pm 0.1$  mV between 800 and 200 nm, illustrating the independence of the stray light on the wavelength.

Finally, with the grating unblanked but with the entrance slit completely blocked off with black tape the inspection lamp was shone on the spectrometer at close range and from various critical angles yet with no change in the output reading, confirming the total insensitivity to strong ambient lighting.

When  $H(\lambda)$  was determined, a DC amplifier gain of 1 was required in order to fit the response curve within the maximum range of the digital voltmeter and therefore the maximum stray light output signal that was observed under zero light conditions was 0.2 mV at all wavelengths.



### 3.4 The Photomultiplier Tube.

The EMI type 9558B photomultiplier tube (PMT) was housed in a two piece enclosure, mounted vertically over the exit slit of the monochromator. Light from the exit slit was reflected onto the PMT's photo-cathode using a small front silvered mirror mounted in the base of the enclosure at  $45^{\circ}$  to the monochromator axis. The enclosure halves were sealed together using high density sponge tape to prevent light entering as described in section 3.3.

The photo-cathode of the 9558B PMT has an "S20" response, which in conjunction with a boro-silicate window permits useable operation between 300 and 800 nm. Investigation of most spectral features of the argon MIP was therefore possible, from the OH molecular spectra at the UV end of the visible spectrum to the near IR atomic argon spectral lines. Use of the UV spectral lines of some introduced analyte species was precluded since a variant of the PMT, the 9558QB with extended UV response, was not available.

The dynodes of the PMT were biased using the resistor chain circuit shown in figure 3.7. Since the anode of a PMT can be considered as an almost ideal current generator, the output current is independent of the value of load resistor used. Choice of the latter is then primarily dictated by the matching of the PMT output signal to the input range of the data recording devices used. It was found that the range of signal amplification provided by the DC amplifier (section 3.5) could best compensate for the range of emission strengths of the MIP spectral features investigated when a PMT load resistor of  $67\text{ k}\Omega$  was used.

When a monochromator entrance slit width of 0.013 mm was used the PMT operating voltage was set to 940 volts. However, it was found that if the PMT was operated at 790 volts, the wider entrance slit of 0.026 mm gave more than adequate signal gain for the spectral features studies with the benefit of improved quality of the output spectral line data due to reduced PMT noise.

After an earlier spectroscopic study had shown that alteration of the supply voltage to vary the PMT response was unreliable, due to the finite time required for stable PMT operation to be re-established, it was decided to leave the PMT permanently energised at either 940 or 790 volts.

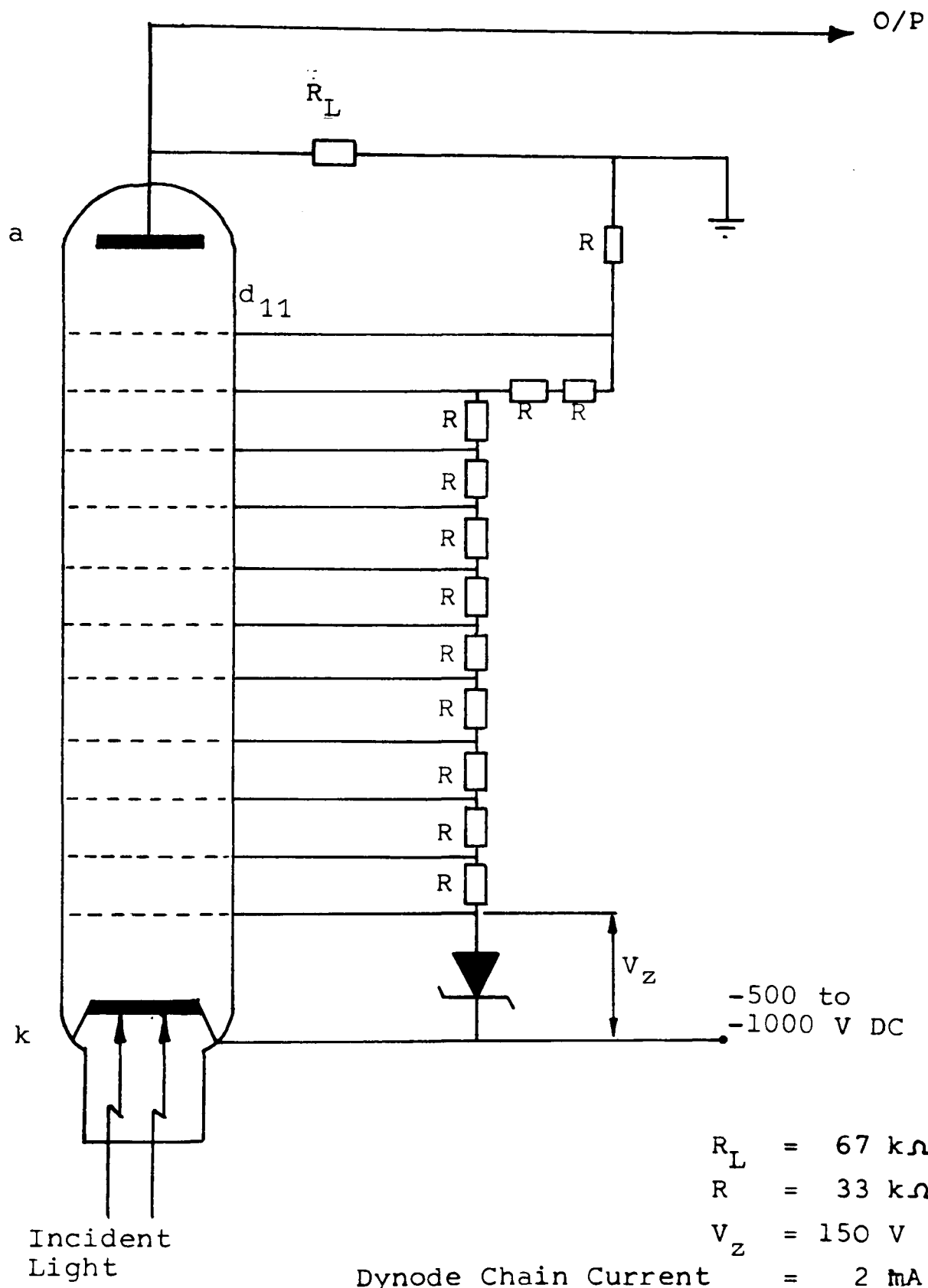


Figure 3.7 PMT Dynode Biasing Circuit.

### 3.5 The DC Amplifier.

The schematic diagram of the DC amplifier, used to amplify the signal voltage developed across the PMT load resistor is illustrated in figure 3.8. The high impedance operational amplifier input stage provides variable signal integration giving immunity from PMT noise. The parallel voltage follower buffers the input stage from the amplification stage, which uses an active feedback device to control its gain. The final stage comprises of a voltage follower with a multiturn potentiometer to adjust the DC offset of the output. This facilitates setting the baseline level on the pen chart recorder (section 3.6.1).

The 'OP-AMP' Cookbook by Jung, 1976 (76) proved invaluable when designing this DC amplifier, which uses many of his suggested circuits.

The gain of the amplification stage is given by the ratio of the decade resistance box,  $R_F$  to the fixed  $10\text{ k}\Omega$  resistor  $R_O$ .  $R_F$  was arranged in decades of  $10\text{ k}\Omega$ ,  $1\text{ k}\Omega$ ,  $100\Omega$ ,  $10\Omega$  and  $1\Omega$  providing variable gain from  $\times 1$  to  $11.1$  in steps of  $0.01$ . When  $R_F$  was reduced below  $10\text{ k}\Omega$ , the amplifier acted as a calibrated attenuator. This was particularly useful for the more intense spectral features. The limit of attenuation was  $0.22$  below which the output oscillated at a frequency of approximately  $700\text{ kHz}$ . For a given gain,  $G$  the output voltage  $V_O$  is linearly related to the input voltage  $V_1$ , i.e.

$$V_O = G.V_1$$



The equipment illustrated in figure 3.9 was used to determine the range of input voltages for which this relationship was satisfied. With an amplifier gain of  $x_1$  and minimum integrator time constant, the peak to peak amplitude of the square wave output from the signal generator was increased from zero to 4 volts in convenient increments and at each setting,  $V_1$  and  $V_o$  were noted using the CRO.

The resultant calibration curve for the amplifier is illustrated in figure 3.10 which shows the linear response over the range of input voltages tested, with a slight departure from true linearity for input voltages greater than 200 mV. However, this 'dynamic range' was more than adequate for the maximum voltages developed across the PMT load resistor (section 3.4).

For all values of gain selectable the response of the amplifier remained linear.

The amplifier gain was adjusted accordingly for each spectral line scanned so that an adequate output signal was obtained (typically, peak height of spectral line between 60 and 90% f.s.d. on the pen chart recorder).

For relative spectral line intensity measurements to be made, it was therefore necessary to refer each argon spectral line scan, taken at some specific amplifier gain,  $G$  to a fixed or reference gain  $G(\text{REF})$ . This was conveniently accomplished by using a gain multiplication factor  $G(\text{MF})$  given by

$$G(\text{MF}) = G(\text{REF})/G$$

The measured intensity (section 3.8) for a particular spectral line was then gain corrected by multiplication by the appropriate  $G(\text{MF})$ .

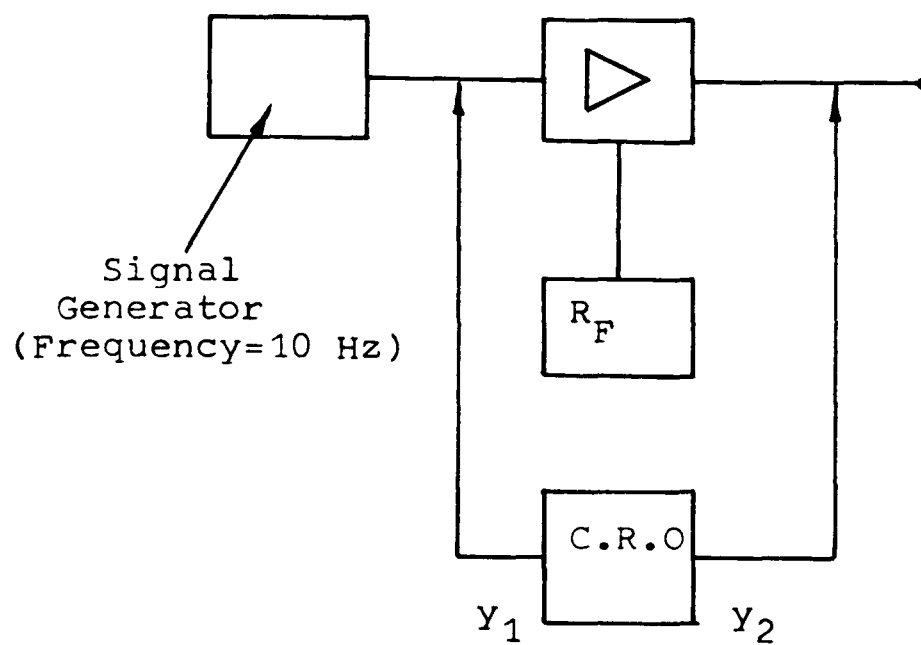


Figure 3.9      Equipment to Check Dynamic Range of DC Amplifier.

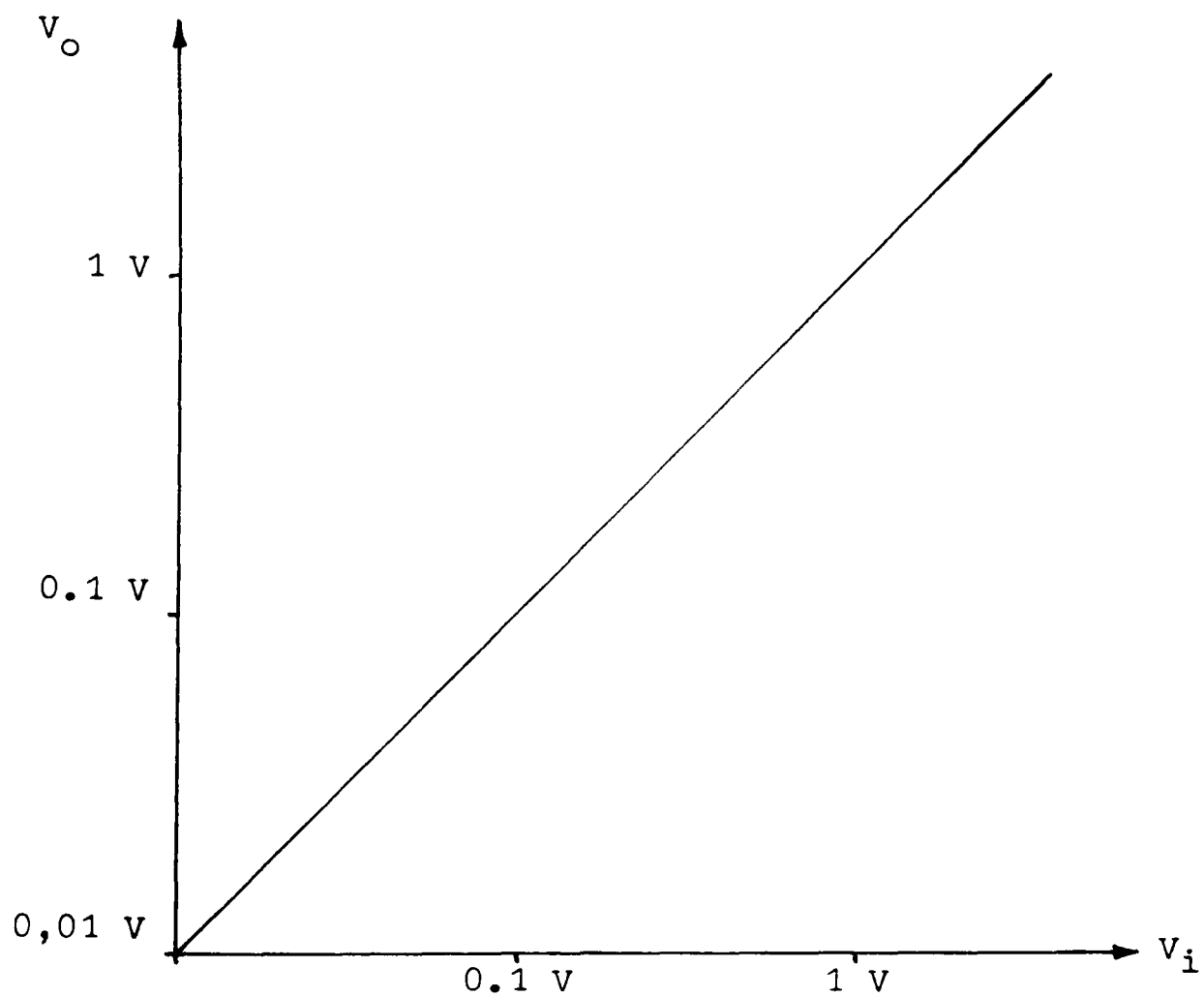


Figure 3.10      DC Amplifier Calibration Curve.

### 3.6 Data Recording Devices.

The devices used to record the spectroscopic data produced by the spectrometer were the pen chart recorder and the digital panel meter. The function of the recorder was to make a hard copy of the spectral line profiles as the lines were scanned by the spectrometer. The meter could be used simply as a milli-voltmeter to manually record the spectrometer calibration data or as part of a "data logger" system in conjunction with the Hewlett Packard HP97S programmable calculator.

A "distribution box" was constructed to house the meter and the interfacing electronics necessary to complete the inter-connection of the data recording devices. A schematic diagram is shown in figure 3.11 and summary data on the devices used is given in table 3.2.

#### 3.6.1 Pen Chart Recorder.

The characteristics of a spectral line profile obtained using the pen chart recorder, in addition to those conferred upon it by the excitation conditions in the MIP itself and by the instrument bandpass (section 3.9), are determined by the gain, output offset and integrator time constant of the DC amplifier, monochromator scan speed and the chart paper speed. Using a suitable amplifier gain the output offset was adjusted to give a convenient baseline reading (corresponding to the spectral background signal) on the chart paper. A value of integrator time constant was chosen which gave sufficient noise reduction and did not introduce any distortion of the line profile peak, the latter determining the time constant upper limit.

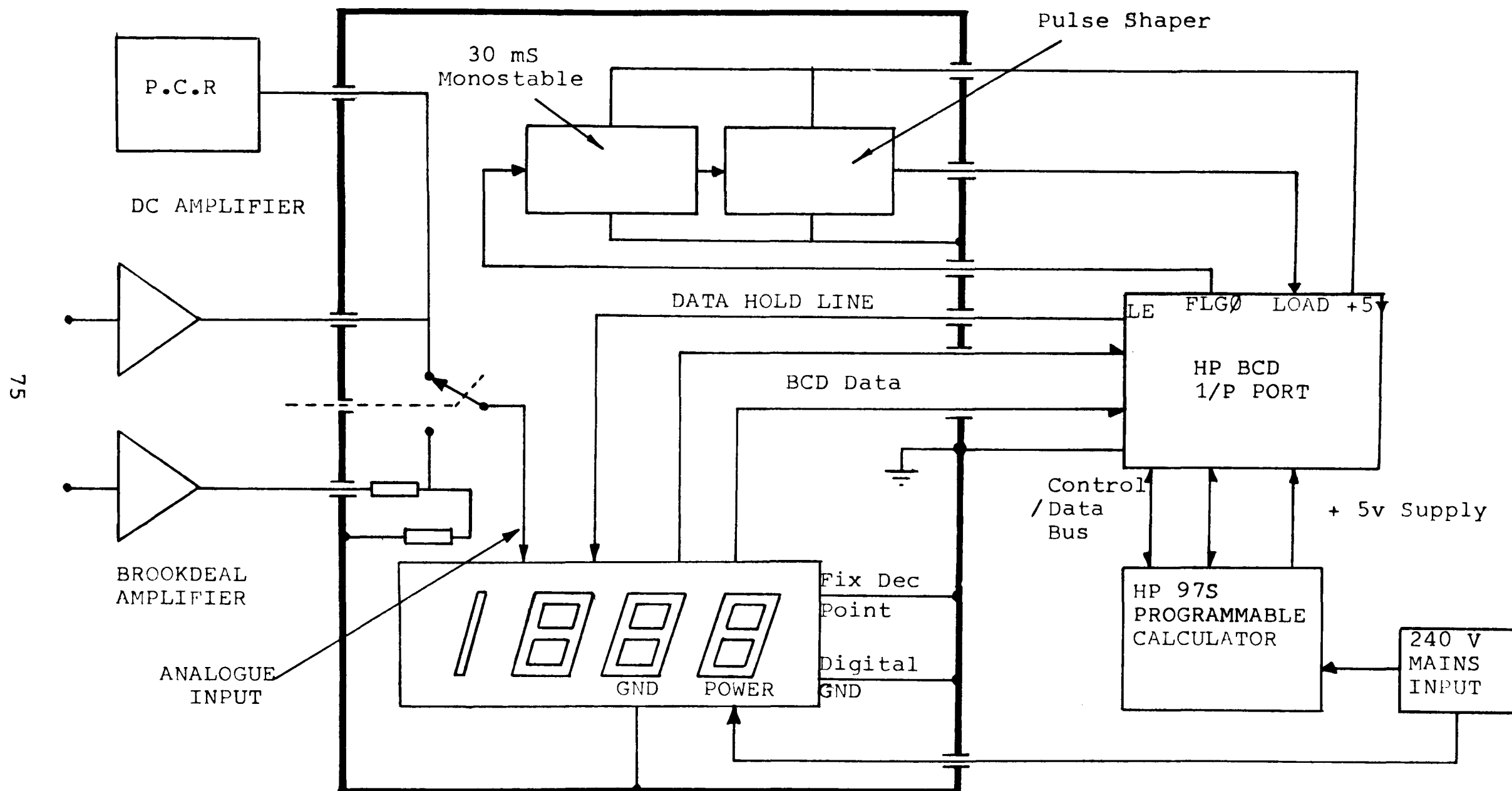


Figure 3.11    Interconnection Schematic for Data Recording Devices.



Pen Chart Recorder	Honeywell Brown Y:t recorder 0.25 sec Response Time 0-10 mV Input voltage Range Variable Chart Paper Speed (by gear selection)
Digital Panel Meter	Analogue Devices AD 2016/B 3 $\frac{1}{2}$ Digit LED Display 100 M $\Omega$ Input impedance 100 $\mu$ V Sensitivity $\pm$ 200 mv input voltage range 13 line BCD output Data output hold facility.
HP97S Programmable Calculator plus I/O Port.	Hewlett Packard programmable/ scientific calculator with I/O (10 digit BCD I/P + 4 Flag O/P lines) "Handshake" Facility Internal Thermal printer and Magnetic Program card reader, LED display.
D.C.Amplifier	See section 3.5
Brookdeal 401A Amplifier	See Section 6.2.1.
30 mS Monostable	74121 T.T.L. Monostable IC Pulse shaping circuit on O/P

Table 3.2     Data Recording Devices, Equipment used.

Chart paper speed gears were selected so that where spectral intensity was to be described by line area, a monochromator scan speed of  $0.1 \text{ nm min}^{-1}$  yielded a suitable line profile which could be integrated using Simpsons method (section 3.8.1). However, when peak height only was used, faster monochromator scan speeds of  $0.5$  and  $1.0 \text{ nm min}^{-1}$  were employed to economize in the time spent taking a complete set of spectral measurements.

When the chart recorder was switched off it was found to slightly load the output of the DC amplifier, subsequently therefore, it was disconnected when not in use.

### 3.6.2. The Digital Panel Meter and HP97S Calculator (Data Logger).

A signal integrator was constructed using the digital panel meter (DPM) and HP 97S calculator for use when evaluating the spectrochemical performance of the MIP (for which the Brookdeal 401A amplifier, shown in figure 3.1 was also used). However, due to the very labour intensive nature of line area determinations using Simpson's method and because the only difference between an integrator and a data logger as herein described is the type of program running on the HP 97S, it was decided to automate the procedure and compute the area as the spectral line was being scanned.

The signal integrator and data logger programs for the HP 97S calculator incorporated an identical method of reading BCD data from the output of the DPM. This consisted of temporarily halting program operation, clearing the input register and inhibiting the updating of the DPM's output. Data entry was self-initiated following a 30 ms pause generated by the monostable and the output signal voltage, measured to a resolution of tenths of milli-volts read into the calculator's input register. With data entry complete, program operation was restarted so that suitable signal processing could be carried out. Data logger program operation was

begun at the start of each spectral line scan so that a mean background signal could be determined (section 3.3).

The line profile data was then read at a sampling rate,  $R$  of  $21.09 \text{ min}^{-1}$ , or a reading every 2.845 seconds. At a scan speed of  $0.1 \text{ nm min}^{-1}$  this corresponds to a wavelength interval between readings of 0.005 nm and therefore constitutes a marked improvement in spectral resolution over Simpson's method. Even so the area of a particular spectral line calculated by both methods were in close agreement, validating the adequate resolution of the wavelength interval used in Simpson's method. When the line scan was complete, any numeric keypress on the HP 97S during a 1 second pause period would cease data entry. After requesting the monochromator scan speed,  $V$  the calculator evaluated the line area using the collected data (section 3.8).

The data logger was slightly sensitive to electrical interference which could corrupt the input data, resulting in large errors in the computed line area. Every effort was made to reduce this sensitivity by suitable shielding but the problem was never completely cured. Therefore the HP 97S data logger and the pen chart recorder were always operated simultaneously so that a hard copy of a spectral line profile was available should the computed line area be in error. The line area could then always be evaluated by Simpson's method to eliminate the need to repeat the scan.

### 3.7 Calibration of the Optical System.

With the filament lamp illuminating the monochromator entrance slit and a wavelength setting of 300 nm, the output of the DC amplifier was recorded, using the DPM. The monochromator was then reset to the next highest required wavelength, using the scanning motor operated at a speed of  $25 \text{ nm min}^{-1}$  and the amplifier output noted again. This procedure was repeated in appropriate steps up to 800 nm producing a set of values denoted  $H_1(\lambda)$ . The procedure was then repeated in the reverse direction down to 300 nm producing a second set of values denoted  $H_2(\lambda)$ .

The mean instrument response function  $H(\lambda)$ , given by

$$H(\lambda) = \frac{H_1(\lambda) + H_2(\lambda)}{2}$$

is automatically compensated for the presence of optical filters in the light path (section 3.2) but as yet is not compensated for the spectral output of the filament lamp given by the Planck formula,

$$B_o(\lambda, T) = \frac{2hc^2}{\lambda^5} \exp\left(\frac{hc}{\lambda kT} - 1\right)$$

where all symbols have their usual meaning.

Having evaluated a set of  $B_o(\lambda, T)$  at the required wavelengths, the values of tungsten emissivity,  $\epsilon(\lambda)$  measured by Ornstein, 1936 (77) were used to calculate the true spectral output of the lamp,  $B(\lambda, T)$  given by

$$B(\lambda, T) = \epsilon(\lambda) \cdot B_o(\lambda, T)$$

the implicit assumption being that the tungsten filament lamp is a 'grey body' light source.

The response of the filament lamp was independently checked using an International Laboratory type 1L 700 radiometer and good agreement was found between measured and calculated spectral intensities over the range of wavelengths used.

The true response of the optical system as a function of wavelength is then given by

$$\frac{H(\lambda)}{B(\lambda, T)}$$

and a typical example is illustrated in figure 3.12. The solid curve shows the actual response with the effect of the filters clearly indicated.

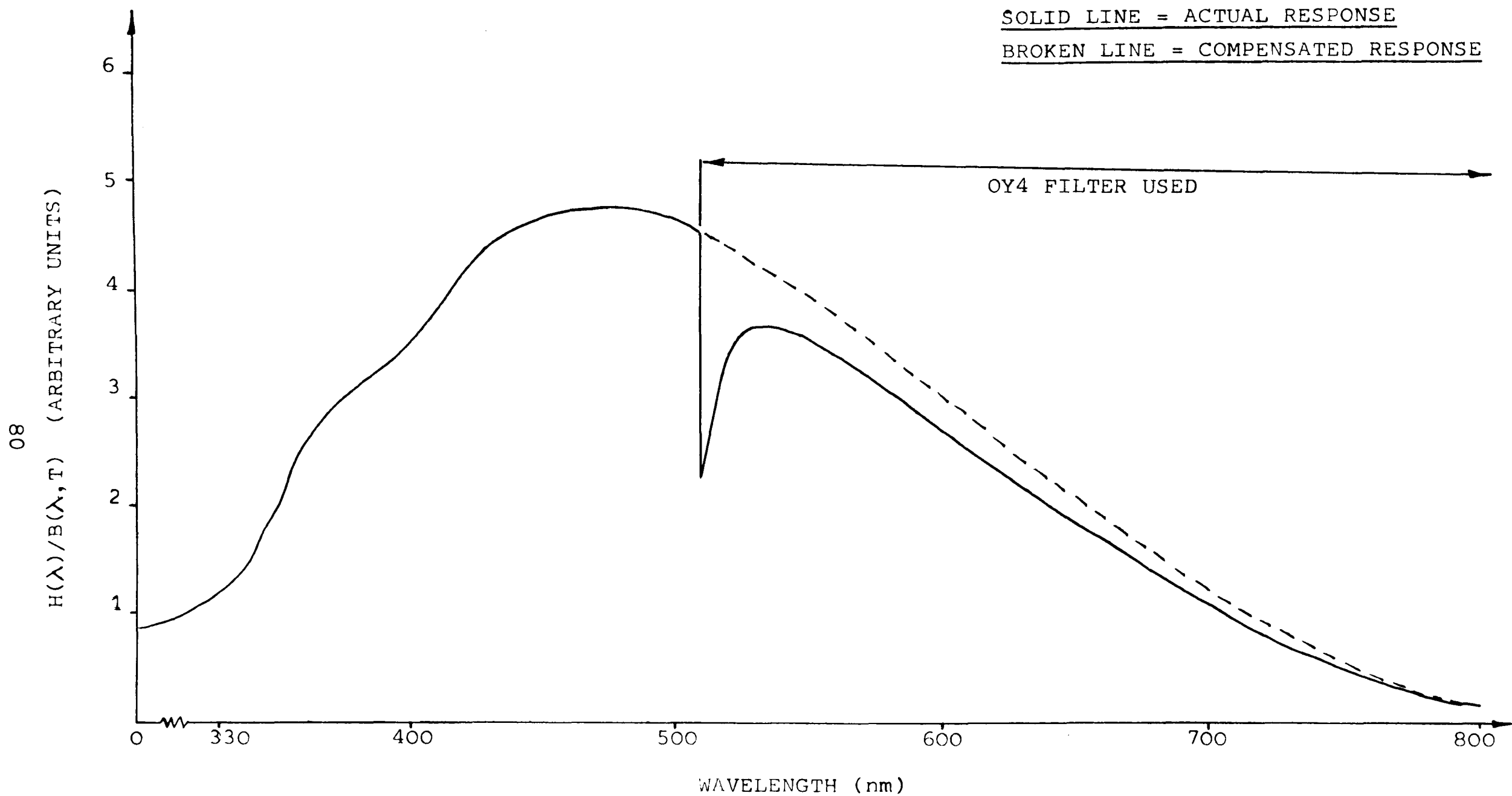


Figure 3.12    Optical System Calibration Curve.

When the calibration was carried out it was found to be convenient to use a DC amplifier gain setting of approximately X 1. Now the value of gain selected will affect the shape of the response curve obtained but the ratio of  $H(\lambda)$  at two different wavelengths will be identical for two different gain settings since the amplifier response is linear for all gain (section 3.5) and zero electrical output is registered on the DPM when light is prevented from entering the monochromator entrance slit (see section 3.3).

To compare the intensity of a spectral line at a wavelength  $\lambda_1$  to another at  $\lambda_2$  it was found to be convenient to evaluate a 'correction factor' for this spectral line given by the ratio of  $H(\lambda_2)$  to  $H(\lambda_1)$ ,

$$CF(\lambda_1) = \frac{H(\lambda_2)}{H(\lambda_1)}$$

such that if the intensity of the spectral line at  $\lambda_1$  is denoted  $i_1$  then the corrected intensity  $I_1$  is given by,

$$I_1 = i_1 \cdot CF(\lambda_1)$$

A value of wavelength,  $\lambda_2$  was chosen to which all intensity measurements were referred. This was denoted the reference wavelength,  $\lambda_{REF}$  and since of arbitrary value was conveniently chosen depending on the spectra under consideration. Table 3.3 gives the values of  $\lambda_{REF}$  for the argon, iron and OH spectra.

Spectra	$\lambda_{REF}(nm)$
Ar	603.21
Fe	370.00
OH	320.00

Table 3.3.    The Reference Wavelengths.

Using the appropriate  $\lambda_{\text{REF}}$  a set of correction factors were evaluated using the equation

$$CF(\lambda) = \frac{H(\lambda_{\text{REF}})}{H(\lambda)}$$

where  $\lambda$  took the values of specific MIP spectral features investigated (chapter 5).

The tolerance on each  $CF(\lambda)$  was evaluated using the expression

$$\Delta CF(\lambda) = \pm \left[ \frac{\frac{H(\lambda_{\text{REF}})^+}{H(\lambda)^-} - \frac{H(\lambda_{\text{REF}})^-}{H(\lambda)^+}}{2} \right]$$

where the superscripts "+" and "-" denote the maximum and minimum values respectively of the measured quantities.

The spectral response of the filament lamp was also express as a correction factor, denoted  $MFB(\lambda, T)$  and evaluated using the expression

$$MFB(\lambda, T) = \frac{B(\lambda_{\text{REF}}, T)}{B(\lambda, T)}$$

with the tolerance given by the expression

$$\Delta MFB(\lambda, T) = \pm \left[ \frac{\frac{B(\lambda_{\text{REF}}, T)^+}{B(\lambda, T)^-} - \frac{B(\lambda_{\text{REF}}, T)^-}{B(\lambda, T)^+}}{2} \right]$$

To simulate the calibration curve in figure 3.12 an overall correction factor,  $C(\lambda)$  was evaluated using the expression,

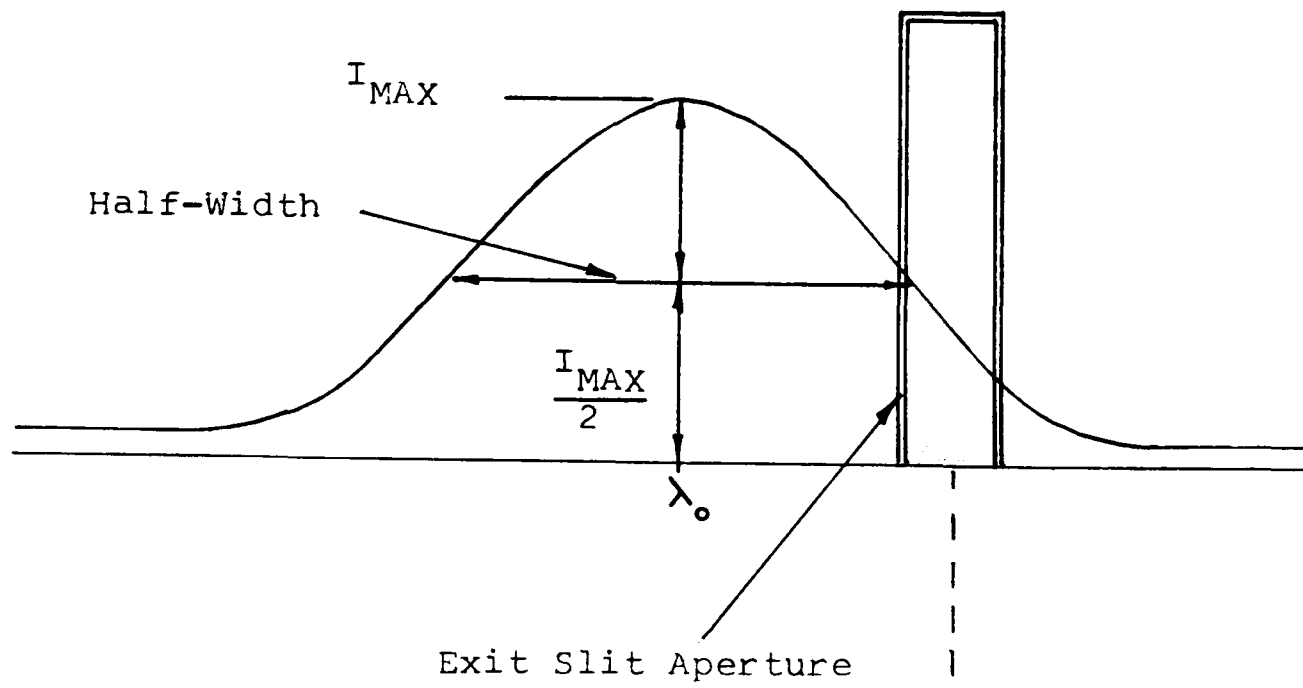
$$C(\lambda) = \frac{CF(\lambda)}{MFB(\lambda, T)}$$

with the tolerance given by the expression,

$$\Delta C(\lambda) = \pm \left[ \frac{\frac{CF(\lambda)^+}{MFB(\lambda, T)^-} - \frac{CF(\lambda)^-}{MFB(\lambda, T)^+}}{2} \right]$$

The optical system calibration was automatically calculated as a set of  $C(\lambda)$  correction factors by the algol 60 program used to evaluate the Boltzmann equation (Appendix A3), so that relative spectral line intensities could be determined directly from the spectral data.

a)



b)

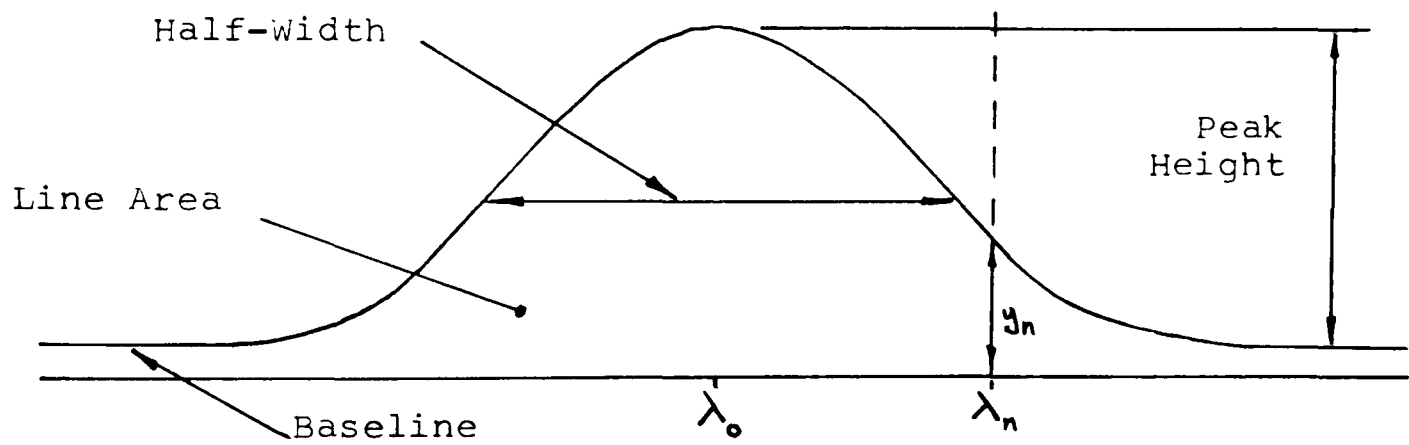


Figure 3.13 a) Observed Spectral Line Profile  
Half-Width = 5 x Exit Slit Aperture  
 b) Resultant Output Profile



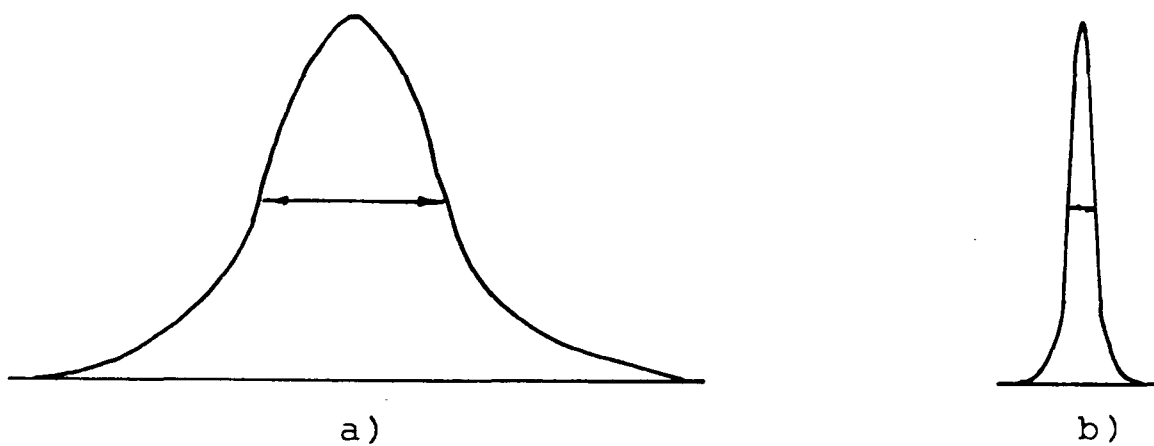
### 3.8 Determination of Spectral Line Intensity

When the monochromator is set to a particular wavelength, the response measured at the output of the DC amplifier is proportional not only to the spectral radiance of the illuminating source at this wavelength but also to the sum of contributions from a given wavelength interval called the instrument bandpass.

Figure 3.13a shows an hypothetical spectral line profile, emitted by the MIP whose image is formed in the plane of the monochromator exit slit and figure 3.13b shows the resultant output line profile which would be produced when the spectral line is scanned past the exit slit, represented by the aperture. The output line profile shows the two parameters which may be used to express the spectral line intensity. These are the peak height, which is the height of the intensity maximum above the baseline and the line area which is the area bounded by the baseline and the curve of the line profile itself. The parameter used to represent the intensity depends primarily on the relative shapes of all the spectral lines belonging to the set used to determine a temperature, eg. all the argon spectral lines scanned.

Every ordinate,  $Y_n$  of the output line profile is proportional to the integral of the total light, shown shaded in figure 3.13a, "seen" by the exit slit when the monochromator is at this wavelength. The observed and output line profiles have similar shapes with virtually identical half-widths which is 5 times larger than the exit slit aperture. A similar situation exists for the line profile illustrated in figure 3.14(a) with a half-width equal to twice the instrument bandpass. Figure 3.14(b) however illustrates the situation when a spectral line with an identical peak height but a half-width equal to one third of the instrument bandpass is scanned. The output profile now produced has a totally different shape to the observed spectral line and its half-width is that of the instrument bandpass itself. When comparing the intensity of the two spectral lines shown in figure 3.14

### Observed Spectral Lines



### Resultant Output Profile

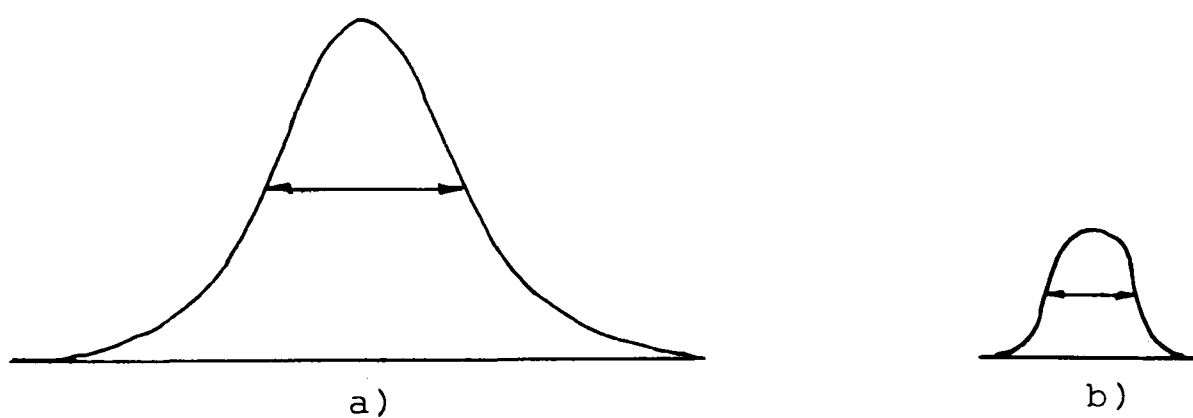


Figure 3.14 a) Observed Spectral Line, Half-Width =  $2x$  Instrument Bandpass.  
 b) Observed Spectral Line, Half-Width =  $\frac{1}{3}x$  Instrument Bandpass.

therefore, use of the peak height of the output profile would be inadequate. However, the area bounded by the output profile and the baseline is still proportional to the area of observed spectral line profile and hence its spectral radiance in both cases shown according to Seshadri and Jones, 1963 (78) or Penner, 1959 (79).

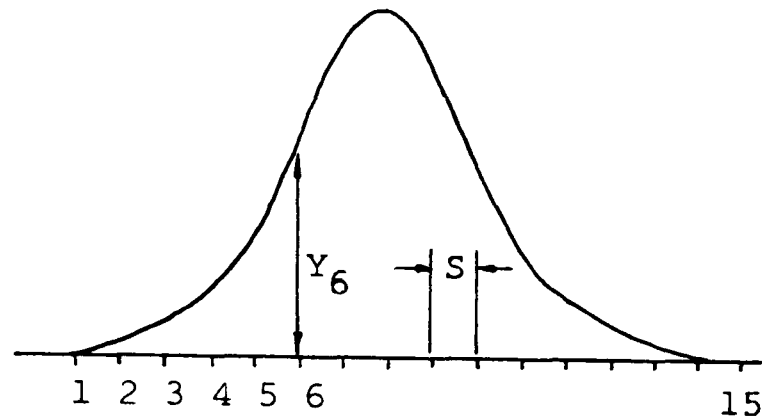
Because of the considerable variability of the shape and half-width of the 20 argon atomic spectral lines scanned, the line area of the output profile was the parameter used to represent the intensity. Only where observed spectral lines were of identical shape, as in the case of the OH molecular spectra, was the peak height of the output profile used as the spectral intensity parameter.

The line area was determined by one of two methods, Simpson's numerical integration method or by automatic computation using the data logger.

#### 3.8.1 Determination of Line Area by Simpson's Method.

The area bounded by the curve of the line profile and the baseline was evaluated using Simpson's method for numerical integration in the usual way. Figure 3.15 summarises the procedure used.

For the narrower spectral lines with half-width less than 0.1 nm the strip width  $S$ , was set to the minimum practical value of 0.01 nm. The resolution was sufficient with the resulting number of  $y$  ordinates for the line profile to be described as accurately as was possible. For the wider spectral lines with half-widths greater than 0.1 nm, a value of  $S$  equal to 0.02 or 0.03 nm reduced the number of  $y$  ordinates and hence the labour involved in the manual calculation of the line area without significantly affecting the line area calculated.



$$\text{AREA} = S/3 \left[ Y_1 + Y_{15} + 4(Y_2 + Y_4 + Y_6 + Y_8 + Y_{10} + Y_{12} + Y_{14}) \right. \\ \left. + 2(Y_3 + Y_5 + Y_7 + Y_9 + Y_{11} + Y_{13}) \right]$$

Figure 3.15      Line Area Determined Using Simpson's Method

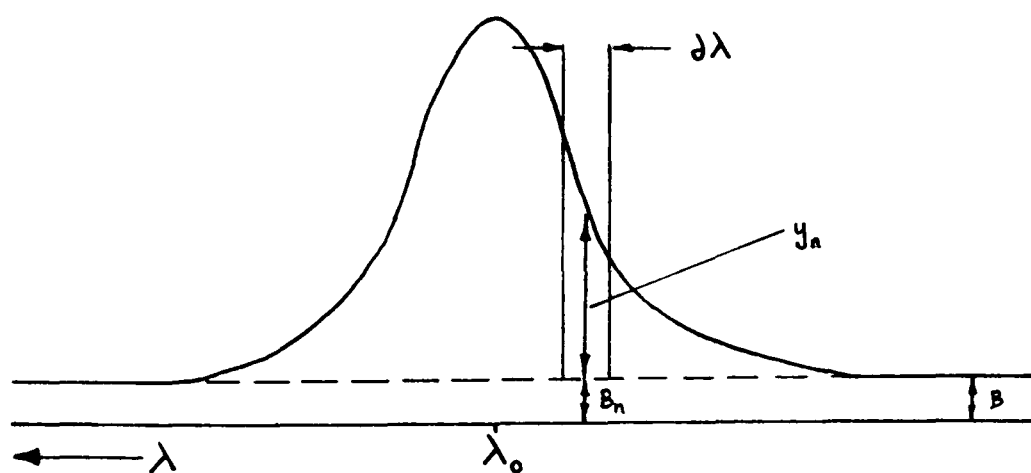


Figure 3.16      Automatic Determination of Line Area

### 3.8.2 Determination of Line Area by the Data Logger.

The data logger system described in section 3.6 yielded the following data from which the line area was computed immediately after the line scan was complete.

Background Signal Intensity	B
Summary of y ordinates	$\sum y_n$
Number of ordinates.	n
Monochromator scan speed	V

The calculator evaluated the small wavelength interval given that  $\delta \lambda = V/R$

and the line area as shown in figure 3.16.

$$\text{Element Area} = (y_n - B_n) \delta \lambda$$

$$\text{Total Line Area} = \sum_n (y_n - B_n) \delta \lambda$$

The background signal B was evaluated on the low wavelength side of  $\lambda_0$ , the centre wavelength of the spectral line. It is assumed that the background intensity is constant over the entire line range. Therefore  $B_n$  can be replaced by the single value B. The equation above for the total line area then simplifies to:-

$$\text{Area} = (\sum_n y_n - B.n) \delta \lambda$$

which was directly evaluated by the calculator.

In the case of the 433.36 nm line which sits on a sloping background signal caused by the proximity of the  $H_\gamma$  spectral line of hydrogen, the line area was calculated only by Simpson's method.

#### Errors on Line Intensity Measurements.

- When peak height was used as the line intensity parameter, the error on this parameter was estimated as the uncertainty of measuring the true peak height above the background signal.
- When line area was used, the error on this parameter was evaluated as the multiple of the peak height uncertainty and the uncertainty on the half-width.

4.1 Tuning of the Unloaded Slab-line Cavity.

The scattering (S) parameter representation of the slab-line cavity formulated by Hammond, 1978 (56) (section 2.3), ignores the two large discontinuities in cavity geometry. These occur where the inner conductor ends (at the point where the discharge tube is placed) and at the junction between the two cavity sections and produce distortions in the electric fields within the cavity.

Hammond found that the effective shunt capacitance of the junction, calculated from the data given in studies by Whinnery et al, 1944 (80) and Kraus, 1960 (81) had a negligible effect on the theoretical model he used to describe the slab-line cavity. However, the 'fringing' electric fields at the end of the inner conductor were found to appreciably lengthen the electrical length of the cavity section. This necessitated tuning the cavity by shortening the inner conductor until the input reflection coefficient had zero phase at a frequency of 2.45 GHz. The equipment illustrated in figure 4.1 and tabulated in table 4.1 was used.

The modulus of the cavity input reflection coefficient, which falls sharply near resonance, could be used to determine the resonant frequency of the slab-line cavity although Hammond reports difficulties in such a measurement. This is because determination of the modulus of the cavity input reflection coefficient requires the measurement of the very large voltage standing wave ratio, VSWR created on the transmission line by the open circuit termination of the unloaded slab-line cavity.

Only the position of the voltage minima, determined by the method of bracketing (section 4.3) is required to determine the phase of the cavity input reflection coefficient. The position of the voltage minima are not nearly so sensitive to any mechanical stresses exerted on the cavity structure or the value of VSWR.

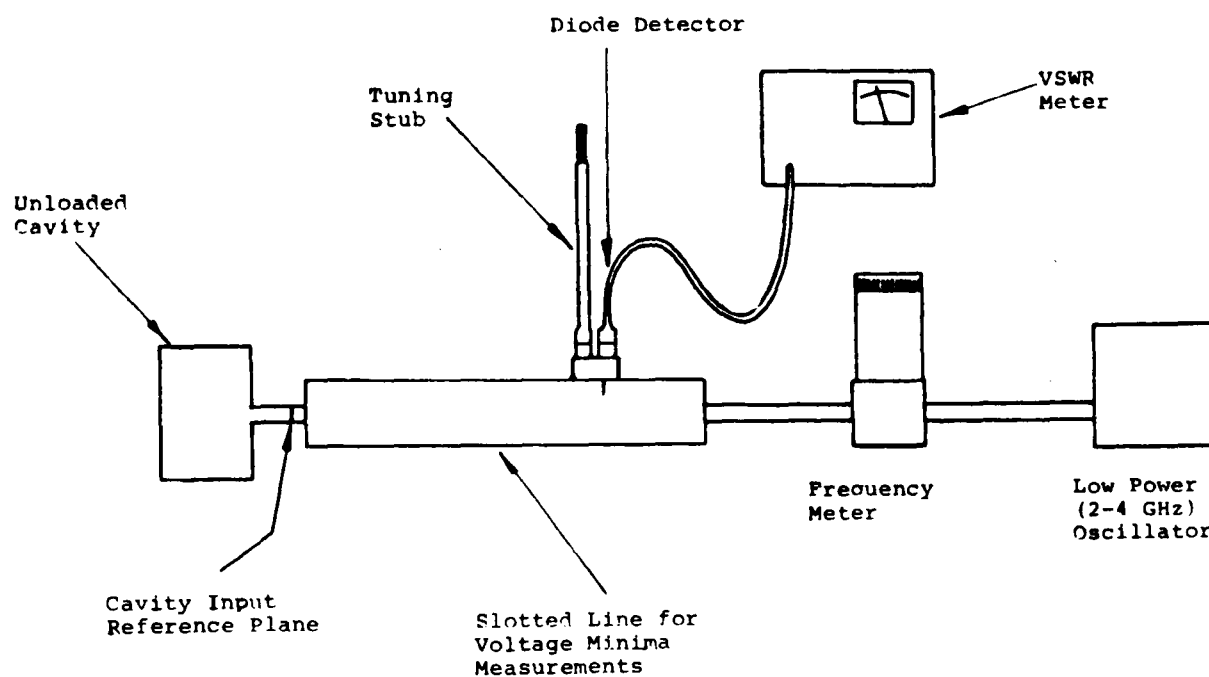


Figure 4.1 Microwave System for Measuring the Phase of the Cavity  
Input Reflection Coefficient.

Equipment	Type	Manufacturer
Microwave Generator	6056	Marconi Saunders Ltd
VSWR Meter	6593A	" " "
Frequency Meter	536A	Hewlett Packard
Slotted Line	874 LBA	General Radio Corp
Detector Diode	IN 21B	Siemens GmBh

Table 4.1 Equipment used to tune the unloaded slab-line cavity.

Measurement of the positions of the voltage minima along the slotted transmission line (section 4.3) were made relative to the 'input reference plane' of the slab-line cavity shown on figure 4.1. This was determined by replacing the slab-line cavity with a high quality short circuit termination. The position of the cavity input reference plane was fully compensated for all dielectric (PTFE) spacers used to support the inner conductors of the transmission line.

The slab-line cavity employed in this work was tuned using two different configurations of the inner conductors (figure 4.2).

Figure 4.3. illustrates the dependence of the phase of the cavity input reflection coefficient on the operating frequency for these two inner conductor combinations used after they have been correctly adjusted for length.

For both inner conductors, the unloaded cavity gain,  $G_o$  was calculated using,

$$G_o = 2 \frac{Z_c}{Z_f}$$

where  $Z_c = 138 \log(4\pi b/a)$ ,  $b$  = separation of the parallel plates  
 $a$  = diameter of the inner conductor  
 and  $Z_f = 138 \log(c/d)$ ,  $c$  = diameter of outer conductor.  
 $d$  = diameter of inner conductor.

The physical dimensions and unloaded gain of the slab-line cavity using these inner conductors are tabulated in table 4.2

When the dry argon MIP was operated in the slab-line cavity (section 3.1), the inner conductor giving  $G_o = 18.5$  was used. However, when the analytical MIP was operated in the slab-line cavity, the inner conductor giving  $G_o = 5.5$  was found to give more reliable operation when varying amounts of different sample solutions were aspirated.

The quartz discharge tube was positioned in the slab-line cavity so that a small 'coupling gap' existed between it and the end of the inner conductor. Hammond reports that without this coupling gap the quartz tube would be rapidly punctured by the coronal discharge formed between it and the end of the inner conductor. The coupling gaps used with each inner conductor configuration are given in table 4.2.



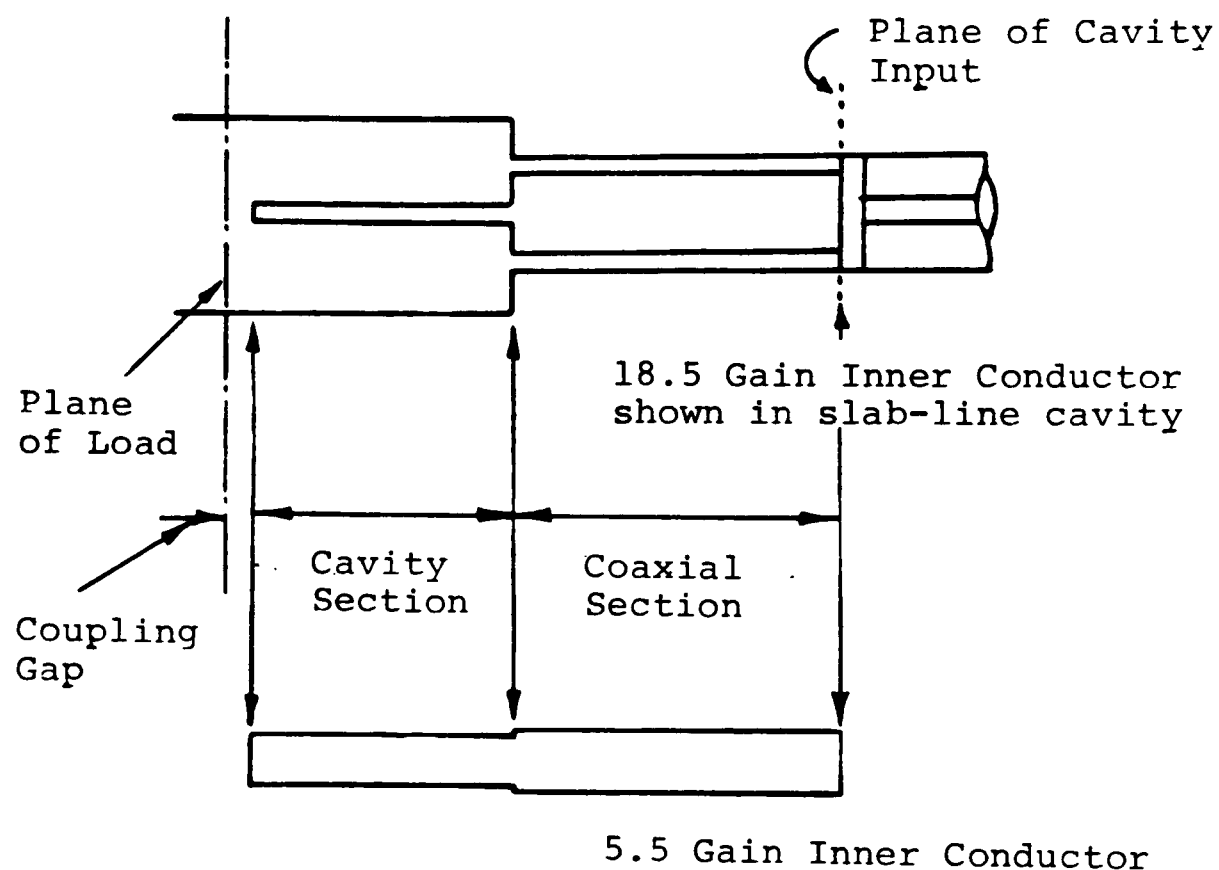


Figure 4.2 Slab-line Cavity Inner Conductors.

Inner Conductor (Slab-line)				Inner Conductor (Coaxial Feed)		Unloaded Cavity Gain $G_o$
OD. $a$ (mm)	Length (mm)	Coupling Gap (mm)	$Z_C$ (Ohm)	OD, $d$ (mm)	$Z_F$ (Ohm)	
3.18	26.6	3.4	139.1	11.11	15.1	18.5
6.35	25.4	1.5	97.5	7.94	35.2	5.5

Parallel Plate Separation,  $b = 25.4$  mm  
Internal Diameter of Coaxial Feed Outer Conductor,  $c = 14.29$  m  
Length " " " Inner " = 30.60 m

Table 4.2. Slab-line Cavity Parameters.

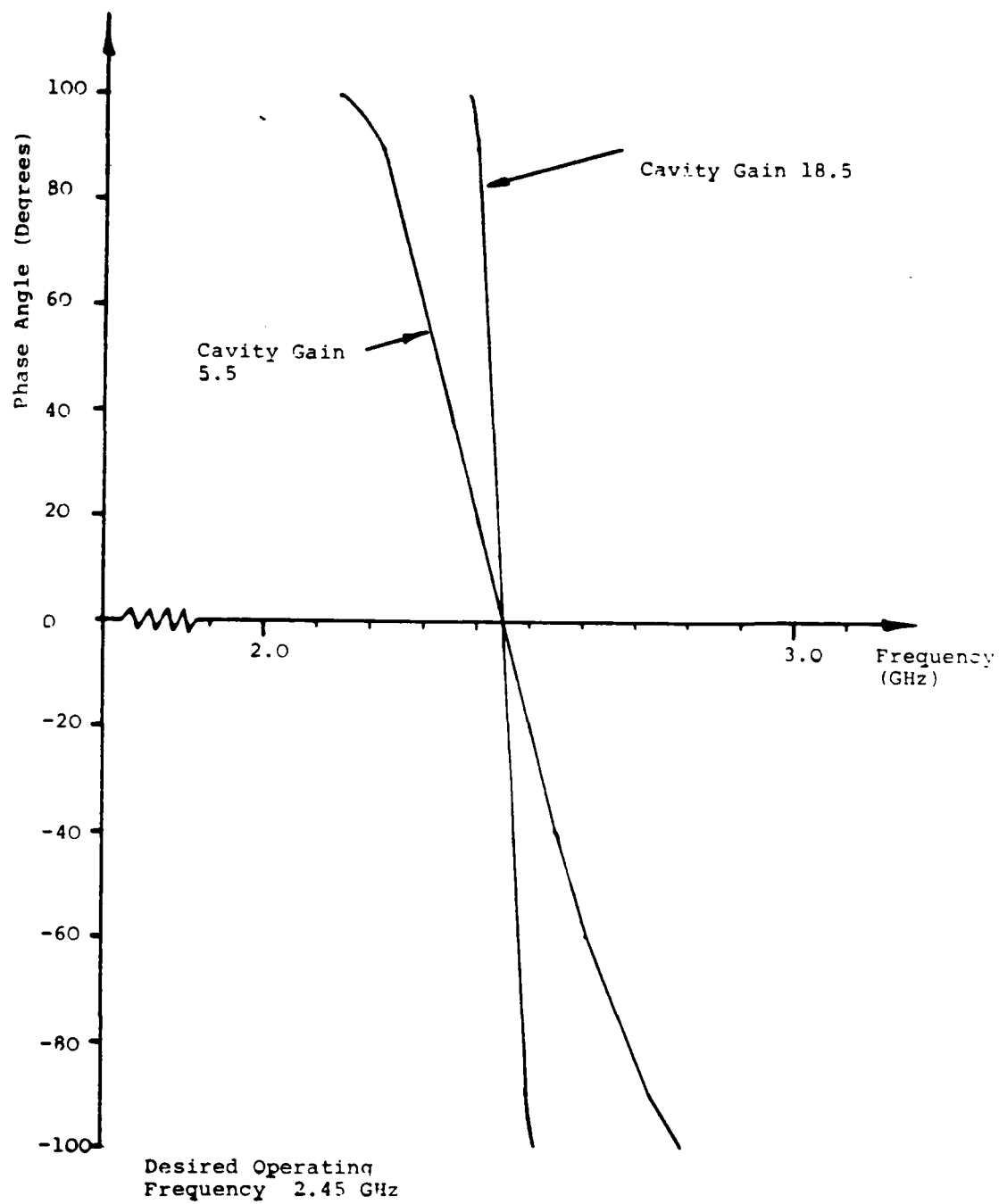


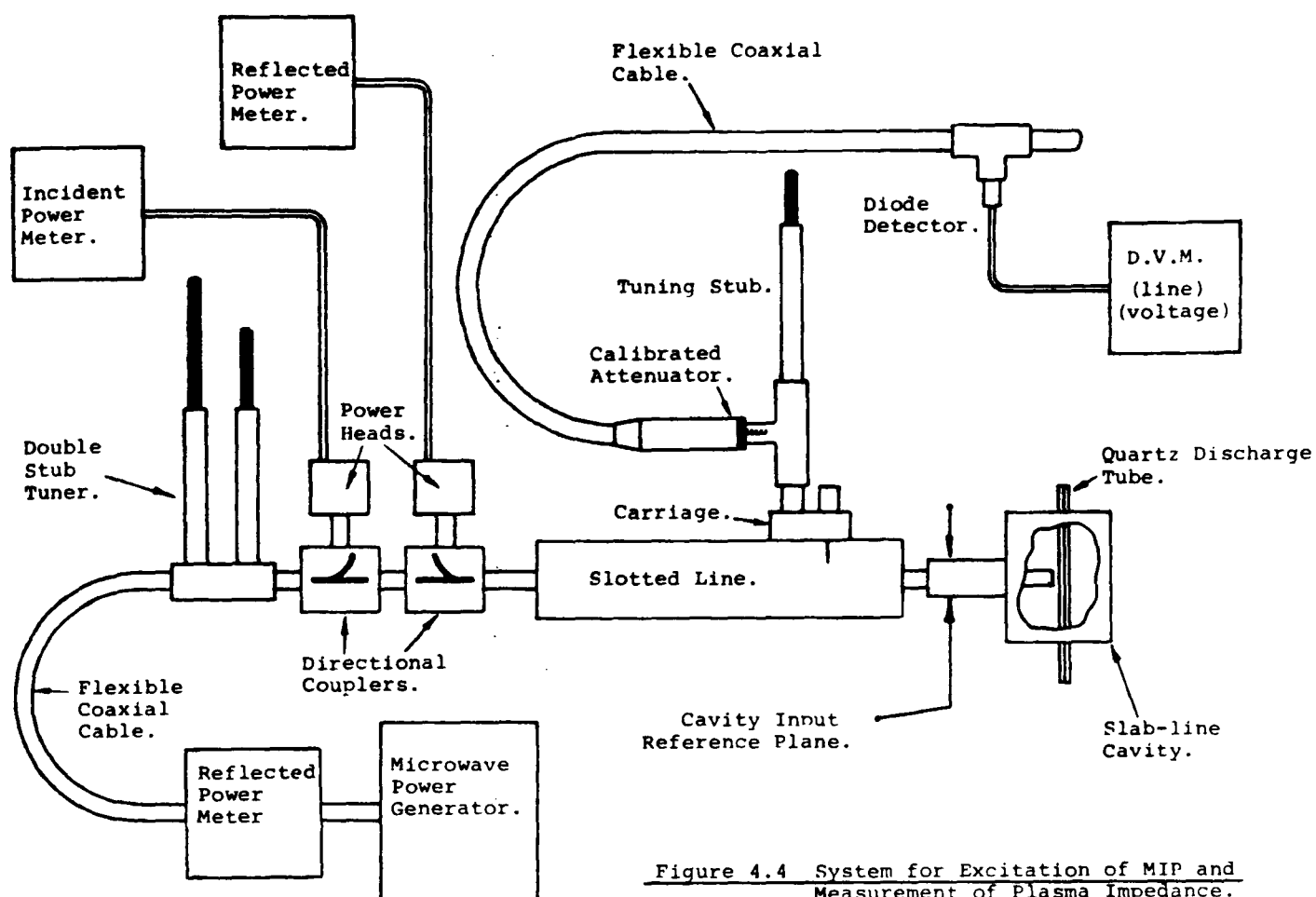
Figure 4.3. Phase of the Cavity Input Reflection Coefficient vs Frequency.

#### 4.2      Microwave Plasma Excitation and Measurement System.

The microwave system used for the argon MIP generated in the slab-line cavity is illustrated in figure 4.4. A list of each item of equipment used may be found in table 4.

The slotted line was used in conjunction with the calibrated attenuator to measure the VSWR on the system. The calibrated attenuator consisted of a waveguide operated below its cut-off frequency. To avoid multiple mode excitation within the attenuator it was necessary to position a minima of the voltage standing wave exactly beneath the aperture coupling energy into the waveguide. This was achieved using the moveable short circuit tuning stub, a voltage minima being correctly positioned when a maximum reading was observed on the DVM. This operation eliminates the need to compensate the attenuator readings, using data supplied by the manufacturer which otherwise would be required. Attenuation is provided in the range -10 db to +40 db in major graduation steps of 1 db.

The Microton 200's output power meter, although marked in 'Watts' actually measures the magnetron anode current and thus relies on the approximately linear relationship between the two for calibration. However, the magnetron's output power and operating frequency are dependant on the magnitude and phase of any reflected wave incident upon it, as can be deduced from a Rieke diagram (82). As a result of this behaviour of the magnetron when the load on its output is varied, power readings deduced from the anode current are unreliable. The system for measuring magnetron output power adopted in this study uses a directional coupler and thin film thermoelectric (TFT) power head as proposed by Outred, 1980 (83). The reflected power from the microwave cavity is also measured using similar components and thus the TRUE NET input power incident upon the cavity may be determined. The power measurements made using this arrangement are not significantly affected by the distance of the directional couplers from the cavity since losses in the slotted line are small, less than  $0.002 \text{ db cm}^{-1}$ . Positioned as shown in figure 4.4, the directional couplers do not affect



Equipment	Type	Manufacturer
Microwave Generator	Microton 200 Mk 3	Electro Medical Supplies
Reflected Power Meter		" "
Directional Coupler	3003-20	Narda Microwave Corp
TFT Power Heads & Power Meters	6423 6460	Marconi Saunders Ltd " " "
Tuning Stubs	874-D2OL	General Radio Corp
Slotted Line	874-LBA	" " "
Attenuator	874-GAL	" " "
Coaxial T Piece	874-VRL	" " "
50 Ohm Load	874-W5OBL	" " "
Diode Detector	IN21B	Siemens GmBh
DVM	LM1420	Solartron Electronic

Table 4.3      Equipment to Produce the MIP in the slab-line cavit

measurement of the cavity input reflection coefficient.

The main purpose of the double stub tuner was to reduce the reflected wave travelling back towards the generator so that any effect on the magnetron's operation frequency and output power is minimised. Being positioned as shown in figure 4.4 means that it is not necessary to include it's effect in the cavity input reflection coefficient calculations.

### 4.3 Microwave Measurement Method.

With the slab-line cavity loaded with an argon MIP running at some desired input power and gas flowrate the VSWR, 'S' was measured using an attenuator method described by Sucher and Fox, 1963 (84) from the equation,

$$S = \text{Antilog} \frac{(\text{db inserted})}{20}$$

using the calibrated attenuator.

The phase,  $\phi_{IN}$  was calculated from the positions, 'x', of the voltage minima on the slotted line, measured using the 'method of bracketing' described by Sucher and Fox, 1963 (84) from the equation,

$$|\phi_{IN}| = \frac{4\pi x}{\lambda} \pm \frac{n\pi}{2}$$

where 'n' is an integer between 2 and 8. Voltage minima positions were measured relative to the 'cavity input reference plane' (figure 4.4), the position of which was determined from the voltage standing wave minima on the slotted line when the slab-line cavity was replaced by a short circuit termination. The plane of the short circuit was known to exactly coincide with the near end of the low-impedance feed section of the cavity.

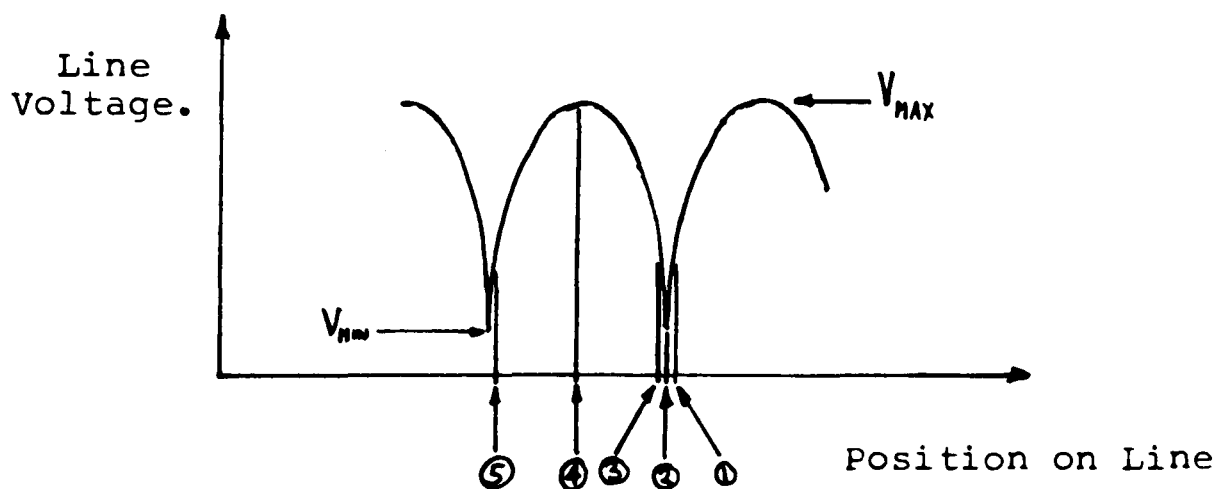


Figure 4.5 Measurement Sequence for Method of Bracketing.

The exact measurement procedure used was as follows,

- 1) With 5 db set on the calibrated attenuator the carriage of the slotted line was moved to approach the first minima position and the DVM monitoring the line voltage observed until the reading fell to some predetermined and convenient value, typically 5 mV. The position of the carriage, corresponding to reading 1 on figure 4.5 was noted.
- 2) The carriage was again moved, in the same direction until the minimum voltage position was reached. The DVM reading, corresponding to reading 2 on figure 4.5 was noted.
- 3) The carriage was again moved until the DVM again read 5 mV, i.e. same as in step 1. The position of the carriage, corresponding to reading 3 on figure 4.5 was noted. The minima position was then calculated from,

$$x = \frac{\text{Reading 1} - \text{Reading 3}}{2}$$

- 4) The carriage was then moved until the position of the first voltage maxima was reached (DVM attains maximum value).

Using the calibrated attenuator, attenuation was added until the DVM showed the same reading as at the voltage minima. The attenuation added, corresponding to reading 4 on figure 4.5 was read from the graduated scales on the attenuator. The 'inserted db' was then given by,

$$\text{db inserted} = \text{Reading 4(db)} - 5(\text{db})$$

and hence the VSWR, S calculated.

- 5) The calibrated attenuator was reset to 5 db, i.e. the value set prior to step 1, it's barrel being turned to a value just less than 5 db and then reversed in direction to approach the 5 db in the same direction as the 'inserted db' was added in step 4. This minimised any effects due to mechanical backlash in the calibrated attenuator's screw thread.

This process detailed in steps 1 to 5 was then repeated for each of the voltage minima and maxima on the line. Using the slotted line it was generally possible to measure the position of 6 voltage minima with 6 corresponding VSWR, S, measurements. Since

$$|\rho_{IN}| = \frac{S - 1}{S + 1}$$

it follows that in the subsequent analysis, the modulus of the cavity input reflection coefficient,  $|\rho_{IN}|$  was evaluated six times using each 'S' value and a mean result calculated. Similarly the phase,  $\phi_{IN}$  was evaluated six times using each 'x' value with a corresponding 'n' value in the equation given on the previous page and a mean result calculated.

For the tuning of the unloaded slab-line cavity described in section 4.1, steps 2 and 4 were omitted since only the phase of the cavity input reflection coefficient is required.

Having measured the modulus and phase of the cavity input reflection coefficient, the S parameter representation of the slab-line cavity (section 2.3) was used to determine the value of the microwave impedance of the plasma load, a complex quantity of the form  $Z_L = R - jX_C$  which includes the effect of the argon MIP, quartz tube and coupling gap. According to Hammond, 1978 (56) the quartz tube and coupling gap give a net capacitive contribution to the complex impedance and therefore appear in it's imaginary part,  $X_C$  leaving the real part, R representative of the argon plasma itself.

The experimental data obtained from the microwave measurement apparatus was processed using a program, written in Algol 60 and run on the Polytechnic's DEC 10 computer. A copy of this program may be found in the appendix A 3. The slab-line cavity S parameters do not completely account for the small electrical losses in the cavity structure. These losses may be accounted for in the full analysis of the experimental data by use of the slab-line cavity transmission (T) parameters which are analogous to the S parameters except that the value of attenuation constant,  $\alpha$  (section 2.3) is not zero. Consequently the computer program calculates the cavity T parameters based on a value of conductivity of  $10^6 \text{ S m}^{-1}$ .



#### 4.4 Relationship Between Load Impedance and the Electron Density

The load impedance,  $Z_L$  of the dry argon MIP generated in the slab-line cavity was measured simultaneously with the electron density,  $N_e$  (section 5.4.2). The aim was to investigate the potential link between these two fundamental properties of the MIP and to show that the value of  $N_e$  would have a particular influence on the real part,  $R$  of the load impedance. In considering a link between  $N_e$  and  $R$  it is useful to discuss the theoretical relationship between the parameters involved.

The electrical conductivity,  $\sigma$  of a plasma, in the absence of an external magnetic field has been shown by Spitzer, 1962 (85) to be

$$\sigma = 0.015 T_e^{3/2} / X \text{ Log}_e \mathcal{L} \text{ Sm}^{-1}$$

where  $T_e$  is the electron temperature,  $X$  is the effective ionic charge and  $\mathcal{L}$  is given by

$$\mathcal{L} = 12\pi \left[ \frac{E_0 k T_e}{e^2} \right]^{3/2} / N_e^{1/2}$$

where  $E_0$  is the permittivity of free space,  $k$  is the Boltzmann constant and  $e$  is the charge on the electron. The effective ionic charge,  $X = 1$  in a predominantly singly ionised plasma, as has been found to be the case for argon MIP studied. Spitzer's equation for  $\sigma$  has been translated into SI units in a manner similar to that used by Leonard, 1965 (86) but may be further expressed in more useful units as suggested by Delcroix, 1960 (87) by converting to the plasma resistivity,  $\eta$  using the equation,

$$\eta = \frac{1}{\sigma} = \frac{1}{0.015} T_e^{-3/2} \text{ Log}_e \mathcal{L} \quad \Omega\text{m}$$

The plasma resistivity may be evaluated for a typical dry argon MIP generated in the slab-line cavity with  $T_e = 7500 \text{ K}$  and  $N_e = 10^{15} \text{ cm}^{-3}$  and is found to be of the order of  $5 \times 10^{-4} \Omega\text{m}$ . In discussing how the real part,  $R$  of the load impedance might be related to  $\eta$ , it is necessary to consider the physical dimensions of the MIP as they appear to the exciting microwave field in the slab-line cavity.

Under most operating conditions the dry argon MIP generated in the slab-line cavity completely fills a 1 mm internal diameter quartz tube to the full inside height of the cavity except for the small region near the end of the cavity inner conductor. For simplicity it may be assumed that the quartz tube, placed with its longitudinal axis perpendicular to the cavity inner conductor contains a plasma column of known dimensions.

This plasma column may be treated as an equivalent resistor through which a current might be induced to flow by the exciting microwave field in a direction parallel to the longitudinal axis of the discharge tube. Taking the cross sectional area,  $A$  and the length,  $l$  of the discharge tube within the confines of the slab-line cavity, a total plasma resistance  $R_T$  may be evaluated using the value of  $\eta$  found for the typical MIP and the equation

$$R_T = \eta \cdot \frac{l}{A}$$

Substituting in real values for  $l$  and  $A$ , a value of  $R_T$  equal to  $61.5 \Omega$  is obtained.

By virtue of the logarithm term in the equation for  $\eta$ , it is apparent that the value of  $R_T$  will be relatively insensitive to changes in  $N_e$ . For example, if  $N_e$  were reduced by 50% to  $5 \times 10^{14} \text{ cm}^{-3}$ ,  $R_T$  would only increase to a value of  $65.5 \Omega$  i.e. a change of approximately 6%.

Conversely, the value of  $R_T$  is seen to be highly dependent on the value of  $T_e$ , a term which appears twice in the equation for  $\eta$ . A doubling of  $T_e$  to 15000 K causes  $R_T$  to reduce to  $25.8 \Omega$  i.e. changes in  $T_e$  cause approximately equal and opposite changes in  $R_T$ .

Since the electron temperature was not directly measured, determination of  $N_e$ , from the Stark broadened  $H\beta$  spectral line profile (section 5.41) required that a value of  $T_e$  be assumed. Although this was not a problem in the determination of  $N_e$ , it is obvious that  $R_T$  is more dependent on a parameter for which a value has to be assumed than one for which actual values were measured.

There are two other practical factors which need to be considered in regard to the validity of the theoretical value of  $R_T$  calculated here. In the event of the dry argon MIP incompletely filling the cross section of the discharge tube, the volume of plasma will be reduced, hence  $R_T$  will increase. Also the investigation of the variation of  $N_e$  along the length of the MIP (section 5.4.2 A) suggests that  $R_T$  might be better calculated using a mean value of  $N_e$  which is somewhat lower than the  $10^{15} \text{ cm}^{-3}$  used, again producing an increase in the theoretical value of  $R_T$ . Thus it would be expected that the value of  $R_T = 61.5 \Omega$  calculated here constitutes an approximate lower limit value.

## 4.5 Microwave Impedance of the Dry Argon MIP.

### 4.5.1 Dependence of Impedance on Argon Flowrate and Input Power.

An important consideration in the interpretation of the impedance results presented here was found to be the actual volume of plasma within the confines of the cavity. Using configuration A (section 3.1), the dry argon MIP, contained within the quartz tube normally filled the entire cross-section except for the central region near the end of the cavity inner conductor where distortions in the electric field pattern cause the MIP to become constricted. The MIP length was found to be especially dependent on the net input power applied to the cavity and to a lesser extent the gas flowrate.

At low input powers, less than 50 W, the MIP length is less than the inside height of the cavity. As the input power was increased, the length of the MIP increased until it extended from top to bottom of the slab-line cavity (a distance of 8.5 cm), i.e. the cavity was 'completely filled'. The input power for which this occurred was found to be slightly dependent on flowrate.

For a flowrate of  $1.0 \text{ l min}^{-1}$ , this input power was found to be in the range 30 to 35 W, whereas at  $0.1 \text{ l min}^{-1}$ , an input power of 45 to 50 W was required. Further increase in input power caused the MIP length to increase until for input powers greater than 120 W, an MIP of approximately 15 cm length was formed irrespective of flowrate. This MIP therefore extended well outside the confines of the cavity.

The dependence of load impedance and electron density on net input power applied to the cavity was investigated at gas flowrates of 0.1, 0.5 and  $1.0 \text{ l min}^{-1}$ . The electron density results are reported in section 5.4.2C.

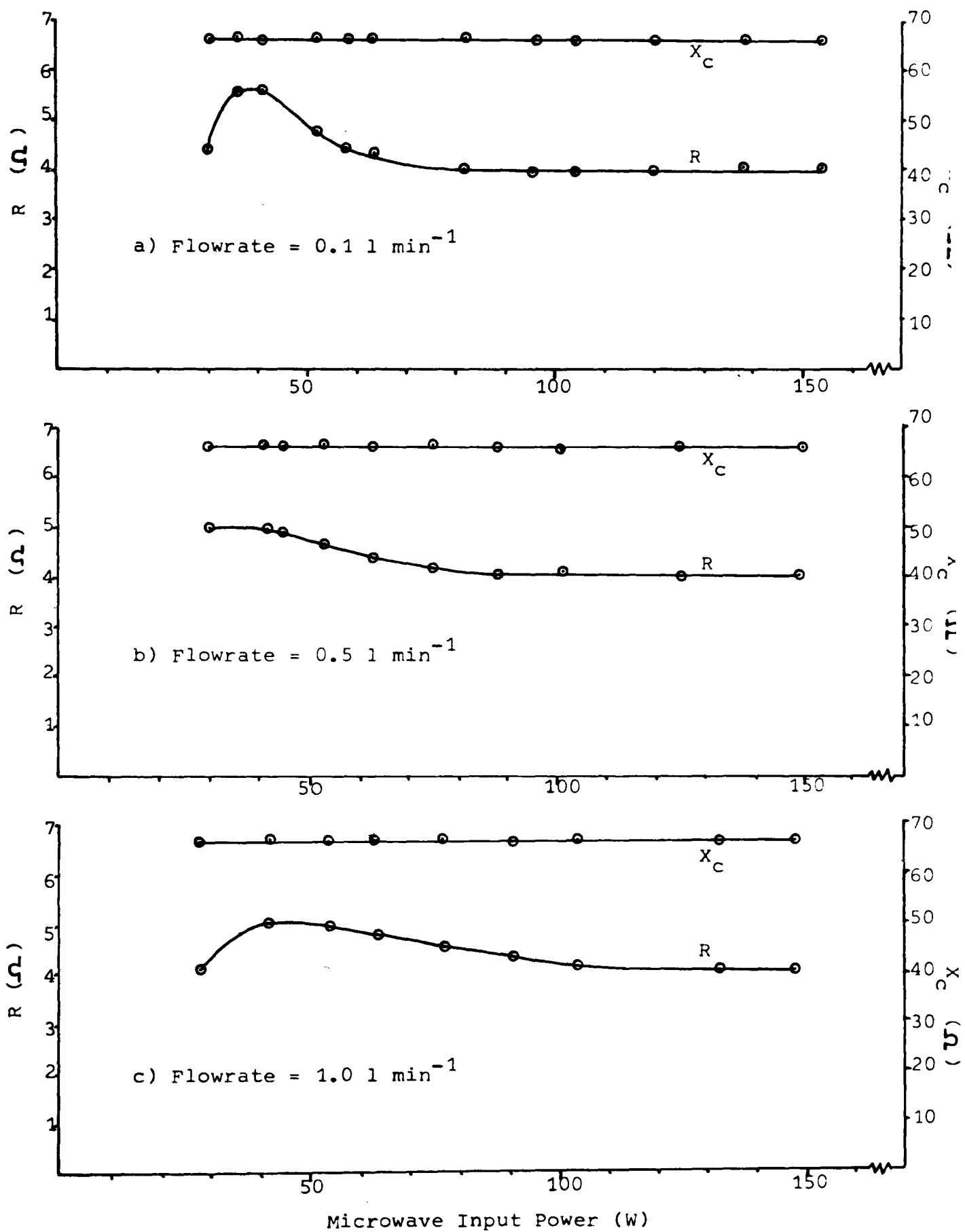


Figure 4.6 Real (R) and Imaginary (X<sub>c</sub>) Parts of Complex Load Impedance as a Function of Net Microwave Input Power.

The impedance results are shown in figure 4.6 for all the three flowrates. The most noticeable feature is the peak in the value of  $R$  at the low end of the range of input powers investigated. This peak in the graph of  $R$  versus input power occurs as the MIP length was increasing to the point where the cavity is just completely filled. Thereafter as the input power was increased, the value of  $R$  settles to a steady  $4.0 \pm 0.1 \Omega$  irrespective of flowrate. It was deduced that this peak in the graph is caused by a change in the volume of MIP within the cavity confines and that the peak shape is dependent on flowrate. At a gas flowrate of  $0.1 \text{ l min}^{-1}$ , the peak in  $R$  is both higher and narrower whereas at  $1.0 \text{ l min}^{-1}$ , the peak is lower and broader.

A possible explanation for the change in the peak width might be that at the point when the MIP just completely fills the cavity, its homogeneity within the cavity confines continues to improve as the input power is further increased. This would appear to occur more rapidly at the flowrate of  $0.1 \text{ l min}^{-1}$  compared to  $1.0 \text{ l min}^{-1}$ . The peak height is undoubtedly a function of the MIP length which was itself found to be a function of flowrate at input powers of approximately 50 W.

This change in the shape of the peak is believed to be symptomatic of the dependence of  $R$  on flowrate when intermediate input powers are applied to the cavity as shown in figures 4.7 and 4.8.

The investigation of the variation of electron density along the length of the dry argon MIP (section 5.2.1 A) suggests that even when the MIP extends well outside the cavity, it never reaches complete homogeneity.

The dependence of load impedance and electron density on the flowrate was determined for flowrates in the range  $0.1$  to  $1.37 \text{ l min}^{-1}$  for microwave input powers of  $50 \pm 2 \text{ W}$  and  $123 \pm 4 \text{ W}$ .

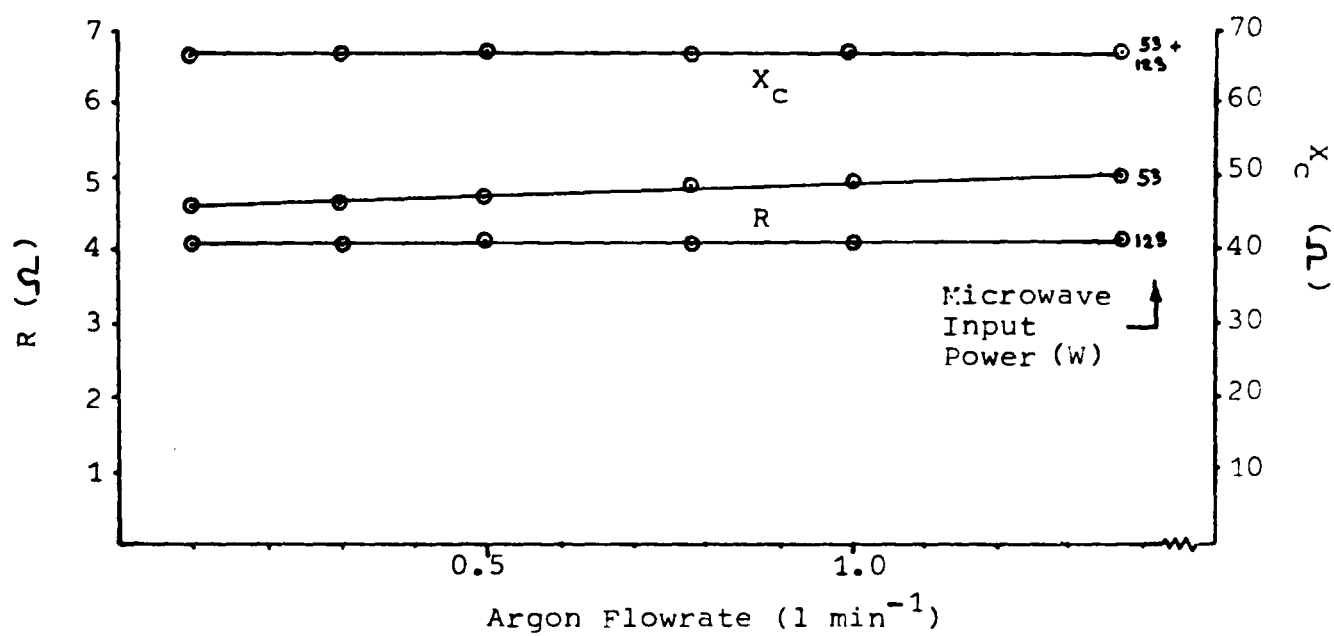


Figure 4.7 Real ( $R$ ) and Imaginary ( $X_c$ ) Parts of Complex Load Impedance as a Function of Gas Flowrate, for different Microwave Input Powers.

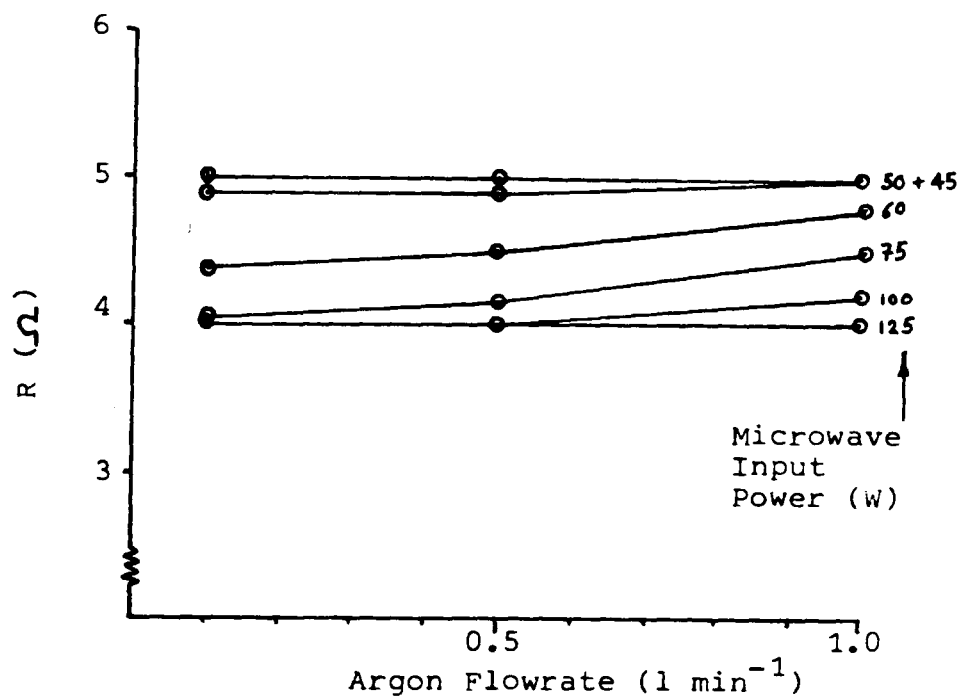


Figure 4.8 Real ( $R$ ) Part of Complex Load Impedance as a Function of Gas Flowrate, for different Microwave Input Powers.

Figure 4.7 shows the impedance results obtained from these measurements which may be summarised as follows. In all measurements, the imaginary part of the plasma impedance was found to be constant at a value of  $66 \pm 1.0 \Omega$  for all flowrates investigated. At an input power of 123 W the real part, R was also found to be constant at  $4.0 \pm 0.2 \Omega$  for all flowrates investigated.

However, for an input power of 53 W, the value of R was found to be dependent on flowrate, varying between 4.0 and 5.0  $\Omega$ . For this particular input power there are two features of the results discussed so far which are significant. Firstly the extent to which the MIP fills the cavity, which is dependent on flowrate and secondly the change in the MIP homogeneity (This being shown by the increasing width of the peak in the graph of R versus input power as the flowrate is increased). Both these are known to affect the value of impedance measured. It is therefore difficult to infer that the variation in R, shown in figure 4.7 for an input power of 53 W, is caused by some fundamental change in the properties of the MIP when such a variation could easily be explained in terms of a combination of these other two processes.

Figure 4.8 is a plot of R versus flowrate for input power in the range 50 to 125 W which has been constructed by transposing the data given in figure 4.6. It quite clearly shows the effect that the level of input power has on the variation of R with flowrate, verifying the data presented in figure 4.7.

The simultaneous measurement of the electron density (section 5.4.2 B) showed that it, unlike the impedance was highly dependent on gas flowrate although only slightly dependent on the microwave input power applied to the cavity.



#### 4.5.2 Dependence of Impedance on Dimensions of Discharge Tube.

A dry argon MIP was generated in the slab-line cavity using configuration A (section 3.1) at a flowrate of  $0.1 \text{ l min}^{-1}$  and the load impedance and electron density determined for the different quartz discharge tubes detailed in table 4.4. The electron density results are reported in section 5.4.2 D.

As can be seen the imaginary part,  $X_c$  of the load impedance is virtually unchanged in progressing from discharge tubes with wall thicknesses of 2.5 down to 1.75 mm and only for the smallest wall thickness (1.0 mm), was any appreciable change in  $X_c$  observed.  $X_c$  is not therefore critically dependent on the amount of quartz within the cavity, a view supported by Outred, 1981 (88) who found  $X_c$  to be more dependent on the size of the coupling gap.

The value of  $R$  is clearly dependent on the exact size of the discharge tube used, varying from 4.0 to  $4.8 \Omega$  as the tube wall thickness employed was changed from 2.5 to 1.0 mm. In all cases the MIP length was appreciably greater than the slab-line cavity height, i.e. the cavity was completely filled. Therefore the value of  $R$  is not dependent on the volume of MIP within the cavity, shown by the fact that where different tubes have the same ID but different OD, i.e. identical MIP volumes, the value of  $R$  measured were different.

It seems more likely that the variation in  $R$  is caused by the shift in the relative positions of MIP and maximum electric field strength in the cavity (see figure 5.15, section 5.4.2 D).

It would appear from the results that  $R$  is not dependent on the MIP only as assumed by Hammond, 1978 (56).

Tube Wall Thickness (mm) (mm)			$R(\Omega)$	$X_c(\Omega)$
ID	OD			
1.0	6.0	2.5	$4.0 \pm 0.1$	$66.7 \pm 0.07$
2.0	6.5	2.25	$4.1 \pm 0.01$	$66.0 \pm 0.1$
2.0	6.0	2.0	$4.2 \pm 0.03$	$66.1 \pm 0.05$
1.5	5.0	1.75	$4.4 \pm 0.04$	$67.2 \pm 0.05$
1.0	3.0	1.0	$4.8 \pm 0.02$	$69.3 \pm 0.05$

Net Input Power =  $75 \pm 3 \text{ W}$ .

Argon Flowrate =  $0.1 \text{ l min}^{-1}$

Table 4.4 Variation of Load Impedance as a Function of Discharge Tube Dimensions.

#### 4.5.3 Dependence of Impedance on Water Vapour Content of Argon Plasma Gas

The effect on the load impedance of removal of the majority of the impurity water vapour, known to be present in the argon plasma gas, was determined in the dry argon MIP operated at a flowrate of  $0.1 \text{ l min}^{-1}$  in the slab-line cavity. Measurements were made first prior to, then after operation of the cold trap described in section 3.1.

The results are given in table 5.4 for both impedance and electron density (see also section 5.4.2 E). During this experiment, argon excitation temperature (section 5.1.1 B) and OH rotational temperature (section 5.3.1) were also measured.

A significant change is noted for the electron density when the cold trap was operated, but both real and imaginary parts of the complex load impedance were little affected. Although the value of R did decrease slightly when the water vapour was removed, this was probably caused by the increase in MIP length and consequent improvement in plasma homogeneity (section 4.5.1).

	MIP Length (cm)	Load Impedance ( $\Omega$ )		Electron Density ( $\times 10^{14} \text{ cm}^{-3}$ )
		R	$X_c$	
No Trap	11.5	4.0	66.8	8.7
Trap Operated	12.5	3.9	66.8	5.4

Argon Flowrate =  $0.1 \text{ l min}^{-1}$ .  
Net Input Power =  $60 \pm 3 \text{ W}$ .

Table 4.5     Dependence of Impedance and Electron Density  
Water Vapour Content of the Argon Plasma Gas.

#### 4.6 Preliminary Discussion of Impedance Results.

A significant fact to emerge from the results reported in the previous section is the considerably lower value of  $R$  measured in the dry argon MIP compared to the theoretical value,  $R_T$ . When the MIP completely filled the slab-line cavity,  $R$  was found to assume a steady value of  $4\Omega$  compared to a value of  $R_T$  equal to  $61.5\Omega$ .

Although it is not clear why such a discrepancy should exist, it is possible to consider two likely causes. i) An underestimate in the value of electron temperature,  $T_e$  would result in an  $R_T$  with too high a value, as indicated in section 4.4. However, despite the sensitivity of  $R_T$  to changes in  $T_e$ , a value approaching 40000 deg K would be required to reduce  $R_T$  to the same order of magnitude as the measured  $R$  values. Even with the certain knowledge that a state of LTE does not exist in the dry argon MIP (section 7.1), there is no evidence for such a high electron temperature.

ii) The other conclusion, strongly supported by the evidence from previous sections, is that the complex load impedance, particularly the real part,  $R$  measured in the slab-line cavity is not influenced by the fundamental properties of the MIP itself. Instead, the load impedance is determined by the operating conditions, eg. dimensions of discharge tube (section 4.5.2) or the physical volume of plasma within the cavity (section 4.5.1).

Further support for this second view is given by the lack of any evidence for a strong inter-relationship between the plasma load impedance and the electron density measured in the dry argon MIP (section 5.4.2). This will be discussed further in section 7.2.

Mainly because of the convincing nature of the second view, it was decided not to measure the load impedance of the analytical MIP incorporating sample aerosol introduction generated in the slab-line cavity.

## Chapter 5. Spectroscopic Measurements on the MIP.

The MIP was generated from industrial grade argon and a survey of the MIP spectrum was undertaken using a 3 m Eagle spectograph. Subsequently, the optical system described in chapter 3 was used to obtain a photo-electric survey of the MIP and, using an EMI 9558B PMT (section 3.4), gave access to additional spectral features not previously observed.

A list of the spectral features observed is given in table 5.1.

<u>Spectrum</u>	<u>Wavelength (or range) (nm)</u>
Ar I	355.4                      811.5
H I	$H_{\alpha}$ , $H_{\beta}$ , $H_{\gamma}$ & $H_{\delta}$
Na I	589.0/589.6 (D lines)
OH	Band Heads at 281.1 & 306.4
NH	Band Heads at 336.0 & 337.0

Table 5.1    MIP spectral features observed.

The general conclusions from early studies of the MIP concerning the usefulness of the emitted spectra were as follows.

(1) That the spectra of the plasma's argon atoms was sufficiently intense that relative spectral line intensity measurements could be made using an appropriate selection of spectral lines and an argon excitation temperature might be determined (section 5.1).

(2) That the spectra emitted by the OH (hydroxide) molecules present in the MIP with direct sample aerosol introduction, due to the dissociation of the introduced water vapour would enable relative intensities to be measured for a set of spectral line components of a suitable branch of the OH molecular spectra and hence for a rotational temperature to be determined (section 5.3)

Also the similar, though much weaker spectra emitted by the dry argon MIP due to the impurity water vapour present in the argon gas might still allow a rotational temperature to be determined using only the stronger spectral components.

(3) That the spectra omitted by the H atoms present, again due to the dissociation of water vapour in the MIP was intense enough under most operating conditions to enable measurements to be made on the line profiles of the Stark broadened Balmer Series spectral lines, particularly the  $H_{\beta}$  line (section 5.4). When the dry argon MIP was operated at gas flowrates of greater than  $0.8 \text{ l min}^{-1}$  the intensity of  $H_{\beta}$  was greatly diminished such that the line profile parameters measured were much less reliable than for lower flowrates.

(4) When analyte atoms, dissolved in aqueous solutions are introduced into the MIP in the form of an aerosol (chapter 6), their characteristic spectra is also observed, as is the case for similar plasma excitation sources used in the spectrochemical analysis of solutions eg. the ICP. Besides being able to determine the concentrations of these analyte atoms in some given sample mixture, certain of these atoms may also be used to determine plasma parameters. Subsequently therefore when iron (Fe) was introduced into the MIP relative intensity measurements were made on a selection of Fe I spectral lines (section 5.2).

## 5.1 Argon Excitation Temperature.

It can be shown that the emission intensity,  $I$  of a spectral line, in unit solid angle per second from an optically thin layer of gaseous plasma is given by

$$I_{21} = N_2 A_{21} l h \nu_{21} / 4\pi \dots\dots\dots 5.1$$

where  $l$  is the plasma thickness  
 $N_2$  is the number density of atoms in the upper state, 2.  
 $A_{21}$  is the probability of a transition from state 2 to 1.  
 $h \nu_{21}$  is the energy difference associated with such a transition.

If a Boltzmann distribution for the excited states in the atoms is assumed, then

$$N_2 = (N g_2 \exp(-E_2/kT)) / Z(T) \dots\dots 5.2$$

where  $N$  is the total atom number density

$g_2$  is the degeneracy of the upper state, 2.

$E_2$  is the energy of the upper state

$k$  is Boltzmann's constant

$Z(T)$  is the Partition Function.

The temperature parameter here is the excitation temperature,  $T_{exc}$  for the excited levels of the atomic argon system. Combining equations 5.1 and 5.2 gives

$$I_{21} = C \cdot g_2 A_{21} \nu_{21} \exp(-E_2/k T_{EXC}) \dots\dots\dots 5.3$$

where  $C = \frac{N l h c}{4\pi} \cdot \frac{1}{Z(T)}$  and  $c$  = velocity of light

rearranging and taking logarithms gives

$$\ln(I_{21} \lambda_{21} / g_2 A_{21}) = \ln C - E_2 / k T_{EXC} \dots\dots\dots 5.4$$

If relative spectral line intensity measurements are made for a set of argon spectral lines corresponding to electronic transitions from a range of upper energy states, a graphical plot of  $\ln(I \lambda / g A)$  versus  $E$  should give a straight line graph with a slope equal to  $1/k T_{exc}$  provided the argon system is described by one unique temperature.

$\lambda$ (nm)	CONFIGURATION OF STATE		ENERGY OF STATE ( $\text{cm}^{-1}$ )		$A_{21}$ ( $\times 10^8 \text{ s}^{-1}$ )	ERROR $A_{21}$ (+/- %)	$g_2$
	UPPER	LOWER	UPPER	LOWER			
355.430	6p ( $3/2$ ) <sub>2</sub>	4s ( $3/2$ ) <sub>2</sub> <sup>o</sup>	121270.68	93143.80	0.0029	50	5
364.983	6p' ( $1/2$ ) <sub>o</sub>	4s' ( $1/2$ ) <sub>1</sub> <sup>o</sup>	122790.61	95399.87	0.0085	50	1
415.858	5p ( $3/2$ ) <sub>2</sub>	4s ( $3/2$ ) <sub>2</sub> <sup>o</sup>	117183.65	93143.80	0.0145	25	5
425.118	5p ( $1/2$ ) <sub>1</sub>	4s ( $3/2$ ) <sub>2</sub> <sup>o</sup>	116660.05	93143.80	0.0013	25	3
425.936	5p' ( $1/2$ ) <sub>o</sub>	4s' ( $1/2$ ) <sub>1</sub> <sup>o</sup>	118870.98	95399.87	0.0415	25	1
426.629	5p ( $3/2$ ) <sub>2</sub>	4s ( $3/2$ ) <sub>1</sub> <sup>o</sup>	117183.65	93750.64	0.0033	25	5
430.010	5p ( $5/2$ ) <sub>2</sub>	4s ( $3/2$ ) <sub>1</sub> <sup>o</sup>	116999.39	93750.64	0.0039	25	5
433.356	5p' ( $3/2$ ) <sub>2</sub>	4s' ( $1/2$ ) <sub>1</sub> <sup>o</sup>	118469.12	95399.87	0.0060	25	5
522.127	7d ( $7/2$ ) <sub>4</sub> <sup>o</sup>	4p ( $5/2$ ) <sub>3</sub>	124609.92	105462.80	0.0092	50	9
549.587	6d ( $7/2$ ) <sub>4</sub> <sup>o</sup>	4p ( $5/2$ ) <sub>3</sub>	123653.24	105462.80	0.0176	25	9
588.262	6s' ( $1/2$ ) <sub>o</sub> <sup>o</sup>	4p ( $1/2$ ) <sub>1</sub>	121096.67	104102.14	0.0128	25	1
588.858	7s ( $3/2$ ) <sub>2</sub> <sup>o</sup>	4p ( $5/2$ ) <sub>3</sub>	122440.11	105462.80	0.0134	25	5
591.208	4d' ( $3/2$ ) <sub>1</sub> <sup>o</sup>	4p ( $1/2$ ) <sub>1</sub>	121011.98	104102.14	0.0105	25	3
603.213	5d ( $7/2$ ) <sub>4</sub> <sup>o</sup>	4p ( $5/2$ ) <sub>3</sub>	122036.13	105462.80	0.0246	25	9
641.631	6s ( $3/2$ ) <sub>2</sub> <sup>o</sup>	4p ( $1/2$ ) <sub>1</sub>	119683.11	104102.14	0.0121	25	5
667.728	4p' ( $1/2$ ) <sub>o</sub>	4s ( $3/2$ ) <sub>1</sub> <sup>o</sup>	108722.67	93750.64	0.0024	25	1
675.284	4d ( $3/2$ ) <sub>2</sub> <sup>o</sup>	4p ( $1/2$ ) <sub>1</sub>	118906.66	104102.14	0.0201	25	5
693.767	4d ( $1/2$ ) <sub>o</sub> <sup>o</sup>	4p ( $1/2$ ) <sub>1</sub>	118512.17	104102.14	0.0321	25	1
714.704	4p' ( $3/2$ ) <sub>1</sub>	4s ( $3/2$ ) <sub>2</sub> <sup>o</sup>	107131.76	93143.80	0.0065	25	3
801.479	4p ( $5/2$ ) <sub>2</sub>	4s ( $3/2$ ) <sub>2</sub> <sup>o</sup>	105617.32	93143.80	0.0960	25	5

TABLE 5.2 SPECTRAL LINE DATA FOR ARGON I

The argon excitation temperature,  $T_{\text{exc}}$  was determined from the relative intensities of the 20 spectral lines listed in table 5.2. Data on the transition probabilities was taken from Wiese et al, 1969 (89) and that for the energy levels from Moore, 1971 (90). Alternative sources of argon transition probability data were tried, for example that of Katsonis and Drawin, 1980 (91) but the data of Wiese produced the most consistent results. Spectral line intensities were measured as a function of integrated line area (section 3.8), compensated for the response of the optical system (section 3.7) and processed using an Algol 60 program (appendix A4) run on the Polytechnic's DEC 10 computer.



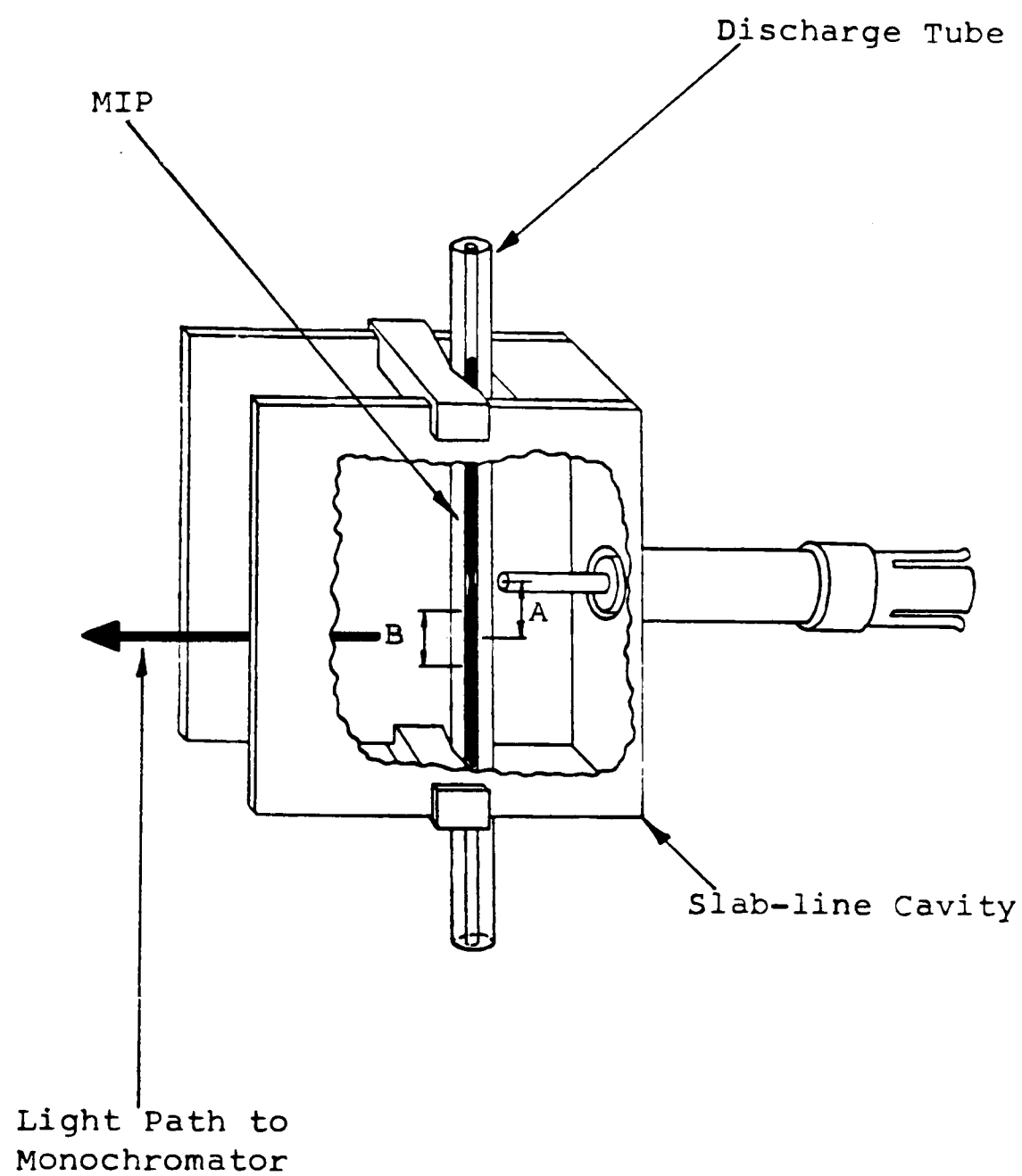


Figure 5.1     Viewing Zone (B) in the Dry Argon MIP  
Generated in the Slab-line Cavity. A=B=10 mm.

### 5.1.1. Argon Excitation Temperature of the Dry Argon MIP

A.

The dependence of the argon excitation temperature on the flowrate of plasma gas in the dry argon MIP operated in the slab-line cavity was determined at the viewing zone shown in figure 5.1. A typical graphical plot of  $\ln(I\lambda/gA)$  versus  $E$ , obtained for a flowrate of  $0.5 \text{ l min}^{-1}$  is shown in figure 5.2. Table 5.3 lists the excitation temperatures determined from the distribution of excited states of the argon atom for gas flowrates of 0.1, 0.5, and  $1.0 \text{ l min}^{-1}$ . The intensity of all the Ar I spectral lines investigated increased by a factor of 2 as the flowrate was increased from 0.1 to  $1.0 \text{ l min}^{-1}$ .

The dependence of the argon excitation temperature on net input power was investigated at each flowrate. The Microtron power generator's output control was set to provide net input powers (section 4.2) of 45, 75, 100 and 130 W, the latter net input power corresponding to the generator's maximum attainable output when the slab-line cavity was loaded with the dry argon MIP.

As the power was increased from 45 to 130 W, a slight dependence on microwave power was observed. However this was minimal, being an increase of less than 5% on the temperatures stated in table 5.3. Since this variation is of the order of the estimated errors in determining the excitation temperature, proof of any such dependence is inconclusive.

B.

In order to investigate whether removing the impurity water vapour entirely from the dry argon MIP had any effect on the plasma excitation conditions, the cold trap described in section 3.1 was used.

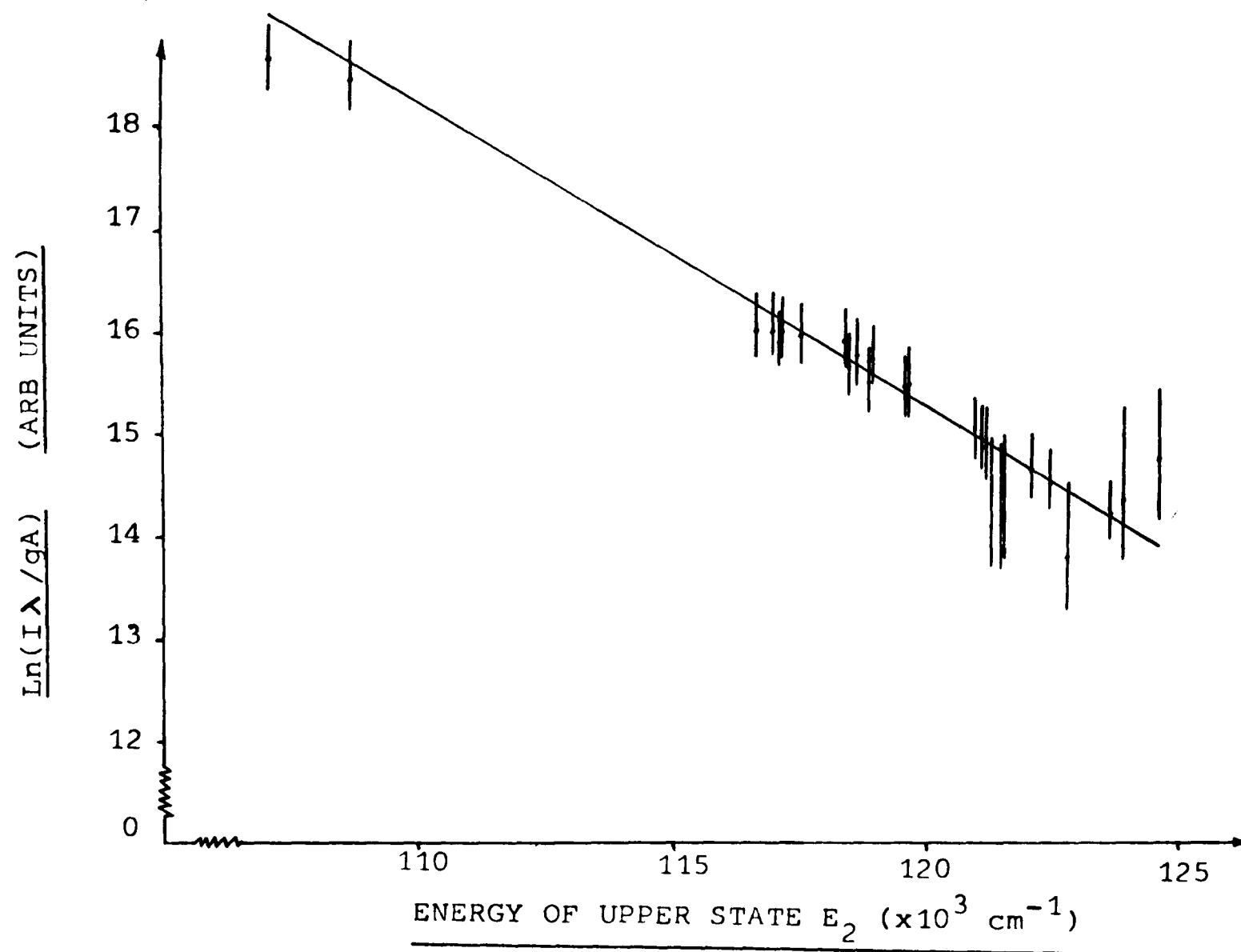


Figure 5.2

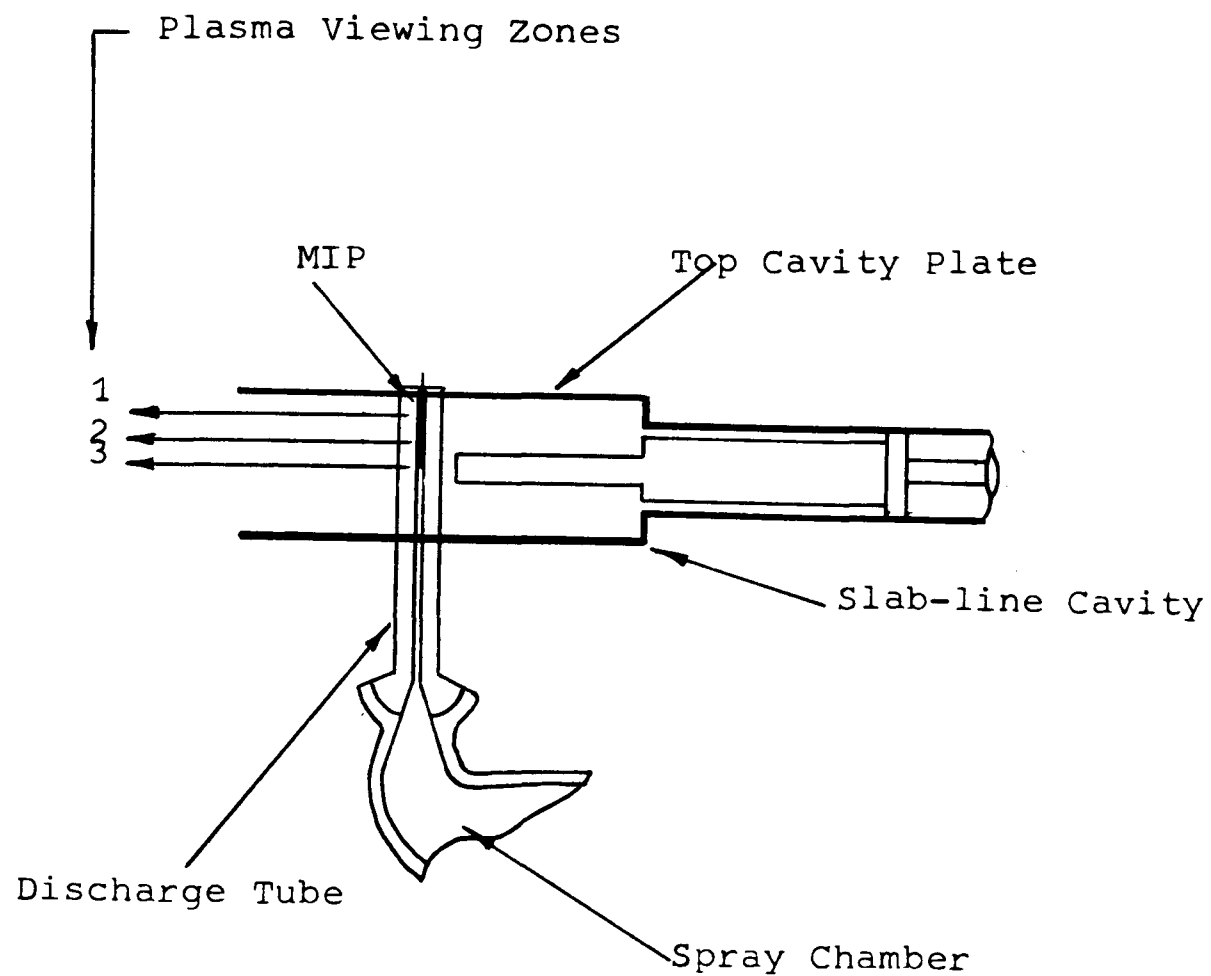
Graph of  $\ln(I\lambda/gA)$  vs  $E$  for Ar I.Flowrate =  $0.5 \text{ l min}^{-1}$  in Slab-line Cavity

When the cold trap was operated it had only a minimal effect on the relative distribution of excited states in the argon atom, ie. leaving the value of excitation temperature unchanged but it did cause an increase of 50% in the intensity of all the argon spectral lines.

Flowrate (l min <sup>-1</sup> )	Argon Excitation Temperature (deg K)
0.1	4850 $\pm$ 150
0.5	4800 $\pm$ 150
1.0	4650 $\pm$ 150

Net Input Power = 72  $\pm$  2 W

Table 5.3    Argon Excitation Temperature as a function of Flowrate in the Dry Argon MIP.



Viewing Zone 1 = 2.5mm below top cavity plate  
 2 = 7.5mm  
 3 = 10.5mm

5 mm length of MIP viewed in each case.

Figure 5.3     Viewing Zones used by the Optical Measurement System for the Analytical MIP Generated in the Slab-line Cavity.

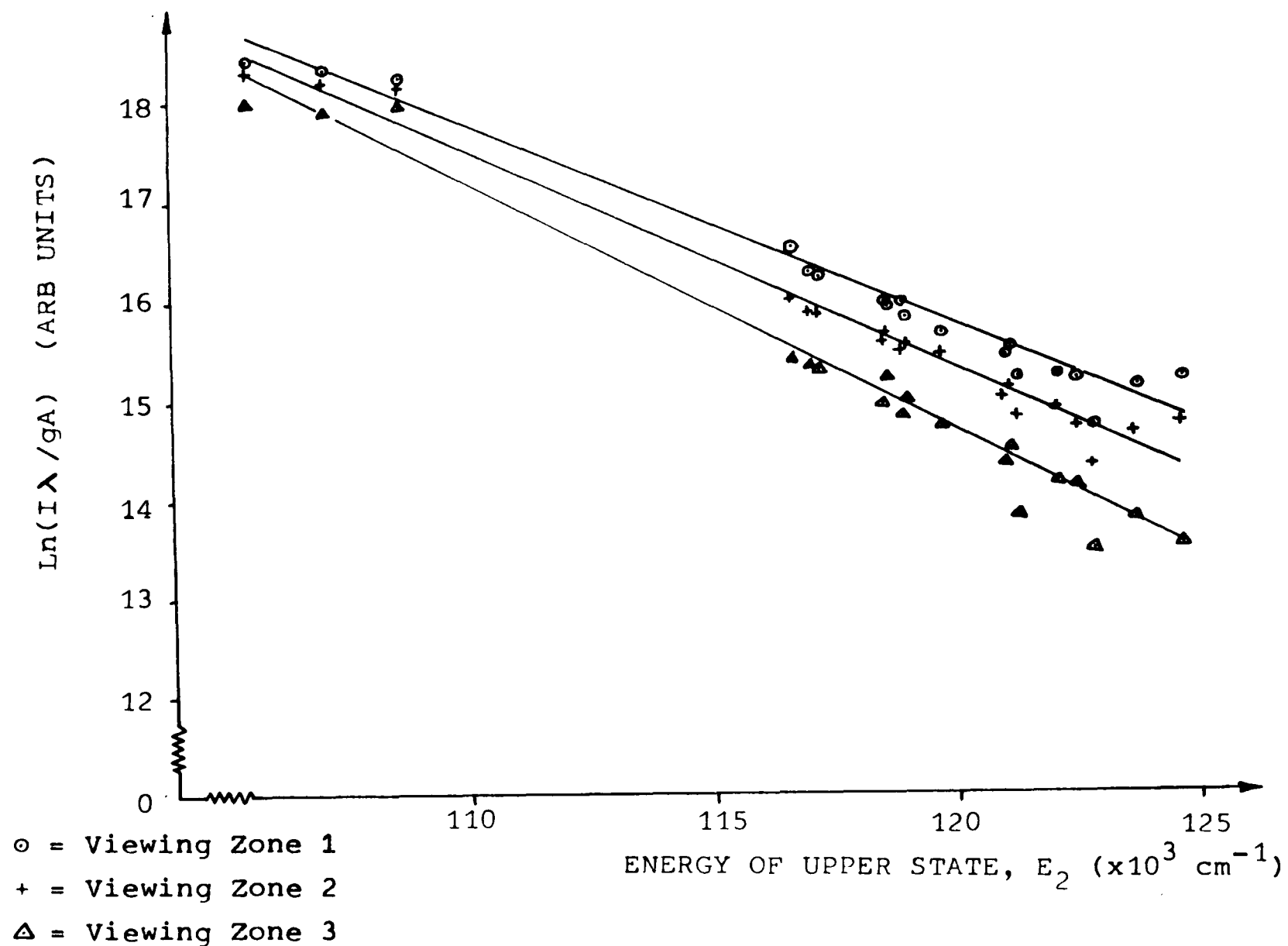
### 5.1.2 Argon Excitation Temperature of the Analytical MIP

A.

The spatial variation of the Ar excitation temperature measure in the analytical MIP generated in the slab-line cavity (Chapter 6) was determined for the 3 viewing zones illustrated in figure 5.3.

Using the crossflow nebulizer, operating at a gas flowrate of  $1.0 \text{ l min}^{-1}$ , de-ionized  $\text{H}_2\text{O}$  was aspirated into the plasma using sample uptake rates (SUR) of 0.5, 1.0 and  $1.5 \text{ ml min}^{-1}$ . The microwave power incident on the cavity was kept approximately constant throughout these measurements and corresponded to a net input power of  $65 \pm 3$  Watts.

Figure 5.4 shows the typical populations of excited states in the argon atom at each viewing zone when an SUR of  $1.0 \text{ ml min}^{-1}$  was used. In addition to the intensity of the argon spectra being lowest at the viewing zone 10.5 mm below the top cavity plate, the measured excitation temperature is also lower at this point. Table 5.4 shows that this result is true for all 3 SUR's used. For any particular viewing zone, the lower energy levels at  $108000 \text{ cm}^{-1}$  appear to be in equilibrium with the higher energy levels greater than  $116000 \text{ cm}^{-1}$ . Later measurements showed that this was not always the case (section 5.1.2 D), and that the thermal limit for the argon system (section 1.3.1) lay between these two ranges of energy levels. The intensity of the Ar I spectral lines was comparable to that measured in the dry argon MIP, even with the changes in the operational conditions of the MIP, eg. slab-line cavity orientation (section 3.1) and sample introduction system (Chapter 6).



Error bars omitted for clarity, similar to figure 5.2.

**FIGURE 5.4.** Graph of  $\text{Ln}(I\lambda/qA)$  vs  $E$  for Ar I. Analytical MIP operated at  $1.0 \text{ l min}^{-1}$  in Slab-Line Cavity  
 $\text{SUR} = 1.0 \text{ ml min}^{-1}$  Blank

Viewing Zone see Figure 5.3	Argon Excitation Temperature (deg K)		
	SUR=0.5 ml min <sup>-1</sup>	SUR=1.0 ml min <sup>-1</sup>	SUR=1.5 ml min <sup>-1</sup>
1	7500	7000	7200
2	7000	6700	7200
3	5700	5700	6000

Table 5.4 Argon Excitation Temperature, deg K in the Analytical MIP. Dependence on position in MIP and SUR.  
Argon Flowrate = 1.0 l min<sup>-1</sup>.  
Input Power = 65 ± 3 W



B.

A  $1.0 \text{ l min}^{-1}$  argon MIP was then generated in the slab-line cavity using the Babington nebulizer (section 6.3.1). Since this nebulizer is designed to operate on a flowrate of  $0.1 \text{ l min}^{-1}$ , an extra  $0.9 \text{ l min}^{-1}$  of argon was delivered into the spraychamber via an auxiliary inlet.

The measured argon excitation temperature (7000 deg K) in this MIP was identical to that measured under similar conditions when the crossflow nebulizer was used (see table 5.4, Viewing Zone 2, SUR =  $0.5 \text{ ml min}^{-1}$ ).

As the auxiliary argon was removed, the MIP stabilized at a flowrate of  $0.1 \text{ l min}^{-1}$  and the slightly different distribution of excited states gave an argon excitation temperature of 6000 deg K. Unlike their behaviour in the dry argon MIP (section 5.1.1A) the Ar I spectral lines did not significantly alter in intensity as the flowrate was reduced.

C.

Following the introduction of a more suitable spraychamber (section 6.3.2), measurements of the argon excitation temperature were made at the viewing zone determined to give optimum spectrochemical performance (section 6.5.1) when different analyte solutions were introduced into the MIP.

With MIP's generated in the slab-line cavity at flowrates of  $0.1$  and  $1.0 \text{ l min}^{-1}$ , using the appropriate nebulizers the distribution of excited states in the argon atom was determined when sample solutions containing Ca, Ni, Fe and KCl were aspirated at the optimum SUR of  $0.75 \text{ ml min}^{-1}$  (section 6.5.2). The results, together with those obtained when only deionized water was aspirated are presented in table 5.5.

Typical graphs of  $\ln(I\lambda/gA)$  versus  $E$  for MIP's operated at  $0.1$  and  $1.0 \text{ l min}^{-1}$  are illustrated in figures 5.5 and 5.6 respectively.

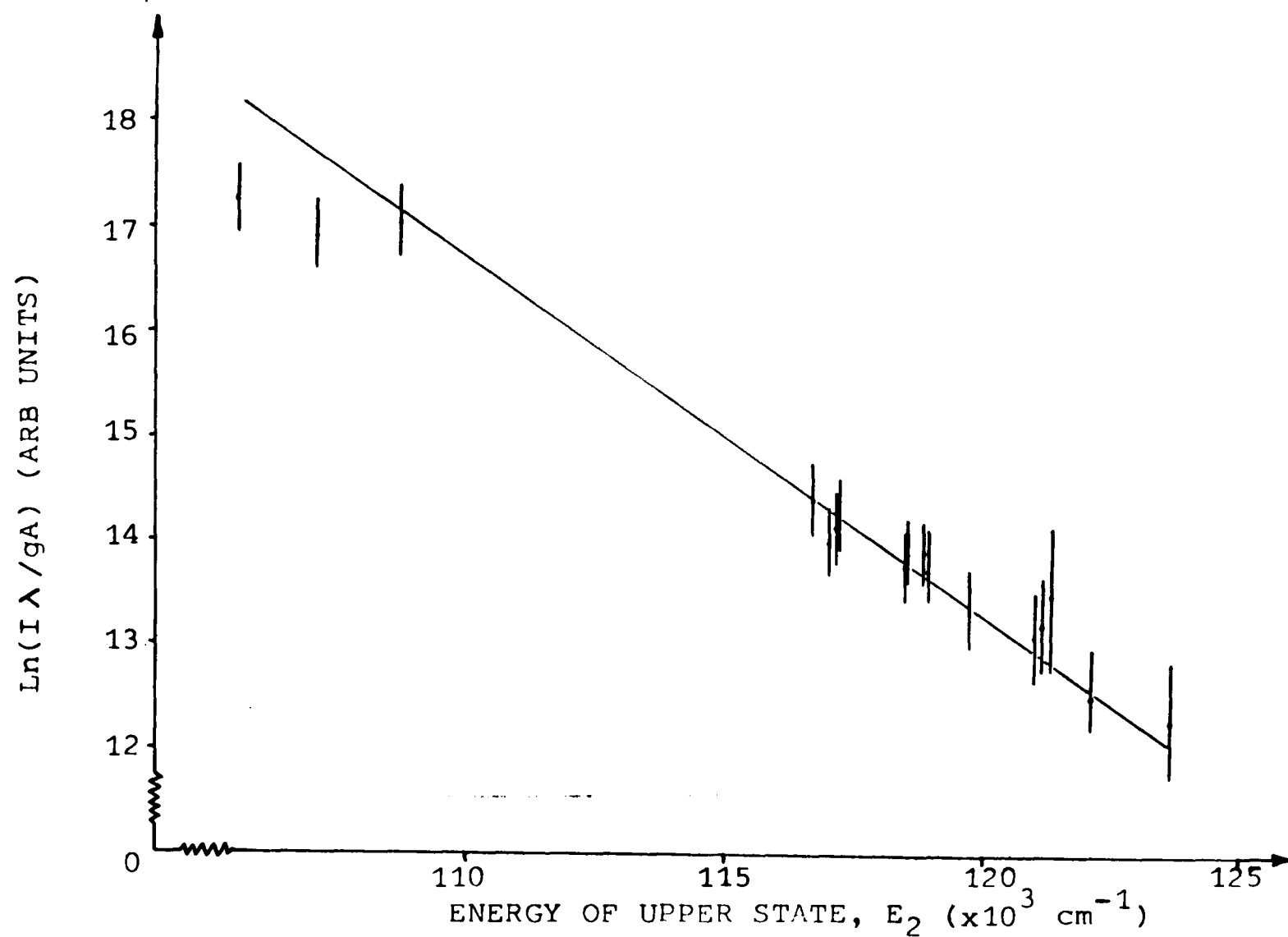
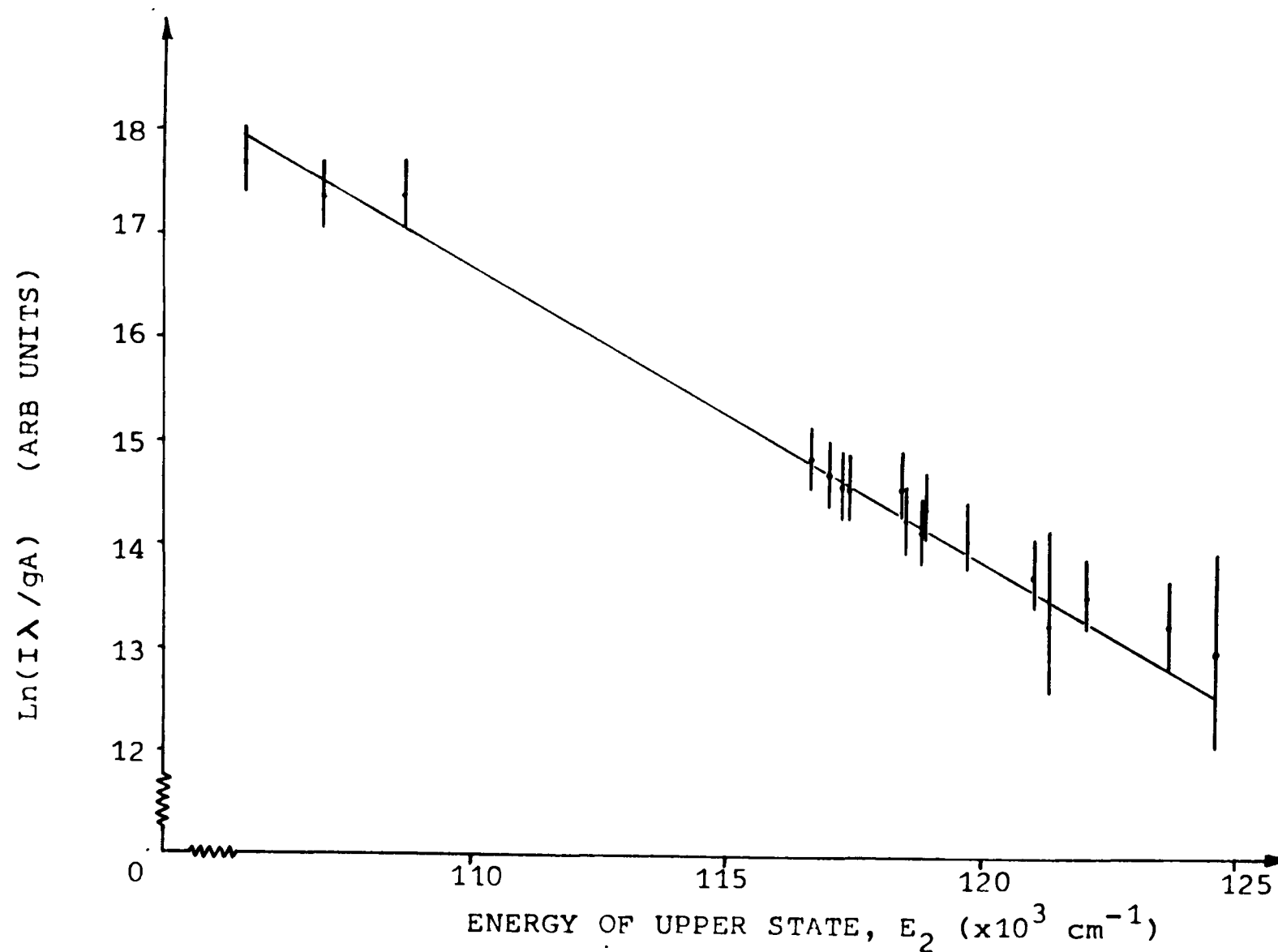


Figure 5.5. Graph of  $\ln(I\lambda/qA)$  vs  $E$  for Ar I. Analytical MIP operated at  $0.1 \text{ l min}^{-1}$  in Slab-line Cavity SUR =  $0.75 \text{ ml min}^{-1}$  of  $10 \mu\text{g ml}^{-1}$  Fe solution.



**Figure 5.6.** Graph of  $\text{Ln}(I\lambda/qA)$  vs  $E$  for Ar I Analytical  
MIP operated at  $1.0 \text{ l min}^{-1}$  in Slab-line Cavity.  
 $\text{SUR} = 0.75 \text{ ml min}^{-1}$  of  $10 \mu\text{g ml}^{-1}$  Fe solution.

		Argon Excitation Temperature (deg K)	
Analyte	Matrix	Flow = 0.1 l min <sup>-1</sup>	Flow = 1.0 l min <sup>-1</sup>
Blank		4100	4400
5 µg ml <sup>-1</sup> Ca		4600	
20 µg ml <sup>-1</sup> Ni		4000	
10 µg ml <sup>-1</sup> Fe		4300	5000
	1 mg ml <sup>-1</sup> K	3700	5000
5 µg ml <sup>-1</sup> Ca	1 mg ml <sup>-1</sup> K	3900	
20 µg ml <sup>-1</sup> Ni	1 mg ml <sup>-1</sup> K	4000	
10 µg ml <sup>-1</sup> Fe	1 mg ml <sup>-1</sup> K	4600	4500

Table 5.5

Argon Excitation Temperature in the Analytical MIP  
Generated in the Slab-line Cavity - Dependence on Sample

As the results given in table 5.5 confirm it was not possible to infer any direct relationship between the nature of the sample constituents introduced into either MIP and the distribution of excited states in the argon atom, although the lower excitation temperature in the  $0.1 \text{ l min}^{-1}$  MIP is again observed.

D.

Similar measurements were made on an MIP generated in the  $\text{TM}_{010}$  cavity at an argon flowrate of  $1.0 \text{ l min}^{-1}$  using the crossflow nebulizer and a suitable spray chamber (section 6.3). The sample solutions were aspirated at an SUR of  $0.5 \text{ ml min}^{-1}$  and light from the plasma was viewed axially down the discharge tube as we are constrained to do (section 6.5).

A typical graph of  $\ln(I\lambda/gA)$  versus  $E$  obtained is shown in figure 5.7. Again it was not possible to infer any relationship between the nature of the sample constituents introduced into the MIP and the argon excitation temperature as the results given in table 5.6 show.

It may be noted that the excitation temperatures measured compare closely with the values measured for the  $1.0 \text{ l min}^{-1}$  MIP generated in the slab-line cavity at a viewing zone 7.5 mm below the top cavity plate. This would be explained by the fact that in both circumstances light from the main body of the plasma is viewed by the optical system. However, unlike the MIP generated in the slab-line cavity, there is a pronounced lack of equilibrium between the low lying 4p excited states of Ar I and the higher excited states. (see figure 5.7).

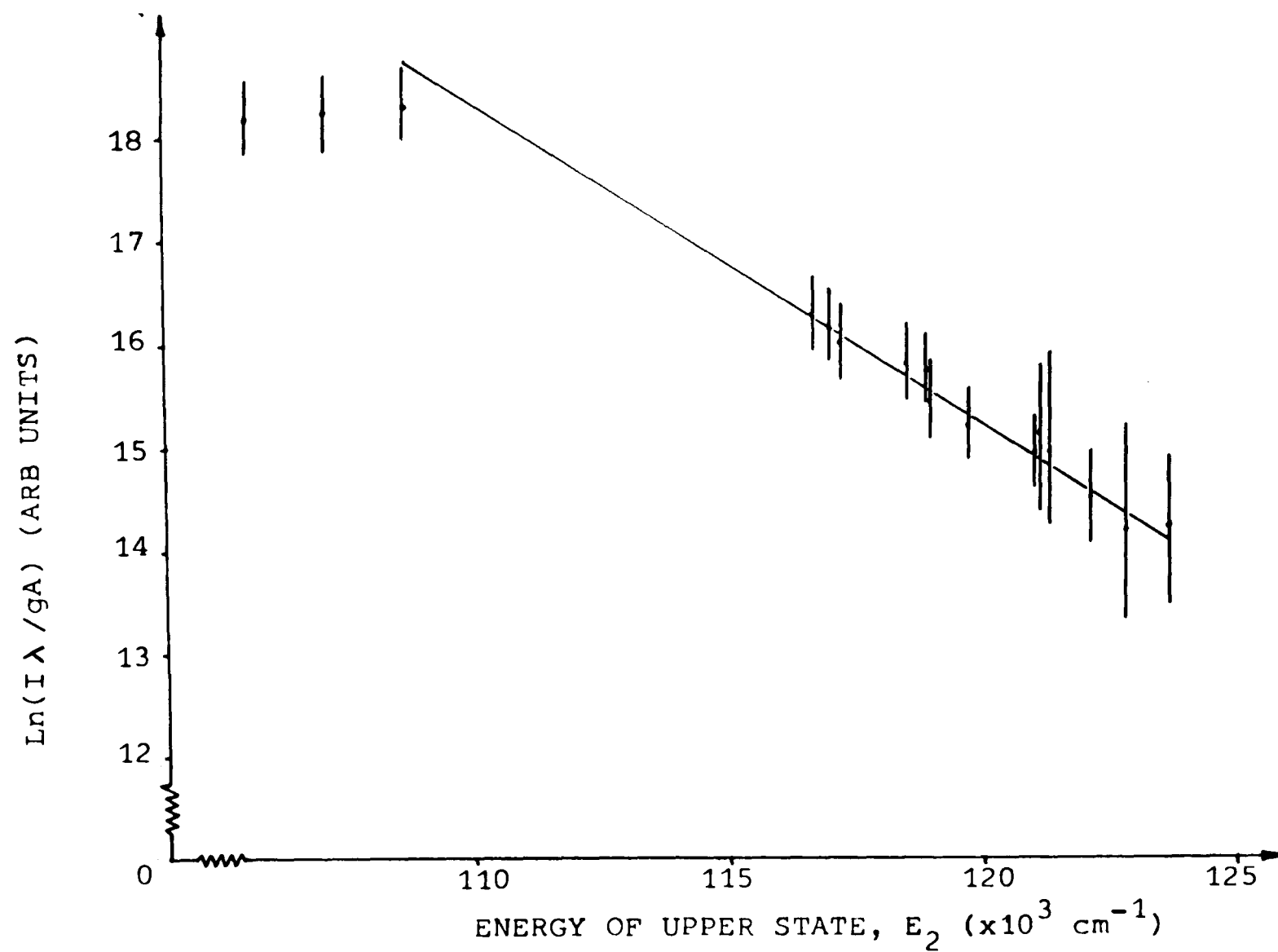


**Figure 5.7** Graph of  $\ln(I\lambda/gA)$  vs  $E$  for Ar I. Analytical  
MIP Generated in the  $TM_{010}$  Cavity at  $1.01 \text{ min}^{-1}$   
 $SUR = 0.5 \text{ ml min}^{-1}$  of  $10 \mu\text{g ml}^{-1}$  Fe/  $1 \text{ mg ml}^{-1}$  K solution

		Argon Excitation Temperature (deg K)
Analyte	Matrix	Flow = 1.0 l min <sup>-1</sup>
Blank		5000
5 µg ml <sup>-1</sup> Ca		4400
20 µg ml <sup>-1</sup> Ni		4500
10 µg ml <sup>-1</sup> Fe		3700
	1 mg ml <sup>-1</sup> K	4400
5 µg ml <sup>-1</sup> Ca	1 mg ml <sup>-1</sup> K	4700
20 µg ml <sup>-1</sup> Ni	1 mg ml <sup>-1</sup> K	5200
10 µg ml <sup>-1</sup> Fe	1 mg ml <sup>-1</sup> K	4600

Table 5.6.     Argon Excitation Temperature in the Analytical MIP  
Generated in the TM<sub>010</sub> Cavity - Dependence on Sample.

## 5.2. Iron Excitation Temperature

Using an identical method to that used for argon (section 5.1) relative spectral line intensity measurements were made for the 8 iron (Fe) spectral lines listed in table 5.7, and a graphical plot of  $\ln(I\lambda/gA)$  versus  $E$  made in order to determine an excitation temperature,  $T_{\text{EXC}}$ .

Table 5.7 presents the atomic transition probability data and atomic energy level data of Bridges and Kornblith, 1974 (92) which was found to give the most consistent results. The transition probability data given in the form,

$$\text{Log } g_1 f$$

used by these authors was converted to the form used in this study, according to Wiese and Martin, 1981 (93) by the equation

$$g_1 f = 1.499 \cdot 10^{-8} \lambda^2 g_2 A_{21} \dots\dots\dots 5.5$$

where  $g_1$  is the degeneracy of the lower energy level involved in the transition,  $f$  is the oscillator strength and all the other symbols are as defined in section 5.1.

Spectral line intensities were measured as a function of the peak heights of the recorded line profiles (section 3.8). One of the reasons for the use of Fe spectra to determine plasma temperatures is that spectral lines corresponding to transitions from a wide range of upper energy levels occur within a fairly narrow range of wavelength. Therefore it is not essential to compensate the measured line intensities for the response of the optical system since  $H(\lambda)$  (section 3.7) changes by only 4% over the 4.4 nm range of Fe wavelengths used.



$\lambda$ (nm)	Energy of State ( $\text{cm}^{-1}$ )		Log $g_1 f$	Accuracy (%)
	Upper	Lower		
371.993	26875	0	-0.43	10
373.486	33695	6928	0.31	10
373.713	27167	416	-0.57	10
374.556	27395	704	-0.77	15
374.826	27560	888	-1.01	10
374.948	34040	7377	0.17	10
375.823	34329	7728	-0.00	10
376.379	34547	7986	-0.19	10

Table 5.7.     Spectral line Data for Fe I

Figure 5.8. illustrates a typical graph of the population of excited states in the Fe atom, when a  $10 \mu\text{g ml}^{-1}$  Fe solution was aspirated into the MIP generated in the slab-line cavity.

Similar measurements were made when the MIP was generated in the  $\text{TM}_{010}$  cavity and the result data is presented for both types of cavity in table 5.8.

A comparison of these results with those given in table 5.5 and 5.6 highlights the fact that irrespective of cavity type or gas flowrate, the Fe excitation temperature is significantly higher than that deduced for Ar I by as much as 1000 deg K. Thus if thermal equilibrium exists in the MIP, it is only within a particular plasma species. Further weight to this hypothesis is added by the results for the OH molecular spectra (section 5.3).

Unlike the argon excitation temperature measured in the MIP generated in the slab-line cavity, the Fe excitation temperature would appear not to be dependent on gas flowrate.

The higher value of Fe excitation temperature measured in the MIP generated in the  $\text{TM}_{010}$  cavity is probably due to the different part of the plasma viewed (section 3.1).

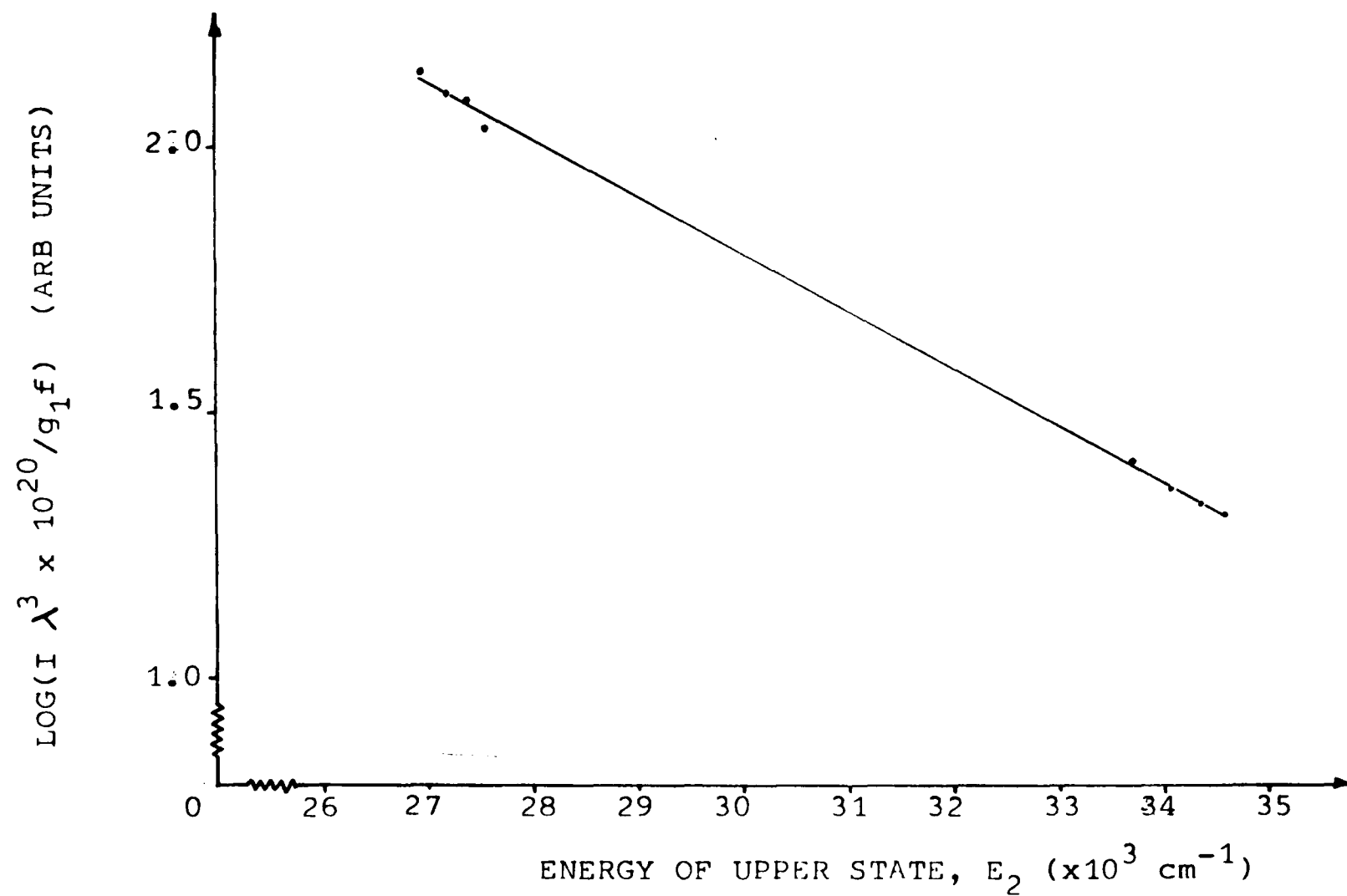


Figure 5.8

Graph of  $\text{Log} (I \lambda^3 / g_1 f)$  vs  $E$  for Fe I

Analytical MIP Generated in Slab-line Cavity at

$0.1 \text{ l min}^{-1}$ . SUR =  $0.75 \text{ ml min}^{-1}$  of  $10 \mu\text{g ml}^{-1}$  Fe solution

Analyte	Matrix	Iron Excitation Temperature (deg K)		
		Slab Line Cavity		TM <sub>010</sub> Cavity
		Flow = 0.1 l min <sup>-1</sup>	Flow = 1.0 l min <sup>-1</sup>	Flow = 1.0 l min
10 µg ml <sup>-1</sup> Fe		5800		
20 µg ml <sup>-1</sup> Fe				6200
100 µg ml <sup>-1</sup> Fe			5600	
10 µg ml <sup>-1</sup> Fe	1 mg ml <sup>-1</sup> K	6000	5900	6600
100 µg ml <sup>-1</sup> Fe	1 mg ml <sup>-1</sup> K		5700	

Table 5.8      Iron Excitation Temperature in Analytical MIP Generated  
in Slab-line and TM<sub>010</sub> Cavities.

### 5.3 OH Rotational Temperature.

Table 5.9 lists the 22 spectral line components of the  $P_1(n)$  branch of the  $^2\Sigma - ^2\Pi$  (0,0) system of the OH molecule on which relative intensity measurements were made. It was then possible to determine a rotational temperature,  $T_{ROT}$  using equation 5.4. in the form suggested by Dieke and Crosswhite, 1961 (94) in their tabulations of the OH transition probabilities, ie

$$\text{Log } I_K - \text{Log } A_K = \text{CONSTANT} - E_K \text{ Log } (e/k T_{ROT})$$

Their values of  $A_K$  are related to the form of transition probability used in this study by the equation

$$A_K \propto \lambda^2 g_2 A_{21}$$

$A_K$ , also proportional to  $g_1 f$ , must theoretically be multiplied by the factor,  $1/\lambda^3$  in order to obtain wavelength corrected line intensities.

Spectral intensities were measured as a function of the peak heights of the recorded line profiles (section 3.8). Some correction to the measured line intensities was necessary to compensate for the response of the optical system over the 23 nm range of wavelength of the spectral line components used.

However, in practice it was found that such a correction, in addition to being slight was approximately equal and opposite to the theoretical wavelength correction required for the  $A_K$ . The effect on the results was negligible and so both these correction processes were omitted.

The  $^2\Sigma - ^2\Pi$  system of OH gives rise to a very complex, crowded spectrum with many spectral line components in close proximity to one another or even superimposed. Consequently, with the instrument bandpass employed (section 3.8) the choice of 'branch' of OH spectra used is important to minimise the effect that spectral interferences have on the rotational temperature determined.

COMPONENT Pl (n)	COMPONENT WAVELENGTH (nm)	ENERGY OF UPPER STATE (cm <sup>-1</sup> )	A <sub>K</sub>
2	308.639	32542.6	12.7
5	310.123	32948.3	24.5
6	310.654	33150.1	28.6
9	312.394	33951.8	40.9
12	314.380	35038.6	53.1
13	315.100	35462.0	57.1
14	315.851	35914.8	61.2
15	316.634	36396.7	65.2
17	318.297	37443.9	73.3
18	319.178	38007.9	77.3
19	320.096	38597.8	81.4
20	321.050	39212.7	85.4
21	322.042	39851.7	89.4
22	323.073	40513.8	93.4
23	324.145	41198.2	97.5
24	325.260	41903.8	101.5
25	326.418	42629.6	105.5
26	327.624	43374.4	109.5
27	328.880	44137.4	113.5
28	330.186	44917.2	117.5
29	331.546	45712.9	121.6

Table 5.9      SPECTRAL LINE DATA FOR OH

In an initial study on the OH spectrum a number of other branches of the  $^2\Sigma - ^2\Pi$  system were utilized, in addition to the  $P_1(n)$  branch, to determine the rotational temperature. It was found that all of the branches investigated, eg.  $P_1(n)$ ,  $P_2(n)$ ,  $Q_1(n)$  for the (0,0) system and  $P_1(n)$  for the (1,1) system gave similar results. However the  $P_1(n)$  branch of the (0,0) system was chosen because it provided the widest range of useable spectral lines which suffered least from spectral interferences.

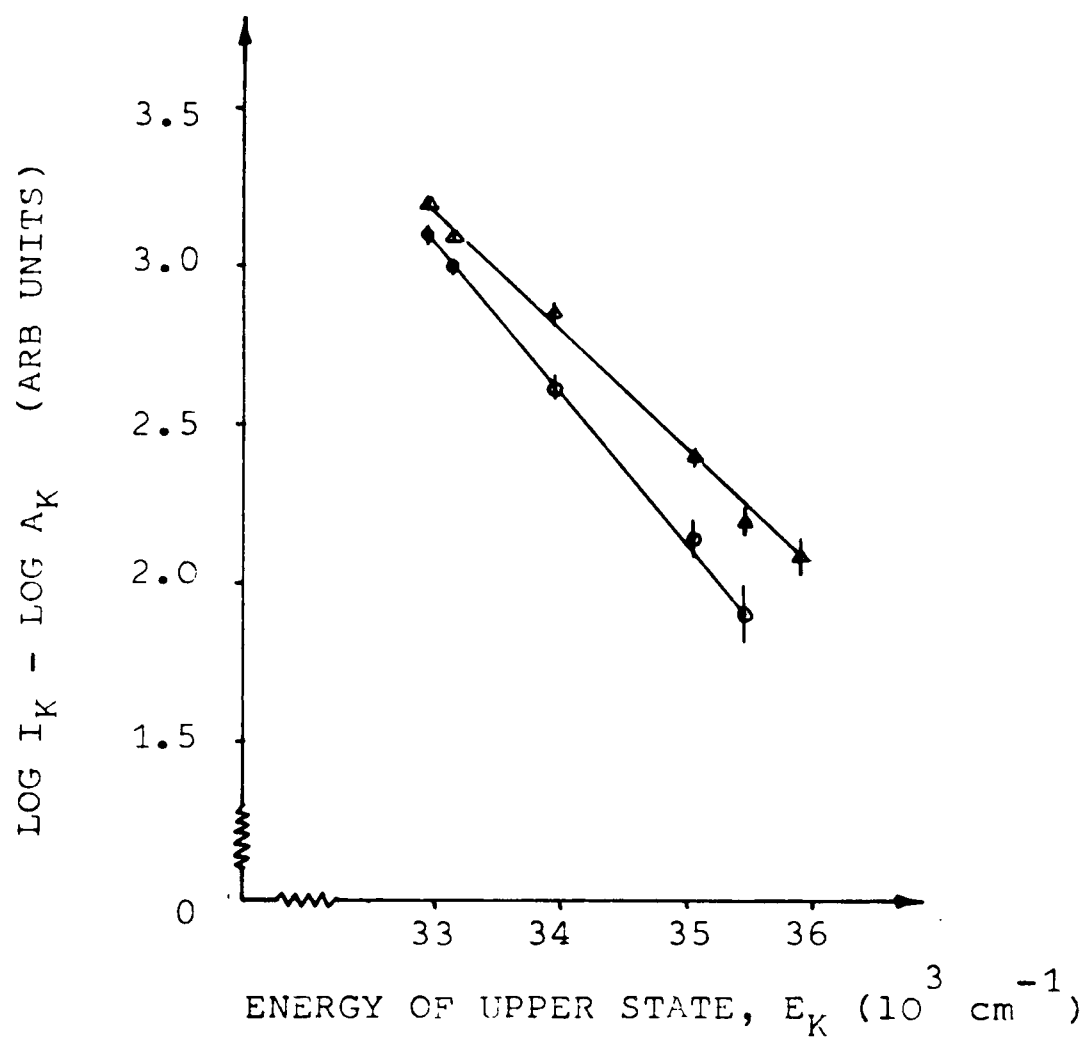
The OH spectra emitted by the dry argon MIP is produced entirely by the impurity water vapour present in the plasma gas. The spectra was therefore not very intense and only the strongest spectral lines near the bandhead at 306.4 nm were measurable. Unfortunately this is the most crowded part of the spectrum where the problem of spectral interferences is most acute. Measurements of an OH rotational temperature in the dry argon MIP would therefore be made using a reduced number of the least reliable spectral lines given in table 5.9. As a consequence of this it was decided to undertake only a limited study of the OH spectra in the dry argon MIP, namely the effect of removal of the water vapour using a cold trap as is described in the next section.

### 5.3.1. Rotational Temperature of the Dry Argon MIP.

Concurrently with measurements on the argon spectra (section 5.1.1B), 6 of the stronger OH spectral lines in table 5.9 were measured before and after the cold trap (section 3.1) was activated. For an MIP operated at  $0.1 \text{ l min}^{-1}$  the reduction in the amount of water vapour reaching the plasma was sufficient to cause a 500% reduction in the OH spectra emission. Figure 5.9 shows the effect this had on the distribution of excited states in the OH molecule and the consequent reduction in the rotational temperature from 1650 to 1320 deg K. This confirmed an earlier study when use of a very much less efficient cold trap had produced a similar though much smaller reduction in the rotational temperature for MIP's operated at gas flowrates of  $0.1 \text{ l min}^{-1}$  and  $0.5 \text{ l min}^{-1}$ .

This earlier study had also shown that the rotational temperature determined for the  $0.5 \text{ l min}^{-1}$  MIP was significantly lower by about 25% than that determined for the  $0.1 \text{ l min}^{-1}$  MIP. This is somewhat surprising since the origin of the impurity water vapour in the argon was thought to be the BOC cylinder itself and presumably more water vapour is entering the plasma at a flowrate of  $0.5 \text{ l min}^{-1}$  than at  $0.1 \text{ l min}^{-1}$ . From the evidence of the experiments made using the cold trap, a higher rotational temperature in the  $0.5 \text{ l min}^{-1}$  MIP would be predicted. It may be that the difference in the amount of water vapour entering the plasma at these two flowrates was minimal and some other mechanism was responsible for the difference in measured rotational temperatures. Certainly the measurements on the analytical MIP described in the next section lend further weight to the idea of greater water vapour in the plasma producing higher rotational temperatures.





$\Delta$  = Normal Argon Flow

$\phi$  = Argon Flow Incorporating Cold Trap

Figure 5.9 Graph of  $\log I_K - \log A_K$  vs  $E_K$  for OH  
Dry Argon MIP operated in Slab-line Cavity  
at  $0.1 \text{ l min}^{-1}$ .

### 5.3.2 Rotational Temperature of the Analytical MIP

The OH rotational temperature was determined using all the spectral lines listed in table 5.9 concurrently with measurements on the argon spectra when different analyte solutions were introduced into the MIP generated in the slab-line cavity (section 5.1.2 C) and the  $TM_{010}$  cavity (section 5.1.2 D).

Figure 5.10 shows a graph of  $\log I_K - \log A_K$  versus  $E_K$  which is typical of all those obtained for the analytical MIP. Table 5.10 shows the rotational temperature results for the two cavity types, argon flowrates and sample constituents investigated.

For the MIP generated in the slab-line cavity the rotational temperature is slightly higher at an argon flowrate of  $0.1 \text{ l min}^{-1}$  compared to  $1.0 \text{ l min}^{-1}$ .

In addition, when a flowrate of  $0.1 \text{ l min}^{-1}$  was used the MIP generated in the slab-line showed a slight sensitivity to the presence of KCl in the sample solutions, which causes a reduction in the rotational temperature.

No such sensitivity was exhibited by the MIP generated in the  $TM_{010}$  cavity, where rotational temperatures were consistently higher than those in the MIP generated in the slab-line cavity at the same flowrate.

It may be noted that all of these rotational temperatures for the analytical MIP's are much higher than those measured in the dry argon MIP (see previous section). This increase may undoubtedly be attributed to the larger amounts of water vapour introduced by the nebulizer.

This suggests that the actual amount of water vapour present in the MIP is the determining factor regarding the distribution of excited states with the OH molecule and hence the rotational temperature in the analytical MIP.

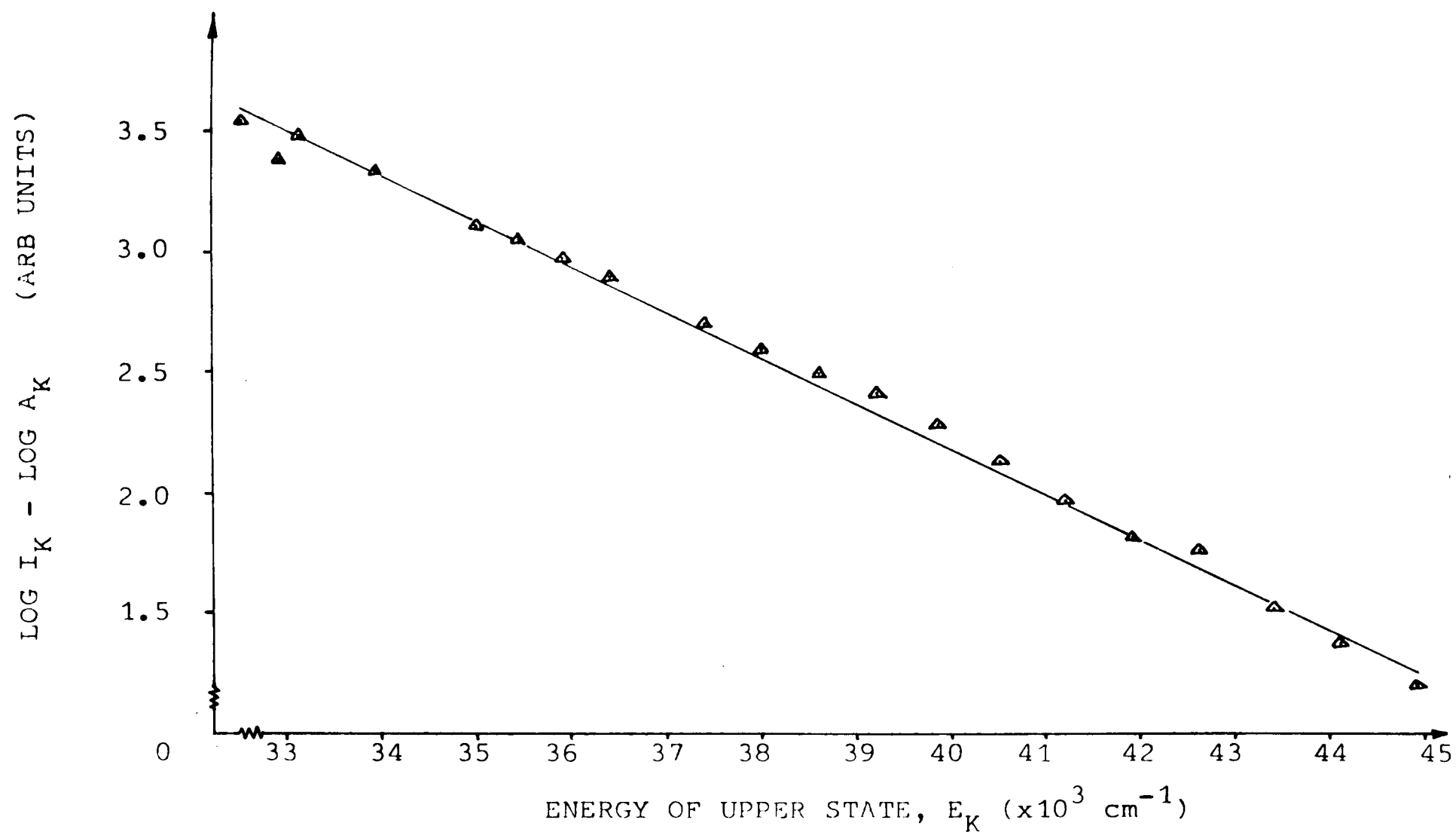


Figure 5.10 Graph of  $\text{Log } I_K - \text{Log } A_K$  Vs  $E_K$  for OH  
Analytical MIP Generated in the Slab-line  
Cavity. SUR =  $0.75 \text{ ml min}^{-1}$  of blank.

## OH Rotational Temperature (deg K)

Analyte	Matrix	Slab-line Cavity		TM <sub>010</sub> Cavity
		Flow = 0.1 l min <sup>-1</sup>	Flow = 1.0 l min <sup>-1</sup>	Flow = 1.0 l min <sup>-1</sup>
Blank		3300	3000	3400
5 µg ml <sup>-1</sup> Ca		3450		3200
20 µg ml <sup>-1</sup> Ni		3400		3600
10 µg ml <sup>-1</sup> Fe		3400	3100	3600
	1 mg ml <sup>-1</sup> K	3200	3100	3600
5 µg ml <sup>-1</sup> Ca	1 mg ml <sup>-1</sup> K	3300		3600
20 µg ml <sup>-1</sup> Ni	1 mg ml <sup>-1</sup> K	3200		3500
10 µg ml <sup>-1</sup> Fe	1 mg ml <sup>-1</sup> K	3100	3050	3600

Table 5.10

OH Rotational Temperature in the Analytical MIP  
 Generated in the Slab-line and TM<sub>010</sub> Cavities.

#### 5.4 Electron Density Measurements.

The width and shape of spectral lines emitted by atoms and ions in gaseous plasmas have come under a considerable amount of investigation by physicists concerned with the interactions between atoms and ions in gaseous plasmas. From these studies has developed a diagnostic technique for electron density measurement applicable to a much wider field of interest, especially in the determination of the fundamental physical properties characterizing laboratory plasmas used for atomic emission spectroscopy.

This electron density diagnostic technique is based on measurement of the Stark broadening of spectral lines emitted by atoms or ions in the plasma. A full treatment of the theory of Stark broadening is beyond the scope of this thesis and the reader is referred to one of the many reviews on the subject, Griem, 1964 (57), Baranger, 1962 (95) or Griem, 1974 (96). However a brief synopsis of the theory is presented here.

The energy levels in an emitting atom of the plasma are subject to the electric fields produced by charged perturbers, electrons and ions which interfere with the frequency spectrum of the emitted photon via the Stark effect, causing a shift in the wavelength of the spectral line. Over the total number of emitting atoms and perturbers these wavelength shifts are smeared out and a Stark broadened spectral line is observed.

The extent of this broadening is dependent to some degree on the density of perturbers and to the type of emitting atom. For hydrogen and hydrogen-like atoms, the wavelength shift produced is directly proportional to the strength of the electric field generated by the perturber, the Linear Stark effect. For other heavier and more complex atoms, the wavelength shift produced is proportional to the square of the electric field strength, the Quadratic Stark effect.

**Explanation** of the effect of the perturber's electric field on the energy levels in the emitting atom is complex, therefore simplifying assumptions are made in order to reduce the problem to one of mathematically manageable proportions. This simplification has been approached from one of two directions depending on the nature of the perturbing particles involved.

For fast moving perturbers like electrons, the effect of the electric field on the atoms's energy levels has been explained in terms of the Impact Approximation in which the generally un-interrupted wavetrain of the photon is interrupted briefly, with a consequent change in it's phase and/or frequency by the passage of the perturber. The impact approximation has been developed, notably by Baranger, 1958 (97) and by Kolb and Griem, 1958 (98) from the impact theory of Anderson, 1949 (99) and has it's origins in the collisional theory of Lorentz, 1906 (100).

For slow moving perturbers like ions, the effect of the electric field on the atoms's energy levels has been explained in terms of the Quasi-Static Approximation in which the perturbation is considered to extend over the entire length of the photon wavetrain causing an overall frequency shift. The quasi-static approximation, which adopts a statistical approach to this type of perturbation over all emitting atoms and perturbers was first applied by Holtzmark, 1919 (101) and has since been modified to allow for the finite particle motion.

For the range of electron densities considered in laboratory plasmas ( $10^{12}$  to  $10^{16}$  cm<sup>-3</sup>), theoretical considerations dictate the validity of these approximations over different parts of the spectral line profile, Griem, 1974 (96). The quasi-static approximation best describes the far wings of the line profile, beyond the half-width, whereas the impact approximation is only properly applicable to the central line region. Comparison of calculated line profiles with observed spectral lines does, however show that some discrepancies between theory and experimental data remain, even for parts of the spectral line profile well within the validity criteria for each approximation.

An example of this is the failure to observe the structure in the centre of many hydrogen spectral lines as is predicted by the impact approximation.

Despite the complexities of producing a general theory, applicable over all regions of the line profile, a unified theory of line broadening has been reported by Smith et al, 1969 (102) and Voslamber, 1969 (103) and for hydrogen spectral lines in particular by Vidal et al, 1971 (104). The unified theory has permitted the formulation of normalised line profiles for a number of hydrogen spectral lines by Vidal et al, 1973 (105). These profiles cover a much wider range of electron density than those tabulated by Griem, 1974 (96), giving greater scope for the applicability of this diagnostic technique. These tabulations have been used by a number of authors, e.g. Kalnicky et al, 1977 (106) in the determination of electron density in an ICP.

Although the impact and quasi-static approximations and the unified theory have been used to describe the observed spectral lines from a number of the heavier elements such as argon, the great majority of theoretical studies and experimental confirmation work has been carried out on the light elements, hydrogen and helium. Consequently, the reliability and precision of electron density determinations made using, e.g. the  $H_{\beta}$  spectral line at 486.13 nm is considerably better than for the spectra of other elements.

#### 5.4.1 Practical Electron Density Determinations in the MIP.

The profile of  $H_{\beta}$  observed in the dry argon MIP under all operating conditions was found to be symmetrical with a complete absence of the intensity dip in the centre of the profile predicted by theory. This is probably due to the low electron density in the dry argon MIP (section 5.4.2), since theoretical predictions show a positive correlation between the depth of the intensity dip and the electron density itself. Since the peak intensity of  $H_{\beta}$  was therefore uniquely determined, the electron density could have been calculated from the half-width parameter only, Griem, 1964 (57). However, Vidal et al, 1973 (105) in their tabulations of normalized line profile for hydrogen, point to the dangers of using only the half-width of the line profile to determine electron density because of the uncertainty in the theory of predicting the shape, and hence the peak of the line centre. In addition, under certain operating conditions when the sample introduction system was used, the intensity dip in the line centre was observed and the peak intensity was not uniquely determined.

In view of this, it was decided to use a method which compared the entire observed spectral line profile with a suitably corrected theoretical profile in a 'best fit' approximation to determine electron density rather than rely on half-width only.

Recently Goode and Deavor, 1984 (107) reported measurements of the electron density in an argon MIP using such a method. They compared theoretical  $H_{\beta}$  line profiles, calculated for a number of electron densities with experimentally measured  $H_{\beta}$  spectral lines using a least squares fit computer program. Professor S.R.Goode of the Department of Chemistry, University of South Carolina, USA has been kind enough to supply a copy of the Fortran program they used, which has been adapted to run on a VAX computer and used to process the experimental data obtained from the MIP investigated in this work.



Vidal et al, 1973 (105) tabulate values for the normalized line profile,  $S(\Delta\infty)$  of the  $H_{\beta}$  spectral line for electron densities between  $10^{11}$  and  $10^{17} \text{ cm}^{-3}$ .  $\Delta\infty$  is called the 'reduced Stark parameter' and is related to the wavelength perturbation,  $\Delta\lambda$  measured in Angstroms from the line centre by the equation.

$$\Delta\lambda = F_0 \times \Delta\infty \quad 5.6$$

where 'F<sub>0</sub>' is the normal field strength due to the electrons, often referred to as the Holtzmark potential, which measured in SI units is given by the equation (Griem, 1974 (96), chapter II.2a),

$$F_0 = 2.603 \times e \times (N_e)^{2/3} \quad 5.7$$

where 'e' is the charge on the electron and 'N<sub>e</sub>' is the number density of electrons in  $\text{cm}^{-3}$ . Substituting 'e' =  $1.603 \times 10^{-19}$  Coulomb into Equation 5.7 gives.

$$F_0 = 4.17 \times 10^{-19} \times (N_e)^{2/3} \quad 5.7$$

Combining equations 5.6 and 5.7 gives

$$\Delta\lambda = 4.17 \times 10^{-19} \times \Delta\infty \times (N_e)^{2/3} \quad 5.8$$

Before using the theoretical Stark profiles, it is necessary to consider two other broadening mechanisms which affect the shape of the observed spectral line, namely Doppler broadening due to the random kinetic motion of the plasma particles and instrument broadening caused by the optical measurement apparatus.

In order to determine the extent of Doppler broadening on the  $H_{\beta}$  spectral line, the gas temperature was measured in that part of the MIP which extended outside the confines of the discharge tube. Using a chrome alumina thermocouple a value of  $1000 \pm 100$  deg K was measured. The gas temperature within the main body of the plasma is expected to be higher in view of it's higher electron density (section 5.4.2 A).

Even given the discharge tube corrosion problem (section 6.3.2), it is unlikely that the temperature of the main body of the MIP is significantly higher than the melting point of quartz (1700 deg K). A figure of 2500 deg K was therefore assumed and a suitable Doppler profile calculated.

The instrument profile was measured using an He-Ne laser and was found to be approximately Lorentzian in form with a half-width of 0.032 or 0.016 nm depending on the slit width used.

The Fortran program does not use the electron temperature,  $T_e$  as a free parameter in the least squares fit. Goode and Deavor, 1984 (107), report that the electron density calculated is hardly affected by the value of  $T_e$  used, probably due to the theoretical Stark profiles having only a slight dependence on this parameter. Convolution with a suitable Doppler profile, further reduces the difference between successive sets of  $S(\Delta\infty)$ , for different  $T_e$ .

In view of this, and the argon excitation temperatures measured in the MIP (section 5.1), a  $T_e$  of 5000 deg K was assumed and the appropriate set of theoretical Stark profiles selected from the tabulated data of Vidal et al, 1973 (105).

Another Fortran program (appendix A 5) was written to process the theoretical Stark profiles into a form that the least squares fit program could use. This entailed re-calculation of the  $S(\Delta\infty)$  profiles to a linear wavelength scale and convolution with Doppler and instrument profiles.

Experimental  $H\beta$  spectral line profiles were recorded on chart paper as the monochromator was scanned at  $0.1 \text{ nm min}^{-1}$  across the wavelength region. Using a suitable over-lay grid, the profiles were digitized at 0.01 nm intervals and the profile intensity ordinates organised into suitable data files for use by the least squares fit program.

The least squares fit program calculates a mean half-profile from the red and blue halves of the original experimental profile. After normalisation, the experimental and theoretical Stark profiles are compared. Because of the failure to observe the same degree of structure in the centre of the  $H\beta$  spectral line as predicted by theory, there is a significant lack of fit in the region near the line centre wavelength. The present curve fit therefore

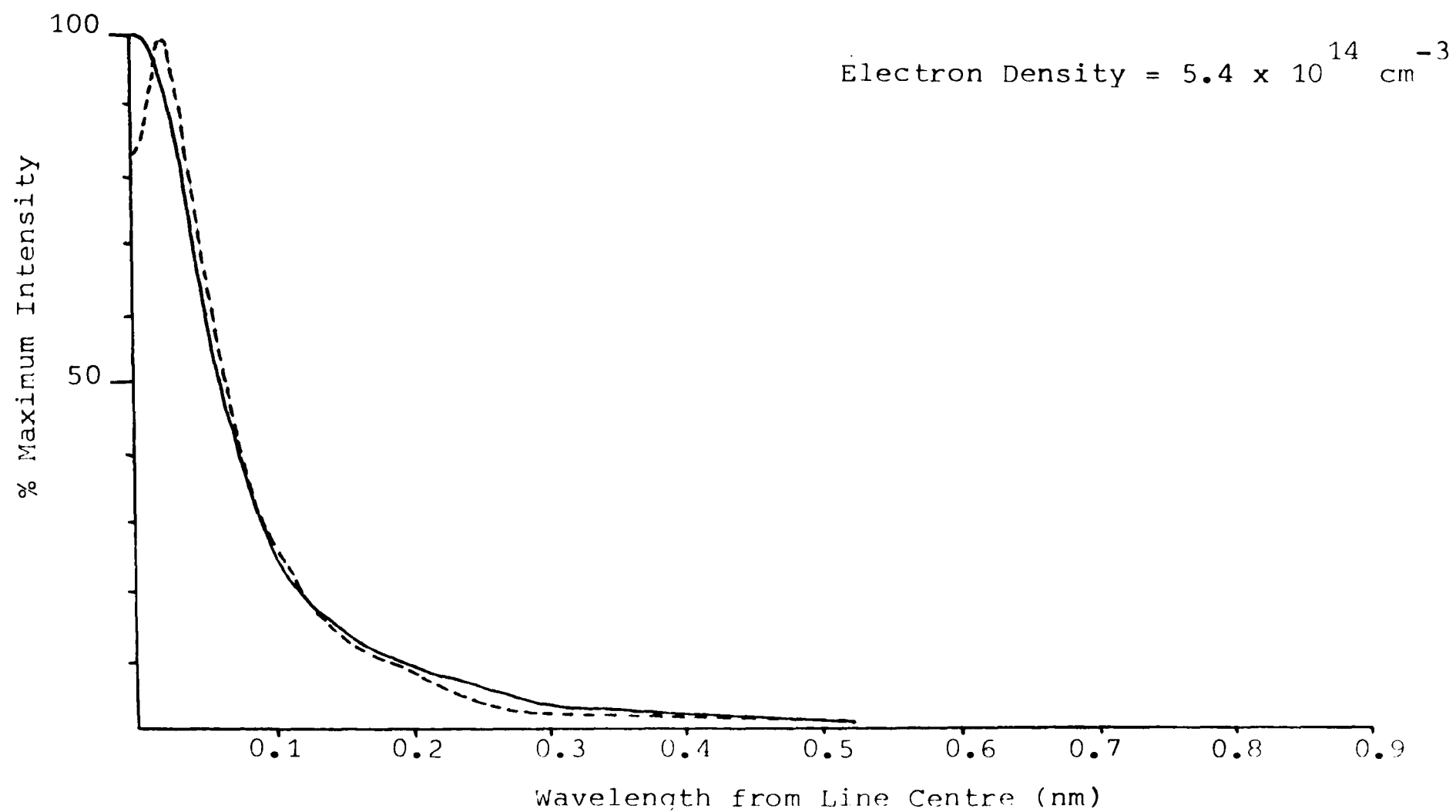


Figure 5.11a      Experimental (Solid Curve) and Best Fit Theoretical (Broken Curve)  
H $\beta$  Profiles Measured in Dry Argon MIP Generated in Slab-line Cavity.

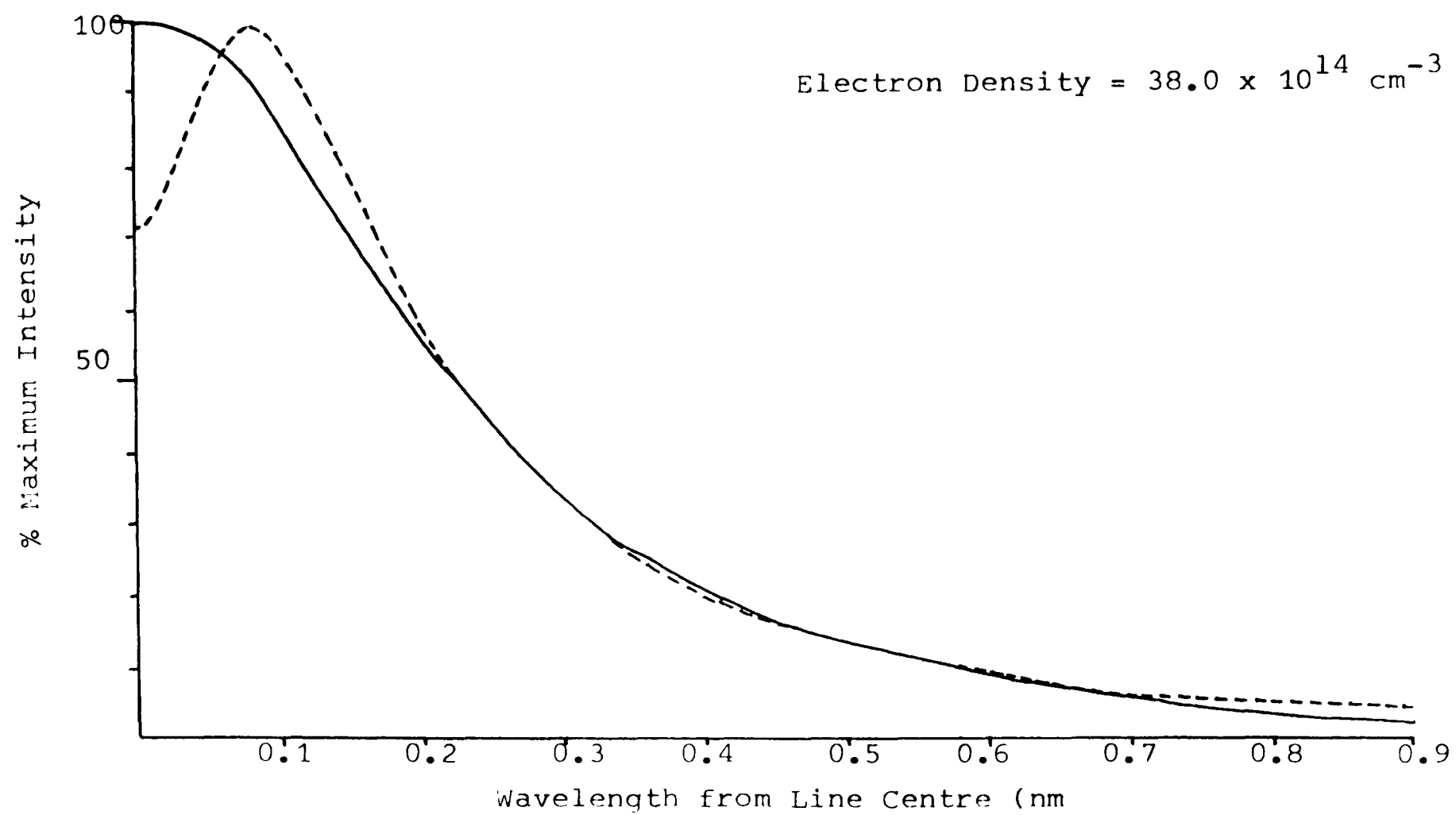


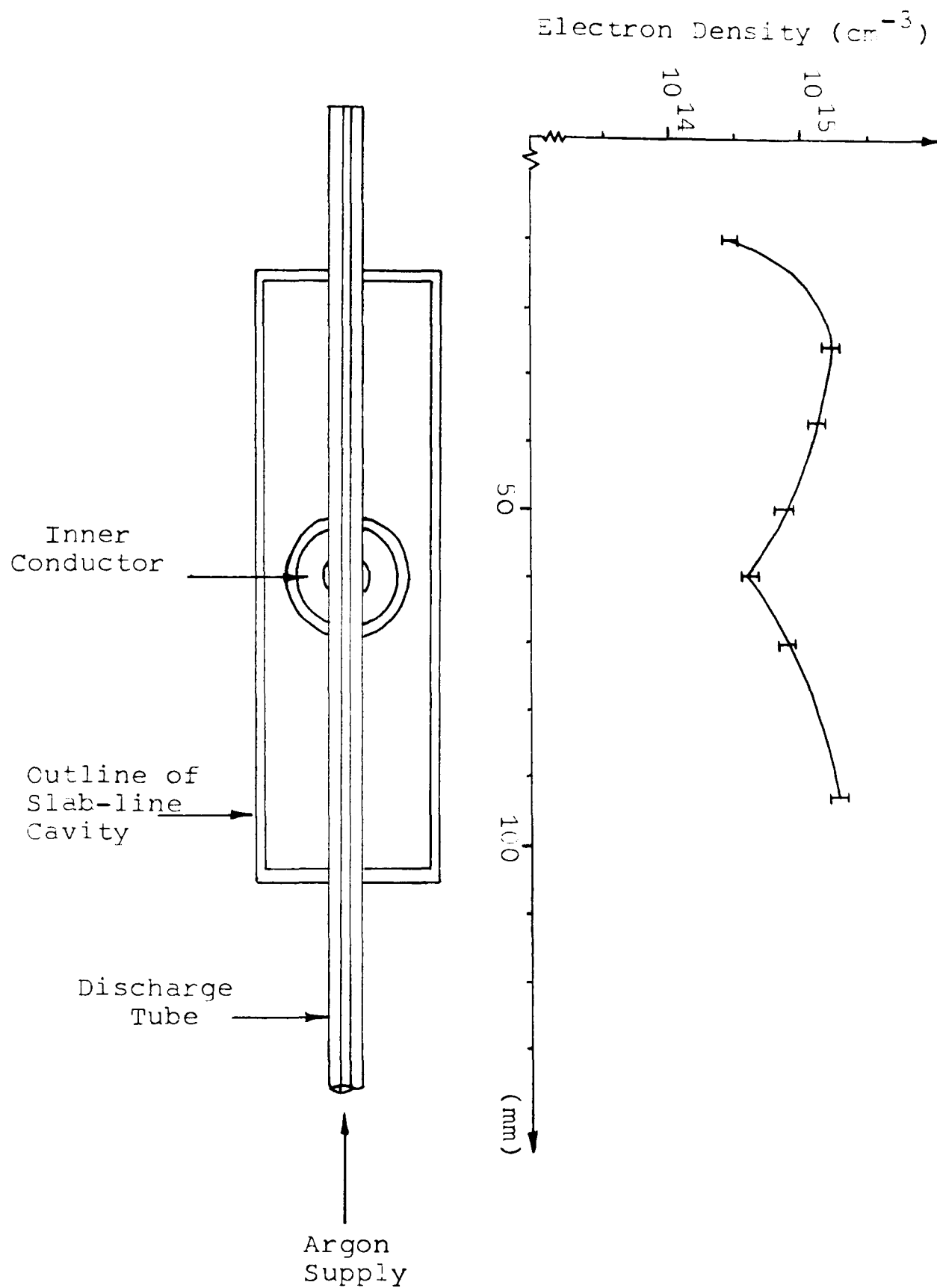
Figure 5.11 b      Experimental (Solid Curve) and Best Fit Theoretical (Broken Curve)  
H $\alpha$  Profiles Measured in Analytical MIP Generated in Slab-line Cavity.

excludes this central region of the profile. The program estimates the two theoretical profiles which 'bracket' the experimental profile using an interval-halving algorithm, James et al, 1977 (108). Iteration of this process reduces the interval between bracketing theoretical profiles until the electron densities calculated from successive estimates are within 5% and the best fit theoretical Stark profile is obtained. The calculated electron density is written to a result file, together with information on the particular experimental operating conditions. Intensity data for experimental and theoretical Stark profiles was also output, permitting a graphical comparison between the two.

The profiles shown in figure 5.11 a) and b) for a dry argon MIP and the analytical MIP respectively, are typical of the narrowest and widest  $H_{\beta}$  spectral lines observed.

Both MIP's were operated at a flowrate of  $1.0 \text{ l min}^{-1}$ , net input power of approximately 65 W and similar viewing zones were employed. Figure 5.11 therefore clearly demonstrates the effect on  $H_{\beta}$ , and consequently the electron density, caused by the introduction of water vapour in the MIP.

For both narrow and wide spectral lines, the curve fit is seen to be quite good beyond the half-maximum intensity point, giving confidence in the validity of this method over the range of electron densities encountered in the MIP. The lack of fit near the line centre is as expected.



Flowrate =  $0.1 \text{ l min}^{-1}$

Net Input Power =  $77 \pm 3 \text{ W}$

Plasma length = 120 mm

Figure 5.12     Dependence of Electron Density on Position in  
Dry Argon MIP Generated in Slab-line Cavity.

#### 5.4.2 Electron Density in the Dry Argon MIP.

A. With the slab-line cavity oriented in configuration A (section 3.1) the electron density was determined at different 'viewing zones' along the length of the dry argon MIP. This was achieved by adjustment of the cavity height with respect to the optical measurement system. An argon flowrate of  $0.1 \text{ l min}^{-1}$  and net input power of  $77 \pm 3 \text{ W}$  was used. Figure 5.12 shows the result, both graphically and with reference to the actual positions within the slab-line cavity.

For the greater length of the MIP, extending both above and below the end of the inner conductor, the MIP completely fills the cross-section of the quartz discharge tube. It is in these regions that the highest electron densities were found.

The rapidly diminishing electron density in those regions of the MIP extending outside the confines of the cavity is to be expected since the microwave energy available to excite the plasma should be much reduced (ideally approaching zero).

The lower electron density at the centre of the MIP, near the end of the inner conductor is caused by the constriction in the plasma which reduces it's luminosity to almost zero.

B. At the viewing zone 10 mm below the end of the inner conductor, the dependence of electron density on argon flowrate was investigated for net input powers of  $53 \pm 2$  and  $123 \pm 4 \text{ W}$ . The results are shown in figure 5.13 a) and important features are summarised in table 5.11.

The electron density is seen to be highly dependent on flowrate, especially over the range  $0.04$  to  $0.5 \text{ l min}^{-1}$ . Above about  $0.7 \text{ l min}^{-1}$ , the electron density attains a steady value. The electron density is also more dependent on input power at the lower flowrates than at higher flowrates.

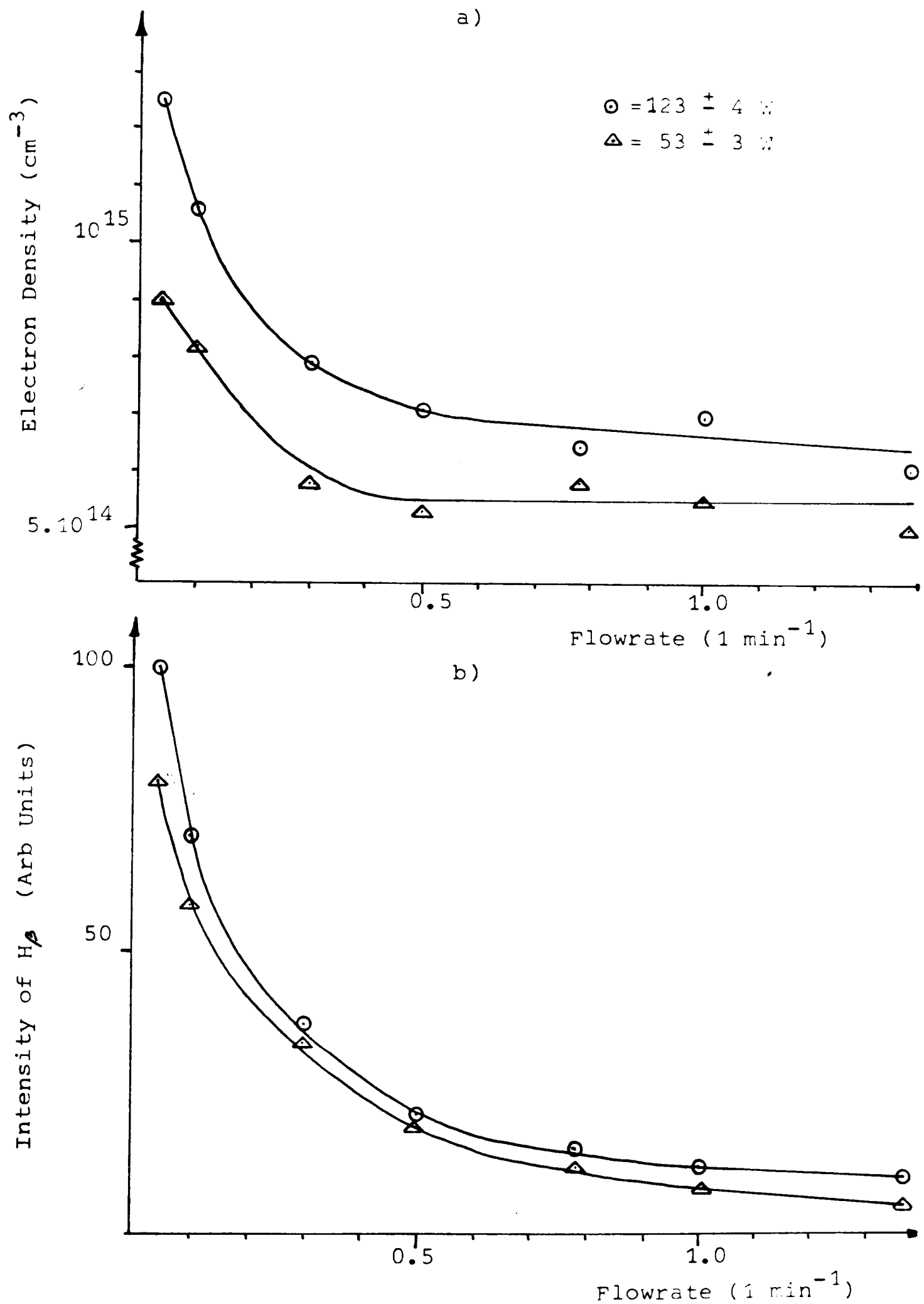


Figure 5.13

a) Electron Density and b)  $H_{\beta}$  Intensity as a Function of Flowrate in Dry Argon MIF Generated in Slab-line Cavity.



Increasing the flowrate from 0.04 to 1.37 l min<sup>-1</sup> also caused a factor of 10 decrease in the intensity of H $\beta$ , for both input powers (figure 5.13 b) again, mostly over the range 0.04 to 0.5 l min<sup>-1</sup>. A preliminary investigation of the dry argon MIP had indicated a similar decrease in the intensity of the  $^2\Sigma - ^2\Pi$  OH molecular spectra (section 5.3) for increasing flowrate. This is not surprising since the H and OH plasma species result from the disassociation of impurity water vapour in the argon, the rate at which the latter process occurs therefore most probably determines their spectral intensity.

Since the intensity of all argon spectral lines investigated increased as the flowrate was increased from 0.04 to 1.37 l min<sup>-1</sup> (section 5.1.1), this suggests an energy transfer between different processes within the MIP as the flowrate is altered.

Flowrate (l min <sup>-1</sup> )	Electron Density ( $\times 10^{14}$ cm <sup>-3</sup> )	
	Input Power = 53 W	Input Power = 123 W
0.04	9.0	12.5
0.5	5.3	7.1
1.37	5.0	6.0

Table 5.11    Dependence of Electron Density on Flowrate in the Dry Argon MIP.

C.

For argon flowrates of 0.1, 0.5 and 1.0 l min<sup>-1</sup>, the dependence of electron density on input power to the cavity was investigated at the viewing zone 10 mm below the end of the inner conductor.

The electron density, for each flowrate, is plotted as a function of input power in figure 5.14 which clearly shows the higher electron density at 0.1 l min<sup>-1</sup> compared to either of the higher flowrates. Electron density is similar at either 0.5 or 1.0 l min<sup>-1</sup> flowrates. This therefore confirms the result data presented in figure 5.13 a). As the input power was increased from 50 to 130 W, the electron density increased by 30 %, and the intensity of H $\beta$  by 10%, for all 3 flowrates.

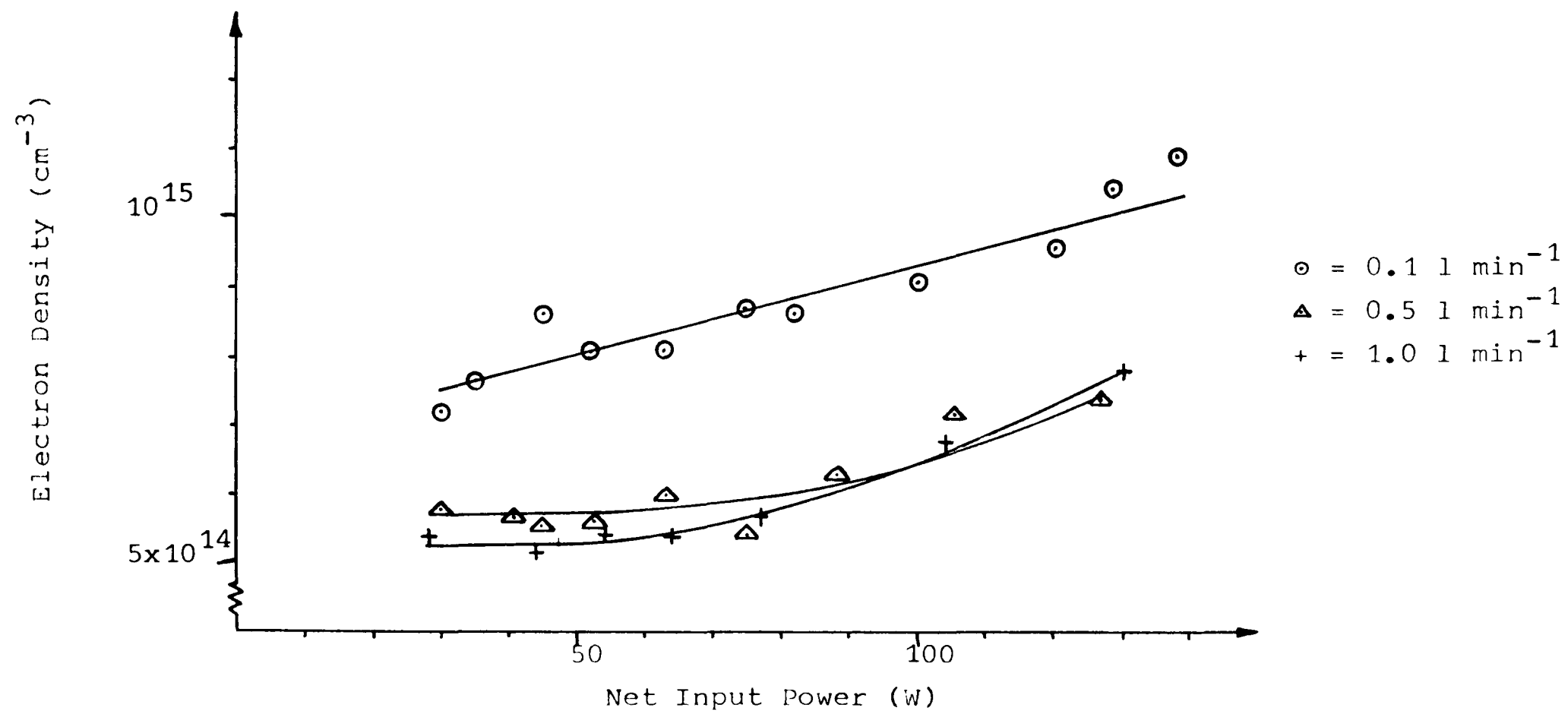


Figure 5.14      Electron Density as a Function of Microwave Input Power in the Dry Argon MIP Generated in the Slab-line Cavity.

D.

To ascertain what effect the tube dimensions might have on the plasma excitation conditions, the electron density was measured in a dry argon MIP contained in different size discharge tubes using a flowrate of  $0.1 \text{ l min}^{-1}$  and net input power of  $77 \pm 2 \text{ W}$ .

The dimensions of these tubes, and the value of electron density measured at the viewing position 10 mm below the end of the inner conductor are given in table 5.12. Figure 5.15 shows an enlarged view of the end of the inner conductor and the discs represent cross-sections through each tube size investigated.

The dry argon MIP generated in the slab-line cavity was contained in discharge tube 1. However, when the sample introduction system was added, it was necessary to change to discharge tube 4 for the reasons stated in section 6.3.2.

When the unloaded slab-line cavity is tuned (section 4.1) the electric field maxima is a distance equal to  $\lambda/4$  (30.6 mm) away from the end wall of the cavity. However, when the quartz discharge tube and MIP are introduced, the cavity is slightly detuned and the electric field maxima shifted from it's unloaded position.

The positions of the electric field maxima, marked on figure 5.15 for each discharge tube investigated, were calculated from the minima in the voltage standing wave on the slotted line (section 4.3). The position of the electric field maxima in the unloaded cavity is also shown.

With the exception of tube 2, the results show a positive correlation between the electron density and the proximity of the electric field maxima to the MIP. However, the peak of the maxima in the voltage standing wave on the transmission line are flat and wide, unlike the very narrow and steep voltage minima (section 4.3). The observed shifts in the position of the electric field maxima in the cavity for different discharge tubes are therefore unlikely to cause a significant change in the power incident on the MIP and hence presumably it's electron density. Furthermore, the electron density in the dry argon MIP is relatively insensitive to changes in the microwave power applied to the cavity.

Again with the exception of tube 2, the MIP's electron density decreases as the discharge tube ID is increased, e.g. switching from tube 1 to tube 4 caused a 60% reduction in the electron density measured in the dry argon MIP. This implies that when compensation is made for tube dimensions, the electron density in the analytical MIP (section 5.4.3) is actually even greater than that measured in the dry argon MIP by an additional factor of 1.6. The precise value of this factor should however, be regarded cautiously, since operational considerations for the analytical MIP dictated that changes were made to, e.g. the cavity orientation (section 3.1) and the inner conductor configuration (section 4.1).

The anomalous result for tube 2 may be due to a feature of this MIP which was different to the other MIP's. The sodium emission, seen previously in the region of the MIP opposite the end of the inner conductor, was particularly intense and extended into the viewing zone used by the optical system. Although this would not have directly affected measurement of  $H\beta$ , it may have signified a change in the plasma excitation conditions, since the sodium emission was previously always associated with a region of lower electron density. Quite why this should occur with this discharge tube is unclear and especially since no additional source of sodium was identified.

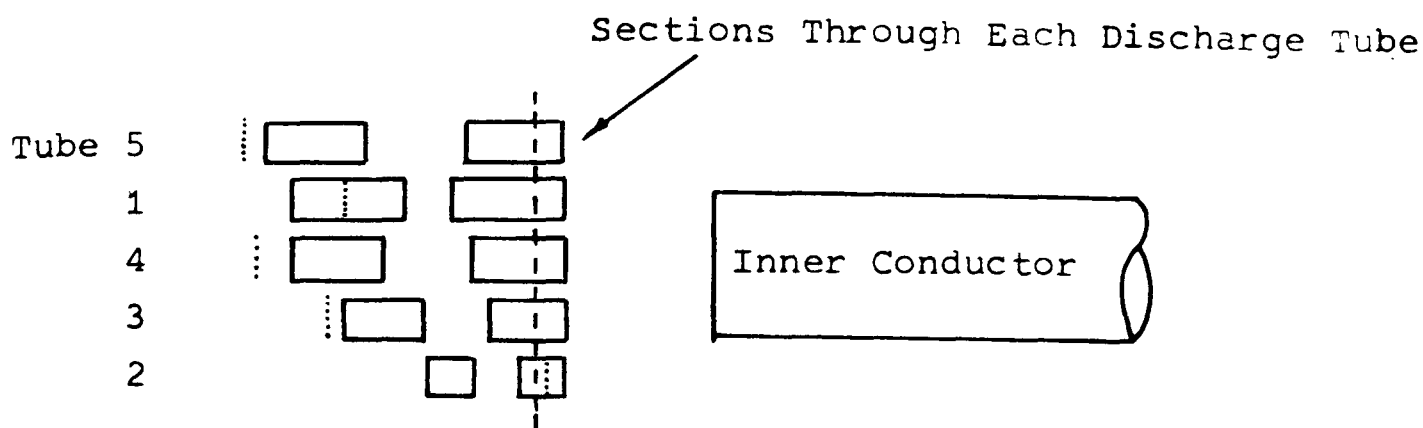
Slight corrosion of the discharge tube wall was also noticeable after only 1 hours operation, compared to the several hours normally experienced for the other discharge tubes.

Tube	ID (mm)	OD (mm)	WT (mm)	Electron Density ( $\times 10^{14} \text{ cm}^{-3}$ )
1	1.0	6.0	2.5	9.3
2	1.0	3.0	1.0	6.5
3	1.5	5.0	1.75	6.7
4	2.0	6.0	2.0	5.6
5	2.0	6.5	2.25	5.9

ID = Internal Diameter. OD = Outside Diameter.  
WT = Wall Thickness.

Tolerance on Electron Density =  $\pm 0.5 \times 10^{14} \text{ cm}^{-3}$

Table 5.12      Discharge Tube Sizes Used and Measured Electron Density.



Scale = 5 times actual size.

High Gain Inner Conductor Configuration (Gain = 18.5).

Coupling Gap = 3.4 mm.

The positions of electric field maxima, for each tube in the loaded slab-line cavity, are shown by a dotted line. The position of electric field maxima in the unloaded cavity is shown by a dashed line.

Figure 5.15      Enlarged View of the Slab-line Cavity Inner Conductor and Discharge Tubes.

E.

The electron density was measured at the viewing zone 17 mm below the end of the inner conductor before and after the cold trap (section 3.1) was activated. An argon flowrate of  $0.1 \text{ l min}^{-1}$  and net input power of  $75 \pm 2 \text{ W}$  was used.

Removal of the majority of the water vapour from the argon in this way caused a 40% reduction in the electron density. This, and the measurements in the analytical MIP (section 5.4.3 A), suggest that the water vapour loading of the MIP is highly influential in determining electron density.

### 5.4.3 Electron Density in the Analytical MIP.

A.

The electron density was determined concurrently with measurements on the argon spectra (section 5.1.2 A) for 3 viewing zones and sample uptake rates (SUR) in the MIP generated in the slab-line cavity. Comparing the results in table 5.13 with the results of the equivalent investigation in the dry argon MIP (section 5.4.2 A), the electron density is seen to be much higher in the analytical MIP. Despite some alteration to the operational conditions for the slab-line cavity, this increase in electron density is considered to be almost entirely due to the introduction of large amounts of water vapour via the nebulizer. The shape of the electron density 'profile', i.e. the variation of electron density along the length of the MIP, is however, very similar to that determined for the dry argon MIP.

Comparing the results in table 5.13 with table 5.4 in section 5.1.2 shows that regions of high electron density in the analytical MIP are associated with regions of high argon excitation temperature. Both of these parameters approach their respective minimum values in the region of the MIP used for optimum spectrochemical performance (section 6.5.1). Here, it should be noted, electron densities are comparable with those found in the dry argon MIP.

The electron density shows little or no dependence on the SUR used, which is somewhat surprising in view of the sensitivity of this parameter to introduced water vapour. It seems likely therefore, that the restrictive spray chamber employed (see figure 6.3, section 6.3.2) limited the amount of water vapour entering the MIP, irrespective of the SUR.

The electron density measured in the analytical MIP operated at a flowrate of  $1.0 \text{ l min}^{-1}$  using the Babington nebulizer was identical to that measured when the crossflow nebulizer was used. Removal of the auxiliary argon supply and stabilization at a flowrate of  $0.1 \text{ l min}^{-1}$  caused the

electron density at viewing zone 2 to reduce by 25% to  $27.0 \times 10^{14} \text{ cm}^{-3}$ . This is the opposite behaviour to that observed in the dry argon MIP (see section 5.4.2 B)

Viewing Zone (see figure 5.3)	Electron density ( $\times 10^{14} \text{ cm}^{-3}$ )		
	SUR = 0.5	SUR = 1.0	SUR = 1.5
1	42.0	42.0	49.0
2	38.0	38.0	37.0
3	23.0	20.0	23.0

Argon Flowrate =  $1.0 \text{ l min}^{-1}$  Net Input Power =  $65 \pm 3 \text{ W}$   
Sample Solution = blank SUR measured in  $\text{ml min}^{-1}$ .

Table 5.13     Dependence of Electron Density in the Analytical MIP on Viewing Zone and SUR in the Slab-line Cavity.

B.

Concurrently with measurements on the argon spectra (section 5.1.2 C), the electron density was determined when different sample solutions were aspirated into the MIP generated in the slab-line cavity. The results are shown in table 5.14 for the 2 argon flowrates used. This followed the introduction of a more suitable spray chamber and spectrochemical parameter optimisation (section 6.5). The tolerances on electron density are calculated from the results of several  $H_{\beta}$  line scans taken under identical operation conditions.

Solution		Electron Density ( $\times 10^{14} \text{ cm}^{-3}$ )	
Analyte	Matrix	Flowrate = 0.1	Flowrate= 1.0
Blank		9.0	14.5
5 $\mu\text{g ml}^{-1}$ Ca		9.3	
20 $\mu\text{g ml}^{-1}$ Ni		9.0	
10 $\mu\text{g ml}^{-1}$ Fe		9.3	19.0
	1 $\text{mg ml}^{-1}$ K	5.0	15.5
5 $\mu\text{g ml}^{-1}$ Ca	" "	5.0	
20 $\mu\text{g ml}^{-1}$ Ni	" "	7.2	
10 $\mu\text{g ml}^{-1}$ Fe	" "	6.5	20.5

Net Input  
Power =  $79 \pm 5 \text{ W}$  (Flowrate =  $1.0 \text{ l min}^{-1}$  all samples).  
=  $76 \pm 3 \text{ W}$  (Flowrate =  $0.1 \text{ l min}^{-1}$  all non K samples).  
=  $68 \pm 2 \text{ W}$  (Flowrate =  $0.1 \text{ l min}^{-1}$  all K samples).

Tolerance on electron density =  $\pm 0.3 \times 10^{14} \text{ cm}^{-3}$   
(Flowrate =  $0.1 \text{ l min}^{-1}$ ).

Tolerance on electron density =  $\pm 0.5 \times 10^{14} \text{ cm}^{-3}$   
(Flowrate =  $1.0 \text{ l min}^{-1}$ ).

Viewing Zone = 12.5 mm below top cavity plate.

Flowrate measured in  $\text{l min}^{-1}$ . SUR =  $0.75 \text{ ml min}^{-1}$ .

Table 5.14 Dependence of Electron Density on Sample  
Constituents in Analytical MIP generated  
in the Slab-line Cavity.

A higher electron density in the analytical MIP operated at a flowrate of  $1.0 \text{ l min}^{-1}$ , compared to a flowrate of  $0.1 \text{ l min}^{-1}$  is again observed. Since the same spray chamber was used at both flowrates, it can only be assumed that this is because more water vapour is carried into the MIP at the higher flowrate.



The addition of K to the samples caused dramatically different responses, depending on the flowrate used. Whereas in the MIP operated at  $1.0 \text{ l min}^{-1}$  flowrate, the addition of K caused a slight increase in electron density, it caused a large decrease in electron density in the MIP operated at  $0.1 \text{ l min}^{-1}$  flowrate. This decrease was accompanied by an increase in the reflected power from the cavity, which caused the change in net input power noted in table 5.14. It was not considered advisable to retune the double stub tuner to maintain constant input power.

An interesting correlation was found between this variation in electron density and the matrix factors (section 6.6.2).

In the MIP operated at a flowrate of  $0.1 \text{ l min}^{-1}$ , matrix factors were generally greater than 1, i.e. analyte signal enhancement. However, in the MIP operated at a flowrate of  $1.0 \text{ l min}^{-1}$ , matrix factors were generally less than 1, i.e. analyte signal depression.

Clearly the sensitivity of the MIP generated in the slab-line cavity to an interfering K matrix is linked to the electron density.

At both argon flowrates, the aspiration of Fe samples also caused an increase in the electron density, although in the MIP operated at a flowrate of  $0.1 \text{ l min}^{-1}$ , this was only in the presence of K. In the MIP operated at  $1.0 \text{ l min}^{-1}$ , the aspiration of  $10 \text{ } \mu\text{g ml}^{-1}$  Fe samples actually caused a much greater increase in electron density than did  $1 \text{ mg ml}^{-1}$  K.

The aspiration of Ni samples into the MIP operated at  $0.1 \text{ l min}^{-1}$  also caused an increase in electron density, although this again was only in the presence of K.

C. The electron density was determined in the MIP generated in the  $TM_{010}$  cavity, concurrently with measurements on the argon spectra (section 5.1.2 D) when different samples were aspirated.

The results in table 5.15 show comparable electron densities to the MIP generated in the slab-line cavity at a flowrate of  $1.0 \text{ l min}^{-1}$ . Much higher electron densities would have been expected due to the axial viewing of the main body of the plasma by the optical system. Failure to observe this is probably as a result of the corrosion of the discharge tube which progressively removed the MIP from the line of sight of the optical system (section 6.3.2).

The relatively poor precision of the electron densities determined for the MIP generated in the  $TM_{010}$  cavity, a result of plasma instability problems (section 3.1), mask any conclusive evidence for the electron density's sensitivity to particular sample constituents.

Solution		Electron Density ( $\times 10^{14} \text{ cm}^{-3}$ ).
Analyte	Matrix	
Blank		20
5 $\mu\text{g ml}^{-1}$ Ca		21
20 $\mu\text{g ml}^{-1}$ Ni		18
10 $\mu\text{g ml}^{-1}$ Fe		23
	1 $\text{mg ml}^{-1}$ K	23
5 $\mu\text{g ml}^{-1}$ Ca	" "	21
20 $\mu\text{g ml}^{-1}$ Ni	" "	26
10 $\mu\text{g ml}^{-1}$ Fe	" "	25

Net Input Power =  $92 \pm 5 \text{ W}$

Tolerance on electron density =  $\pm 2 \times 10^{14} \text{ cm}^{-3}$ .

Viewing Zone = Axial down length of discharge tube.

Argon Flowrate =  $1.0 \text{ l min}^{-1}$ . SUR =  $0.5 \text{ ml min}^{-1}$ .

Table 5.15      Dependence of Electron Density on Sample  
Constituents in the Analytical MIP generated  
in the  $TM_{010}$  Cavity.

6.1 Introduction

A sample introduction system was developed to enable a pneumatic nebulizer to be directly coupled to the MIP and its suitability for use in the spectrochemical analysis of solutions investigated for a number of elements.

Using a spray chamber similar to that used in a commercially available ICP source, two nebulizers were separately used to support argon MIP's generated in the slab-line cavity having gas flowrates of  $0.1 \text{ l min}^{-1}$  and  $1.0 \text{ l min}^{-1}$ . When the MIP was generated in the  $\text{TM}_{010}$  cavity at an argon flowrate of  $1.0 \text{ l min}^{-1}$  a different spray chamber with a side exit for the sample aerosol was used. These three sample introduction systems are discussed in greater detail in the following sections of this chapter.

Table 6.1 lists the elements for which the spectrochemical performance of the MIP was investigated. Elements were chosen with a range of first and second ionization potentials and where possible, ionic as well as atomic analyte spectral lines were observed. The spectrochemical performance of the MIP will be critically compared to the published results for:-

- a) similar MIP systems eg. Beenakker et al, 1978 (20) and Kawaguchi et al, 1972 (32)
- b) ICP systems eg. Boumans and De Boer, 1976 (33) and Kornblum et al, 1979 ( 7)
- c) CMP systems eg. Dahmen, 1981 (36)

Element	Spectrum	Wavelength (nm)	Ionisation I	Potential (eV) II	Atomic No.
Al	I	396.15	5.96	18.74	13
Ca	I	422.67	6.09	11.82	20
	II	393.37			
		396.85			
Co	I	345.35	7.81	17.3	27
Fe	I	371.99	7.83	16.16	26
		373.49			
		381.58			
Li	I	670.78	5.36	75.26	3
Mn	I	403.08	7.41	15.70	25
Ni	I	341.48	7.61	18.2	28
		352.45			
		361.94			
Pb	I	405.78	7.38	14.96	82
Sr	I	460.73	5.67	10.98	38
	II	407.77			

Table 6.1      Table of Elements Investigated in the MIP

## 6.2      Modification to the Detection System.

The detection system of the monochromator described in chapter 3 was slightly modified when the assessment of the spectrochemical performance of the MIP was made. The supplementary equipment used is listed in table 6.2

Item	Description	Make
AC Amplifier	'Lock in' type 1 $\mu$ V - 100 mV Sensitivity 1 Hz - 50 kHz Frequency Range	Brookdeal 401A
Signal Integrator	HP 97S Programmable Calculator with BCD Data Interface Adaptor.	Hewlett Packard
Light Chopper Disc	8 Blade, 240 V 50 Hz operation Chopping Frequency 400 Hz	

Table 6.2      Equipment Added to the Monochromator Detection System.

### 6.2.1 The Brookdeal AC Amplifier.

It is important when making either spectroscopic or spectrochemical measurements on the MIP that if, over a time interval of several minutes the input signal to the amplifier should remain constant then the output signal should also remain constant or drift by a negligible amount. The DC amplifier used when making the spectroscopic measurements on the MIP proved to be more than adequate in this respect as would be expected since modern integrated circuit OP-AMPS and ancillary components were used which possess excellent stability characteristics. However, due to the relatively long integration times used here it was decided to replace the DC amplifier with a Brookdeal 401A lock in AC amplifier and use a chopped light path between the MIP and the monochromator because this provides inherently low drift performance.

The signal input of the Brookdeal amplifier was connected in parallel to the anode load resistor of the PMT.

A resistor potential divider (ratio approx  $\div 5$ ) was connected to the output of the Brookdeal amplifier to match the latter's  $\pm 1$  volt maximum output signal to the  $\pm 200$  mV input range of the DPM. This potential divider was placed in the 'distribution box' (figure 3.11 section 3.6).

### 6.2.2      The Signal Integrator

The sample introduction system described in section 6.3 delivered sample aerosol to the plasma at an approximately steady rate governed by the argon flowrate and the sample flowrate to the nebulizer. There are however, small random fluctuations in the concentration of the aerosol entering the plasma which cause fluctuations in the spectral emission intensities of the analyte atoms observed by the optical system. To average out these fluctuations a signal integrator was constructed using a digital panel meter and HP 97S programmable calculator. This hardware was described in section 3.6.2, where it was configured, using the appropriate software, as a data logger. The main points of the signal integrator program are summarised below.

1) Data corresponding to the analyte or blank signals emitted by the atoms introduced into the MIP was entered into the calculator using an identical method to that described in section 3.6.2. Ten consecutive data entries in a period of approximately 13 seconds formed the standard integration period of the program. This rate of data entry corresponded to the maximum that could be practically achieved with the HP 97S.

2) The standard integration period was repeated 5 times, corresponding to the entry of 50 values of signal level and a mean signal reading with a standard deviation were then evaluated by the calculator.

3) The measurement process described in 2) was repeated 5 times, corresponding to the entry of 250 values of signal level in 25 consecutive 13 second integration periods, and a final mean signal level, with a standard deviation, SD was evaluated. These values were then used to calculate the spectrochemical parameters for the various elemental atoms (Section 6.4).

#### 6.2.3 The Light Path Chopper.

An eight bladed chopper disc was mounted directly in front of the monochromator entrance slit and driven via a flexible Bowden cable from a 240 V A.C synchronous motor. The 400 Hz chopper reference signal input to the Brookdeal was derived from an IR sensitive diode illuminated by a 12 V tungsten filament lamp through the arc of the chopper disc.



## 6.3      Sample Introduction Systems

### 6.3.1    The Nebulizer

#### (A)      The Crossflow Nebulizer

When operating the MIP with sample aerosol introduction at a total argon flowrate of  $1.0 \text{ l min}^{-1}$ , a nebulizer of the crossflow type, similar to that described by Kniseley et al, 1974 (19) was employed. This nebulizer, supplied by Pye Unicam, was a Hilger device originally designed to operate in atomic absorption flame spectrometers at gas (normally air) flowrates of  $5 \text{ l min}^{-1}$ . Using small bore stainless steel capillary tubing of the appropriate dimensions, it was sleeved down to operate on an argon flowrate of  $1.0 \text{ l min}^{-1}$ . Figure 6.1 illustrates this nebulizer in the form finally used with the MIP. The relative positions of the sample and gas capillaries were optimised, using various packing shims and the lateral adjustment screws, to achieve a fine aerosol spray from the nebulizer. For this procedure the aerosol was viewed against a dark background with the nebulizer spraying into an open space.

The original development work on this nebulizer, and other types originally tested, was carried out during an initial working period at the collaborating industrial establishment (Pye Unicam of Cambridge).

#### (B)      The Babington Nebulizer

When operating the MIP with sample aerosol introduction at a total argon flowrate of  $0.1 \text{ l min}^{-1}$ , a nebulizer constructed on the Babington principle was used (Babington 1973 (24)). This particular nebulizer was developed by Ripson et al, 1981 (28) during their work on the low flowrate ICP. Construction of such a nebulizer is fairly demanding since to achieve the desired gas flowrate of  $0.1 \text{ l min}^{-1}$  it is necessary to drill a  $100 \text{ }\mu\text{m}$  diameter hole in stainless steel over a length of 2mm.

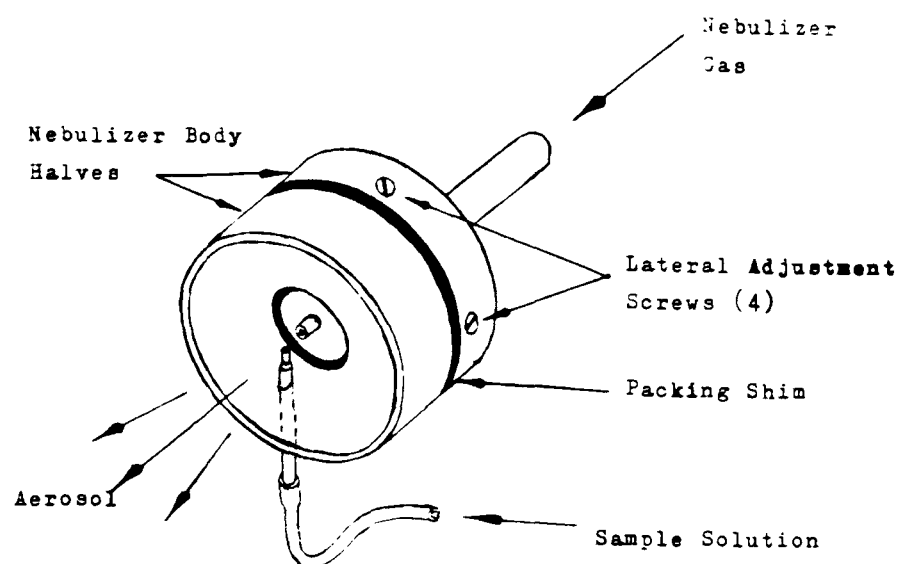


Figure 6.1 The Crossflow Nebulizer.

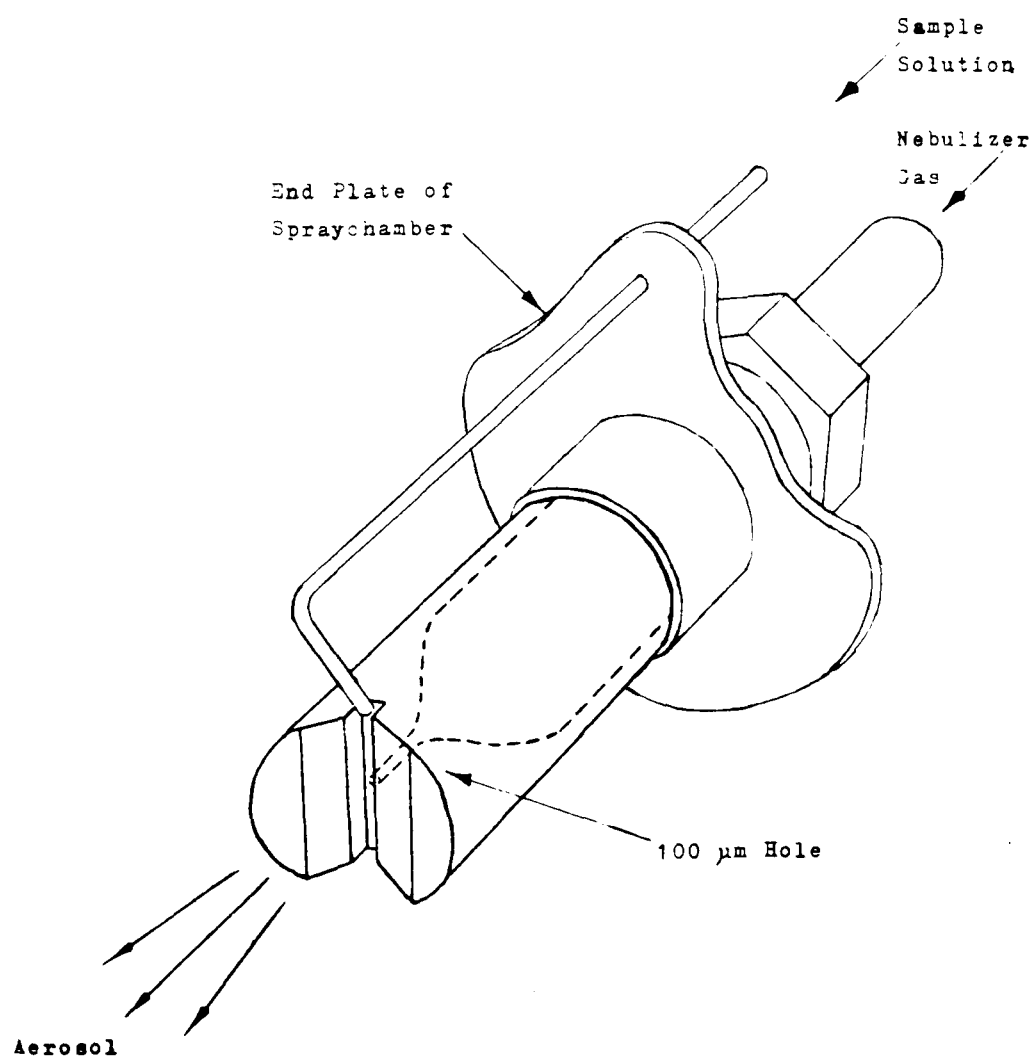


Figure 6.2 The Babington Nebulizer.

It was not possible to get a nebulizer manufactured to this specification by the engineering and manufacturing establishments who were approached. However, it was possible to borrow such a nebulizer from Professor de Galan of the Delft Technische Hogeschool, Netherlands for which sincere thanks are extended. Figure 6.2 illustrates the Delft Babington nebulizer with the sample introduction tube optimally positioned.

### 6.3.2      The Spray Chamber and Discharge Tube.

The intolerance of the atmospheric pressure argon MIP to the large amounts of water that can be introduced when using a pneumatic nebulizer has been reported by several authors, eg. Lichte and Skogerboe, 1973 (39). Beenakker et al, 1980 (10) found it necessary to use a restrictive spray chamber in order to remove most of the water droplets prior to entering the MIP. Fallgatter et al, 1971 (11) found that aerosol desolvation was required in order to achieve satisfactory results.

Since it was not intended to use any form of aerosol desolvation in this MIP, it soon became obvious that the design of spray chamber used was going to have a critical role in whether an atmospheric pressure argon MIP with direct sample aerosol introduction could be reliably maintained so that spectrochemical measurements could be made.

The design of spray chamber used first was strongly influenced by that described by Ripson and de Galan, 1981 (28) in their development of the low flowrate ICP. However this spray chamber proved to be unsuitable since it allowed too much aerosol to enter the MIP and, it was suspected, did not remove enough of the larger water droplets. This spray chamber was modified in stages by the inclusion of restrictive baffles until the aerosol entering the plasma was fine enough for the MIP to be reliably maintained at sample flowrates up to  $1.5 \text{ ml min}^{-1}$ . Figure 6.3 illustrates the side exit version of this spray chamber used when the analytical MIP was generated in the  $\text{TM}_{010}$  cavity.

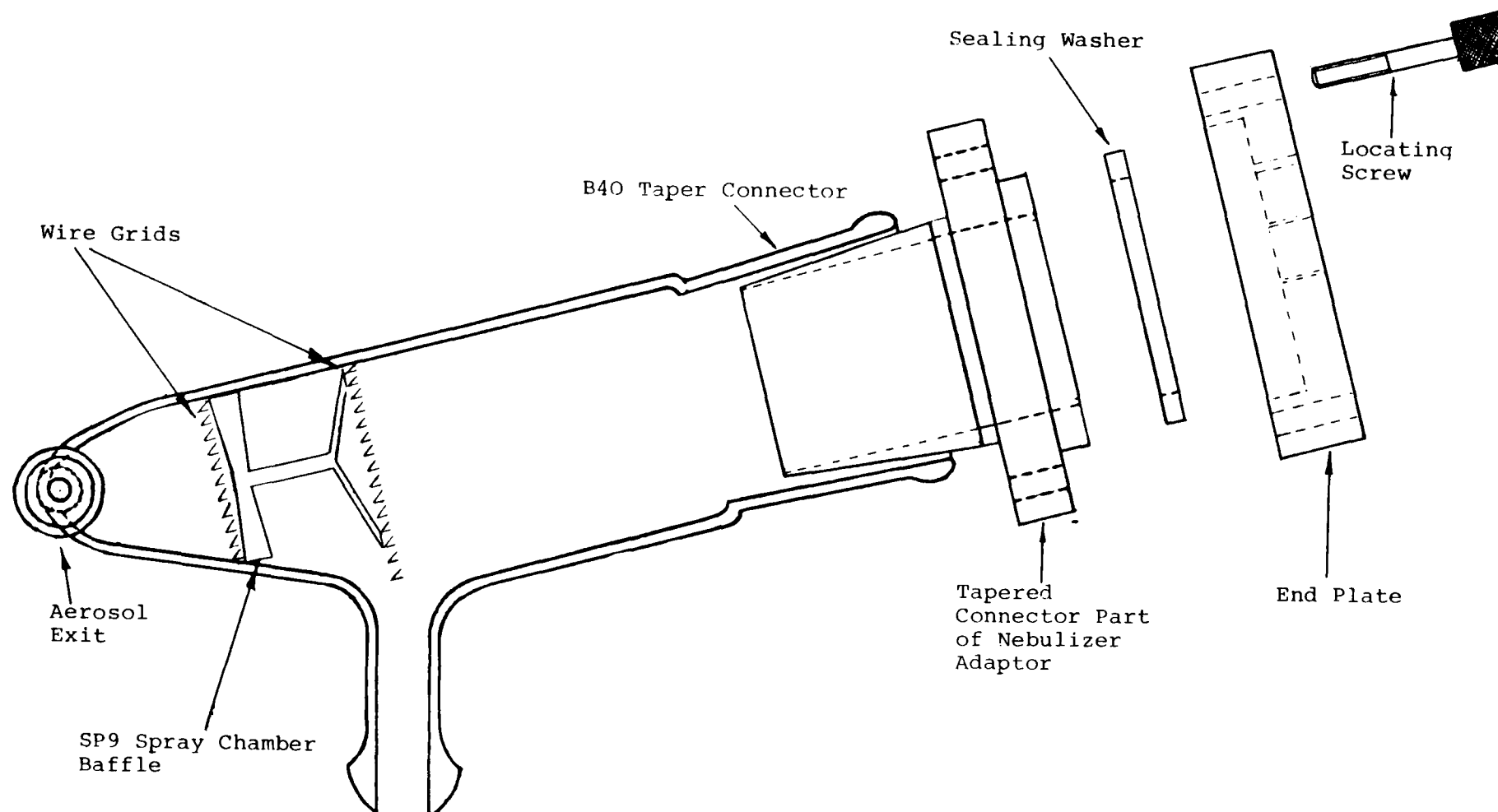


Figure 6.3 'Baffled' Spray Chamber with Side Exit for use with the TM<sub>100</sub> Cavity, showing the Nebulizer Mounting Adaptor. Scale=0.75, Material=Glass(spray chamber), Polypropylene(adaptor).

Although actual aerosol droplet size and distribution was not measured in this study, back illumination of the aerosol (through the glass walls of the spray chamber) using an ordinary tungsten filament lamp was found to be useful in assessing the effect of modifications to the internal baffles on the aerosol delivered to the MIP.

The use of such baffles did give rise to a noticeable though transient 'memory effect' when changing from one sample solution to another. eg.  $10 \mu\text{g ml}^{-1}$  Fe to deionized water. It could typically take 1 minute for all of the Fe to be flushed through the spray chamber such that its emission signal was no longer detectable by the optical system. Although this would have been no more than an inconvenience in this study it was appreciated that the use of such a spray chamber would hardly be practical in the typical analytical laboratory environment. Also, given the mineral acids and organic solvents commonly used in spectrochemical analysis, the baffles would have a very short lifetime. It was therefore decided to look for another, more suitable type of spray chamber.

The second type of spray chamber employed was a 0.8 scale version of a commercially available ICP source unit, the Philips PV8490, described by Boumans and Lux-Steiner, 1982 (37). This employs a spherical obstruction, or flow spoiler onto which the aerosol from the nebulizer impinges. The action of the flow spoiler is to further divide the large water droplets present in the aerosol. It is from the relatively calm region behind the flow spoiler (relative to the nebulizer) that the aerosol is transported to the plasma via a hole in the back of the flow spoiler itself.

When initially operating the MIP with this spray chamber, a phenomena was observed whereby the MIP would sporadically splutter and occasionally be extinguished. Investigations into the likely causes of this gave rise to the theory that large water droplets were being removed from the rear wall of the spray chamber by the action of

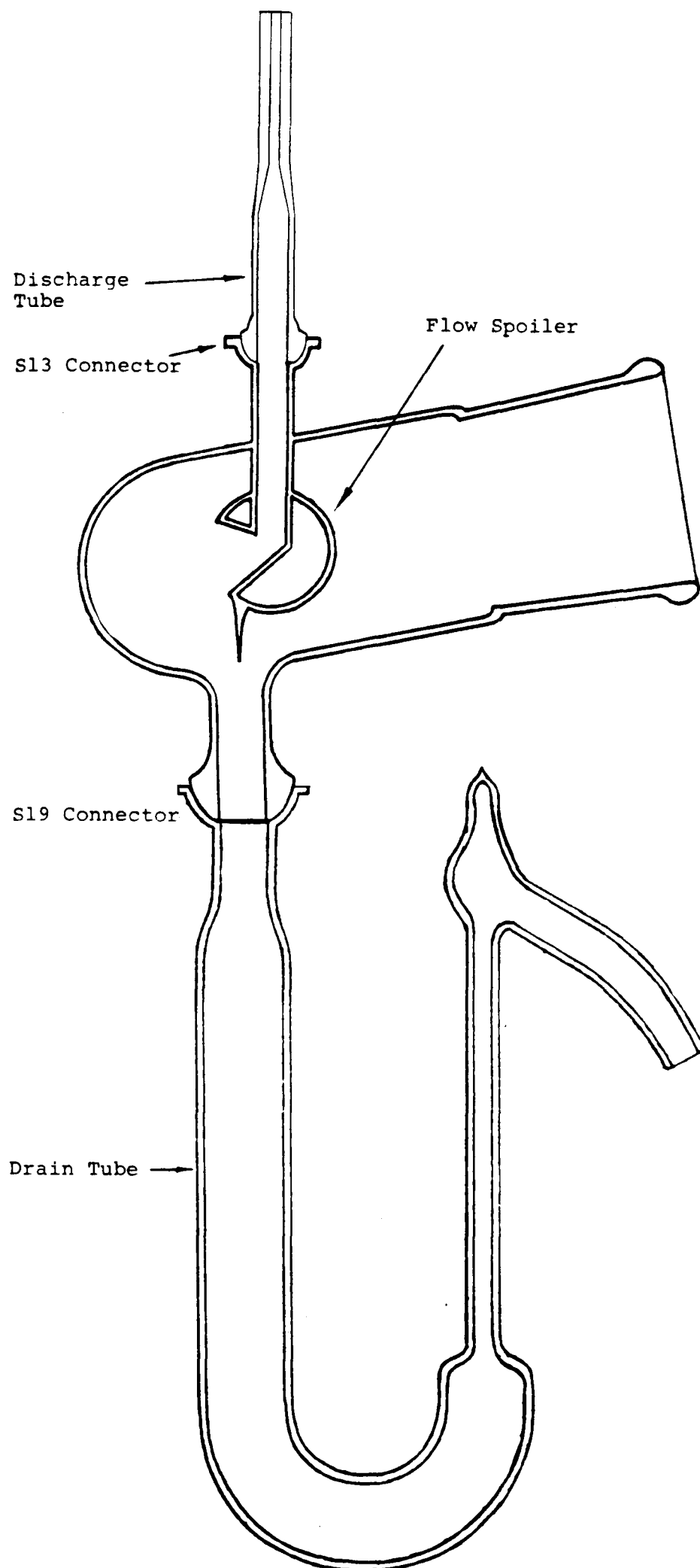


Figure 6.4 ICP type Spray Chamber, showing Discharge Tube and U-tube Drain. Scale=0.75, Material=Glass(spray chamber), Quartz(discharge tube).

the aerosol and these droplets were reaching the back of the flow spoiler and being carried up to the MIP. To test whether such a mechanism might be responsible for the erratic behaviour of the MIP, a second version of this spray chamber was constructed with the rear wall moved back by 10mm relative to the flow spoiler. When the MIP was operated with this spray chamber, the erratic behaviour previously observed had disappeared and this version, illustrated in figure 6.4, was used for all subsequent MIP's generated in the slab-line cavity.

Parts from the polypropylene spray chamber used in a Pye-Unicam SP9 atomic absorption spectro-photometer were modified in order to mount the nebulizers into either of the spray chambers shown in figures 6.3 and 6.4. Figure 6.3 shows the end plate suitable to carry the Babington nebulizer and the tapered adaptor to fit into the female B40 taper on the end of the spray chamber. A similar end plate was used to mount the crossflow nebulizer into the spray chamber.

All the sample introduction systems used an identical U tube drain, shown attached to a spray chamber in figure 6.4, to remove the excess sample solution. The unequal diameters of the tubes on either side of the bend assist in damping any oscillations of the drain fluid level following an inrush of fluid from the spray chamber.

The discharge tube used for both the MIP generated in the slab-line and  $TM_{010}$  cavities is shown attached to a spray chamber in figure 6.4. An internal diameter (ID) of 2mm was used so as to maximise plasma stability and tolerance to introduced water vapour, which was found to be worse in smaller ID tubes. The overall length of the discharge tube was kept as short as was practically possible to prevent condensation of the sample aerosol on the walls of the tube before reaching the MIP. Also a smooth transition from the quartz S13 ball joint to the quartz discharge tube was preferable to ensure laminar flow of the aerosol and argon as it entered the plasma region.



The lifetime of a discharge tube was determined by the extent of corrosion where the MIP was attached to the tube wall. A tube became unserviceable when the corrosion had eaten almost completely through the wall, after which it was difficult to ignite or maintain the MIP. Since only limited stocks of 6.5 mm outside diameter (OD) tube were available (wall thickness = 2.25 mm), it was necessary to use 6.0 mm OD tube giving a wall thickness of 2.0 mm. In normal operation these discharge tubes would last approximately 100 hrs.

When the MIP was operated in the slab-line cavity the plasma formed was always attached to the rear wall of the discharge tube which is therefore where the corrosion took place. Thus there was no obstruction of the light from the plasma reaching the optical system via the front wall of the discharge tube. Only when a discharge tube was nearing the end of its life did the corrosion start to extend around the front walls.

When the MIP was operated in the  $TM_{010}$  cavity, light from the plasma was always viewed axially and so corrosion in this respect again was not a problem. However, the plasma did tend to disappear from the line of sight of the optical system as it ate into the discharge tube wall and this necessitated renewal of the discharge tube after approximately 10 hrs.

Sample introduction systems of this type, commonly employed in the ICP normally exhibit poor efficiencies of sample delivery to the plasma, usually less than 5% and the systems used here were not exceptions to this norm.

The average efficiency for all 3 systems was approximately 3%, determined by measuring the volume of waste solutions drained from the spray chamber over a fixed interval of time for a known delivery rate to the nebulizer. This is NOT an accurate method and gives only an approximate figure for efficiency. More accurate methods have been described recently by Smith and Browner, 1982(109). Collection of the drain solution would commence only after the inside walls of the spray chamber were uniformly wetted by the aerosol and a stable MIP had been maintained for approximately one hour, thus the sample introduction system was stabilized from nebulizer to drain.

Sample solutions were delivered to both the crossflow and Babington Nebulizers using an LKB Microperpex 2132 peristaltic pump. Forced feeding of sample solutions to the crossflow nebulizer is desirable to achieve a constant sample flowrate but is actually essential with the Babington nebulizer, which does not produce a sample uptake vacuum of its own.

The Microperpex peristaltic pump was chosen in preference to pumps from other manufacturers because it was felt that its multiple roller pump head would give the smoothest delivery of sample solution to the nebulizer. However, in practice it produced very small pulsations in the fluid flow which were clearly visible as pulsations in the aerosol produced by the nebulizer. This had a slight but noticeable affect on the standard deviation of the analyte and blank signals recorded by the optical measuring system. In order to eliminate these aerosol pulsations a pulse damper was introduced into the sample line between the pump and the nebulizer. The pulse damper (figure 6.5) consisted of a T-piece and a 1 ml disposable medical syringe. The trapped volume of air in the syringe absorbed the energy of the pulsations and ensured a smooth flow of solution to the nebulizer. Because of the imperfect air tightness of the damper the sample solution did slowly creep up the tube connecting the syringe to the T-piece, albeit over a long period of time. This solution was conveniently expelled by a slight movement of the syringe plunger to eliminate any possibility of contamination of the sample being aspirated with that previously used. Since the pulse damper was in parallel with the sample delivery tube it did not increase its' dead volume. Therefore the time taken for a sample solution to replace the previous solution in the tube was unaffected by the presence of the damper.

1 mg ml<sup>-1</sup> standard solutions as used in atomic absorption spectrophotometry (AAS) were diluted in deionized water to produce the desired sample concentrations. These were approximately 10 to 100 times the expected detection limits defined in section 6.4. To investigate the effect of an interfering matrix on the detection limit for all the elements tested sample solutions containing 1 mg ml<sup>-1</sup> K (KCl) were delivered to the nebulizer. These solutions were prepared by dissolving the appropriate quantity of the solute in deionized water.

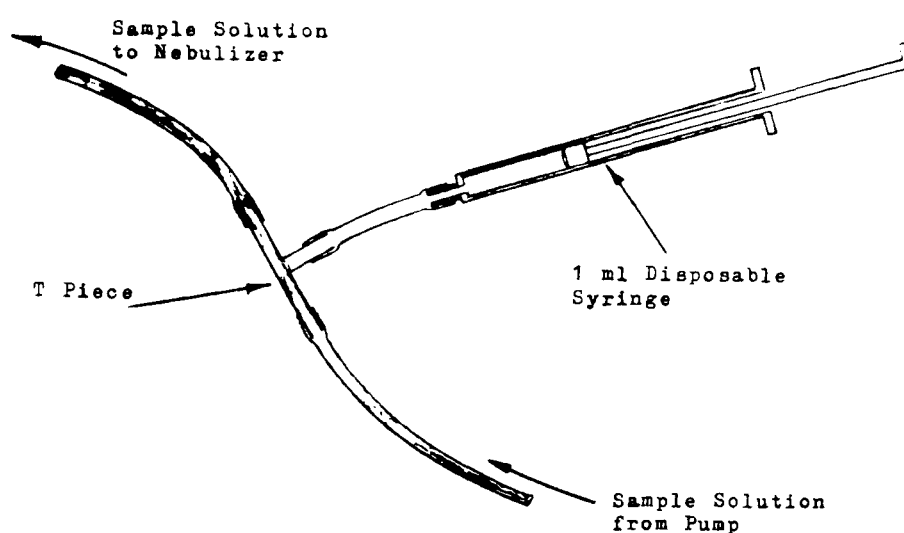


Figure 6.5     The Pulse Damper

#### 6.4      Definition of Spectrochemical Parameters.

The detection limit for the elements investigated in the MIP is defined as the concentration of that element that would produce a net line signal equal to twice the relative standard deviation,  $\sigma_B$  of the background signal as described by Boumans and de Boer, 1972 (12), 1975 (29).  $\sigma_B$  was evaluated from 25 consecutive, 13 second integrations of the background signal,  $X_B$  (section 6.2.2), when the monochromator was set to the wavelength of the analyte line and an  $H_2O$  blank solution was aspirated into the MIP.

The net analyte signal,  $X_L$  was measured when the sample element of given concentration,  $C$  was aspirated into the MIP and evaluated from the expression

$$X_L = X_{L+B} - X_B$$

where  $X_{L+B}$  is the analyte plus background signal (see figure 6.6). The signal to background ratio (SBR) was then evaluated from

$$SBR = X_L / X_B$$

The detection limit,  $C_L$  for the element was then calculated using the definition above from

$$C_L = 2 \cdot \sigma_B \frac{C}{SBR}$$

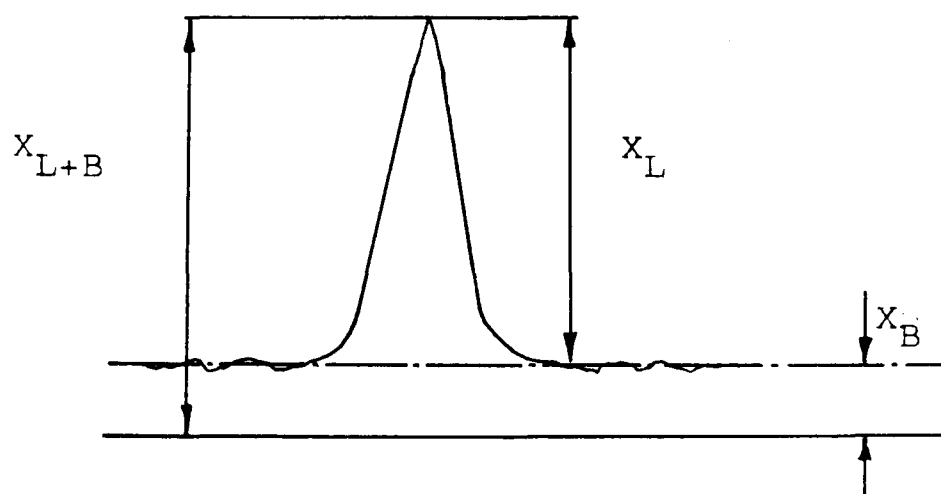


Figure 6.6.      Analyte, Background and Net Line Signals.

Measured values of  $\sigma_B$  were closely scattered around a value of 0.006 for the two MIP's generated in the slab-line cavity, suggesting that these systems were fluctuation noise limited. However, the individually evaluated values of  $\sigma_B$  for each spectral line of the elements investigated were used in calculating  $C_L$ . Measured  $\sigma_B$  values in the MIP generated in the  $TM_{010}$  cavity were scattered around a value of 0.01 with a much larger maximum range than for the MIP's generated in the slab-line cavity. This is most probably due to the less stable nature of the MIP generated in the  $TM_{010}$  cavity as discussed in section 6.7.

The behaviour of the MIP when an interfering matrix chemical of concentration  $C_M$  is added to the analyte sample solution under investigation, is expressed in the matrix factor,  $X(C_M, 0)$  defined as the ratio of net analyte signals measured when a sample plus interfering matrix compared to the sample alone are aspirated into the MIP.

The net analyte signal when the interfering matrix is added to the sample solution is measured relative to a background signal,  $X_B$  measured when an interfering matrix 'blank' is aspirated, NOT the background signal measured when an  $H_2O$  blank is aspirated into the MIP. This ensures that the results are compensated for any movement in the plasma position, resulting from the slight degradation in plasma stability caused by aspiration of the interfering matrix as observed in the MIP generated in the slab-line cavity (section 6.6.2).

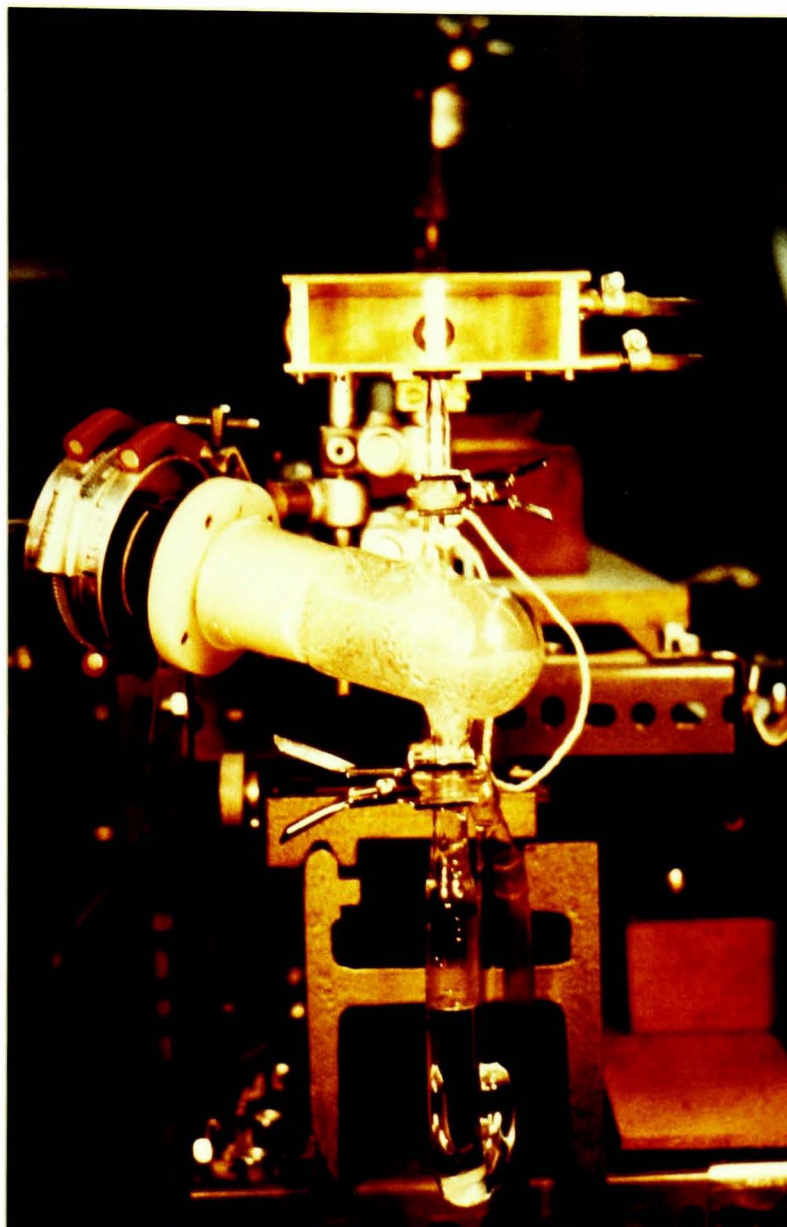


Figure 6.7     Plate of Analytical Argon MIP Generated  
in Slab-line Cavity.

## 6.5 Optimization of Plasma Operational Parameters.

It was found, during operation of the atmospheric pressure argon MIP, in either the slab-line or the  $TM_{010}$  cavity, that maintenance of the plasma was improved for higher net input microwave power. Therefore in order to reduce the number of occasions when the MIP was extinguished due to, eg. aspiration of the matrix solution into the MIP, the output power from the EMS Microtron power generator was set to maximum for all measurements of the spectrochemical parameters reported in section 6.6 and 6.7. As noted in section 4.2 this does not mean that the true input power applied to the slab-line cavity is identical to that applied to the  $TM_{010}$ . The reflected power from the cavities was always reduced to a minimum using the double stub tuner, commensurate with reliable operation and the net input power calculated from the readings on the TFT power heads and meters.

### 6.5.1 Optimization of the Viewing Position.

With either of the sample introduction systems connected to the MIP generated in the slab-line cavity, the plasma so formed occupies only the top half of the discharge tube, above the end of the inner conductor (figure 6.7) and is not of uniform consistency along its entire length. The maximum luminosity occurs in the centre of plasma with more transparent regions at either end. A study was therefore made to ascertain the dependence of the analyte and background emission intensities on position in the plasma and hence to determine the optimum viewing zone for the spectrochemical analysis of solutions.

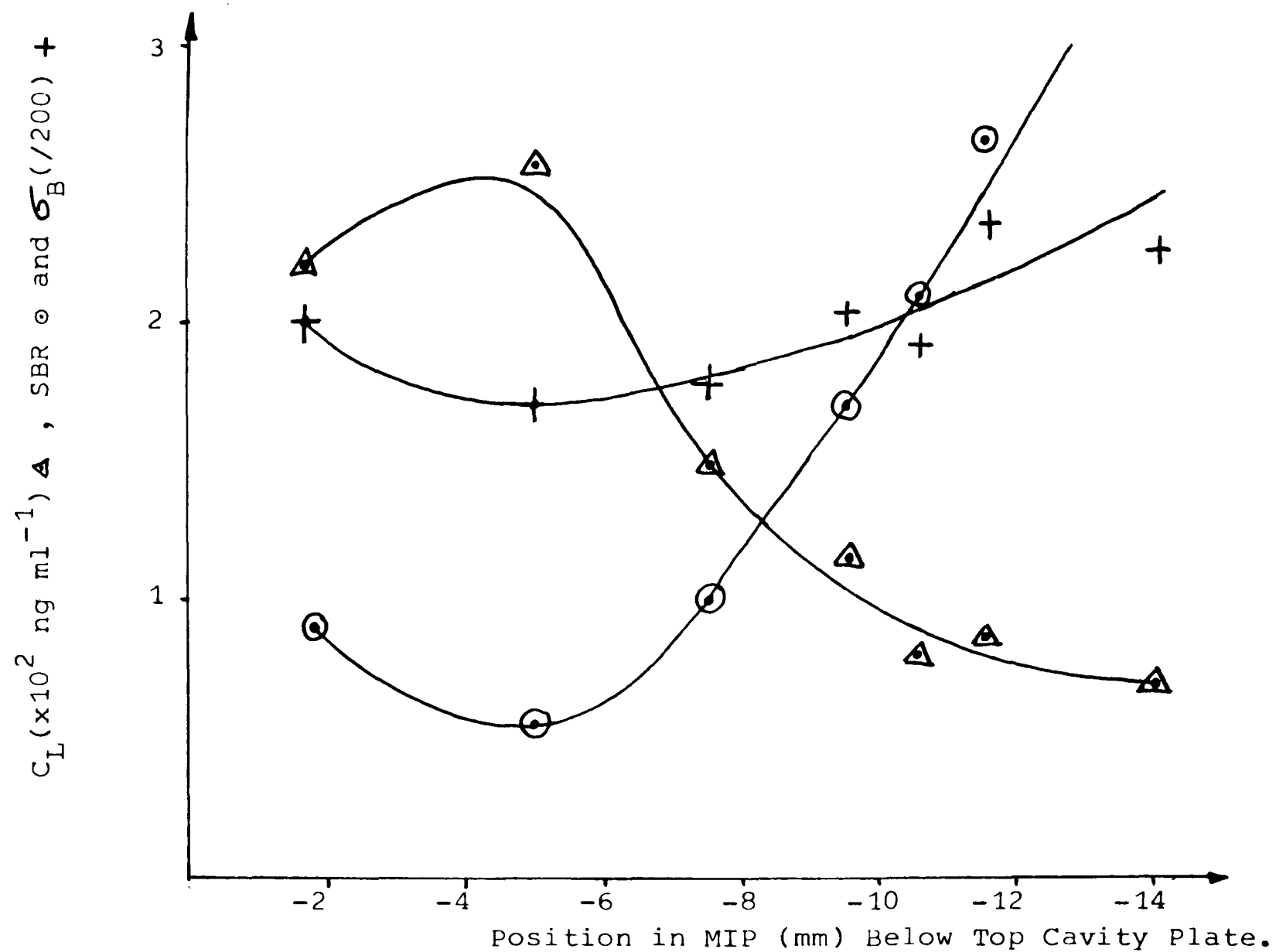


Figure 6.8 Graph of SBR,  $\sigma_B$  and  $C_L$  as a Function of Position in MIP  
Generated in Slab-line Cavity.  $10 \mu\text{g ml}^{-1}$  Sample Solution



The position of the cavity was adjusted relative to the optical axis of the monochromator so that different sections of the MIP could be imaged on the entrance slit. With the monochromator set to the Mn analyte wavelength of 403.08 nm, a  $10 \mu\text{g ml}^{-1}$  solution of manganese was aspirated into the MIP and the values of  $\sigma_B$ , SBR and  $C_L$  determined for each viewing zone.

A typical result, for either the  $1.0 \text{ l min}^{-1}$  or the  $0.1 \text{ l min}^{-1}$  MIP which exhibited similar behaviour is shown in figure 6.8. As can be clearly seen the values of  $\sigma_B$  and SBR observed yield an optimum viewing zone in the MIP, ie. where the minimum value of  $C_L$  is achieved of between -10 to -13 mm measured relative to the inner face of the top cavity plate. The higher SBR in the optimum viewing zone is due mainly to the very much lower background emission rather than any great increase in analyte emission. The lower background intensity, which is the result of the very much lower luminosity in this part of the plasma, is also the reason why  $\sigma_B$  is increased here rather than any decrease in plasma stability. All subsequent spectrochemical measurements on the MIP generated in the slab-line cavity were made at a viewing position of approximately -12.5 mm.

Being able to view the MIP generated in the slab-line cavity radially, away from its most luminous core offers a significant advantage over the  $\text{TM}_{010}$  cavity where, constrained to view the MIP axially in the discharge tube, analyte emission is always seen against the background signal generated by the most luminous core of the plasma. This is believed to be the main reason for the poorer SBR values observed in the MIP generated in the  $\text{TM}_{010}$  cavity compared to that generated in the slab-line cavity.

### 6.5.2 Optimization of the Sample Flowrate.

At the optimum viewing zone of the MIP generated in the slab-line cavity, a  $10 \mu\text{g ml}^{-1}$  Mn solution was aspirated at sample uptake rates (SUR) to the nebulizer of from  $0.25$  to  $1.5 \text{ ml min}^{-1}$  in steps of  $0.25 \text{ ml min}^{-1}$  and the values of  $\sigma_B$ , SBR and  $C_L$  measured. It was found for both the  $1.0 \text{ l min}^{-1}$  and the  $0.1 \text{ l min}^{-1}$  MIP's that as the SUR increased the SBR reached a maximum plateau value at  $0.5 \text{ ml min}^{-1}$  and no further increase was obtained for higher SUR's. Also as the SUR was increased above  $0.75 \text{ ml min}^{-1}$ ,  $\sigma_B$  started to increase. Consequently the minimum value of  $C_L$  observed occurred at an SUR of between  $0.5$  and  $0.75 \text{ ml min}^{-1}$ . A typical graphical representation of this phenomena for the  $1.0 \text{ l min}^{-1}$  MIP is illustrated in figure 6.9. All subsequent measurements on the MIP generated in the slab-line cavity were made with a SUR of  $0.75 \text{ ml min}^{-1}$ .

The optimization of the SUR described above was carried out using the ICP type of spray chamber which, as noted in section 6.3.2 was the second and preferred type to be used. A similar optimization procedure was also carried out for the initial, baffled spray chamber (with the  $1.0 \text{ l min}^{-1}$  MIP generated in the slab-line cavity) and a similar dependence of  $\sigma_B$ , SBR and  $C_L$  on the SUR was observed. It was therefore deduced that despite the differences between the two types of spray chamber, the throughput of sample aerosol to the MIP was similar. Since the MIP generated in the  $\text{TM}_{010}$  cavity used a side exit version of this initial, baffled type of spray chamber it is with confidence that comparisons may be made between the spectrochemical results obtained using the two cavities.

Optimization of the SUR when the MIP was generated in the  $\text{TM}_{010}$  cavity was a somewhat limited procedure since this MIP was not nearly so tolerant to introduced sample aerosol as that generated in the slab-line cavity. SUR's much above  $0.5 \text{ ml min}^{-1}$  appeared to be sufficient to quench the discharge and regularly extinguished it. It was therefore decided to operate at an SUR of  $0.5 \text{ ml min}^{-1}$  in order to enable the best comparison of the spectrochemical results between the two cavities used.

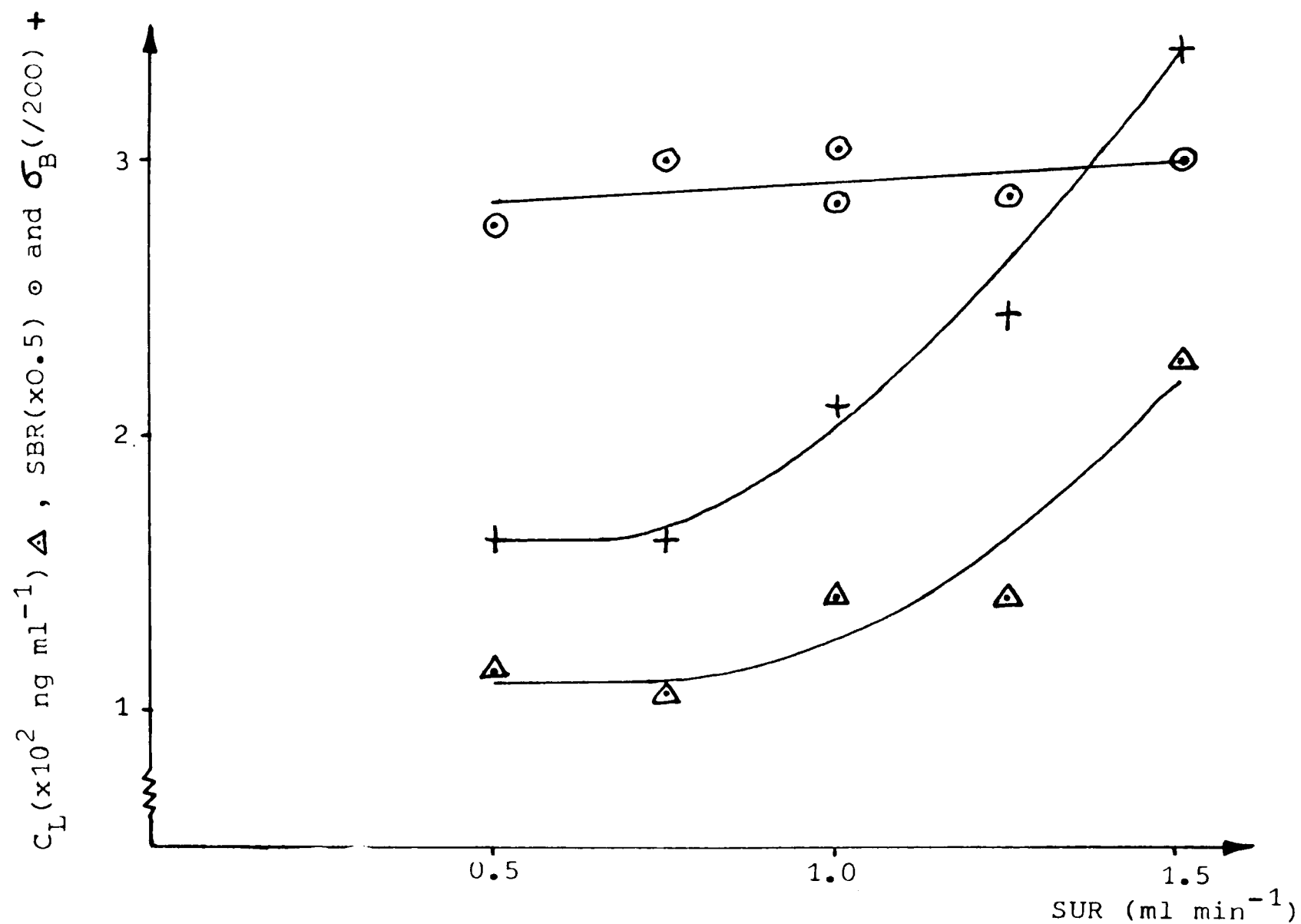


Figure 6.9

Graph of  $SBR$ ,  $\sigma_B$  and  $C_L$  as a Function of  $SUR$  in the MIP

Generated in the Slab-line Cavity.  $10 \mu\text{g ml}^{-1}$  Sample Solution.

## 6.6 Spectrochemical Results for the MIP Generated in the Slab-line Cavity.

### 6.6.1 Detection Limits.

As can be seen from Tables 6.3 and 6.4, the detection limits ( $C_L$ ) obtained for the elements investigated are similar in the MIP's operated at either 0.1 or 1.0 l min<sup>-1</sup> flowrates, with the exception of certain Ca, Mn, Ni and Pb spectral lines. These gave significantly better detection limits in the MIP operated at 0.1 l min<sup>-1</sup>. Here "significantly better" is used to describe a factor of 2 or more difference between  $C_L$  values observed in the two MIP's.

Where differences in  $C_L$  values were found between the two MIP's, they were due almost exclusively to an improved signal to background ratio (SBR) of the analyte emission. In the case of the Li spectral line studied, however the relative standard deviation of the background signal ( $\sigma_B$ ) was also degraded in the MIP operated at 0.1 l min<sup>-1</sup> and the reason for this will be discussed later. Otherwise the  $\sigma_B$  values observed were similar for all the spectral lines of the elements investigated in both MIP's and a reliable mean value of  $\sigma_B$  equal to 0.006 was evaluated.

The detection limit that can be achieved for any particular element is sensitive to the particular region of the MIP viewed by the optical measurement system (section 6.5.1). Slight re-optimization of the viewing zone was therefore necessary when changing between MIP's operated at the different argon flowrates.

Element/ Spectrum	Wave- length (nm)	$\sigma_B$	SBR	$C_L$ (ng ml <sup>-1</sup> )	$M(1000,0)$
Al I	396.15	0.0055	1.11	980 $\pm$ 80	0.8 $\pm$ 0.1
Ca I	422.67	0.0086	19.79	4.3 $\pm$ 0.2	0.5 $\pm$ 0.03
Ca II	393.37	0.0055	8.02	6.8 $\pm$ 0.2	1.2 $\pm$ 0.05
" "	396.85	0.0105	4.16	25.3 $\pm$ 1.5	1.0 $\pm$ 0.05
Co I	345.35	0.0054	1.17	92.9 $\pm$ 1.5	1.4 $\pm$ 0.04
Fe I	371.99	0.0054	0.47	234 $\pm$ 15	1.3 $\pm$ 0.14
" "	373.49	0.0067	0.54	248 $\pm$ 15	1.3 $\pm$ 0.13
" "	381.58	0.0063	0.14	878 $\pm$ 110	1.2 $\pm$ 0.4
Li I	670.78	0.0145	12.19	2.4 $\pm$ 0.3	
Mn I	403.08	0.0044	2.44	36 $\pm$ 2	1.6 $\pm$ 0.04
Ni I	341.48	0.0054	2.66	81 $\pm$ 2	1.2 $\pm$ 0.03
" "	352.45	0.0039	1.97	79 $\pm$ 1	1.2 $\pm$ 0.03
" "	361.94	0.0043	1.49	115 $\pm$ 2	
Pb I	405.78	0.0035	0.82	87 $\pm$ 2	1.2 $\pm$ 0.05
Sr I	460.73	0.0073	5.64	13 $\pm$ 2	1.2 $\pm$ 0.03
" II	407.77	0.0072	3.69	19 $\pm$ 1	2.2 $\pm$ 0.05

Net Input Power = 78  $\pm$  9 W (70  $\pm$  8 W when K added)

Viewing Zone = 12.5 mm below top cavity plate.

SUR = 0.75 ml min<sup>-1</sup>

Table 6.3      Spectrochemical Results for the 0.1 l min<sup>-1</sup>  
MIP Generated in the Slab-line Cavity.

Element/ Spectrum	Wave- length (nm)	$\sigma_B$	SBR	$C_L$ (ng ml <sup>-1</sup> )	$\bar{x}(1000.0)$
Al I	396.15	0.0043	0.86	997 $\pm$ 18	0.7 $\pm$ 0.04
Ca I	422.67	0.0076	7.79	9.7 $\pm$ 0.2	0.5 $\pm$ 0.02
" II	393.37	0.0061	7.25	8.5 $\pm$ 0.3	0.8 $\pm$ 0.04
" "	396.85	0.0081	3.76	21.5 $\pm$ 0.5	0.7 $\pm$ 0.05
Fe I	371.99	0.0050	0.40	247 $\pm$ 14	0.6 $\pm$ 0.08
" "	373.49	0.0053	0.45	238 $\pm$ 13	0.7 $\pm$ 0.09
" "	381.58	0.0056	0.17	677 $\pm$ 67	0.6 $\pm$ 0.2
Li I	670.78	0.0054	18.27	0.6 $\pm$ 0.07	1.2 $\pm$ 0.1
Mn I	403.08	0.0055	1.19	92 $\pm$ 3	0.6 $\pm$ 0.04
Ni I	341.48	0.0054	2.31	94 $\pm$ 2	0.6 $\pm$ 0.06
Ni I	352.45	0.0051	1.73	118 $\pm$ 3	0.6 $\pm$ 0.05
" "	361.94	0.0048	0.77	251 $\pm$ 8	0.7 $\pm$ 0.05
Pb I	405.78	0.0067	0.55	244 $\pm$ 12	0.7 $\pm$ 0.09
Sr I	460.73	0.0050	2.68	18.5 $\pm$ 0.8	0.5 $\pm$ 0.05
" II	407.77	0.0062	3.32	18.8 $\pm$ 0.5	0.7 $\pm$ 0.04

Net Input Power = 85  $\pm$  3 W

Viewing Zone = 12.5 mm below top cavity plate

SUR = 0.75 ml min<sup>-1</sup>

Table 6.4    Spectrochemical Results for the 1.0 l min<sup>-1</sup>  
MIP Generated in the Slab-line Cavity.

Since the results show generally higher SBR values for spectral lines investigated in the MIP operated at  $0.1 \text{ l min}^{-1}$  flowrate it might be considered that the viewing zone was slightly more optimally set than for the MIP operated at  $1.0 \text{ l min}^{-1}$  argon flowrate.

This possibility could not however, be responsible for causing the larger SBR values observed for the 4 spectral lines of Ca, Mn, Ni and Pb which yielded better  $C_L$  values in the MIP operated at  $0.1 \text{ l min}^{-1}$  argon flowrate. This may be proven by consideration of the 3 Ni spectral lines investigated where only 2 of the 3 lines showed a significantly different SBR between the 2 MIP's. Since for each MIP, measurements were made concurrently using the same analyte solution, the greater SBR for the 361.94 nm Ni line obtained in the MIP operated at  $0.1 \text{ l min}^{-1}$  argon flowrate may be seen to be due to the properties of the plasma itself. A similar example could be made of the 3 Ca spectral lines where only the Ca I line at 422.67 nm showed a significantly higher SBR in the MIP operated at  $0.1 \text{ l min}^{-1}$  whereas the Ca II lines showed similar SBR values in both MIP's.

The only element for which the MIP operated at  $1.0 \text{ l min}^{-1}$  argon flowrate gave a significantly better detection limit was Li, but the reasons for this may be explained in terms of operational considerations. The addition of lithium, in the form LiCl, to both MIP's caused a slight reduction in plasma stability, in a similar manner to when KCl was added to the analyte solutions (section 6.6.2). This is perhaps not unreasonable since both are alkali-metal salts, although the concentration of lithium,  $1 \mu\text{g ml}^{-1}$  was considerably less than the  $1 \text{ mg ml}^{-1}$  of K used. This reduction in plasma stability was more noticeable in the MIP operated at  $0.1 \text{ l min}^{-1}$  flowrate and is reflected in the poor  $\sigma_B$  value for this element. The lower SBR value observed for Li in the MIP operated at  $0.1 \text{ l min}^{-1}$  argon flowrate was found to be caused by a raised background signal due to lithium contamination of

the discharge tube wall. This contamination, which was permanent and prevented the determination of the Li matrix factor, was not experienced in the MIP operated at  $1.0 \text{ l min}^{-1}$  argon flowrate.

#### 6.6.2 Matrix Factors

Ideally, an atomic emission source to be used for the spectroscopic analysis of solution should be unaffected by the presence of large concentrations of an interfering matrix, since in a great number of practical analyses the element of interest is dissolved in some type of matrix. Thus the analyte signal measured would be the same when either the sample solution alone or the sample plus matrix solution were aspirated and matrix factors, would equal 1 (Section 6.4). Although it is unlikely that any emission source exactly meets this requirement the degree to which it is met provides a useful criteria by which to judge that emission source.

The matrix factors given in table 6.3 and 6.4 demonstrate that the MIP generated in the slab-line cavity approaches this requirement for most of the elements investigated but only for the Ca II line at 396.85 nm ( $0.1 \text{ l min}^{-1}$ ) is the requirement precisely met.

For the MIP operated at  $1.0 \text{ l min}^{-1}$  flowrate the ideal requirement is most nearly met for the element lithium. However, the discharge tube contamination observed for this element in the MIP operated at  $0.1 \text{ l min}^{-1}$  flowrate warns against its regular aspiration into either MIP.



The positional stability of the MIP generated in the slab-line cavity at either argon flowrate was generally excellent when either H<sub>2</sub>O blank or most analyte solutions were aspirated. However, stability was affected by the aspiration of certain elements, such as lithium and when the 1 mg ml<sup>-1</sup> potassium matrix was added. Under these circumstances a noticeable, though mostly small degradation in plasma stability was observed. For certain elements however, this degradation in plasma stability could be severe, which caused fluctuations in the net line signals measured. This was found to particularly be the case for iron in the MIP operated at 0.1 l min<sup>-1</sup> where the fluctuations in the net line signals measured resulted in the poor precision of the  $X(Cm,0)$  calculated.

A particularly interesting feature of the results is that in the MIP operated at 0.1 l min<sup>-1</sup>, the addition of the potassium matrix generally caused analyte signal enhancements, ie.  $X(Cm,0)$  greater than 1, whereas in the MIP operated at 1.0 l min<sup>-1</sup>, the opposite was true and analyte signal depression, ie.  $X(Cm,0)$  less than 1 was mostly observed. There are exception to this in the Ca I, Al I and Li I spectra however.

There is a correlation between this behaviour and the electron density measurements, made under similar conditions and reported in section 5.4.3 B. In summary, this is that the analyte signal enhancement in one MIP is accompanied by a reduction in the electron density and the analyte signal depression in the other MIP, is accompanied by an increase in the electron density.

## 6.7 Spectrochemical Results for the MIP generated in the TM<sub>010</sub> Cavity.

Obtaining a stable image of the MIP generated in the TM<sub>010</sub> cavity at a flowrate of 1.0 l min<sup>-1</sup> was found to be difficult since the plasma wandered around the inside wall of the discharge tube. Careful alignment of the tube (section 3.1) minimised this wander, but it was never entirely eliminated. As a consequence of this behaviour a very limited spectrochemical assessment of the MIP generated in the TM<sub>010</sub> cavity was conducted for the elements Ca, Fe and Ni. The results are presented in table 6.5.

### 6.7.1 Detection Limits.

Even when the MIP generated in the TM<sub>010</sub> cavity remained attached to a particular part of the inside wall of the discharge tube, the plasma stability was seldom as good as the MIP generated in the slab-line cavity. This is reflected in the high figures for  $\sigma_B$  in nearly half of the spectral lines investigated.

Since analyte signal emission is always viewed against the bright background of the main body of the plasma, the generally lower values of SBR recorded, compared to the MIP generated in the slab-line cavity are to be expected. However, the SBR values for the Ni I line at 361.9 nm and Fe I line at 371.99 nm are identical to those recorded in the MIP operated at a flowrate of 1.0 l min<sup>-1</sup> in the slab-line cavity.

Element/ Spectrum	Wave- length (nm)	$\sigma_B$	SBR	$C_L$ (ng ml <sup>-1</sup> )	$X(1000,0)$
Ca I	422.67	0.0208	1.82	114.0 <sup>±</sup> 3.2	0.8 <sup>±</sup> 0.06
Ca II	393.37	0.0060	2.19	27.4 <sup>±</sup> 0.9	1.3 <sup>±</sup> 0.15
Ca II	396.85	0.0115	1.01	113.8 <sup>±</sup> 3.3	1.3 <sup>±</sup> 0.1
Fe I	371.99	0.0108	0.40	540.0 <sup>±</sup> 55	0.5 <sup>±</sup> 0.17
Fe I	373.49	0.0061	0.30	400.0 <sup>±</sup> 20	2.1 <sup>±</sup> 0.9
Fe I	381.58	0.0068	0.06	2400.0 <sup>±</sup> 800	1.7 <sup>±</sup> 0.8
Ni I	341.48	0.0066	1.77	150.0 <sup>±</sup> 10	1.2 <sup>±</sup> 0.08
Ni I	352.45	0.0074	1.25	240.0 <sup>±</sup> 10	1.2 <sup>±</sup> 0.17
Ni I	361.94	0.0122	0.75	650.0 <sup>±</sup> 30	1.1 <sup>±</sup> 0.09

Net Input Power = 85 <sup>±</sup> 5 W

Viewing = Axially along length of Discharge Tube.

SUR = 0.5 ml min<sup>-1</sup>

Table 6.5      Spectrochemical Results for the 1.0 l min<sup>-1</sup>  
MIP Generated in the TM<sub>010</sub> Cavity.

The reason for this may be found in the way in which the MIP corrodes the discharge tube, since when this happens the plasma disappears from the line of sight of the optical measuring system. Thus the background illumination is diminished, leading to better measured SBR's for any MIP operated in a well used discharge tube with the  $TM_{010}$  cavity.

The discharge tube used in this particular study was little used prior to measurement of the Ca detection limit and matrix factors. However, subsequent to the similar measurements for Ni and finally Fe the discharge tube was becoming badly corroded and the main body of the plasma had noticeably sunk into the tube wall.

In summary therefore, the poor detection limits obtained in the MIP generated in the  $TM_{010}$  cavity are the result of a combination of poor plasma stability and the inherent disadvantages of viewing analyte signal emission against the bright background of the main body of the plasma.

#### 6.7.2 Matrix Factors.

The stability of the MIP generated in the  $TM_{010}$  cavity actually improved when an interfering matrix of  $1\text{ mg ml}^{-1}$  potassium was added to the sample solutions. The rather poor precision of the matrix factors is primarily a function of the small net line signals and poor plasma stability without the added potassium.

The magnitude of the sensitivity of the MIP generated in the  $TM_{010}$  cavity to the potassium matrix, is similar to that found for the MIP generated in the slab-line cavity. However, matrix factors are generally greater than 1 for the MIP generated in the slab-line cavity at an identical argon flowrate. The behaviour of the analyte emission in the different MIP's when the potassium matrix is added is therefore probably more dependent on the part of plasma viewed by the optical system. This is not unreasonable in view of the different excitation temperatures and electron densities (chapter 5) measured for the viewing zones used in these two spectrochemical assessments.

## 6.8 Discussion on Spectrochemical Performance.

### 6.8.1 Performance of MIP's Investigated.

The spectroscopic measurements of temperature and electron density (chapter 5) have shown that the 3 MIP's investigated are basically similar. If the optical system is aligned so as to view the main body of the MIP generated in the slab-line cavity, similar values of temperature and density are observed to those found in the MIP generated in the  $TM_{010}$  cavity.

The main differences between the MIP operated in the two types of microwave cavity arise as a result of operational factors and these are particularly important when considering the MIP as an atomic emission source for the spectrochemical analysis of sample solutions.

In addition to generating an MIP with far better positional stability, the slab-line cavity has the advantage over the  $TM_{010}$  cavity of permitting radial viewing through the walls of the discharge tube. The ability to select the part of the plasma viewed by the optical measuring system has been found to be the most important factor in achieving maximum SBR's and hence minimizing the detection limits obtained. Although some experimenters, eg. Matousek et al, 1984 (41) have achieved radial viewing of an MIP generated in a  $TM_{010}$  cavity they have viewed regions of the plasma outside the confines of the cavity. Whereas this may provide similar optimum viewing conditions for maximum SBR's as those achieved using the slab-line cavity, experiences in this work (section 3.1) have shown that the positional stability of plasma filaments outside of either cavity type is not guaranteed. This could lead to similar operational difficulties to those encountered in the present work for the  $TM_{010}$  cavity.

The problem of contamination of the discharge tube wall by analyte solutions aspirated into the MIP could undoubtedly be eliminated if the entire plasma, or at least that part which encountered the sample aerosol was prevented from touching these walls. This is naturally

a general comment applicable to all MIP's but would particularly have prevented the lithium contamination problem in the MIP operated in the slab-line cavity at a flowrate of  $0.1 \text{ l min}^{-1}$  (section 6.6).

This could be achieved by use of the discharge tube described by Bollo-Kamara and Coddington, 1981 (45), which being similar to an ICP torch uses two gas flows, one to sustain the plasma and the other, carrying the sample aerosol to punch a hole through the centre of the plasma. Thus the sample aerosol is kept away from the wall of the discharge tube and the analyte atoms are maximally excited due to their increased contact with the hot plasma. The latter feature is particularly important since some experimenters, Beenakker et al, 1978 (20) have opined that the majority of the sample aerosol by-passes the MIP which usually occupies a fraction of the discharge tube cross-section. It is to be hoped that wider appreciation of the virtues of the slab-line cavity as a means of producing an atmospheric pressure MIP might lead to the use of such a torch in the future.

It perhaps should be remembered that the  $\text{TM}_{010}$  cavity used in this investigation was of a basic design, almost identical to that described originally by Beenakker, 1976 (2). This basic design has been developed further by some experimenters, eg. Van Dalen et al, 1978 (67) and Kollotzek et al, 1982 (38) and the modifications proposed are said to greatly enhance the  $\text{TM}_{010}$  cavities operational behaviour and performance.

During construction of the  $\text{TM}_{010}$  cavity used in the present work, particular emphasis was put on the design of an efficient input coupling (section 3.1). This, in conjunction with the use of a double stub tuner (section 4.2) largely circumvents the need for the modifications suggested by Van Dalen et al, 1978 (67) and thus at the time of experimentation, the  $\text{TM}_{010}$  cavity used might be considered to be the state of art design. In view of the difficulties encountered in this work in achieving a positionally stable MIP in the  $\text{TM}_{010}$  cavity, the later modifications to the discharge tube mounting mechanism

suggested by Kollotzek et al, 1984 (23) might be considered essential for the successful operation of the MIP in the  $TM_{010}$  cavity as an atomic emission source for use in spectrochemical analysis.

#### 6.8.2 Comparison of Spectrochemical Results with Published Values for the MIP.

Table 6.6 illustrates a representative selection of recent investigations into MIP's used for spectrochemical analysis of sample solutions.

Since there is no common consensus amongst experimenters as to the particular elements and spectral lines which might usefully be examined, maximizing the breadth of comparison between different analytical plasma systems is difficult. The elements and spectral lines shown in table 6.6 are those investigated by Beenakker et al, 1978 (20) in conjunction with those of the present work.

In view of the similar results obtained for the MIP generated in the slab-line cavity at either argon flowrate employed, only those results for the MIP operated at  $0.1 \text{ l min}^{-1}$  are shown in table 6.6.

Given the fundamental differences between the MIP operated in the slab-line cavity and that reported for the  $TM_{010}$  cavity by Beenakker et al, 1978 (20) it is somewhat surprising that there is not a greater difference in the detection limits observed. However, they used entrance optics which focussed a diffuse image of the MIP onto the monochromator entrance slit, which reduced the problem of plasma instability affecting light levels received. Measured values of  $\sigma_B$  should then be reduced, and hence detection limits improved. Analyte emission from the MIP will however, still be viewed against the high background illumination of the main body of the plasma and therefore SBR values would not necessarily be improved.

Note: Their arrangement of entrance optics was not necessary for the MIP generated in the slab-line cavity, and was not therefore used for the MIP generated in the  $TM_{010}$  cavity.

Element/ Spectrum	Wavelength (nm)	Detection Limits (ng ml <sup>-1</sup> )					
		Present MIP in Slab-line Cavity 0.1 l min <sup>-1</sup>	Present MIP in TM <sub>010</sub> Cavity 1.0 l min <sup>-1</sup>	MIP in TM <sub>010</sub> Cavity ref.20	MIP in TM <sub>010</sub> Cavity * ref.23	MIP in TM <sub>010</sub> Cavity ref.110	MIP in TM <sub>013</sub> Cavity * ref.32
Ag I	338.29			6			
Al I	396.15	980		400		650	600
Ca I	422.67	4.3	114		0.6		
Ca II	393.37	6.8	27		0.8		6
" "	396.85	25.3	114				
Co I	345.35	93		150			600
" "	240.73				60		
Cr I	425.43			150		4.0	
Cu I	327.40			9			
Fe I	371.99	234	540			8.3	600
" "	373.49	248	400				
" "	381.58	878	2000				
Fe II	259.94			200		4.1	
Ga I	417.21			10	3		
Li I	670.78	2.4		1			
Mg I	285.21			5	1.3	4.8	
Mg II	279.55			6	3	2.6	300
Mn I	403.08	36		50	27	3.9	
Mn II	257.61			30	20	1.4	
Ni I	341.48	81	150	80		6.7	
" "	352.45	79	240	200			
" "	361.94	115	650				
Pb I	405.78	87		100			60
Sb I	259.80			400			
Sr I	460.73	13		10			
Sr II	407.77	19		5	2		
Ti I	498.17			400			60
Ti II	334.92			600			

Table 6.6 Comparison of Detection Limits for Various MIP's

\* recalculated to 2 x from 3 x



The problem of discharge tube corrosion (section 6.7) has been proposed as a mechanism whereby SBR values reported for the MIP generated in the  $TM_{010}$  cavity in this work might not be as low as expected.

This is an unlikely explanation for possibly better SBR values obtained by Beenakker et al, 1978 (20) however, since they used alumina discharge tubes and report minimal corrosion. Also their entrance optics would preclude viewing of specific regions of the MIP, ie. away from the main plasma body, by which higher SBR values might have been observed.

Where the limited spectrochemical investigation of the MIP generated in the  $TM_{010}$  cavity in this work permits a comparison with the results reported by Beenakker et al, 1978 (20), some further useful observations may be made. Despite the similarity of the two MIP's generated in the  $TM_{010}$  cavity, the results reported for the present work do not support those of Beenakker et al, 1978 (20) and there is an inconsistency in the detection limits reported for two Ni lines at 341.48 nm and 352.45 nm. SBR values may be more reliably used here, avoiding the poor  $\sigma_B$  values incurred as a result of the plasma instability problems encountered for the present MIP in the  $TM_{010}$  cavity. SBR's for the two Ni lines, calculated from Beenakker et al, 1978 (20) results, are 3.0 and 1.2 respectively for a  $20 \mu\text{g ml}^{-1}$  Ni solution aspirated into the MIP. Equivalent SBR's from the present work are 1.8 and 1.2 respectively (table 6.5). Given the number of similarities between the two MIP's generated in the  $TM_{010}$  cavity, eg. cavity dimensions, argon flowrate and type of nebulizer, it may be concluded that some other fundamental difference exists between them. However, although an SUR of only  $0.5 \text{ ml min}^{-1}$  was used for the MIP generated in the  $TM_{010}$  cavity in this work (Beenakker et al, 1978 (20) used  $1.5 \text{ ml min}^{-1}$ ), experiences related in section 6.5 suggest that this is unlikely to cause a great difference.

Since an identical microwave power generator, the EMS Microton 200 mk II was used in both studies, it seems unlikely that greater microwave input power was coupled into the MIP generated in the  $TM_{010}$  cavity reported by Beenakker et al, 1978 (20) but this cannot be checked due to lack of true net input powers (section 4.3) being reported.

These inconsistencies in spectrochemical results, although they may be attributable to the difficulty of successful operation of an analytical argon MIP, do highlight the problems encountered in comparing different analytical plasma systems.

Recent developments in MIP's operated in the  $TM_{010}$  cavity have been reported by several experimenters. These developments are equally applicable to other types of microwave cavity/MIP systems. Kollotzek et al, 1984 (23) have used a mechanism which permits precision alignment of the plain cylindrical discharge tube within the  $TM_{010}$  cavity, producing a toroidal shaped MIP. The sample aerosol passed through the centre of this plasma and the analyte atoms are optimally excited in a region of relatively low background illumination. Thus considerable improvements in SBR values are obtained for most elements. The effect this has on the detection limits calculated is demonstrated by their results given in table 6.6. Haas and Caruso, 1984 (110) used the novel discharge tube described by Bollo-Kamara and Coddling 1981 (45) to operate a moderate power (100-500 Watts) MIP in the  $TM_{010}$  cavity. The use of this discharge tube torch also enables a toroidal shaped plasma to be formed and hence the ability to view the analyte emission away from strong background illumination of the plasma. Whilst this too improves the SBR values observed for most elements, the increased power coupled into the cavity also dramatically improves the detection limits observed (table 6.6).

Their internally tuned  $TM_{010}$  cavity did require modification to prevent overheating and internal coronal discharges. Such an approach to the MIP generated in the slab-line cavity would undoubtedly affect improvements in its analytical capability. The use of the Bollo-Kamara and Coddling torch would however, be primarily to eliminate

the contamination problem mentioned earlier and might not necessarily lead to a great increase in the SBR values observed should the MIP be viewed axially.

For completeness Table 6.6 shows the analytical results reported by Kawaguchi et al, 1972 (32) for certain elements analysed in an MIP generated in a  $TM_{013}$  waveguide cavity (section 2.1). Although it is apparent that considerable improvements have been effected in all aspects of operation of an MIP it is interesting to note that Kawaguchi used an ultra sonic nebulizer to introduce sample aerosols into the plasma. Thus, no obvious advantage is shown in the use of such a device compared to the much less efficient pneumatic nebulizer.

As with most studies of MIP's used in the spectro-chemical analysis of solutions that have been reported in the literature, neither one of the MIP's investigated here has been totally free of inter-elemental interference effects, caused when a  $1 \text{ mg ml}^{-1}$  K matrix was added to the sample solutions. In line with current thinking on the causes of these interference effects Beenakker et al, 1978 (20) proposed three possible mechanisms.

- 1) Change in efficiency of the nebulizer/spray chamber assembly.
  - 2) Chemical interferences effect in the plasma.
  - 3) Changes in the excitation conditions within the plasma.
- Without a precise method of measuring the amounts of sample solutions taken into the plasma as described by Smith and Browner, 1982 (109) investigation of the first process is not possible. The exact nature of chemical interference effects within any type of analytical plasma is little understood and most analytical chemists adopt a highly empirical approach to the problem, ie. matrix modification. This is the addition of other chemicals to the sample solutions to change the way in which dissociation of the sample constituents occurs in the plasma.

The results reported in section 5.4.3 which show a change in the electron density,  $N_e$ , in the plasma when the interfering matrix is added to the sample solutions clearly implicate process 3 in this effect. Furthermore in conjunction with the observations reported in section 6.6, for the MIP generated in the slab-line cavity at flow rates of 0.1 and 1.0  $\text{ml min}^{-1}$  this shows that, for most

elements investigated, an analyte signal enhancement on addition of the interfering matrix is linked with a reduction in electron density and conversely an analyte signal depression with an increase in electron density. Only very much smaller changes have been observed in the argon excitation temperature,  $T_{\text{EXC}}$  (section 5.1.2) and OH rotational temperature  $T_{\text{ROT}}$  (section 5.3.2) on addition of the interfering  $1 \text{ mg ml}^{-1}$  K matrix, but these parameters have generally shown little sensitivity to quite large changes in the plasma operating conditions.

### 6.8.3 Comparison of Spectrochemical Results with Published Values for Competing Analytical Plasma Systems.

Table 6.7 lists the results for the MIP generated in the slab-line cavity at a flowrate of  $0.1 \text{ l min}^{-1}$  and for comparison, the results published for the conventional ICP studied by both Fassel's (30) and Bouman's (111) research groups. Although precise reasons for the considerable differences in detection limits for many elements reported by the two groups have not been defined, it seems likely that differences in ICP operating conditions are responsible, eg. frequency of excitation energy, sample injection rate and possibly the use of an ultrasonic nebulizer by Boumans and de Boer, 1975 (29). The resolution of the optical measuring system used also affects the detection limits obtained. In an inter-laboratory comparison of the ICP with the CMP, Boumans et al, 1975(112) comment on the degradation observed in ICP performance incurred by use of an inferior optical system to that normally employed.

Inspection of table 6.7 shows that except for Fe and Al the detection limits found for the MIP operated in the slab-line cavity compare favourably with those reported for the ICP where the spectral line considered is emitted by the analyte atom. However, where the spectral line is emitted by the analyte ion, the ICP detection limit is vastly superior to that found in the MIP. This is well

Element/ Spectrum	Wave- length (nm)	MIP	Conv ICP		Low Flowrate ICP			CMP
			Ref30 <sup>&amp;</sup>	Ref111	Ref 7	Ref8	Ref9 <sup>5</sup>	
Al I	396.15	980	19	1		31	27	300
Al I	309.27*		15	1	2300			
Ba I	553.55			20				500
Ba I	455.40		0.9	0.05	30	1.4		
Ca II	393.37*	6.8	0.13	0.04	9	0.31	0.3	400
Ca II	396.85	25.3	0.3	0.08				1000
Ca I	422.67	4.3	6.7	3				50
Co I	345.35	93		4			12	50
Co II	238.89*		4	1.5		7.1	47	
Cu I	324.75*		3.6	0.3	250		6.7	10
Cu I	327.40		6.5	0.6				30
Fe I	371.99	234		10				150
Fe I	373.49	248		4				
Fe II	238.20		3.1	0.7				
Fe II	259.94*		4.1	0.5	1000		40	
Li I	670.78*	2.4		0.3				2
Li I	460.29		570	150				
Li I	610.36			4				700
Mg I	285.21		1.1	0.2				30
Mg II	279.55*		0.1	0.02	15	0.13	0.4	300
Mn I	403.08	36	29	2				50
Mn II	257.61*		0.9	0.14	80	0.84		
Ni I	341.48	81	32	4				100
Ni I	352.45	79	30	4				
Ni II	231.60*		10	2				
Ni II	221.65		6.7			12		
Ph I	405.78	87	180	20				800
Ph II	220.35*		28					
Sr I	460.73	13	45	2				40
Sr II	407.77*	19	0.3	0.02				
Ti I	498.17			15				1500
Ti II	334.94		2.5	0.3		1.6		

\* Denotes best detection limit in the conventional ICP.

& Denotes recalculated from 3σ to 2σ.

Table 6.7 Comparison of Spectrochemical Results for the 0.1 l min<sup>-1</sup> MIP Generated in the Slab-line Cavity with Competing Spectroscopic Analytical Systems.

illustrated for calcium where similar detection limits are found for the Ca I spectra in both the MIP and ICP but the detection limits for the Ca II spectra are 1 to 2 orders of magnitude smaller in the ICP. This 'ionic line advantage' has been reported previously by other experimenters, eg. Beenakker et al, 1978 (20). With similar values of  $\sigma_B$  in both the MIP studies here and the conventional ICP, the superior detection power of the ICP is clearly due to higher SBR values. The observation zone in the ICP is usually above the main plasma core and thus background illumination is relatively low which therefore enhances SBR's. A similar attempt to view analyte spectra in the tailflame of the MIP outside the discharge tube and slab-line cavity did not however produce similar results to the ICP. Although SBR values were much higher, the RSD of the (very low) background signal was poor.

Because of this, and despite the attractions of the MIP in terms of its compactness, low power and gas flow requirements it will never seriously threaten the superiority of the ICP whenever the ultimate in detection power is sought by the analyst. Where more modest detection power is required, then the MIP does make an attractive alternative to the ICP but for the majority of analysts this will require that MIP systems are offered by commercial instrument manufacturers. However, experiences gained in this investigation during the operation of an analytical MIP suggest that a high level of skill will be required on the part of the analyst. This requirement will need to be reduced or even eliminated before a commercial MIP system is made available.

As noted earlier, steps have been taken by some experimenters, eg. Haas and Caruso, 1984 (110) to improve the spectrochemical performance of the MIP by increasing the input power to the MIP, and this in conjunction with an ICP like torch has significantly improved detection limits. However, these detection limits are still poorer by a factor of 10 than the ICP and there is no strong 'ionic line advantage' displayed. To increase the power input to an MIP still higher so as to lower detection

even more is somewhat self-defeating since one of the attractions of the MIP is lost, namely low power requirements.

The future for the MIP, if it is to remain basically a low power, low gas consumption atomic emission source perhaps lies in the use of a different form of sample introduction. Discrete sample introduction into the MIP has been investigated by many experimenters, eg. Deutsch & Hieftje, 1984 (4) and has shown considerable promise with detection limits approaching those for the ICP. Removal of the requirement for a plasma gas with an atomic weight sufficient for efficient aerosol nebulization also has attractions in that helium can then be used. This was shown by Beenakker et al, 1980 (10) to prove particularly beneficial in the determination of the halogens. However, the use of discrete sampling techniques will never match the convenience of continuous sampling methods unless a high level of automation is introduced into the process, as is commonly found in most modern electro-thermal atomizer (ETA) atomic absorption spectrophotometers.

Table 6.7 also lists the results reported by Kawaguchi et al, 1980 (8) for a 1 Kw ICP using a water cooled torch and operated at a total gas flowrate of  $5 \text{ l min}^{-1}$  and those reported recently by Ripson et al, 1982 (9) for an ICP operated at a total argon flowrate of only  $0.85 \text{ l min}^{-1}$  using an air cooled torch. Table 6.7 illustrates that the detection limits for these two low flowrate ICP systems, whilst still somewhat inferior to the conventional ICP are noticeably better for most elements than the present MIP investigated. Should further development result in the production of a reliable ICP system with low flowrate, less than  $1 \text{ l min}^{-1}$  and low input power, less than 1 Kw, as suggested by the work of Ripson et al, 1982 (9), then undoubtedly the MIP with direct sample aerosol introduction will be eliminated as a serious contender to the ICP.

However, should a compromise value of gas flowrate, eg. near to  $5 \text{ l min}^{-1}$  be necessary to achieve results identical to the conventional ICP then, provided more moderate detection power is acceptable, the very much simpler MIP system will find applications.

It isn't clear how the CMP has come to be regarded as a separate entity from the MIP since it not only shares many of the same operational parameters, eg excitation frequency and use of microwave cavity but also the same inherent advantages and disadvantages as an analytical atomic emission source.

However, the level of spectrochemical performance attained with a CMP, as reported by Dahmen, 1981 (36) is significantly worse than the MIP investigated in this study and indeed most other MIP's. For the elements investigated detection limits greater by a factor of 10 compared to the MIP are not uncommon as evidenced by the data in table 6.7. In addition, its sensitivity to interfering matrixes, discussed later is far worse than the MIP.

Certain operational factors also favour the MIP since it generally operates at lower input power and gas flowrate, although the CMP reported Feuerbacher, 1981 (13) can be operated on nitrogen gas and so some economy may be made here compared to using more expensive argon gas.

From the foregoing discussions there can be little recommendation for using the CMP compared to the various other MIP configurations available and indeed in an earlier inter-laboratory comparison of the spectrochemical performance of the CMP and conventional ICP, Boumans et al, 1975 (112) were unequivocal in their rejection of the CMP.

The degree of sensitivity to an interfering matrix in the sample solution was noted in section 6.6.2 to be an important criteria by which to judge the suitability of an atomic emission source used in spectrochemical analysis.

The suitability of the atmospheric pressure argon MIP generated in the slab-line cavity has been investigated for various elements when a matrix of K<sup>+</sup>, at a concentration of  $1 \text{ mg ml}^{-1}$  was added to the sample solutions. The results of this investigation (section 6.6.2) are compared to those



for the conventional ICP in table 6.8. The ICP data used is taken from two sources, Boumans and de Boer, 1975 (29) and Boumans and de Boer, 1976 (33).

Compared to the MIP, and indeed many other atomic emission sources the conventional ICP is very nearly an ideal atomic emission source showing little or no sensitivity to the K matrix. Boumans and de Boer, 1976 (33) showed that this insensitivity was typical for a large range of interfering matrixes, eg.  $\text{NH}_4\text{Cl}$ ,  $\text{CsCl}$ ,  $\text{MgCl}_2$  and  $\text{FeCl}_3$ .

Therefore the conventional ICP is the standard by which comparisons are made and clearly the MIP generated in the slab-line cavity deviates by a considerable margin from this standard. By comparison the CMP investigated by Boumans et al, 1975 (112) showed variable sensitivity depending on the interfering matrix used but this was partly caused by changes in the size and shape of the plasma when different concentrations of the matrix were introduced. This, it was suggested, prevented the definition of a meaningful matrix factor if a fixed viewing height was employed because different parts of the plasma were viewed with, and without the matrix.

When the K matrix was introduced into the MIP generated in the slab-line cavity, slight movement of the plasma was observed for which the precautions described in section 6.4 were taken when measuring the matrix factor. However, unlike the CMP these small movements, much less than 0.5 mm did not appreciably change the part of the plasma viewed by the optical measuring system. Therefore although the behaviour of the MIP is inferior to the conventional ICP it clearly does not suffer with the serious operational difficulties encountered with the CMP when interfering matrixes are added.

Although tabulated data on the sensitivity of the low flowrate ICP to the presence of interfering matrixes is not available, graphical data reported by various authors suggests that the behaviour is inferior to the conventional ICP. Kornblum et al, 1979 ( 7 ) estimated that the sensitivity of their low flowrate ICP was however less than 25% worse than the conventional ICP.

Element/ Spectrum	$\lambda$ (nm)	<sup>1</sup> ICP	<sup>2</sup> MIP	<sup>3</sup> MIP
Al I	396.15	1.00	0.8	0.7
Ca I	422.67	1.03	0.5	0.5
Li I	670.78	1.09	-	1.2
Mn I	430.08	0.98	1.6	0.6
Sr I	460.73	1.15	1.2	0.5
Sr II	407.77	0.94	2.2	0.7

1. Al, Ca & Li, Boumans & de Boer, 1976 (33).

Mn, Sr " " " , 1975 (29).

2. Present MIP operated at  $0.1 \text{ l min}^{-1}$  argon flowrate

3. " " " at  $1.0 \text{ l min}^{-1}$  " "

Matrix Concentration =  $1 \text{ mg ml}^{-1}$  Potassium as KCl.

Table 6.8      Matrix Factors for the Conventional ICP and the  
MIP Generated in the Slab-line Cavity.

The sensitivity of the MIP generated in the slab-line cavity to interfering matrixes may be compared to the low flowrate ICP using the Ca II spectral line at 393.37 nm. Such a comparison, illustrated in table 6.9 is, however only intuitive since different types of matrix have been used. Also, use of the Ca II spectral line at 393.37nm by Ripson et al, 1982 (9) is not explicitly stated in their paper but is inferred from their tabulated "detection power" data. Even so, for an alkali-metal matrix of either K or Na, behaviour of the MIP is seen to be only slightly inferior to the low flowrate ICP and overall (considering all matrixes) performance is similar.

Undoubtedly a more extensive investigation of this particular aspect of MIP operation is needed before a definitive comparison with either the conventional or low flowrate ICP can be made. Such an investigation will require the use of different types of matrix and probably optimization of the slab-line cavity and/or the sample delivery system (including the discharge tube). However, the present results give encouragement that even modest improvements in performance would make the MIP comparable with the ICP. Such improvements will require further understanding of the major causes of spectral and chemical interferences in atmospheric pressure plasmas.

Types of Plasma	Matrix Factor $X(C_M, 0)$			
	K matrix	Na matrix	Al matrix	PO <sub>4</sub> matrix
0.1 l min <sup>-1</sup> MIP.	1.2			
1.0 l min <sup>-1</sup> MIP.	0.8			
1.0 l min <sup>-1</sup> ICP. a *		1.05	1.15	0.88
2.0 l min <sup>-1</sup> ICP. b *		0.89	0.93	0.79
4.8 l min <sup>-1</sup> ICP. c *		0.80		2.00

Ca II spectral line at 393.37 nm

Matrix concentration = 1 mg ml<sup>-1</sup>

- References:
- a ICP operated at 1.0 l min<sup>-1</sup> total argon flowrate in an air cooled torch, Ripson et al, 1982 (9).
  - b ICP operated at 2.0 l min<sup>-1</sup> argon flowrate in a water cooled torch, Kornblum et al, 1979 (7).
  - c ICP operated at 4.2 l min<sup>-1</sup> argon flowrate in a water cooled torch, Kawaguchi et al, 1980 (8).
  - \* Calculated from percentage sensitivities.
  - \* Calculated from relative intensities.

Table 6.9      Comparison of Matrix Factors for the MIP and Various Low Flowrate ICP's.

7.1 Plasma Models Applicable to the MIP.

The investigation of the fundamental physical properties of an atmospheric pressure argon MIP, reported in this thesis has considered several different operational conditions. These may be rationalized to define 4 MIP systems as follows.

- i) The slab-line cavity used to support a dry argon MIP at different flowrates and microwave input power.
- ii) In a different configuration to i), the slab-line cavity used to support an analytical argon MIP incorporating sample introduction, operated at a flowrate of  $0.1 \text{ l min}^{-1}$  using a Babington nebulizer.
- iii) Identical to ii) but operating at a flowrate of  $1.0 \text{ l min}^{-1}$  using a crossflow nebulizer.
- iv) The  $\text{TM}_{010}$  cavity used to support an analytical argon MIP operating at a flowrate of  $1.0 \text{ l min}^{-1}$  and using a similar sample introduction system to iii).

Significant differences have been observed in the electron density, excitation and rotational temperatures between these 4 MIP's. Furthermore, evidence has been obtained which shows differences in the excitation conditions between different physical locations of the same MIP.

In LTE, only one temperature parameter is required to describe the entire MIP system (section 1.3.2 ii), applicable to every plasma species present. Clearly from the different argon excitation temperature (section 5.1), iron excitation temperature (section 5.2) and rotational temperature (section 5.3), none of the MIP's considered is in a state of LTE.

If the MIP were in LTE, Saha equilibrium would exist between the Ar I excited levels (including the atom ground level) and the ion ground level (section 1.3.3 ii). The Saha equation

$$\frac{N_e N^+}{N_i} = \frac{2g^+}{g_i} \left[ \frac{2\pi m k T_e}{h} \right]^{3/2} \exp \left[ \frac{-E^+ - E_i}{k T_e} \right]$$

where  $N_e$  = electron density.

$N^+$  = ion ground state density.

$N_i$  = density of an excited level.

$g_i$  = degeneracy of an excited level.

$E_i$  = excitation energy of an excited level.

$E^+$  = ionisation energy from atom ground level.

$g^+$  = degeneracy of ion ground level.

$T_e$  = electron temperature.

and all other symbols have their usual meaning.

could then be used to calculate the electron temperature from the measured electron density. For LTE, the excitation and electron temperatures are identical. If this calculation is performed for each of the MIP systems defined, the results are as shown in table 7.1. The difference between the electron and excitation temperatures provides further evidence for the lack of LTE in any of the MIP's.

However, the results for the analytical MIP generated in the slab-line cavity at  $1.0 \text{ l min}^{-1}$  suggest that in the 'main body' of the plasma, the departure from LTE is less than when the viewing zone for optimum spectrochemical performance is used. When the main body of the MIP is viewed, measured excitation and calculated electron temperatures differ by only 900 deg K (see '&' on table 7.1).

MIP System	$T_{\text{EXC}}(\text{degK})$	$N_e(\text{cm}^{-3})$	$T_e(\text{degK})$
i) Dry Argon MIP in Slab-line Cavity.	4800	$6 \times 10^{14}$	7000
ii) Analytical MIP in Slab-line Cavity. Flowrate = $1.0 \text{ l min}^{-1}$ %	4100	$9 \times 10^{14}$	7500
iii) Analytical MIP in Slab-line Cavity Flowrate = $1.0 \text{ l min}^{-1}$ %	4400	$1.5 \times 10^{15}$	8100
	& 7500	$4.2 \times 10^{15}$	8400
iv) Analytical MIP in $\text{TM}_{010}$ Cavity. Flowrate = $2.0 \text{ l min}^{-1}$	5000	$2 \times 10^{15}$	8200

Blank solution aspirated for all analytical MIP's.

% using viewing zone for optimum spectrochemical performance.

& using viewing zone 2 (see figure 5.3, section 5.1.2).

Table 7.1     Summary of Excitation and Electron Temperatures and Electron Densities in the MIP.

In the progressive deviation from the state of LTE in a plasma, a pLTE regime is characterised by an under population of the atom ground level but Saha equilibrium still exists between the excited levels and ion ground level (section 1.3.3 iii). The under (or over) population of the ground level,  $N_1$  compared to the ground level population,  $N_1(S)$  where Saha equilibrium includes the ground level, is expressed by Raaijmakers et al, 1983 (51) in terms of a parameter,  $b_1$ , given by

$$b_1 = \frac{N_1}{N_1(S)}$$

They also make the assumption that for typical atmospheric pressure plasmas like the ICP,  $b_1$  lies in the range 0.1 (for an under populated ground level) to 10 (for an over populated ground level). Naturally if Saha equilibrium exists between all levels,  $N_1 = N_1(S)$  and  $b_1 = 1$ .

If an under population of the ground level is assumed in the main body of the  $1.0 \text{ l min}^{-1}$  analytical MIP generated in the slab-line cavity, then the electron temperature may be re-calculated using  $b_1 = 0.1$  and a modified Saha equation. The resultant electron temperature is 7500 deg K, identical to the measured excitation temperature and therefore it seems highly likely that a state of pLTE exists in this part of the plasma. Re-calculation of electron temperature in this way, for the other MIP's does not produce an equality with the measured excitation temperatures, therefore deviations from LTE must be greater.

Some of the graphs of  $\ln(I\lambda/gA)$  versus  $E$  for Ar I, obtained in the MIP under various operating conditions, showed a slight under population of the 4p excited levels. This was particularly noticeable in the analytical MIP generated in the  $TM_{010}$  cavity (see figure 5.7, section 5.1.2). Schram et al, 1983 (113) observed that this behaviour may be a consequence of significant radiative losses due to the 4p - 4s electronic transition in a recombining plasma in which pLTE does not exist.

Further deviations from LTE are likely to be indicated by depopulation of the excited levels, starting with the levels near the ground level of the atom. Based on their parameter,  $b_1$ , Raaijmakers et al, 1983 (51) define a set of  $b_i$  describing the under (or over) population of progressively higher excited levels.

In the analytical MIP generated in the  $TM_{010}$  cavity there is therefore some certainty that deviation from LTE (or indeed pLTE) is sufficient that the concept of Saha equilibrium is no longer applicable. Under these circumstances it is suggested that the MIP has entered a quasi saturation phase (van der Mullen et al, 1980 (50)) and a collisional-radiative (CR) model may be a more realistic representation of the plasma (section 1.3.3 v).



There is some slight graphical evidence of an under population of the 4p excited levels in both the dry argon MIP (see figure 5.2, section 5.1.1) and the analytical MIP operated in the slab-line cavity at  $0.1 \text{ l min}^{-1}$  (see figure 5.5, section 5.1.2). It is therefore possible that in these MIP's also, a CR model may be more applicable than pLTE.

For the analytical MIP generated in the slab-line cavity at  $1.0 \text{ l min}^{-1}$  and using the viewing zone for optimum spectrochemical performance there is no suggestion of an under population of the 4p excited levels (see figure 5.6, section 5.1.2). The calculated electron temperature, even assuming pLTE to exist in this part of the MIP, is however much greater than the measured excitation temperature. This suggests that the limits to  $b_1$  set by Raaijmakers et al, 1983 (51) are not realistic if an interpretation of this particular MIP in terms of a pLTE model is desired. However, an alternative explanation could be an under population of the 4s excited levels, which would not be observed in this work. This would then be suggestive of a slight, though definite deviation from pLTE into a CR regime.

Iron excitation temperatures (see table 5.8, section 5.2) in the analytical MIP generated in either cavity are always significantly higher than the corresponding argon excitation temperatures (see table 5.5 and 5.6, section 5.1.2). They also more closely approach the electron temperature calculated from the measured electron density, assuming the MIP to be in pLTE. Even so, the iron excitation temperature is not representative of the MIP as a whole and the aspiration of Fe samples was also observed to influence the measured electron density (section 5.4.3 B). Since the introduction of Fe changes the nature of the plasma, it's routine addition to other types of samples as a means of plasma temperature determination would be ill advised.

OH rotational temperatures measured in the MIP systems investigated are considerably lower than the argon or iron excitation temperatures. This was also reported by Abdullah and Mermet, 1982 (47) in a comparison of argon and helium MIP's and ICP's. However, the OH rotational temperature has shown some sensitivity to changes in the conditions within the dry argon MIP (section 5.3.1) when the argon excitation temperature was unaffected (section 5.1.1 B). Since water vapour is normally automatically present in any analytical MIP (or ICP) incorporating a nebulizer, measurement of OH rotational temperatures provide a useful indicator of plasma conditions and is recommended.

## 7.2 Conclusions on Simultaneous Electron Density and Plasma Load Impedance Measurements.

Variation of the argon flowrate or microwave input power has been shown to cause a significant change in the electron density (section 5.4.2 B/C). However, much smaller and apparently unrelated changes were observed in the real part,  $R$  of the complex load impedance. These changes in impedance have been attributed to operational factors (section 4.5.1) such as the volume of plasma within the cavity.

The electron density was shown to be dependent on the internal volume of the discharge tube, and hence the MIP volume (section 5.4.2 D). However, the electron density was not nearly so dependent on the relative positions of the MIP and cavity inner conductor except for the smallest discharge tube used. The exact opposite was found to be true for the real part,  $R$  of the impedance (section 4.5.2), ie. more dependent on the amount of quartz within the cavity and the relative positions of MIP and inner conductor than the MIP volume. The imaginary part,  $X_c$  of the impedance was found to be virtually independent of any of the parameters.

The removal of the majority of the water vapour from the argon plasma gas produced a 40% reduction in the measured electron density (section 5.4.2 E). Allowing for the slight reduction in electron temperature, calculated from the Saha equation (section 7.1), such a decrease in electron density should have produced a 2.4% increase in  $R_T$ . However, a slight decrease (2.5%) in the real part of the load impedance was observed (section 4.5.3), attributed to the increase in MIP length within the cavity.

Simultaneous measurement of the electron density and plasma load impedance in the dry argon MIP generated in the slab-line cavity has therefore clearly failed to produce any firm evidence of an inter-dependence between the two parameters.

This is in contrast to the results of Allemand and Barnes, 1978 (55) who measured the impedance of a 1 kW, 27 MHz argon ICP and obtained a value of  $0.98 + j1.9 \Omega$ . They also report variations in impedance for different RF input powers, gas flowrates and the introduction of sample aerosols.

### 7.3 Correlation Between Electron Density and Matrix Factors in the Analytical MIP Generated in the Slab-line Cavity.

The dramatic decrease in electron density (section 5.4.3 B) observed when sample solutions containing a  $1 \text{ mg ml}^{-1}$  potassium matrix were aspirated into the  $0.1 \text{ l min}^{-1}$  MIP generated in the slab-line cavity coincided with analyte signal enhancement for most of the elements investigated (section 6.6.2). Conversely, the slight increase in electron density observed under similar conditions in the  $1.0 \text{ l min}^{-1}$  MIP generated in the slab-line cavity coincided with analyte signal depression.

It was originally thought that this signified some fundamental change in the physical properties of the analytical MIP (section 5.4.3 B). However, this behaviour is now believed to be entirely due to the slight physical movements of the MIP upon aspiration of the potassium matrix.

The viewing zone used for optimum spectrochemical performance was critically set at the very end of the MIP. In this region, electron density is diminishing as distance from the main body of the plasma increases (section 5.4.3 A). Also signal to background ratios (SBR) for analyte spectral lines are large, mainly due to the reduced luminosity of the plasma (section 6.5.1). Any slight movement of the MIP upwards would both decrease electron density and increase analyte SBR. Similarly, slight movement of the MIP downwards would both increase electron density and decrease analyte SBR. This is precisely the behaviour observed in the  $0.1 \text{ l min}^{-1}$  and  $1.0 \text{ l min}^{-1}$  respectively. The greater effect noted for the  $0.1 \text{ l min}^{-1}$  MIP is probably due to its slightly greater sensitivity to the introduced potassium (section 6.6.1) compared to the  $1.0 \text{ l min}^{-1}$  MIP.

The aspiration of Ni and Fe samples, also found to influence the measured electron density (section 5.4.3 B) presumably had a similar effect on the position of the MIP.

In order to minimise this problem in the future, it will be necessary to sacrifice some of the detection power and set the viewing zone used for spectrochemical analysis nearer to the main body of the plasma. However, matrix factors closer to unity may then be obtained.

## List of References.

- (1) S.Greenfield, I.L.Jones and C.T.Berry,  
Analyst 89, 713 (1964).
- (2) C.I.M.Beenakker, Spectrochim Acta 31B, 483 (1976).
- (3) R.M.Dagnall, T.S.West and P.Whitehead,  
Anal Chem 44, 2024 (1972).
- (4) R.D.Deutsch and G.M.Hieftje,  
Anal Chem 56, 1923 (1984).
- (5) R.M.Barnes, N.Kovacic and H.Matusiewicz, ICP Information  
Newsletter, 408 (1984).
- (6) C.D.Allemand and R.M.Barnes,  
Appl Spectrosc 31, 434 (1977)
- (7) G.R.Kornblum, W. van der Waa and L. de Galan,  
Anal Chem 51, 2378 (1979).
- (8) H.Kawaguchi, T.Ito, S.Rubi and A.Mizuike,  
Anal Chem 52, 2440 (1980).
- (9) P.A.M.Ripson, L. de Galan and J.W.Ruiter,  
Spectrochim Acta 37B, 733 (1982).
- (10) C.I.M.Beenakker, P.W.J.M.Boumans and P.Rommers,  
Philips Tech Rev 39, 3/4 (1980).
- (11) K.Fallgatter, V.Svoboda and J.D.Winefordner,  
Appl Spectrosc 25, 347 (1971).
- (12) P.W.J.M.Boumans and F.J.de Boer,  
Spectrochim Acta 27B, 391 (1972).
- (13) H.Feuerbacher, ICP Information Newsletter 6, 571 (1981).
- (14) A.T.Zander and G.M.Hieftje,  
Appl Spectrosc 35, 357 (1981).
- (15) J.W.Carnahan, International Lab 36, Nov (1983).
- (16) F.E.Lichte, PhD Thesis, University of Colorado State,  
USA, (1973).
- (17) C.I.M.Beenakker, Spectrochim Acta 32B, 173 (1977).
- (18) S.E.Valente and W.G.Schrenk,  
Appl Spectrosc 24, 197 (1970).
- (19) R.N.Kniseley, H.Amenson and V.A.Fassel,  
Appl Spectrosc 28, 285 (1974)
- (20) C.I.M.Beenakker, B.Bosman and P.W.J.M.Boumans,  
Spectrochim Acta 33B, 373 (1978).

- (21) C.Veillon and M.Margoshes,  
Spectrochim Acta 23B, 553 (1968).
- (22) J.E.Meinhard, ICP Information Newsletter 4, 314 (1978).
- (23) D.Kollotzek, P.Toschopel and G.Tolg,  
Spectrochim Acta 39B, 625 (1984).
- (24) R.S.Babington, "Popular Science", May, 102 (1973).
- (25) R.C.Fry and M.B.Denton,  
Appl Spectrosc 33, 393 (1978).
- (26) J.F.Wolcott and C.Butler-Sobel,  
Appl Spectrosc 32, 591 (1978).
- (27) N.Mohammed, R.M.Brown and R.C.Fry,  
Appl Spectrosc 35, 153 (1981).
- (28) P.A.M.Ripson and L. de Galan,  
Spectrochim Acta 36B, 71 (1981).
- (29) P.W.J.M.Boumans and F.J. de Boer,  
Spectrochim Acta 30B, 309 (1975).
- (30) R.K.Winge, V.Peterson and V.A.Fassel,  
Appl Spectrosc 33, 206 (1979).
- (31) K.W.Olson, W.J.Haas and V.A.Fassel,  
Anal Chem 49, 632 (1977).
- (32) H.Kawaguchi, H.Hasegawa and A.Mizuike,  
Spectrochim Acta 27B, 205 (1972).
- (33) P.W.J.M.Boumans and F.J. de Boer,  
Spectrochim Acta 31B, 335 (1976).
- (34) R.F.Browner and A.W.Boorn,  
Anal Chem 56, 875A (1984)
- (35) R.H.Scott, V.A.Fassel, R.N.Kniseley and D.E.Nixon,  
Anal Chem 46, 75 (1974)
- (36) J.Dahmen, ICP Information Newsletter 6, 576 (1981).
- (37) P.W.J.M.Boumans and M. Ch.Lux-Steiner,  
Spectrochim Acta 37B, 97 (1982).
- (38) D.Kollotzek, P.Tschopel and G.Tolg,  
Spectrochim Acta 37B, 91 (1982)
- (39) F.E.Lichte and R.K.Skogerboe,  
Anal Chem 45, 399 (1973)
- (40) R.K.Skogerboe and G.N.Coleman,  
Anal Chem 48, 611A (1976).
- (41) J.P.Matousek, B.J.Orr and M.Selby,  
Appl Spectrosc 38, 231 (1984).

- (42) F.E.Lichte and R.K.Skogerboe,  
Anal Chem 44, 1490 (1972).
- (43) F.C.Fehsenfeld, K.M.Evenson and H.P.Broida,  
NBS Report 8701, (1964).
- (44) R.J.Watling, Anal Chim Acta 75, 281 (1975).
- (45) A.Bollo-Kamara and E.G.Coddling,  
Spectrochim Acta 36B, 973 (1981).
- (46) K.Tanabe, H.Hawaguchi and K.Fuwa,  
Spectrochim Acta 38B, 49 (1983)
- (47) M.H.Abdullah and J.M.Mermet,  
Spectrochim Acta 37B, 391 (1982).
- (48) P.F.E. van Montford and J.Agterdenbos,  
Talanta 28, 629 (1981).
- (49) T.Fujimoto, Y.Ogata, I.Sugiyama, K.Tachibana and K.Fukuda,  
Japan J Appl Phys 11, 718 (1972).
- (50) J.J.A.M. van der Mullen, B. van de Sijde and D.C.Schram,  
Physical Letters 79A, 51 (1980)
- (51) I.J.M.M.Raaijmakers, P.W.J.M.Boumans, B. van der Sijde,  
and D.C.Schram, Spectrochim Acta 38B, 697 (1983).
- (52) G.R.Kornblum and L.de Galan,  
Spectrochim Acta 29B, 249 (1974).
- (53) J.F.Alder, R.M.Bombelka and G.F.Kirkbright,  
Spectrochim Acta 35B, 163 (1980).
- (54) H.Uchida, K.Tanabe, Y.Nojiri, H.Haraguchi and K.Fuwa,  
Spectrochim Acta 36B, 711 (1981)
- (55) C.D.Allemand and R.M.Barnes  
Spectrochim Acta 33B, 513 (1978).
- (56) C.B.Hammond, PhD Thesis, University of London (1978).
- (57) H.R.Griem, "Plasma Spectroscopy", McGraw Hill (1964).
- (58) H.Schluter, Z Naturforsch 18A, 439 (1963).
- (59) H.Drawin, Ann Physik 17, 374 (1966).
- (60) K.W.Busch and T.J.Vickers,  
Spectrochim Acta 28B, 85 (1973).
- (61) P.Brassem, F.J.M.J.Maessen and L. de Galan,  
Spectrochim Acta 31B, 537 (1976).
- (62) P.Brassem, F.J.M.J.Maessen and L. de Galan,  
Spectrochim Acta 33B, 753 (1978).
- (63) K.Tachibana and K.Fukuda. Japan J.Phys 12, 895 (1973)
- (64) J.F.S.Haarsma, G.J. de Jong and J.Agterdenbos  
Spectrochim Acta 29B, 1 (1974).
- (65) P.Brassem and F.J.M.J.Maessen,  
Spectrochim Acta 29B, 203 (1974).

- (66) R.Avni and J.D.Winefordner,  
Spectrochim Acta 30B, 281 (1975).
- (67) J.P.J. van Dalen, P.A. de Lezenne Coulander and  
L. de Galan, Spectrochim Acta 33B, 545 (1978).
- (68) S.R.Goode, N.P.Buddin, B.Chambers, K.W.Baughman and  
J.P.Deavor. Spectrochim Acta 40B, 317 (1985).
- (69) J.W.Carnahan, K.J.Mulligan and J.A.Caruso,  
Anal Chem 130, 227 (1981).
- (70) C.B.Hammond and M.Outred, Physica Scripta 14, 81 (1976).
- (71) J.Hubert, M.Moisan and H.Ricard,  
Spectrochim Acta 33B 1 (1979).
- (72) R.Darrah, Gov Rep Announce Index (US) 79 (10) 261 (1979).
- (73) M.Outred and C.Howard. J Phys E 11, 276 (1978).
- (74) J.C.Slater, "Microwave Electronics" van Nostrand (1952).
- (75) S.Ramo, J.R.Whinnery and T. van Duzer, "Fields and Waves  
in Communication Electronics",  
Wiley (1965).
- (76) W.G.Jung "IC OP-Amp Cookbook", Howard Sams (1976).
- (77) L.S.Orstein, Physica III, 651 (1936).
- (78) K.S.Seshadri and R.N.Jones,  
Spectrochim Acta 19B, 1013 (1963)
- (79) S.S.Penner, "Quantitative Molecular Spectroscopy and  
Gas Emissivities", Adison Wesley (1959).
- (80) J.R.Whinnery, H.W.Jamieson and T.E.Robbins,  
Proc IRE, Nov (1944).
- (81) A.Kraus, J.Brit. IRE 20, 137 (1960)
- (82) Mullard Technical Handbook,  
"Microwave Tubes and Components" (1976).
- (83) M.Outred, Spectrochim Acta 35B, 447 (1980).
- (84) Sucher and Fox, "Handbook of Microwave Measurements",  
Vol I, 3rd Edition (1963).
- (85) L.Spitzer Jnr, "The Physics of Fully Ionised Gases",  
Wiley (1962).
- (86) S.L.Leonard, in "Plasma Diagnostic Techniques", Editors  
R.H.Huddlestone and S.L.Leonard,  
Academic Press (1965).
- (87) J.L.Delcroix, "Introduction to the Theory of Ionised  
Gases", Wiley (1960).
- (88) M.Outred, Private Communication (1981).



- (89) W.L.Wiese, M.W.Smith and B.M.Miles, "Atomic Transition Probabilities" Vol II, NSRDS NBS 22 (1969).
- (90) C.E.Moore, "Atomic Energy Levels" Vol I, NSRDS NBS 35 (1971)
- (91) K.Katsonis and H.Drawin,  
J.Quant Spectrosc Radiat Transfer 23, 1 (1980).
- (92) J.M.Bridges and R.L.Kornblith,  
Astrophys J 192, 793 (1974).
- (93) W.L.Wiese and G.A.Martin,  
"Atomic Transition Probabilities" 61st Edition CRC "Handbook of Chemistry and Physics", (1981).
- (94) G.H.Dieke and H.M.Crosswhite,  
J.Quant Spectrosc Radiat Transfer 2, 97 (1961)
- (95) M.Baranger, "Atomic and Molecular Processes",  
Academic Press, (1962).
- (96) H.R.Griem, "Spectral Line Broadening by Plasmas",  
Academic Press, (1974).
- (97) M.Baranger, Phys Rev 111, 481 (1958).  
Phys Rev 111, 494 (1958).  
Phys Rev 112, 855 (1958).
- (98) A.C.Kolb and H.R.Griem,  
Phys Rev 111, 514 (1958).
- (99) P.W.Anderson, Phys Rev 76, 647 (1949).
- (100) H.A.Lorentz, Proc Acad Sci Amsterdam 8, 591 (1906).
- (101) J.Holtzmark, Ann Phys 58, 577 (1919).
- (102) E.W.Smith, J.Cooper and C.R.Vidal,  
Phys Rev 185, 140 (1969).
- (103) D.Voslamber, Z Naturforsch 24A, 1458 (1969).
- (104) C.R.Vidal, J.Cooper and E.W.Smith,  
J.Quant Spectrosc Radiat Transfer 10,1011,(1971).
- (105) C.R.Vidal, J.Cooper and E.W.Smith,  
Astrophys J.Suppl, Ser 25, 37 (1973).
- (106) D.J.Kalnicky, V.A.Fassel and R.N.Kniseley  
Appl Spectrosc 31, 137 (1977).
- (107) S.R.Goode and J.P.Deavor,  
Spectrochim Acta 39B, 813 (1984).
- (108) M.L.James, G.M.Smith and J.C.Wolford, "Applied Numerical Methods for Digital Computing with Fortran & CSMP", 93, New York (1977).

- (109) D.D.Smith and R.F.Browner,  
Anal Chem 54, 533 (1982).
- (110) D.L.Haas and J.A.Caruso,  
Anal Chem 56, 2014, (1984).
- (111) P.W.J.M.Boumans and M.Bosveld,  
Spectrochim Acta 34B, 59 (1979).
- (112) P.W.J.M.Boumans and F.J. de Boer,  
F.J.Dahmen, H.Hoelzel and A.Meier,  
Spectrochim Acta 30B, 449 (1975).
- (113) D.C.Schram, I.J.M.M.Raaijmakers, B van der Sijde,  
H.J.W.Schenkelaars and P.W.J.M.Boumans,  
Spectrochim Acta 38B, 1545 (1983).

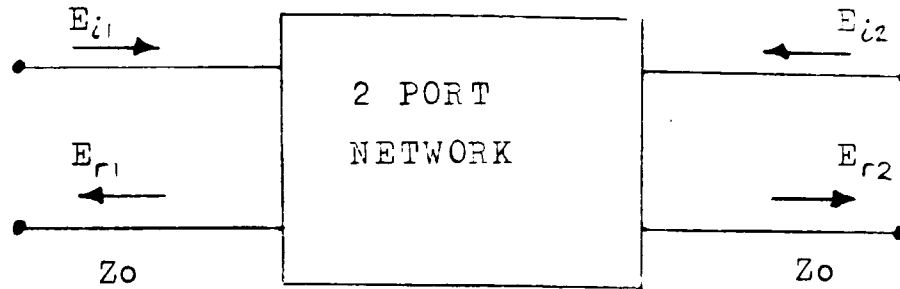
Figure A 1.1 A General 2 Port Network

Figure A 1.1 shows a general two-port network inserted into a transmission line of characteristic impedance  $Z_0$ . Voltage like waves  $E_{i1}$  and  $E_{i2}$  are incident upon each port of the network and similar waves,  $E_{r1}$  and  $E_{r2}$  are reflected from them. Total voltages and currents on the transmission line may be deduced from these incident and reflected waves by the simple equations:-

$$\begin{aligned} V_1 &= E_{i1} + E_{r1} & V_2 &= E_{i2} + E_{r2} \\ I_1 &= \frac{E_{i1} - E_{r1}}{Z_0} & I_2 &= \frac{E_{i2} - E_{r2}}{Z_0} \end{aligned}$$

Where  $V_1$ ,  $I_1$  are the total voltage and current values on the left side of the two-port network and  $V_2$ ,  $I_2$  are similar values for the right side.

As for eg. the hybrid (H) parameter representation of a two-port network these incident and reflected waves may be used to define a parameter set for the network, ie.

$$\begin{aligned} E_{r1} &= P_{11}E_{i1} + P_{12}E_{i2} \\ E_{r2} &= P_{21}E_{i1} + P_{22}E_{i2} \end{aligned}$$

where  $P_{11} \dots P_{22}$  are the defined parameters. Furthermore if each of the incident and reflected waves is normalized to the characteristic impedance of the

transmission line a new set of variables are obtained, ie.

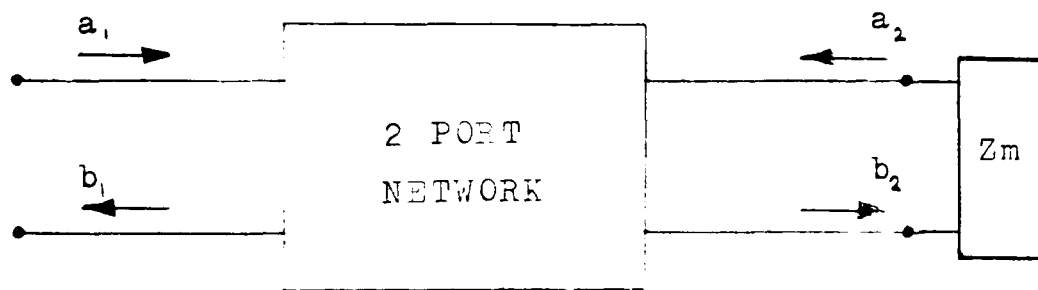
$$a_1 = \frac{E_{i1}}{Z_0}$$

$$a_2 = \frac{E_{i2}}{Z_0}$$

$$b_1 = \frac{E_{r1}}{Z_0}$$

$$b_2 = \frac{E_{r2}}{Z_0}$$

Substitution of these new variables back into the parameter set equations gives a new parameter set. Due to the alternative use of the word scattered to refer to waves reflected from a network as a consequence of waves incident upon it, this new parameter set has traditionally been referred to as the scattering (S) parameters of the network (See figure A 1.2). S parameter equations are also shown in the form of a matrix. The S parameter matrix is often referred to as the normalized scattering matrix  $[S^N]$ .



$$b_1 = S_{11}a_1 + S_{12}a_2$$

$$b_2 = S_{21}a_1 + S_{22}a_2$$

$$\begin{bmatrix} b_1 \\ b_2 \end{bmatrix} = \begin{bmatrix} S_{11} & S_{12} \\ S_{21} & S_{22} \end{bmatrix} \begin{bmatrix} a_1 \\ a_2 \end{bmatrix}$$

$$= [S^N] \begin{bmatrix} a_1 \\ a_2 \end{bmatrix}$$

Figure A 1.2      Scattering Parameter Representation of  
a 2 Port Network

For any parameter set, each parameter is physically measured when one or other of the variables is equal to zero. In the case of parameter sets used in low frequency circuits, eg. Z parameters, this normally involves attaining either zero voltage or current.

The open and short circuit terminations necessary to achieve such conditions at high frequencies are not easy to produce. The major advantage of S parameters is that to measure each parameter it is necessary only to set either an incident or reflected wave to zero. This may be illustrated if the right hand end of the transmission line (see figure A 1.2 is terminated with a matched load,  $Z_m$  equal in value to  $Z_o$ . Then the wave  $a_2$  will go to zero since all of the energy represented by wave  $b_2$  incident upon the matched load will be absorbed and no reflection will take place. The relevant S parameters are then expressed formally as:-

$$S_{11} = \left. \frac{b_1}{a_1} \right|_{a_2 = 0} \quad \text{and} \quad S_{21} = \left. \frac{b_2}{a_1} \right|_{a_2 = 0}$$

$S_{11}$  is the input reflection coefficient and  $S_{21}$  is the forward transmission coefficient with output port terminated in a matched load. By analogy, if a matched load is used to terminate the other end of the transmission line in figure A 1.2 then the remaining two S parameters may be measured, ie.

$$S_{22} = \left. \frac{b_2}{a_2} \right|_{a_1 = 0} \quad \text{and} \quad S_{12} = \left. \frac{b_1}{a_2} \right|_{a_1 = 0}$$

$S_{22}$  is the output reflection coefficient and  $S_{12}$  is the reverse transmission coefficient with the input port terminated in a matched load. The number of independent S parameters may be reduced when the exact physical properties of the two port network under discussion are considered. It should be noted that since generally the S parameters are complex quantities having modulus and argument there are 8 independent parameters involved.

If the network is reciprocal then  $S_{12} = S_{21}$ . If the network is lossless then the unitary matrix properties yield further reductions in the number of independent parameters, namely -

$$\begin{aligned} |S_{11}| &= |S_{22}| \\ |S_{12}| &= \sqrt{1 - |S_{11}|^2} \\ \phi_{12} &= \frac{\phi_{11} + \phi_{22}}{2} + \frac{\pi}{2} \pm n\pi \text{ where } n \text{ is an integer.} \end{aligned}$$

ie. the modulus and argument of  $S_{12}$  is completely specified by the reflection coefficients  $S_{11}$  and  $S_{22}$ . If the right hand end of the transmission line in figure A 1.2 is terminated in an unmatched load, ie. of a value not equal to  $Z_0$  the  $a_2 \neq 0$ . A load reflection coefficient  $\rho_L$  may be defined as

$$\rho_L = \frac{a_2}{b_2}$$

It can be shown that the normalized load impedance  $\hat{Z}_L$  is given by

$$\hat{Z}_L = \frac{1 + \rho_L}{1 - \rho_L}$$

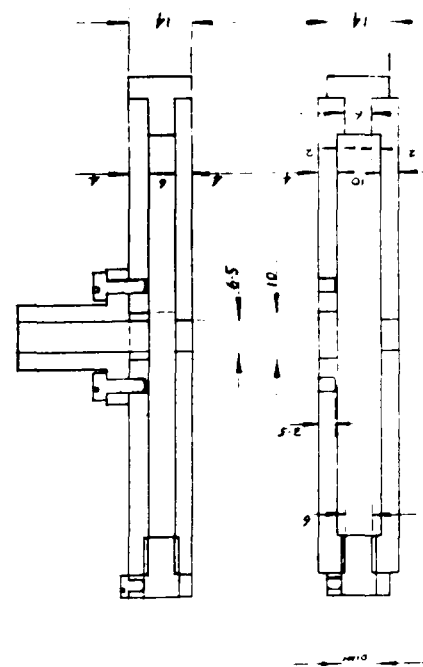
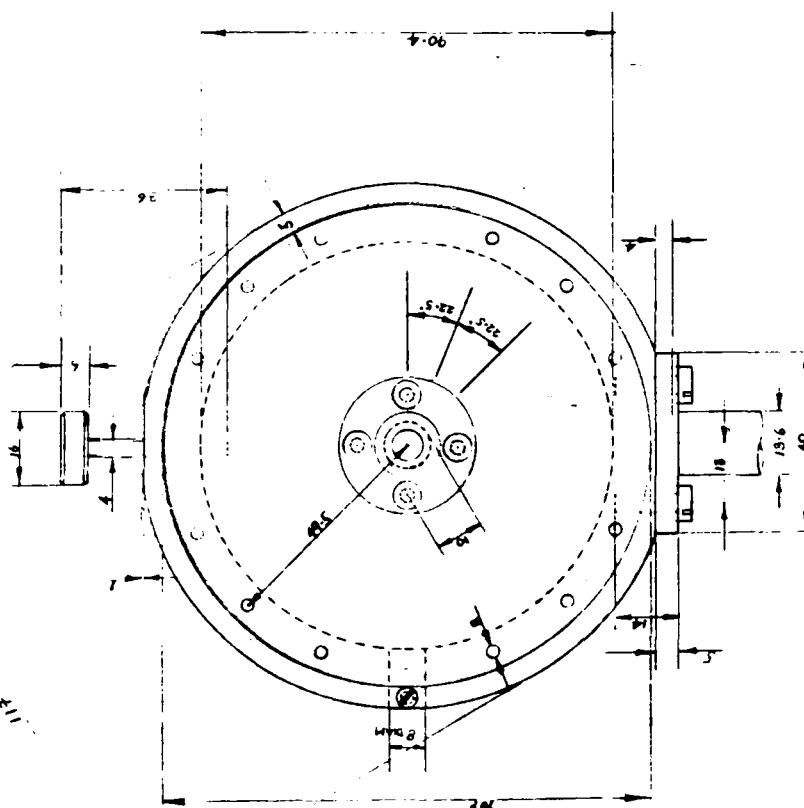
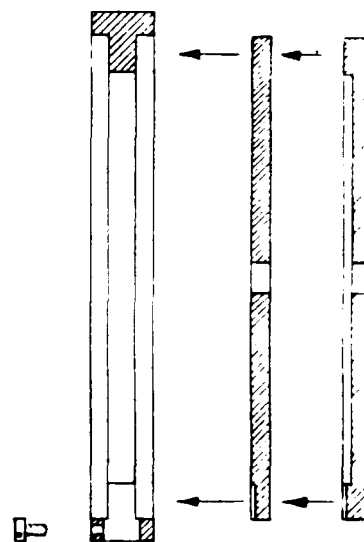
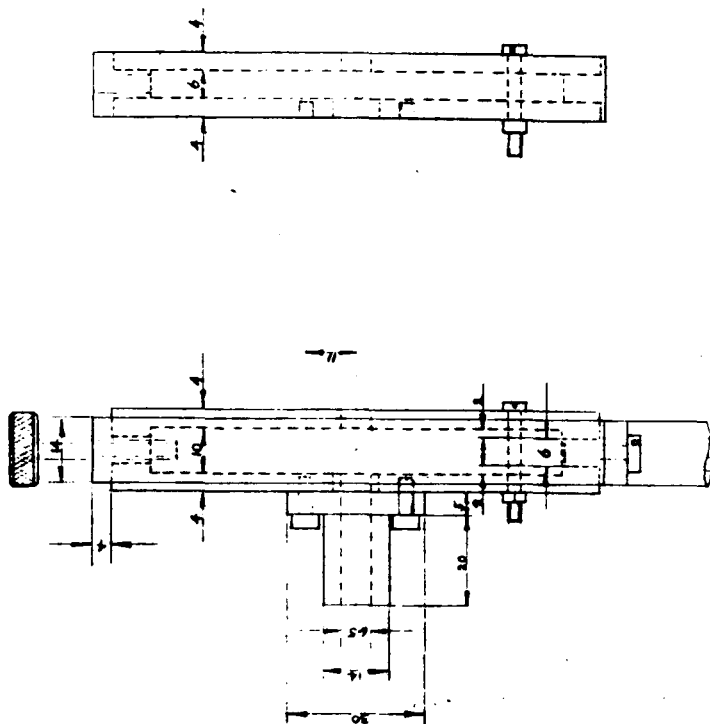
With the output of the network thus terminated an input reflection coefficient,  $\rho_{IN}$  may be defined as  $\rho_{IN} = \frac{b_1}{a_1}$

and expressed in terms of the network S parameters and  $\rho_L$  as

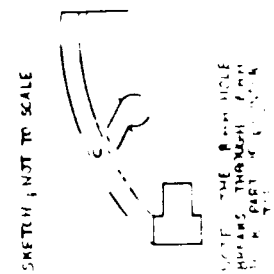
$$\rho_{IN} = \frac{b_1}{a_1} = \frac{S_{11} - S_{12} S_{21} \rho_L}{\rho_L - S_{22}}$$

This is an important feature of the S parameter representation of a two-port network, since measurement of the input reflection coefficient enables the load impedance to be determined when the network S parameters are known. This is of particular importance to the slab-line cavity since we may then calculate the impedance of the argon MIP from measurements of  $\rho_{IN}$  as detailed in section 4.3

Appendix A 2      Engineering Drawings of the TM<sub>C10</sub> Cavity  
and Input Coupling.



Modified TM<sub>010</sub> Cavity.  
 3rd Angle Projection.  
 Dimensions in mm  
 Scale 1: 1  
 Material: Brass  
 Note: 1 main body  
 plus 2 pairs side plates.





Input  
Cavity  
Scale  
Material  
(shaded  
sheet

Input Coupling for TM<sub>010</sub>  
Cavity. Sectional View  
Scale 4:1  
Material: Brass and PTFE  
(shaded). PTFE to be from  
sheet stock.  
Dimension A =  $1.79 \pm 0.025$  mm  
B =  $6.00 \pm 0.025$  mm

Appendix A 3

Computer Program to Calculate the Plasma  
Load Impedance from Measurements on the  
Slotted Line.

```

BEGIN
COMMENT    MICROWAVE PROGRAMME NUMBER 9 CALCULATES THE MICROWAVE
           IMPEDANCE OF THE PLASMA FOR ALL FLOW-RATES AND POWER
           LEVELS;

COMMENT    SLAB LINE CAVITY PARAMETERS.
           SL1=SPACING BETWEEN SLAB LINE PLATES (CMS).
           SL2=O.D OF SLAB LINE INNER (CMS).
           LSL2=LENGH OF SLAB LINE INNER (CMS).
           ZC=CHARACTERISTIC IMPEDANCE OF SLAB LINE (OHMS).
           ALPHAS=ATTENUATION IN SLAB LINE (DBS PER CM).

           COAXIAL FEED LINE PARAMETERS.
           CO1=I.D OF COAXIAL LINE OUTER (CMS).
           CO2=O.D OF COAXIAL LINE INNER (CMS).
           LCO2=LENGH OF COAXIAL LINE INNER (CMS).
           ZC=CHARACTERISTIC IMPEDANCE OF COAXIAL LINE (OHMS).
           ALPHAC=ATTENUATION IN COAXIAL LINE (DBS PER CM).

           COAXIAL CABLE PARAMETERS.
           ZO=CHARACTERISTIC IMPEDANCE OF CABLE (OHMS).;

EXTERNAL PROCEDURE G01AAA ;

REAL X1,X2,X3,X4,PI;
REAL MODRHOINMAX,MODRHOINMIN,PHYMIN,PHYMAX,WSUM,S3,S4;
REAL RPF,RPPSD,A,B,C,D,E,F;
REAL RS11,IMS11,RS12,IMS12,RS21,IMS21,RS22,IMS22,U1,U2;
REAL RT11,IMT11,RT12,IMT12,RT21,IMT21,RT22,IMT22;
REAL SL1,SL2,LSL2,ZC,CO1,CO2,LCO2,ZC,ZO,YO,SL1A;
REAL BETA,B1,B2,A1,A2,B11,B12,B13,B14,AM1,AM2;
REAL T1,T2,T3,T4,T5,T6,X,Y,Y1;
REAL CGAP,SPACER,IDTUBE,ODTUBE,SIGMA;
REAL ALPHA,ALPHA1,ALPHA2,ACCALPHAC,ACCALPHAS,FRE;

INTEGER I,J,K,N,M,V,FL,T,IWT,IFAIL;

STRING GAS,GAIN,VIEWPOS,EXPTDATE;

ARRAY  LMINC1:63,  SUBC1:63,  PHYRHOINC1:63,  SC1:63,
       MODRHOINC1:63,WTE1:63;

```

```

PROCEDURE MULTIPLY (A,B,C,D,E,F);
REAL A,B,C,D,E,F;
BEGIN
A:=C*D-E*F ; B:=D*E+C*F ;
END;

```

```

PROCEDURE DIVIDE (A,B,C,D,E,F);
REAL A,B,C,D,E,F;
BEGIN
A:=(C*D+E*F)/(E*E+F*F); B:=(D*E-C*F)/(E*E+F*F);
END;

```

```

PROCEDURE ADD (A,B,C,D,E,F);
REAL A,B,C,D,E,F;
BEGIN
A:=C+E; B:=D+F;
END;

```

```

PROCEDURE SUBTRACT (A,B,C,D,E,F);
REAL A,B,C,D,E,F;
BEGIN
A:=C-E; B:=D-F;
END;

```

```

OUTPUT(2,"DSK");
OPENFILE(2,"M9DATA.OUT");
OUTPUT(3,"TTY");
INPUT(0,"TTY");
SELECTINPUT(0);
INPUT(4,"DSK");
OPENFILE(4,"M9DATA.RAW");

```

```

WRITE("ENDTHIS IS PROGRAM FRED? EVALUATING PLASMA IMPEDANCEEND");
WRITE("TODAYS DATE IS ");WRITE(VDATE);

```

```

WRITE("ENDDO YOU REQUIRE HIGH OR LOW GAIN CAVITY DIMENSIONS
FROM STOREEND");

```

```

READ(GAIN);
BEGIN
IF GAIN="HIGH" THEN
BEGIN
INPUT(1,"DSK");
OPENFILE(1,"M9DATA.INH");
END
ELSE
BEGIN
INPUT(1,"DSK");
OPENFILE(1,"M9DATA.INL");
END;
END;

```

```

SELECTINPUT(1);

READ(SL1);READ(SL2);READ(LSL2);READ(CO1);READ(CO2);READ(LCO2);
READ(SPACER);
WRITE("DATA ENTERED ISCNJ ");WRITE("SL1 = ");PRINT(SL1,3,2);
WRITE("ENJSL2 = ");PRINT(SL2,3,3);
WRITE("ENJLSL2 = ");PRINT(LSL2,4,3);WRITE("ENJCO1 = ");
PRINT(CO1,3,2);WRITE("ENJCO2 = ");PRINT(CO2,3,2);
WRITE("ENJLCO2 = ");PRINT(LCO2,3,2);
WRITE("ENJCAVITY SPACER = ");PRINT(SPACER,4,3);

COMMENT      CALCULATION OF ADDITIONAL PARAMETERS;
              PI:=3.14159;
              SL1A := SL1 * 4.0/PI;
              ZO := 50 ;
              SIGMA := 10^(6) ;

COMMENT      CALCULATION OF IMPEDANCES ;
              ZC := 59.933*LN(CO1/CO2);
              ZS := 59.933*LN(SL1A/SL2);

COMMENT      CALCULATION OF U VALUES;
              U1 := (ZO + ZC)/(2.0*ZO);
              U2 := (ZO - ZC)/(2.0*ZO);

COMMENT      CALCULATION OF ATTENUATION VALUES (PART 1);
              ALPHA := 9.95*(10^(-6))/0.434294;
              ALPHA1 := ALPHA*(1/CO1 + 1/CO2)/LN(CO1/CO2);
              ALPHA2 := ALPHA*(1/SL1A + 1/SL2)/LN(SL1A/SL2);

READ(GAS);
WRITE("ENJPLASMA GAS=");WRITE(GAS);

COMMENT      CALCULATION OF S PARAMETERS;
              RS11 := (ZC + ZS)/(2*ZC);
              IMS11 := 0.0;
              RS22 := RS11;
              IMS22 := IMS11;
              RS12 := (ZC - ZS)/(2*ZC);
              IMS12 := 0.0;
              RS21 := RS12;
              IMS21 := IMS12;

COMMENT      CALCULATION OF COUPLING GAP;
              CGAP := (SPACER - 0.5) - LSL2 ;

READ(ODTUBE);READ(IDTUBE);
WRITE("ENJPLASMA TUBE O.D =");PRINT(ODTUBE,3,2);
WRITE("      MMSCNJ");
WRITE("PLASMA TUBE I.D =");PRINT(IDTUBE,3,2);
WRITE("      MMSCNJ");

READ(RPF);READ(RPPSD);
WRITE("RPF=");PRINT(RPF,5,3);WRITE("  CMS.  ");WRITE("RPPSD=");
PRINT(RPPSD,4,3);WRITE("  CMSCNJ");

```

```

SELECTINPUT(4);

READ(EXPTDATE);
WRITE("ENDDATA ACQUIRED ON ");WRITE(EXPTDATE);

READ(T);
WRITE("ENDNO OF FLOW-RATES USED=");PRINT(T,2,0);

READ(VIEWPOS);WRITE("ENDSPECTROMETER VIEWING POSITION IS ");
WRITE(VIEWPOS);

BEGIN

ARRAY FLOWC1:T3, SUMALPHAC1:T3, SUMALPHASE1:T3;

        ACCALPHAS := 0.0;
        ACCALPHAC := 0.0;

FOR FL:=1 STEP 1 UNTIL T DO
BEGIN

SELECTOUTPUT(3);

READ(FLOWCFL3);
WRITE("ENDFLOW-RATE=");PRINT(FLOWCFL3,5,1);
WRITE(" ML PER MINE2N");

READ(J);
WRITE("NO OF POWER READINGS=");PRINT(J,2,0);

M:=6; V:=7;
SUMALPHASEFL3 := 0.0; SUMALPHACEFL3 := 0.0;

BEGIN

ARRAY POWERINC1:J3, POWEROUT1:J3, NETINPUTPWR1:J3,
        LAMDA1:J3, LENC1:J3, UFREQ1:J3,
        ALPHAC1:J3, ALPHASE1:J3,
        RRHOINC1:J3, IMRHOINC1:J3,
        MODRHOINMEANC1:J3, SM2C1:J3, PHYMEANC1:J3, S2C1:J3,
        RZINC1:J3, IMZINC1:J3, MODZINC1:J3, PHYZINC1:J3,
        RRHOLE1:J3, IMRHOLE1:J3, MODRHOLE1:J3, PHYRHOLE1:J3,
        RZLE1:J3, IMZLE1:J3, MODZLE1:J3, PHYZLE1:J3,
        CSE1:J3, SNE1:J3;

FOR K:=1 STEP 1 UNTIL J DO
BEGIN
READ(POWERINEK3);READ(POWEROUTEK3);

POWERINEK3 := POWERINEK3 * 93.325 ;
POWEROUTEK3 := POWEROUTEK3 * 89.125 ;

```

```

SELECTOUTPUT(3);

WRITE("I2N]INPUT POWER=");PRINT(POWERIN[K],5,2);WRITE(" WATTSEN]");
WRITE("REFLECTED POWER=");PRINT(POWEROUT[K],5,2);
WRITE(" WATTSEN]");

COMMENT CALCULATION OF NET INPUT POWER ;
NETINPUTPWR[K]:=POWERIN[K] - POWEROUT[K] ;
WRITE("NET INPUT POWER=");PRINT(NETINPUTPWR[K],5,2);
WRITE(" WATTSE2N]");

READ(LEN[K]);
WRITE("PLASMA LENGTH=");PRINT(LEN[K],3,1);WRITE(" CMSEN]");

COMMENT READING LMIN DATA;
BEGIN
FOR I:=1 STEP 1 UNTIL M DO
BEGIN
READ(LMINE[I]);
END;
END;

COMMENT CALCULATION OF VSWR & MODRHOIN ;
BEGIN
FOR N:=1,N+1 WHILE N<=V DO
BEGIN
READ(SDBEN]);
SDBEN]:=SDBEN]/20;
SEN]:=10^SDBEN];
MODRHOINEN]:=(SEN]-1)/(SEN]+1);
END;
END;

COMMENT CALCULATION OF LAMDA[K] & UFREQ[K] ;
X1:=LMINE1] - LMINE4];X2:=LMINE2] - LMINE5];
X3:=LMINE3] - LMINE6];
X4:=X1+X2+X3;LAMDA[K]:=X4*2/9;
UFREQ[K]:=29.9777/LAMDA[K];

COMMENT CALCULATION OF ATTENUATION VALUES (PART 2);
FRE := SQRT(UFREQ[K] * (10^(9))/SIGMA);
ALPHACK] := ALPHA1 * FRE/20 ;
ALPHASEK] := ALPHA2 * FRE/20 ;

COMMENT CALCULATION OF RUNNING MEAN(S) OF ALPHACK]
AND ALPHASEK];
SUMALPHACEFL] := SUMALPHACEFL] + ALPHACK];
SUMALPHASEFL] := SUMALPHASEFL] + ALPHASEK];

ALPHACK] := SUMALPHACEFL] /K;
ALPHASEK] := SUMALPHASEFL] /K;

```

```

COMMENT  CALCULATION OF PHYRHOIN ;
BEGIN
FOR I:=1 STEP 1 UNTIL M DO
BEGIN
PHYRHOINCII:=4.0*PI*((RPP-LMINCII)-((I+2)*LAMDACKI/2)
                                     *LAMDACKI/4)/LAMDACKI);
END;
END;

COMMENT  CALCULATION OF MEAN VALUE OF PHYRHOIN ;
BEGIN
IFAIL:=0;
GO1AAA(M,PHYRHOIN,IWT,WT,PHYMEANCKI,S2CKI,S3,S4,
PHYMIN,PHYMAX,WSUM,IFAIL);
IWT:=0;
IF IFAIL=0 THEN
BEGIN
WRITE("ENMEAN VALUE OF PHYRHOIN=");PRINT(PHYMEANCKI,5,3);
WRITE("  RAD");
WRITE("ENSTANDARD DEVIATION=");PRINT(S2CKI,5,4);
WRITE("  RAD");
WRITE("ENNO OF VALUES USED=");PRINT(M,2,0);NEWLINE;
END;
END;

COMMENT  CALCULATION OF MEAN VALUE OF MODRHOIN ;
BEGIN
IFAIL:=0;
GO1AAA(V,MODRHOIN,IWT,WT,MODRHOINMEANCKI,SM2CKI,S3,S4,
MODRHOINMIN,MODRHOINMAX,WSUM,IFAIL);
IWT:=0;
IF IFAIL=0 THEN
BEGIN
WRITE("ENMEAN VALUE OF MODRHOIN=");
PRINT(MODRHOINMEANCKI,4,3);
WRITE("ENSTANDARD DEVIATION=");PRINT(SM2CKI,5,4);
WRITE("ENNO OF VALUES USED=");PRINT(V,2,0);
END;
END;

COMMENT  CALCULATION OF REAL AND IMAGINARY PARTS OF INPUT
REFLECTION COEFFICIENT;
CSEKI :=COS(PHYMEANCKI);
SNEKI := SIN(PHYMEANCKI);
RRHOINEKI := MODRHOINMEANCKI * CSEKI;
IMRHOINEKI := MODRHOINMEANCKI * SNEKI;

COMMENT  CALCULATION OF T PARAMETERS;
BETA:=2.0*PI/LAMDACKI;
B1:=BETA*(LSL2 + LC02);
B2:=BETA*(LSL2 - LC02);
A1:=ALPHASEKI*LSL2 + ALPHACEKI*LC02 ;
A2:=ALPHASEKI*LSL2 - ALPHACEKI*LC02 ;
B11:=COS(B1);B12:=SIN(B1);B13:=COS(B2);B14:=SIN(B2);

```



```

COMMENT      CALCULATION OF T11;
              AM1:=U1*EXP(A1);
              AM2:=U2*EXP(A2);
              MULTIPLY(T1,T2,RS11,IMS11,B11,B12);
              MULTIPLY(T3,T4,RS12,IMS12,B13,B14);
              RT11:=AM1*T1 + AM2*T3 ;
              IMT11:=AM1*T2 + AM2*T4 ;

COMMENT      CALCULATION OF T12;
              AM1:=U2*EXP(A1);
              AM2:=U1*EXP(A2);
              MULTIPLY(T1,T2,RS11,IMS11,B11,B12);
              MULTIPLY(T3,T4,RS12,IMS12,B13,B14);
              RT12:=AM1*T1 + AM2*T3 ;
              IMT12:=AM1*T2 + AM2*T4 ;

COMMENT      CALCULATION OF T21;
              B12:=-SIN(B1); B14:=-SIN(B2);
              AM1:=U1*EXP(-A2);
              AM2:=U2*EXP(-A1);
              MULTIPLY(T1,T2,RS21,IMS21,B13,B14);
              MULTIPLY(T3,T4,RS22,IMS22,B11,B12);
              RT21:=AM1*T1 + AM2*T3 ;
              IMT21:=AM1*T2 + AM2*T4 ;

COMMENT      CALCULATION OF T22;
              AM1:=U2*EXP(-A2);
              AM2:=U1*EXP(-A1);
              MULTIPLY(T1,T2,RS21,IMS21,B13,B14);
              MULTIPLY(T3,T4,RS22,IMS22,B11,B12);
              RT22:=AM1*T1 + AM2*T3 ;
              IMT22:=AM1*T2 + AM2*T4 ;

SELECTOUTPUT(2);

COMMENT      PRELIMINARY PRINTING OF T PARAMETERS;
              WRITE("INIT PARAMETERS EVALUATED ARECN");
              WRITE("T11 =");PRINT(RT11,5,3);WRITE(" ");
              PRINT(IMT11,5,3);WRITE(" JCN");
              WRITE("T12 =");PRINT(RT12,5,3);WRITE(" ");
              PRINT(IMT12,5,3);WRITE(" JCN");
              WRITE("T21 =");PRINT(RT21,5,3);WRITE(" ");
              PRINT(IMT21,5,3);WRITE(" JCN");
              WRITE("T22 =");PRINT(RT22,5,3);WRITE(" ");
              PRINT(IMT22,5,3);WRITE(" JCN");

COMMENT      CALCULATION OF LOAD REF COEFF;
              MULTIPLY(T1,T2,RRHOINEKJ,IMRHOINEKJ,RT11,IMT11);
              ADD(T3,T4,T1,T2,RT12,IMT12);
              MULTIPLY(T1,T2,RRHOINEKJ,IMRHOINEKJ,RT21,IMT21);
              ADD(T5,T6,T1,T2,RT22,IMT22);
              DIVIDE(RRHOLEKJ,IMRHOLEKJ,T3,T4,T5,T6);
              MODRHOLEKJ:=SQRT((RRHOLEKJ^2) + (IMRHOLEKJ^2));
              PHYRHOLEKJ:=180/PI * ARCTAN(IMRHOLEKJ/RRHOLEKJ);

```

```

COMMENT    CALCULATION OF CAVITY INPUT AND LOAD IMPEDANCE;
X:=(1 + RRHOINEKJ);
Y:=(1 - RRHOINEKJ)/50;
Y1:=-IMRHOINEKJ/50;
DIVIDE(RZINEKJ,IMZINEKJ,X,IMRHOINEKJ,Y,Y1);
MODZINEKJ:=SQRT((RZINEKJ^2) + (IMZINEKJ^2));
PHYZINEKJ:=180/PI * ARCTAN(IMZINEKJ/RZINEKJ);

X:=1 + RRHOLEKJ;
Y:=(1 - RRHOLEKJ)/ZC;
Y1:= -IMRHOLEKJ/ZC;
DIVIDE(RZLEKJ,IMZLEKJ,X,IMRHOLEKJ,Y,Y1);
MODZLEKJ:=SQRT((RZLEKJ^2) + (IMZLEKJ^2));
PHYZLEKJ:=180/PI * ARCTAN(IMZLEKJ/RZLEKJ);

SELECTOUTPUT(2);
END;
WRITE("C2NJFINAL TABLE OF DATAENJ");

WRITE("ENIGAS FLOW-RATE=");PRINT(FLOWEFLJ,5,0);
WRITE("    ML PER MINENJ");WRITE("THIS FLOW-RATE IS NO(");
PRINT(FL,2,0);WRITE(")OF(");PRINT(T,2,0);
WRITE(")FLOW-RATE READINGSENJ");
WRITE("VALUE OF RPP USED=");
PRINT(RPP,5,3);WRITE("    CMS,    ");
WRITE("SD ON RPP=");PRINT(RPPSD,4,3);WRITE("    CMSENJ");

WRITE("ENIMICROWAVE POWER (W),      LAMDA      FREQ  DIS LENGTHENJ");
WRITE("    I/P,      REF, NET-I/P,    CMS      GHZ      CMSENJ");
    BEGIN
    FOR K:=1 STEP 1 UNTIL J DO
    BEGIN
    NEWLINE;
    PRINT(POWERINEKJ,4,1);PRINT(POWEROUTEKJ,3,1);
    PRINT(NETINPUTPWEKJ,4,1);WRITE("    ");PRINT(LAMDAEKJ,4,2);
    WRITE("    ");PRINT(UFREKEKJ,4,3);WRITE("    ");PRINT(LENKJ,3,3);
    END;
    END;

WRITE("C2NJNET MCWAVE      CAVITY INPUT REFLECTION  COEFF");
WRITE("    LOAD  IMPEDANCE ENJ");
WRITE("    I/P PWR(W)      MOD      SD      PHY      SD      ");
WRITE("REAL      IMAGENJ");

    BEGIN
    FOR K:=1 STEP 1 UNTIL J DO
    BEGIN
    PRINT(NETINPUTPWEKJ,4,1);WRITE("    ");
    PRINT(MODRHOINMEANEKJ,4,3);PRINT(SH2EKJ,5,4);
    PRINT(PHYMEANEKJ,5,3);
    PRINT(S2EKJ,5,4);
    PRINT(RZLEKJ,5,3);WRITE("    ");PRINT(IMZLEKJ,5,3);
    WRITE("    JENJ");
    END;
    END;
END;

```

```

COMMENT    CALCULATION OF ATTENUATION VALUES(PART 3)
            EVALUATION OF MEAN VALUES OF ALPHAC AND
            ALPHAS OVER ALL J READINGS;
            SUMALPHACEFLJ := SUMALPHACEFLJ/J;
            SUMALPHASEFLJ := SUMALPHASEFLJ/J;

END;

COMMENT    CALCULATION OF ATTENUATION VALUES (PART 4)
            EVALUATION OF MEAN VALUE OF ALPHAC AND
            ALPHAS OVER ALL T READINGS;
            BEGIN
            FOR FL :=1 STEP 1 UNTIL T DO
            BEGIN
            ACCALPHAC := ACCALPHAC + SUMALPHACEFLJ;
            ACCALPHAS := ACCALPHAS + SUMALPHASEFLJ;
            END;
            END;
            ACCALPHAC := ACCALPHAC/T;
            ACCALPHAS := ACCALPHAS/T;

END;

WRITE("EN]TABLE OF PHYSICAL PARAMETERS]EN]");
WRITE("SEPARATION OF SLAB-LINE PLATES=");PRINT(SL1,3,2);
WRITE("  CMS]EN]");
WRITE("O.D OF SLAB-LINE INNER=");PRINT(SL2,3,3);WRITE("  CMS]EN]");
WRITE("LENGTH OF SLAB-LINE INNER=");PRINT(LSL2,4,3);WRITE("  CMS]EN]");
WRITE("CHARACTERISTIC IMPEDANCE OF SLAB-LINE=");PRINT(ZS,4,1);
WRITE("  OHMS]EN]");
WRITE("ATTENUATION IN SLAB-LINE(MEAN OF ALL READINGS)=");
PRINT(ACCALPHAS,4,4);WRITE("  DB PER CM]EN]");
WRITE("EN]LENGTH OF CAVITY SPACER=");PRINT(SPACER,4,3);
WRITE("  CMS]EN]");
WRITE("COUPLING GAP=");PRINT(CGAP,3,3);WRITE("  CMS]EN]");
WRITE("EN]I.D OF COAXIAL LINE OUTER=");PRINT(CO1,4,3);WRITE("  CMS]EN]");
WRITE("O.D OF COAXIAL LINE INNER=");PRINT(CO2,4,3);WRITE("  CMS]EN]");
WRITE("LENGTH OF COAXIAL LINE INNER=");PRINT(LCO2,4,3);WRITE("  CMS]EN]");
WRITE("EN]CHARACTERISTIC IMPEDANCE OF COAXIAL LINE=");PRINT(ZC,3,1);
WRITE("  OHMS]EN]");
WRITE("ATTENUATION IN COAXIAL LINE(MEAN OF ALL READINGS)=");
PRINT(ACCALPHAC,4,4);WRITE("  DB PER CM]EN]");

write("En]plasma gas=");WRITE(GAS);

WRITE("EN]PLASMA TUBE O.D=");PRINT(ODTUBE,3,2);WRITE("  MM]EN]");
WRITE("PLASMA TUBE I.D=");PRINT(IDTUBE,3,2);WRITE("  MM]EN]");

WRITE("VIEWING POSITION IS ");
WRITE(VIEWPOS);

```

```

WRITE("I2N]SCATTERING PARAMETERS FOR CAVITY AREI2N]");
WRITE("S11 = S22 =");PRINT(RS11,4,2);
WRITE(",          S12 = S21 =");PRINT(RS12,4,2);

WRITE("I2N]U VALUES FOR CAVITY COAXIAL FEED/50 OHM JUNCTION AREI2N]");
WRITE("U1 =");PRINT(U1,4,2);
WRITE(",          U2 =");PRINT(U2,4,2);

WRITE("I3N]TODAYS DATE IS ");
WRITE(VDATE);WRITE(" ,IE WHEN DATA PROCESSED");
WRITE("I2N]EXPERIMENTAL DATA ACQUIRED ON ");
WRITE(EXPTDATE);

SELECTOUTPUT(3);

WRITE("I10N]          FINAL RESULTS TABLES ,T PARAMETERS AND A TABLE OF
          PHYSICAL PARAMETERS ARE PRINTED ON DATAFILE
          NAMED M9DATA.OUTI2N]");

CLOSEFILE(2);
CLOSEFILE(1);
CLOSEFILE(4);
END

```



```

BEGIN

COMMENT PROGRAMME CALCULATES LOGE(ID/CA) FOR SELECTED ARGON.
SPECTRAL LINES.;

REAL TEMP,C1,C2,A1,A2,B1,PWR,SUR,FL;

INTEGER I,J,K,L,P,N;

ARRAY   LAMDAE1:303,BOE1:303,BE1:303,EPSILONE1:303,MFBE1:303,
MONOMFE1:303,MONOMFTOLE1:303,
SYSTEMMFE1:303,PLUSE1:303,MINUSE1:303,SYSTEMMFTOLE1:303;
ARRAY   INTE1:303,INTTOLC1:303,INTERRE1:303,
INTMAXE1:303,INTMINE1:303,GAINC1:303,GAINMFE1:303,
WAVELENGTHE1:303,TRANPROBE1:303,TRPRBERRE1:303,
STATWTE1:303,UPPENERGYE1:303,YE1:303,YMAXE1:303,
YMINE1:303;

STRING EXPTDATE,CALDATE,TYPE,TUBE,VIEWSPOS;

INPUT(1,"DSK");
OPENFILE(1,"MONO.DAT");
INPUT(4,"DSK");
OPENFILE(4,"EXPT.DAT");
INPUT(5,"DSK");
OPENFILE(5,"FUND.DAT");
OUTPUT(2,"DSK");
OPENFILE(2,"DATA1.OUT");
OUTPUT(3,"TTY");

WRITE("C2N3THIS PROGRAMME EVALUATES BOLTZMANN FORMULA FROM SPECTRAL
INTENSITY DATAEND");
WRITE("TODAYS DATE IS ");WRITE(VDATE);

COMMENT READING OF SYSTEM CALIBRATION DATA.;

SELECTINPUT(1);

READ(CALDATE);
READ(I);

    FOR J:=1 STEP 1 UNTIL I DO
    BEGIN
    READ(LAMDAEJJ);
    END;
    FOR J:=1 STEP 1 UNTIL I DO
    BEGIN
    READ(EPSILONEJJ);
    END;
READ(TEMP);

    FOR J:=1 STEP 1 UNTIL I DO
    BEGIN
    READ(MONOMFEJJ);READ(MONOMFTOLEJJ);
    END;

C1:=1.19109* 10(-16);
C2:=0.014375;

```

COMMENT CALCULATION OF BLACK BODY AND GREY BODY COEFFICIENTS.;

```
BEGIN
  FOR J:=1 STEP 1 UNTIL I DO
    BEGIN
      A1:=TEMP*LAMDALCJJ;
      A2:=C2/A1;
      A2:=A2*10(9);
      A2:=EXP(A2);
      A2:=A2 - 1;
      B1:=LAMDALCJJ * 10(-9);
      B1:=B1(5);
      BOEJJ:=C1 * 10(-7)/(A2*B1);
      BEJJ:= BOEJJ * EPSILONCJJ;
    END;
  END;
```

COMMENT CALCULATION OF GREY BODY COEFF MULTIPLYING FACTOR.;

```
BEGIN
  FOR J:=1 STEP 1 UNTIL I DO
    BEGIN
      MFBEJJ:=BE153/BEJJ;
    END;
  END;
```

COMMENT CALCULATION OF OVERALL SYSTEM MULTIPLYING FACTOR INCLUDING THE EFFECT OF GREY BODY RADIATION AND MONOCHROMATOR RESPONSE WHICH INCLUDES THE EFFECT OF THE OY4 AND SMOKED GLASS FILTERS USED IN BOTH CALIBRATION AND LINE SCANS.;

```
BEGIN
  FOR J:=1 STEP 1 UNTIL I DO
    BEGIN
      SYSTEMMFEJJ:=MONOMFEJJ/MFBEJJ;

      PLUSEJJ:=MONOMFEJJ+MONOMFTOLEJJ;
      PLUSEJJ:=PLUSEJJ/MFBEJJ;
      PLUSEJJ:=PLUSEJJ-SYSTEMMFEJJ;

      MINUSEJJ:=MONOMFEJJ-MONOMFTOLEJJ;
      MINUSEJJ:=MINUSEJJ/MFBEJJ;
      MINUSEJJ:=SYSTEMMFEJJ-MINUSEJJ;

      SYSTEMMFTOLEJJ:=(PLUSEJJ+MINUSEJJ)/2;
    END;
  END;
```

```
SELECTOUTPUT(2);
WRITE("C2NITUNGSTEN EMISSION LAMP DATA TABLEND");
WRITE("MONOCHROMATOR RESPONSE CHECKED ON ");WRITE(CALDATE);NEWLINE;
WRITE("FILAMENT TEMPERATURE IS ");PRINT(TEMP,5,0);
WRITE(" DEG KELVINEND");
WRITE("END  LAMDA(NM)      BO      EMISS      B
      MFB#END");
```

```

BEGIN
  FOR J:=1 STEP 1 UNTIL I DO
  BEGIN
    NEWLINE;
    PRINT(LAMDAEJJ,6,3);WRITE(" ");
    PRINT(BOEJJ,7,2);WRITE(" ");
    PRINT(EPSILONEJJ,5,4);WRITE(" ");
    PRINT(BEJJ,6,2);WRITE(" ");
    PRINT(MFBEJJ,5,3);
  END;
END;

WRITE("I4N3SYSTEM CALIBRATION MULTIPLYING FACTOR TABLEEN3");
WRITE("EN3      LAMDA(NM)          SYSTEM MF#      TOLERANCEIN3");
BEGIN
  FOR J:=1 STEP 1 UNTIL I DO
  BEGIN
    NEWLINE;
    PRINT(LAMDAEJJ,6,3);WRITE(" ");
    PRINT(SYSTEMMFEJJ,6,3);WRITE(" ");
    PRINT(SYSTEMMFTOLEJJ,5,3);
  END;
END;

WRITE("I2N3# ALL MULTIPLYING FACTORS HAVE BEEN EVALUATED USING THE
603.213NM LINE AS A REFERENCEEN3");
WRITE("I4N3FINAL TABLES OF COMPUTED VALUESEN3");

COMMENT READING OF FUNDAMENTAL DATA ON ARGON AND HYDROGEN SPECIES.;

SELECTINPUT(5);
SELECTOUTPUT(3);
READ(L);

BEGIN
  IF L=I THEN
  BEGIN
    WRITE("I2N3PROGRAMME RUNNING OK ,L=IEN3");
  END
  ELSE
  BEGIN
    WRITE("I2N3L DOES NOT EQUAL I ,SUGGEST YOU ABORTEN3");
  END;
END;

BEGIN
  FOR J:=1 STEP 1 UNTIL L DO
  BEGIN
    READ(WAVELENGTHEJJ);READ(TRANPROBEJJ);
    READ(TRFRBERREJJ);READ(STATWTEJJ);
    READ(UPFENERGYEJJ);
  END;
END;

COMMENT READING OF EXPERIMENTAL DATA AND CALCULATION OF INTENSITY.
OF SPECTRAL LINES WITH ERRORS.;

SELECTINPUT(4);
READ(N);

```



```

SELECTOUTPUT(2);
WRITE("NUMBER OF EXPERIMENTAL RUNS ANALYSED = ");PRINT(N,2,0);

BEGIN
    FOR P:=1 STEP 1 UNTIL N DO
    BEGIN

        READ(EXPTDATE);
        READ(TUBE);
        READ(FL);
        READ(SUR);
        READ(VIEWPOS);
        READ(PWR);
        READ(K);
        READ(TYPE);

        SELECTOUTPUT(3);

        BEGIN
            IF K = I THEN
            BEGIN
                WRITE("E2N1PROGRAMME RUNNING OK , I = KEN1");
            END
            ELSE
            BEGIN
                WRITE("E2N1I DOES NOT EQUAL K,SUGGEST YOU
                    ABORTEN1");
            END;
        END;

        BEGIN
            FOR J:=1 STEP 1 UNTIL K DO
            BEGIN

                READ(INTEJ);READ(INTERREJ);READ(GAINEJ);

                GAINMFEJ:=3/GAINEJ;

                INTERREJ:=INTERREJ/100;
                INTERREJ:=INTERREJ*INTEJ;
                PLUSEJ:=INTERREJ+INTEJ;
                MINUSEJ:=INTEJ-INTERREJ;

                INTMAXEJ:=GAINMFEJ*PLUSEJ*(SYSTEMMFEJ+
                    SYSTEMMFTOLEJ);
                INTMINEJ:=GAINMFEJ*MINUSEJ*(SYSTEMMFEJ-
                    SYSTEMMFTOLEJ);

                INTEJ:=GAINMFEJ*INTEJ*SYSTEMMFEJ;

                PLUSEJ:=INTMAXEJ-INTEJ;
                MINUSEJ:=INTEJ-INTMINEJ;
                INTERREJ:=(PLUSEJ+MINUSEJ)/2;
                INTERREJ:=(INTERREJ/INTEJ)*100;
            END;
        END;
    END;

```

COMMENT CALCULATION OF FINAL FIGURES IN BOLTZMANN.  
EQUATION..;

BEGIN

```

FOR J:=1 STEP 1 UNTIL L DO
BEGIN
  YEJJ:=(INTEJJ*WAVELENGTHEJJ*10)/(TRANPROBEJJ
    *STATWTEJJ);
  YEJJ:=LN(YEJJ);

  PLUSEJJ:=TRANPROBEJJ*(TRFRBERREJJ/100);
  MINUSEJJ:=TRANPROBEJJ-PLUSEJJ;
  PLUSEJJ:=TRANPROBEJJ+PLUSEJJ;

  YMAXEJJ:=(INTMAXEJJ*WAVELENGTHEJJ*10)/
    (MINUSEJJ*STATWTEJJ);
  YMINEJJ:=(INTMINEJJ*WAVELENGTHEJJ*10)/
    (PLUSEJJ*STATWTEJJ);

  YMAXEJJ:=LN(YMAXEJJ);
  YMINEJJ:=LN(YMINEJJ);

```

END;

END;

SELECTOUTPUT(2);

```

WRITE("END]EXPERIMENT OF ");WRITE(EXPTDATE);
WRITE("END]DISCHARGE TUBE DIAMETER = ");WRITE(TUBE);
WRITE(" MM ID/OD RESPEN");
WRITE("ARGON FLOWRATE = ");PRINT(FL,3,1);
WRITE(" ML/MINEN");
WRITE("SAMPLE FLOWRATE = ");PRINT(SUR,3,2);
WRITE(" ML /MINEN");
WRITE("SPECTROMETER VIEWING POSITION = ");WRITE(VIEWPOS);
WRITE(" WRT CAVITY TOP PLATEEN");
WRITE("NET MICROWAVE INPUT POWER = ");PRINT(PWR,3,1);
WRITE(" WATTS");
WRITE("END]NUMBER OF SPECTRAL LINES SCANNED WAS ");
PRINT(I,2,0);
WRITE("END]INTENSITIES AS A FUNCTION OF ");WRITE(TYPE);
WRITE("END]WAVELENGTH(NM) INT ZERR E2(CM^-1)
      LN(ID/GA) MAX MINEN");

```

FOR J:=1 STEP 1 UNTIL I DO

```

BEGIN
  NEWLINE;
  PRINT(WAVELENGTHEJJ,6,3);
  PRINT(INTEJJ,6,2);WRITE(" ");
  PRINT(INTERREJJ,2,0);WRITE(" ");
  PRINT(UPPENERGYEJJ,8,2);WRITE(" ");
  PRINT(YEJJ,4,2);WRITE(" ");
  PRINT(YMAXEJJ,4,2);
  PRINT(YMINEJJ,4,2);
  END;

```

END;

END;

```
WRITE("ENDTODAYS DATE IS ");WRITE(VDATE);  
CLOSEFILE(1);  
CLOSEFILE(2);  
CLOSEFILE(4);  
CLOSEFILE(5);  
END;END;END
```

Appendix A 5

Computer Program to Convolute Theoretical  
Stark Profile with Doppler and Instrument  
Profiles.

```

CCCCCCCCCCCCCCCCCCCCCCCCCCCCCCCCCCCCCCCCCCCCCCCCCCCCCCCCCCCCCCCC
C
C      PROGRAM: Convolution
C
C      This program is based on DATAPROC.FOR and is used to FULLY
C      PROCESS the Hydrogen Beta spectral line data tabulated by :-
C      C.R.Vidal, J.Cooper and E.W.Smith, The Astrophysical Journal
C      Supplement Series No 214, 25:37-136 (1973).
C
C      It uses "FLYNNN" (convert log to lin data every 0.01 nm).
C
C      Full processing now includes convolution of the theoretical
C      Stark profiles firstly with a Doppler profile (given Gas Temp).
C      then this corrected profile is convoluted with the Instrument
C      profile, assumed to be of Lorentzian form.
C
C      21/10/85, Phil Burke.
C
C      Modified : 23/10/85 Various mods to get program working.
C                : 24/10/85 Now re-arrange data in DoppDat(I) and InstDat(I)
C                :                as required.
C                : 28/10/85 Now output to FinalDat(I) in correct form.
C                : 6/1/86 Change I3 to I4 in "906 Format line" and
C                :                increase array size of FinalDat and ResultDat
C                :                to 2000 because of overflow problem at run time.
C                : 9/1/86 Continuing problems with "array overflows".
C                :                Increase size of arrays to cope plus other mods.
C                : 16/1/86 Small modifications,
C                :                i) Obtain correct total number of points in
C                :                datafile "Final.dat".
C                :                ii) Increase size of search for NoPts in final
C                :                output profile to 2000.
C                : 26/3/86 Can input MEASURED instrument profile as desired.
C
CCCCCCCCCCCCCCCCCCCCCCCCCCCCCCCCCCCCCCCCCCCCCCCCCCCCCCCCCCCCCCCC
C
C      DESCRIPTION OF ARRAYS:
C      ARRAY X          = VALUES OF DELTA ALPHA FROM TABULATED DATA
C      ARRAY Y          = VALUES OF S(ALPHA) -----
C      ARRAY STARKDAT    = VALUES OF S(LAMBDA) FOR LAMBDA AT 0.01 NM INTERVALS
C
C      DESCRIPTION OF VARIABLES:
C      A                = NAME OF SOURCE FILE FROM WHICH THEORETICAL PROFILE
C                        DATA IS READ
C      B                = NAME OF DESTINATION FILE TO WHICH CONVERTED DATA WILL
C                        BE WRITTEN
C      FO               = HOLTZMARK POTENTIAL. "CONVERSION FACTOR", DELTA ALPHA TO
C                        DELTA LAMBDA
C      NE               = ELECTRON DENSITY (INFO ONLY AT THIS STAGE)
C      TE               = ELECTRON TEMPERATURE (-----)
C      NUMX             = MAX NUMBER OF POINTS IN ARRAYS X AND Y
C      NPOLY            = NUMBER OF NEAREST KNOWN POINTS USED IN INTERPOLATION (5)
C      XXX              = X COORDINATE, IN NM FOR WHICH STARKDAT(X) IS REQUIRED
C      POLYN            = RESULT VARIABLE
C
CCCCCCCCCCCCCCCCCCCCCCCCCCCCCCCCCCCCCCCCCCCCCCCCCCCCCCCCCCCCCCCC
C
C      Intend to run program on batch, sequentially reading Stark data
C      from files copied into the default directory from eq. [5000K]
C      then deleted.

```



```

C      Output of Doppler data for checking (Half Profile Only).
      OPEN(LUN3,STATUS='NEW',FILE='InterMed.Dat')
      WRITE(LUN3,50)
      WRITE(LUN3,52) (Tgas, DeltaLam)
      WRITE(LUN3,906) (NoDpPts, Increment)
      WRITE(LUN3,958) (DoppDat(J), J=1, NoDpPts)
50     FORMAT(/,/,/,/, ' DOPPLER PROFILE DATA')
52     FORMAT(' Gas Temp = ', F7.1, ' K : Doppler 1/2 width = ', F7.3, ' nm')

C      Rearrange data in DoppDat(I) using TempDat(I) array.
      DO 58 I = 1, NoDpPts
58     TempDat(I) = DoppDat(NoDpPts+1-I)

C      Now revert to array DoppDat(I).
      DO 59 I = 1, NoDpPts
59     DoppDat(I) = TempDat(I)

C      'Fold' data around the point, NoDpPts and add a mirror image of
      ' profile data into array.

      DO 60 I = 1, NoDpPts-1
60     DoppDat((2*NoDpPts)-I) = DoppDat(I)

C      DEBUG ONLY
C      WRITE(LUN3,958) (DoppDat(J), J=1, 2*NoDpPts-1)

C      Re-initialise USED elements of TempDat(I) to zero.
      DO 64 J=1, NoDpPts
64     TempDat(J)=0.0

C      Now have a full Doppler profile ready to convolute with the
C      Stark profile.

C      END OF CALCULATE DOPPLER PROFILE.

C      BEGIN OF CALCULATE INSTRUMENT PROFILE.

      READ(LUN2,*) InstWidth

C      Now read value of "NoInPts" from file FUND.DAT to decide which
C      instrument profile to use.

      READ(LUN2,*) NoInPts

C      IF NoInPts is zero then calculate Lorentzian as previously done.
C      ELSE NoInPts is actual number of points in measured instrument
C      profile TO BE USED.

      IF (NoInPts .NE. 0) THEN
         READ(LUN2,*) ( InstDat(J) ,J = 1,NoInPts )
      ELSE
C      Convert Half-width of profile to wavenumbers in cm-1.
         DeltaSig=(InstWidth*10**7)/Lamda**2

C      Init Vars and calculate profile until 'cut-off' point reached.
         InstDat(1)=1.000
         LLamda=Lamda
         J=2

```

```

        DO WHILE ((InstDat(J-1) .GT. 0.001) .AND. (J .LE. 1000))
            LLamda=LLamda+Increment
            LSigma=(10**7)/LLamda
            InstDat(J)=1/(1+(2*(Sigma-LSigma)/DeltaSig)**2)
            J=J+1
        END DO
        NoInPts=J-1

    END IF

C      Output of Instrument data for checking (Half Profile Only).
    WRITE(LUN3,70)
    WRITE(LUN3,72) (Lamda, InstWidth)
    WRITE(LUN3,906) (NoInPts, Increment)
    WRITE(LUN3,958) (InstDat(J), J=1, NoInPts)
70    FORMAT(/,/,/,/, " INSTRUMENT PROFILE DATA")
72    FORMAT(" Wavelength = ", F7.3, " nm : 1/2 width = ", F7.3, " nm")

C      Rearrange data in InstDat(I) using TempDat(I) array.
    DO 78 I = 1, NoInPts
78    TempDat(I) = InstDat(NoInPts+1-I)

C      Now revert to array InstDat(I).
    DO 79 I = 1, NoInPts
79    InstDat(I) = TempDat(I)

C      "Fold" data around the point, NoInPts and add a mirror image of
C      profile data into array.

    DO 80 I = 1, NoInPts-1
80    InstDat((2*NoInPts)-I) = InstDat(I)

C      DEBUG ONLY
C      WRITE(LUN3,958) (InstDat(J), J=1, 2*NoInPts-1)

C      Re-initialise USED elements of TempDat(I) to zero.
    DO 84 J=1, NoInPts
84    TempDat(J)=0.0

C      Now have a full Instrument profile ready to convolute with the
C      Doppler corrected Stark profile.

C      END OF CALCULATE INSTRUMENT PROFILE.

C      BEGIN CONVERT THEORETICAL STARK DATA.

C      This part of program deals with conversion of unprocessed
C      Stark data into linear data suitable for convolution.

    OPEN(LUN1,STATUS="OLD",FILE="stark.dat")

C      Read in unprocessed Stark (literature) data (free format).

    READ(LUN1,*) (NE, TE, FO, NUMX,((X(I),Y(I)),I= 1,NUMX ))

C      Use ***FIVE*** nearest points for the polynomial interpolation.
    NPOLY = 5
    MAXPTS = 0

```



```

C      Convert "delta alpha" to "delta lambda" in 'nm'.
C      Note: "delta lambda" is still logarithmically tabulated.

      DO 100 I=1,NUMX
100    X(I)=X(I)*FO*0.1

C      Set first element in array,
C      It is the same for either "delta alpha" or "delta lambda".
      STARKDAT(1)=Y(1)

C      Initialise loop counter.
      I=2
C      Set first wavelength interval to Increment (normally 0.01 nm)
      XXX=Increment
      DO WHILE ((XXX .LT. X(NUMX)) .AND. (I .LE. 1000))
          CALL PLYNN
          STARKDAT(I)=POLYN
          I=I+1
          XXX=Increment*(I-1)
      END DO
      MAXPTS=I-1

C      Determine where the maximum value of the profile stored in
C      STARKDAT( ) occurs. Assign the relevant J value to "NORMX"
C      and the actual profile value to "NORMVAL".
      J=2
      DO WHILE ((STARKDAT(J) .GT. STARKDAT(J-1)) .AND. (J .LE. 1000))
          J=J+1
      END DO
      NORMX=J-1
      NORMVAL=STARKDAT(NORMX)

C      Normalise all values of STARKDAT(J) to NORMVAL

      DO 200 J=1,MAXPTS
200    STARKDAT(J)=STARKDAT(J)/NORMVAL

C      Determine cut-off point, "NoSkPts" after which data
C      values become < 0.02
      I=1
      DO WHILE ((Starkdat(I) .GE. 0.02) .AND. (I .LE. 1500))
          NoSkPts=I
          I=I+1
      END DO
C      This loop SHOULD terminate when StarkDat(NoSkPts+1) is < 0.02

C      Output of Stark (intermediate) data for checking in
C      linear form.
      WRITE(LUN3,248)
      WRITE(LUN3,902) NE
      WRITE(LUN3,904) TE
      WRITE(LUN3,906) (NoSkPts, Increment)
      WRITE(LUN3,958) (StarkDat(I), I=1,NoSkPts)
248    FORMAT(/,/,/,/, " STARK PROFILE DATA (LINEAR FORM)")

C      Rearrange data in StarkDat(I) using TempDat(I) array.
C      So first element in TempDat(I) is the cut-off value (not line
C      centre value) etc., etc.

```

```

DO 300 I = 1, NoSkPts
300 TempDat(I) = StarkDat(NoSkPts+1-I)

C      Now revert to array StarkDat(I)..

DO 350 I = 1, NoSkPts
350 StarkDat(I) = TempDat(I)

C      'Fold' data around the point, NoSkPts and add a mirror image of
C      profile data into array StarkDat(I)..

DO 400 I = 1, NoSkPts-1
400 StarkDat(2*NoSkPts-I) = StarkDat(I)

C      DEBUG ONLY
C      WRITE(LUN3,958) (StarkDat(J), J=1, 2*NoSkPts-1)

C      We now have a correctly arranged theoretical Stark profile ready
C      for the first convolution.
C      END CONVERT THEORETICAL STARK DATA.

C      BEGIN OF CONVOLUTION...1

C      The process devised here may hopefully be explained by taking
C      the first convolution as an example. In this the theoretical
C      Stark profile is corrected for the effect of the random kinetic
C      motion of the emitting hydrogen atoms (convolution with a Doppler
C      profile). This can be thought of as adding up the contributions
C      to the 'observed' profile from all the emitting H atoms, where
C      each atom possesses a different 'Doppler shift' from the unshifted
C      line centre wavelength. The number of atoms possessing the same
C      shift is expressed in the shape of the Doppler profile itself which
C      therefore determines the 'weighting' of each atom's contribution to
C      the observed profile.
C      The convolution process mimics this by evaluating a 'result profile'
C      in which each element of the profile is the summation of all the
C      contributions from ONE Stark profile but centred on different
C      Doppler shift distances from the unshifted line centre wavelength.
C      This is described as 'centring' a 'foreground (Stark) profile' on
C      each wavelength ordinate of a 'background (Doppler) profile'.
C

C      For each point on the background profile, ie
DO 600 I = 1, 2*NoDpPts - 1

C      Evaluate the contribution to the result profile from every point
C      on the foreground profile, ie
DO 500 J = 1, 2*NoSkPts - 1

500 ResultDat(J+(I-1)) = ResultDat(J+(I-1))+(StarkDat(J)*DoppDat(I))
600 CONTINUE

C      DEBUG ONLY
C      WRITE(LUN3,958) (ResultDat(J), J=1, 2*NoSkPts + 2*NoDpPts -2)

C      Information. The mid point of the array ResultDat occurs at
C      (NoSkPts + NoDpPts - 1) and the total number of points in the

```

```

C      array is twice this value.

C      Find position of maximum in array, to enable normalisation.
      J=2
      DO WHILE ((ResultDat(J) .GT. ResultDat(J-1)) .AND. (J .LE. 1500))
        J=J+1
      END DO
      PeakVal=ResultDat(J-1)

C      Now do actual normalisation.
      DO 650 J=1, 2*NoSkPts + 2*NoDpPts - 2
650    ResultDat(J)=ResultDat(J)/PeakVal

C      Output of Doppler corrected Stark profile data for checking,
C      (half profile only).
      J=NoSkPts+NoDpPts-1
      WRITE(LUN3,700)
      WRITE(LUN3,702) NE
      WRITE(LUN3,704) TE
      WRITE(LUN3,706) (J, Increment)
      WRITE(LUN3,758) (ResultDat(I), I=J, 2*J-1)
700    FORMAT(/,/,/,/, 'DOPPLER CORRECTED STARK PROFILE DATA')

C      END OF CONVOLUTION...1

C      BEGIN OF CONVOLUTION...2
C      Same as first convolution except using the Doppler corrected Stark
C      profile as the foreground profile and the Instrument profile as the
C      background profile.

C      For each point on the background profile, ie
      DO 800 I = 1, 2*NoInPts - 1

C      Evaluate the contribution to the profile from every point
C      on the foreground profile, ie
      DO 750 J = 1, 2*NoSkPts + 2*NoDpPts - 2

750    FinalDat(J+(I-1)) = FinalDat(J+(I-1))+(ResultDat(J)*InstDat(I))
800    CONTINUE

C      Information. The mid point of the array FinalDat occurs at
C      (NoSkPts + NoDpPts + NoInPts - 2) and the total number of points
C      in the array is twice this value.

C      Find position of maximum in array, to enable normalisation.
      J=2
      DO WHILE ((FinalDat(J) .GT. FinalDat(J-1)) .AND. (J .LE. 1500))
        J=J+1
      END DO
      PeakVal=FinalDat(J-1)

C      Now do actual normalisation.
      DO 850 J=1, 2*NoSkPts + 2*NoDpPts + 2*NoInPts - 4
850    FinalDat(J)=FinalDat(J)/PeakVal

C      Output of Instrument and Doppler corrected Stark profile data,
C      (half profile only).
C      Output to TWO data files, one of which will be the actual
C      source file for EDFIT.FOR

```

```

J=NoSkPts+NoDpPts+NoInPts-2
WRITE(LUN3,900)
WRITE(LUN3,902) NE
WRITE(LUN3,904) TE
WRITE(LUN3,906) (J, Increment)
WRITE(LUN3,958) (FinalDat(I), I=J, 2*J-1)
900  FORMAT(/,/,/,/, ' INSTRUMENT AND DOPPLER CORRECTED STARK PROFILE DATA')
902  FORMAT(' Electron Density = ', E12.4, ' CM-3')
904  FORMAT(' Electron Temperature = ', I4, ' K')
906  FORMAT(' Number of points = ', I4, ' : Interval = ', F7.3, ' nm',/)
958  FORMAT(40(10(F7.3,X),/),/)

C      Open the file used to hold the Stark data for EDFIT.FOR
OPEN(LUN4,STATUS='NEW',FILE='Final.Dat')

C      Determine cut-off point, "NoPts" after which data
C      values become < 0.01, Note: Starting from the line centre.
I=J
DO WHILE ((FinalDat(I) .GE. 0.01) .AND. (I .LE. 2000))
    NoPts=I
    I=I+1
END DO

C      This loop SHOULD terminate when FinalDat(NoPts+1) is < 0.01

WRITE(LUN4,966) (NoPts-J+1)
WRITE(LUN4,968) (FinalDat(I), I=J, NoPts)
966  FORMAT(' ',I5)

C      968      FORMAT(40(10(F7.3,' ',X),/),/)
968  FORMAT(' ',E12.4)

C      END OF CONVOLUTION...2

C      END OF PROGRAM.

CLOSE(LUN1)
CLOSE(LUN2)
CLOSE(LUN3)
CLOSE(LUN4)
CLOSE(LUN5)
END

```

```

CCCCCCCCCCCCCCCCCCCCCCCCCCCCCCCCCCCCCCCCCCCCCCCCCCCCCCCCCCCCCCCC
C
C      This program module contains the subroutine given in the paper
C      by C.R.Vidal, J.Cooper and E.W.Smith, The Astrophysical Journal
C      Supplement Series No 214, 25:37-136 (1973).
C
C      This subroutine is used to interpolate between their tabulated
C      data by evaluating a polynomial of degree N-1 to pass through
C      N user selected points. It is essential for the conversion of
C      profile data from reduced Stark parameter "delta alpha" to
C      actual wavelengths at 0.01 nm intervals ie, tables contain
C      insufficient points to do this.
C
C      Date           :      12/3/85.
C      Programmer     :      Phil Burke.
C      Modified       :      26/3/85, Phil Burke. "J" possibly not
C                        defined on exit from "J=NM1,NUP" do loop
C                        so loop replaced with a "Do While" loop.
C
CCCCCCCCCCCCCCCCCCCCCCCCCCCCCCCCCCCCCCCCCCCCCCCCCCCCCCCCCCCCCCCC

```

```

      SUBROUTINE PLYNN
C      For the point XXX to be interpolated the NPOLY nearest known points
C      are chosen and a polynomial of degree NPOLY-1 is fitted through
C      these points.
C      X and Y are the arrays which contain the "delta alpha" and Stark
C      profile ordinates respectively. NUMX is the total number of the
C      known points on the curve.
C      I intend to read in raw Stark data sequentially and assign it to
C      these arrays.
C      The result is POLYN.

      COMMON/F45/ X(100), Y(100), NUMX, NPOLY, POLYN, XXX

      POLYN = 0.0
      NM = (NPOLY + 1)/2
      NM1 = NM + 1
      NUP = NUMX + NM1 - NPOLY

      J=NM1
      DO WHILE ((J .LT. NUP) .AND. (XXX .GT. X(J)))
      J=J+1
      END DO

      L = J - NM
      LLL = L + NPOLY - 1
      DO 6 K = L,LLL
      TERM = 1.0
      DO 5 M = L,LLL
      IF (K .EQ. M) GO TO 5
      TERM = TERM * (XXX - X(M))/(X(K) - X(M))
5      CONTINUE
      TERM = Y(K) * TERM
6      POLYN = POLYN + TERM
      RETURN
      END

```